Elucidation of Reaction Mechanism for High Energy Cathode Materials in Lithium Ion Battery using Advanced Analysis Technologies

Hideyuki Komatsu

Contents

Chapter 1. General Introduction

1.1. Background

Global warming is a problem that has not been solved in recent environmental problems. The atmospheric temperature rises due to the emission of greenhouse gases. Carbon dioxide (CO_2), methane, nitrous oxide, hydrofluorocarbons, perfluorocarbons, sulfur hexafluoride are regulated greenhouse gases under the Kyoto Protocol international treaty. CO_2 accounts for about 70% of the greenhouse gas emissions, 70% of which are generated by power stations, industrial processes and transportation fuels. From 1909 T type Ford mass production by Ford Motor Company to the present, the main source of power for automobiles is still the gasoline engine. The rotational kinetic energy is transferred to the driving system via the piston by the combustion energy of gasoline. Since the combustion efficiency of the internal combustion engine is consumed by heat loss, the theoretical efficiency is also about 30%, but actually practical efficiency is less than 20% even in an ideal constant speed operation state. On the other hand, electric car first produced by Thomas Parker in 1884 by using high-capacity rechargeable batteries, the energy efficiency is about 80% by converting the electric energy stored in the battery into kinetic energy by a motor. Considering Well to Wheel (overall efficiency from Well (Well = oil well, oil field) to Wheel (Wheel = car, terminal consumption)), electric vehicles are about 3 to 4 times more energy efficient than gasoline cars, even if all electricity generation is thermal power generation. Lithium-ion batteries capable of repeated charging and discharging are used for these electric vehicles.

1.2. History of Lithium-ion Batteries for EVs

The commercialization of lithium-ion batteries for mobile electronics was made by Sony Corporation in 1991.[1] Lithium-ion batteries are common rechargeable batteries with a high energy density, few memory effect and low self-discharge. This lithium-ion battery is configured $LiCoO_2$ for the positive electrode[2], graphite for the negative electrode[3], and organic solvent with lithium salt for electrolyte[4]. As shown in Figure 1, lithium-ion batteries are superior to other storage batteries in energy density.[5] After that, improvements of additives in electrolyte to suppress side reactions, electrode structure and active materials have been studied for over ten years, and the application to electric vehicles became realistic due to the appearance of cost-effective cathode materials such as $LiMn_2O_4$[6] and $LiMeO_2$ (Me = Ni[7], $Ni_{1-x}Co_x$[8], $Ni_{0.8}Co_{0.15}Al_{0.05}$[9], $Ni_{1-x}Mn_x$[10], $Ni_{1/3}Mn_{1/3}Co_{1/3}$[11-12]), which is an alternate candidate cathode to $LiCoO_2$ containing expensive and less minable quantity cobalt. Mitsubishi Motors began production of the world's first mass-produced electric vehicle, i-MiEV, in 2009, followed by production of LEAF by Nissan Motor Company in 2010 with lithium-ion batteries. Nine years have passed since commercial electric cars were released, but the sales ratio of electric vehicles including plug-in hybrid cars in is still few as shown in Figure 2.[13] It is delaying the popularization of electric vehicles that the energy density of the battery is insufficient, that it takes a long time to charge, and that the electric vehicle itself becomes expensive by loading a large amount of expensive batteries. Moreover, lithium-ion batteries are low in safety, so it is necessary to take robust and excessive safety measures. That is, high energy, quick chargeable, low-cost, non-flammable batteries are required.

1.3. Mechanism of Lithium-ion Batteries

Lithium-ion battery is a device which can take out electrical energy to an external circuit by utilizing the electrochemical potential difference between positive and negative electrodes with insertion and extraction of lithium-ion. The components of the lithium-ion battery in the typical $LiMeO_2$/graphite cell are shown in the Figure 3. Lithium-ion battery is composed of cathode, anode, separator, non-aqueous electrolyte, current collector, and exterior case. Electrode is composed of the active material for storing electric energy by insertion/reinsertion of lithium, conductive additive for electron conductivity, and a binder for mechanical strength. Electrolyte penetrates the air gap, and ions are delivered in this air gap. The separator is provided to prevent electrical contact between the positive and negative electrodes, and a porous polypropylene separator is generally used. The electrolyte is organic solvent containing 1 M $LiPF_6$, and a mixed solvent system of a dissociative solvent and a low viscosity solvent shows excellent battery characteristics. For the current collector, aluminum and copper is used for cathode and anode, respectively.

In the charging process (storing energy in the cell), the cathode active material oxidizes and releases Li into the electrolyte. While at the same time, the electrons are conducted from cathode to anode, and anode become reduced by insertion of lithium-ion. In the charging process, each electrode reaction and total reaction are expressed as the following equations;

$$\textit{Cathode Reaction} \qquad LiMeO_2 \rightarrow Li_{1-x}MeO_2 + xLi^+ + xe^- \qquad \textbf{(1.1)}$$

$$\textit{Anode Reaction} \qquad C_6 + xLi^+ + xe^- \rightarrow Li_xC_6 \qquad \textbf{(1.2)}$$

$$\textit{Cell Reaction} \qquad C_6 + LiMeO_2 \rightarrow Li_xC_6 + Li_{1-x}MeO_2 \qquad \textbf{(1.3)}$$

In the discharge process, releasing energy to the external circuit by reverse reaction. During cell reaction, the active material keeps the host structure so-called topotactic reaction and it consequently shows high reversibility in the current generally lithium-ion battery system. Equation (1.1) and (1.2) is called a half-cell reaction, since it will occur at a specific electrode-electrolyte interface. It cannot occur in isolation, but only when coupled to another half-cell reaction within a two-electrode electrochemical cell. The open-circuit voltage V_{OCV} of such a lithium cell is given by the difference in the lithium chemical potential between the cathode ($\mu_{Li(c)}$) and the anode ($\mu_{Li(a)}$) in space-charge layer as:

$$FV_{OCV} = \mu_{Li(c)} - \mu_{Li(a)} \quad \textbf{(1.4)}$$

where F is the Faraday constant. Space-charge layer is defined subsurface in active material in the applying of an electric field. The cell voltage V_{OCV} is determined by the energies involved in both the electron transfer and the Li^+ transfer. Figure 4 shows a schematic energy diagram of a cell at open circuit. Each reaction has a characteristic Gibbs energy change that determines whether it is thermodynamically favorable. The Gibbs energy change is related to the equilibrium potential difference from the electrode to the electrolyte according to:

$$E_{eq} = -\frac{\Delta G}{nF} \quad \textbf{(1.5)}$$

where E_{eq} is the potential difference on some external reference scale for which the reaction is at equilibrium ($\Delta G = 0$). This is called the equilibrium potential or the standard cell potential of the electrochemical reaction. From the standard

thermodynamic relation as:

$$G\Delta = -RTlnK \tag{1.6}$$

is follows

$$E - E_{eq} = \frac{RT}{nF} lnK \tag{1.7}$$

This is the Nernst equation which is a universal thermodynamic expression and most important equation in the field of electrochemistry. Where *E* is the electrode potential, *R* is the molar gas constant, *T* is the temperature, *n* is the number of mobile electrons, and *K* is the rate constant of systems. It is absolutely consisting of systems at thermodynamic equilibrium, but it does not applicable apply to systems at non-equilibrium. If the reactants are ideal, and that activation energy can be treated as constant, then for the conversion between unimolecular reduced and oxidized species:

$$[O_x] = [Red] exp\left(\left(\frac{nF}{RT}\right)(\varphi_s - \varphi_l - E_f)\right) \tag{1.8}$$

Hence at equilibrium, the concentrations of reactants and products at the electrolyte and space-charge layer are related by an expression which depends on the potential difference between the two phases, and reaction parameters: E_f, the reduction potential of the reaction measured on the same potential scale as the electrode and space-charge layer potential difference. The quantity

$$\eta = \varphi_s - \varphi_l - E_{eq} \quad \textbf{(1.9)}$$

where η is known as the overpotential and is to reaction occurring at the space-charge layer. Where φ_s and φ_s are the electric potential in the electrode and in the electrolyte potential, respectively. In actual battery systems, resistive film (so called solid-electrolyte interface, SEI) might form on the surface of solid particles which is resulting in additional potential losses in the electrodes. The governing equation is then according to

$$\Delta\varphi_{SEI} = i * R_{SEI} \quad \textbf{(1.10)}$$

where R_{SEI} is denotes a generalized film resistance. The activation overpotentials η, for all electrode reactions in the electrode then receives an extra potential contribution, which yields

$$\eta = \varphi_s - \Delta\varphi_{SEI} - \varphi_l - E_{eq} \quad \textbf{(1.11)}$$

Actual cell voltage contains the Ohmic loss, interface reaction resistance, and the diffusion resistance in electrolyte and solid of active materials. The work energy of the battery (Wh/L or kg) is multiplied by the capacity (Ah) and the voltage (V) per volume or weight. Therefore, the measures for high energy density are conceivable as follows: (1) Increase the available capacity of the cathode active material. Theoretical capacity of current $LiMeO_2$ system is almost 275 to 280 mAh g^{-1}. However, Available capacity is less than 150 to 200 mAh g^{-1} due to considering the use within a reaction range that does not cause an irreversible change in the crystal structure. Optimization of transition

metal species and new solid material search for stabilization of the host structure are main strategy.

(2) Increase the reaction potential of the cathode active material. The operating potential of the positive electrode is determined by the transition metal species, anion species and crystal structure.

(3) Increase the capacity of the anode active materials. The graphite anode shows a sufficiently low voltage around 50 mV vs Li. Increase the volumetric or gravimetric capacity needs for higher energy density.

(4) Reduce the overvoltage by optimizing the electrode structure and controlling the active material interface with SEI.

(5) Reduce the amount of inactive materials that are not involved in energy storage directly. Thinning of current collector and separator, reduction of conductive additive and binder usage can be cited. As a result, cell volume and weight are reduced, however, if conductive additive is reduced too much, the voltage loss is increase due to electronic resistance. It is necessary to consider the mechanical strength design of the battery and manufacturing process adaptation in the field of engineering.

1.4. High Energy Cathode Materials

In this section, we described developing the cathode materials, and the potentiality of high electric potential and high capacity cathode materials is discussed. Figure 5 shows the relationship between theoretical capacity and average reaction potential of cathode materials. Theoretical capacity is calculated based on the case that all of lithium delithiated/lithiated from cathode active material, which is determined lithium content and molecular weight of the active material. An ideal positive electrode

material has a path through which lithium-ions can diffuse in the structure with large mobility. It is important that the potential-energy gap is small between occupied site of lithium-ion and vacant site that can be moved to Lithium-ion. In addition, it is required for rapid reaction that the activation energy during lithium migration is small, the polarizability of the anion is large, and the crystal structure is easy to distort. Currently, positive electrode materials having excellent physical properties are limited to three types of crystal structures of spinel, layered rocksalt and olivine.

Crystalline structure of spinel $LiMn_2O_4$ cathode material as shown in Figure 6 contain half lithium for transition metal, which is almost half theoretical capacity compare to layered rocksalt-type cathode material. $LiMn_2O_4$ is the most common spinel cathode material[14-16] because it is easy to synthesize, has high temperature stability and is inexpensive due to manganese is relatively stable market price and supply. $LiMn_2O_4$ is a cubic spinel structure of space group $Fd\bar{3}m$, lithium occupies the tetrahedral 8*a* site, and manganese occupies octahedral 16*d* sites. Oxygen occupies 32*e* site and takes the coordination of face-centered cubic lattice. The 16*c* octahedral site is vacant, and when lithium-ions diffuse within the structure, it occurs by hopping to three-dimensionally from 8*a* site to 16*c* site and from 16*c* site to 8*a* site as shown in Figure 7.[17]

Partly substituted spinel cathodes were reported with two kinds of performance improvement. One is structural stabilization related to weak Mn-O bonding during charging and discharging.[18] Pure $LiMn_2O_4$ spinel is inferior in cycle durability for practical use, which capacity decrease 60% for initial capacity at 100th cycle.[19] Partial substitution of elements such as Me-O (Me = Cr, Co, Al, Ni) with high binding energy has improved cycle performance.[19-21] These partially substituted $LiMe_xMn_{2-x}O_4$ spinel are suitable for practical LIB cathode materials. The second effect of pertly substitution

is increased reaction potential over 4.5 V vs. Li/Li^+. These unique behaviors were explained that substituted element mainly assume charge compensation during delithiation and lithiation of lithium-ion.[22-24]

Nickel-substituted lithium manganese spinel $LiNi_{0.5}Mn_{1.5}O_4$ shown in Figure 8 has been extensively studied as a preferred candidate of high-voltage positive electrode materials because it shows a wide potential plateau at ~4.75 V vs Li/Li^+ as well as its low toxic nature.[25,26] Compare to other applied candidate cathode materials, it can be a high energy density as shown in Figure 9.[27] However, cyclability, initial charging and discharging efficiency, and columbic efficiency during cycle are not enough for practical use due to high potential redox above the HOMO of the carbonate electrolytes at 4.0-4.3 V vs Li. Moreover, lattice volume change is largely 6% with cracking of particles, which is difficult making stable SEI, as a result, continuous irreversible reaction occurs with the electrolyte. In order to stabilize the interface structure, third element of dopant was reported by Liu *et al.* in 2009.[28] Few Fe substituted $LiNi_{0.42}Fe_{0.08}Mn_{1.5}O_4$ exhibits remarkably superior cycling performances and higher rate capabilities than the pristine $LiMn_{1.5}Ni_{0.5}O_4$. Liu *et al.* also suggested that the enhancement mechanisms are attributed to (i) stabilization of the structure with cation-disorder in the 16*d* octahedral sites of the spinel lattice, (ii) suppression of the formation of a thick SEI layer due to the Fe-enrichment and Ni-deficiency on the surface, (iii) production of Mn^{3+} and the consequent enhancement in electronic conductivity, and (iv) much reduced polarization loss arising from both fast charge transfer kinetics and lithium-ion diffusion kinetics in the bulk.[28] $LiNi_{0.5}Mn_{1.5}O_4$ has two kinds of crystallographic symmetries, primitive simple cubic of space group $P4_332$ in which Ni and Mn are ordered superlattice arrangement at 4*b* and 12*d* site, and face-

centered disordered spinel of space group $Fd\bar{3}m$.[29-31] These can be selectively synthesized by changing the calcinating conditions,[32] and the disordered $LiNi_{0.5}Mn_{1.5}O_4$ is characterized by excellent electron conductivity and excellent in high rate capability even for micron-sized primary crystal particles.[33]

First practical applied $LiCoO_2$ layered rocksalt-type oxide cathode material shown in Figure 10 has high theoretical capacity 274 mA h g^{-1}. But actually, their electrochemical capacities are conventionally limited to ca. 150 mA h g^{-1} with a potential up to 4.2 V *vs.* Li/Li^+, which is limited to only half of lithium delithiation due to irreversible phase transformation occurred as hexagonal to monoclinic. Increase the amount of mobile lithium is possible to by enabling reversible phase change by surface coating.[34] However cobalt itself is expensive rare metal, so new layered positive electrode material that replaces $LiCoO_2$ is still present have been studied.

$LiNiO_2$ is same crystalline structure of $LiCoO_2$, which is α-$NeFeO_2$-type structure of space group $R\bar{3}m$. It is capable of stably delithiation/lithiation to 0.7Li and its practical capacity is corresponding to 190 mA h g^{-1}. It is expected to be an alternative cathode material to $LiCoO_2$ because nickel is a transition metal less expensive than cobalt with large capacity, but it has several problems in practical application. It is difficult to synthesize high purity[35-41] and it is necessary to synthesize it under an oxygen atmosphere sufficient to obtain chemical stoichiometric composition. Ni^{2+} is easily cation-mixed into the 3*a* site of the Li layer, and $Li_{1-x}Ni_{1+x}O_2$ is easily generated at synthesis. It is reported that this non-chemical stoichiometric composition hinders the diffusion performance of Li and deteriorates battery characteristics.[42] In addition, delithiated $Li_{1-y}NiO_2$ ($y > 0.7$) easy release oxygen around 200 ºC with significant exothermic reaction.[43]

Due to the above-mentioned problems, single phase $LiNiO_2$ has not been practical

use. However, solid solution layered cathode with Co, Mn and Al exhibited excellent electrochemical characteristics, and practical use for advanced lithium-ion battery cathode materials. Cobalt in the $LiNi_{0.8}Co_{0.2}O_2$ and $LiNi_{0.8}Co_{0.15}Al_{0.05}O_2$ suppress cation mixing of Ni into the lithium layer and contributes to stabilizing the structure during charge and discharge. These cobalt substitutions facilitate simple synthesis, and thermal stability is improved by further doping of Al.[44] Also $LiNi_{0.5}Mn_{0.5}O_2$ and $LiNi_{1/3}Mn_{1/3}Co_{1/3}O_2$ are under intense investigation because there has high capacity about 200 mA h g^{-1} charging at 4.5 to 4.6 V even less cobalt content.

Recently, solid solutions of lithium-rich layered oxide materials (LLOs) especially lithium-rich manganese oxide (Li_2MnO_3) and other layered transition metal (TM) oxide ($LiMeO_2$, Me = Co, Ni, Al etc.) are the most featured active material for the cathode of LIBs.[45,46] A high capacity of over 250 mA h g^{-1} and comparatively stable cyclability have been reported for these LLOs cathode.[47] It has been reported that the battery characteristics drastically change depending on the solid solution amount of Li_2MnO_3 and a discharge capacity of approximately 280 mA h g^{-1} can be obtained by charging over 4.6 V to 4.8 V at room temperature.[48-52] Two factors are assumed as a high-capacity mechanism that activation of Li_2MnO_3 phase and structure stabilization of $LiMeO_2$ phase. Li_2MnO_3 structure is monoclinic of space group $C2/m$, which structure arrangement with $Li[Li_{1/3}Mn_{2/3}]O_2$ is very similar to the rhombohedral $LiMeO_2$ structure as shown in Figure 11a. In an ideal Li_2MnO_3 structure, lithium is arranged in the transition metal layer at a triple period, $[\sqrt{3} \times \sqrt{3}]$ R30° type super lattice structure formed as shown in Figure 11b. It has been reported that Li_2MnO_3 having good crystallinity is inherently electrochemically inactive and shows electrochemical activity with a decrease in crystallinity.[53] It was suggested that partially substitution of other element into Li_2MnO_3 phase leads to decrease in

crystallinity and activated by solid solution of $LiMeO_2$. On the other hand, it is considered that the electrochemically inactive Li_2MnO_3 phase disperses in the $LiMeO_2$ phase to play a role of a stable pillar and it is possible to extract a large amount of Li from the $LiMeO_2$ layer. In any case, it is a very difficult task to elucidate the reaction mechanism of the Li-rich positive electrode where other elements are present at the same crystal structure site, and discussion by innovative analysis method is necessary.

Olivine-type cathode material was firstly reported by Padhi *et al.* in 1997.[54] $LiFePO_4$ is one of commercially low-cost cathode material. Not only that the cost effectiveness, $LiFePO_4$ has some superior cell performances as follows, react at relatively high potential around 3.5 V vs. Li/Li^+ by Fe^{2+}/Fe^{3+} redox[54], stable cyclability durable for practical use[55], available capacity close to theoretical capacity of 170 mA h g^{-1} optimized by synthesized condition[56], and its reached 550 Wh kg^{-1} over $LiCoO_2$ and $LiNiO_2$, and superior thermal property at charging state of $FePO_4$ due to strong polyanion bonding affect oxygen desorption.[56] Crystalline structure shown in Figure 12, it enables high-speed Li diffusion by one-dimensional path. In the same manner, $LiMePO_4$ (Me = Mn, Co, Ni) in which redox species are replaced with other metals has also been studied. $LiMnPO_4$ has an operating potential of about 4.1 V by redox of Mn^{2+}/Mn^{3+}, which is expected to have higher energy than $LiFePO_4$.[54] However, the vacancy-formation energy of $LiMnPO_4$ higher than $LiFePO_4$, which is expected that the nucleation rate of $MnPO_4$ phase in $LiMnPO_4$ is 10^{-3} times slower than that in $LiFePO_4$.[57] Nonetheless, improving the synthesis method and the surface condition, it is reported that reversible capacity rise to 140 mA h g^{-1}.[58] However, sufficient battery characteristics for practical use such as $LiFePO_4$ is not obtained due to the above-mentioned slow phase transition kinetics. $LiCoPO_4$ shows more high redox potential around 4.8 V, available capacity was reported 100 mA h g^{-1}, which is equivalent energy

density to that of layered rocksalt-type $LiCoO_2$ (120 mA h g^{-1} × 4 V = 480 mW h g^{-1}).[59] $LiNiPO_4$ is expected that Ni^{2+}/Ni^{3+} redox reaction occurred over 5 V by the first principle calculation,[60] and in the experimental result, since electrolyte is no stable at 5 V or higher, sufficient battery characteristics have not been obtained yet.[61]

Currently confirmed available high-potential and high-capacity cathode are shown in Figure 13. $LiNi_{0.5}Mn_{1.5}O_4$ spinel and LLOs are the most candidate high-potential and high-capacity cathode materials in the liquid organic solvent electrolyte system, respectively.

1.5. Advanced Analysis Technology for Battery

Battery reaction with electrochemical lithiation/delithiation is black box behavior due to the reaction occurred in the sealed cell. Especially, nonequilibrium behavior doesn't kept with disassemble the cell, as a result, we achieved only the final equilibrium state of the complex battery reaction. These battery reactions are classified roughly into three groups according to time and space scale as shown in Figure 14. All the reactions occur at the sequence of events with interact with each other, although they differ in time-space scale. Formerly, many researchers relied on the perfuming and analyzing used electrochemical impedance spectroscopy[62,63], galvanostatic and potentiostatic intermittent titration technique[64-69], and ex situ analysis[70]. Ex situ studies represented by laboratory X-ray sources and other characterization techniques are still important for understanding equilibrium behavior of battery materials.[70]

The first in situ study was reported by Chianelli *et al.* investigating structural changes induced by lithium insertion into the Li-TiS_2 cell.[71] With the time resolution at that time, it was thought that it is advantageous that the material damage is less by

non-disassembled, and the analysis error between samples is reduced by observing the same sample. Due to the improvement of time-resolution and spatial-resolution, analytical methods corresponding to the behaviors in the battery have been remarkably developed in recent years, understanding of irreversible reaction of the interface[72,73], non-equilibrium phase transition behavior of the cathode material[74,75], and reaction distribution of the electrode[76,77] has advanced. Hence, understanding of the non-equilibrium behavior with operando analysis and multiscale analysis with specialized method for batteries are very important for improving the next generation battery.

1.6. Research Objective

As mentioned above, high-potential $LiNi_{0.5}Mn_{1.5}O_4$ and high-capacity LLOs cathode materials are necessary to improve the lithium-ion battery performance from the viewpoint of high energy. By using advanced analysis technology specialized for battery analysis, we clarify the unexplained of these candidate materials and contribute to the realization of next generation batteries.

Recently, several operando techniques have been developed to investigate the local structure and crystalline structure in the batteries. There are in situ (in operando) static NMR[78-88], time resolved X-ray diffraction (TR-XRD) and X-ray absorption spectroscopy (XAS)[74,89-92]. The in situ NMR can investigate the local structure with element and isotopic-selective especially powerful tools for light-element. The in operando XRD and XAS can investigate the non-equilibrium crystalline and electronic structure of electrode materials. On another front, more sophisticated ex situ analysis also has been developed to investigate the detailed crystalline structure corresponding to the local atomic level.[93-95]

In the present thesis, we focused attention the two material of high-energy cathode materials, attempted to understand the detailed reaction phenomena with advanced analysis techniques. One of them is phase transition behavior with delithiation/lithiation of $LiNi_{0.5}Mn_{1.5}O_4$, which was investigated by applying the in situ NMR and TR-XRD. The second is complexed charge compensation phenomena of LLOs, which was investigated by applying the neutron and synchrotron X-ray diffraction, hard X-ray photoelectron spectroscopy (HAX-PES), and resonant X-ray diffraction spectroscopy (RXDS).

1.7. Outline of the Present Thesis

The present thesis consists of seven chapters, presenting high-energy cathode materials and advanced analysis techniques of lithium-ion batteries, observing the fast phase transition behavior, and elucidating the reaction mechanism of complexed charge compensation phenomena.

In chapter 1, basic of the lithium-ion batteries and the phenomena occurring within the batteries are described. Especially, the research strategy for high-energy battery are focused on the three major type of cathode materials. In order to apply these candidate cathode materials to practical use, understanding the reaction behavior inside the battery is important. On the basis of the previous reports, application of advanced analysis technology is presented (this chapter).

In chapter 2, delithiation and lithiation behaviors of ordered spinel $LiNi_{0.5}Mn_{1.5}O_4$ and comparative disordered spinel $LiNi_{0.4}Mn_{1.6}O_4$ were investigated by using in situ (in operando) and ex situ $^{6,7}Li$ MAS NMR spectroscopy. The Li environment and lithiation of each material is discussed.

In chapter 3, the phase transition dynamics of $LiNi_{0.5}Mn_{1.5}O_4$ is elucidated on high rate charging-discharging using operando TR-XRD. The phase transition pathways dependent on the reaction rate are shown, together with possible explanation for this unique transition behavior is discussed.

In chapter 4, the crystal structures of Li-rich manganese-based layered oxide to elucidate the relationship between the structure and electrochemical performance of the compounds using neutron and synchrotron X-ray powder diffraction analyses in combination is discussed.

In chapter 5, the redox behavior of lattice oxygen and transition metals in a LLOs are investigated by using HAX-PES. The reversibility and structural rearrangement with charge and discharge subsequent cycling are discussed.

In chapter 6, the effect of the substituted Ni into LLOs cathode performances by using a combination of RXDS and operando XAS. We discuss the influence of the irreversible and reversible migration of Ni and Mn ions on the electrode performance.

In chapter 7, conclusion obtained from the present studies and prospect for the future lithium-ion batteries are presented.

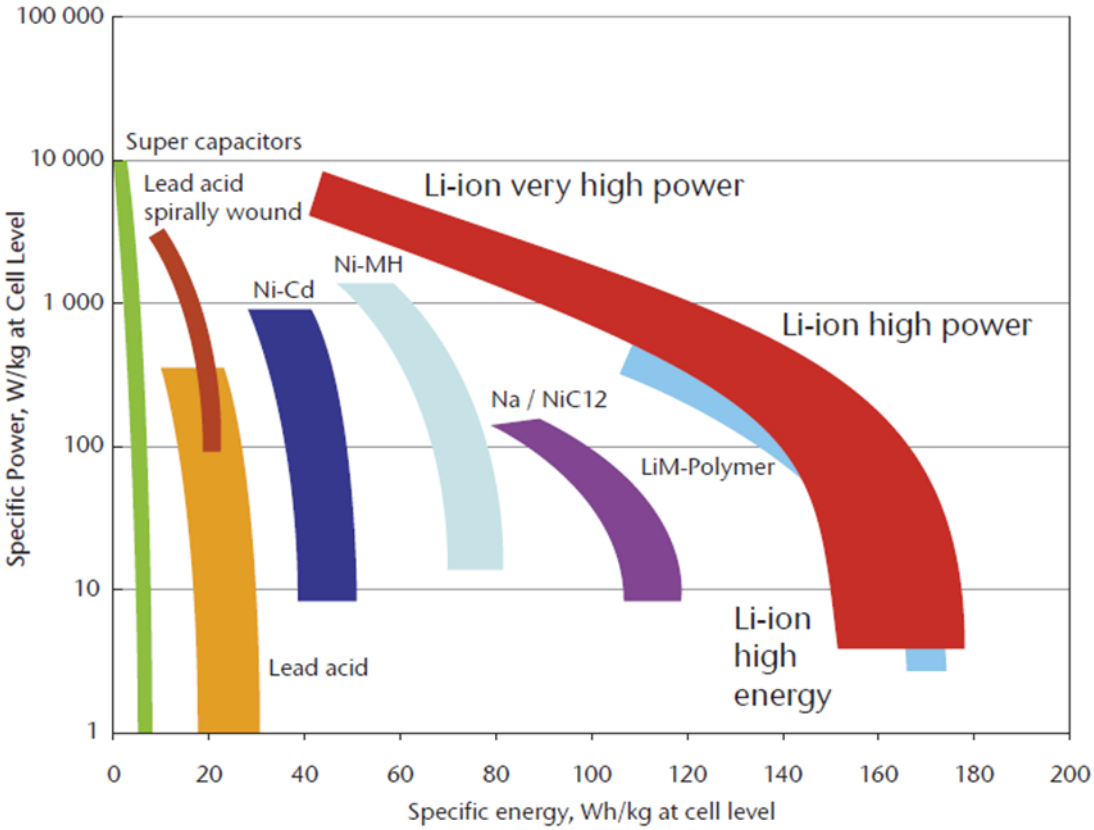

Figure 1. Specific energy and specific power of different battery types.[5]

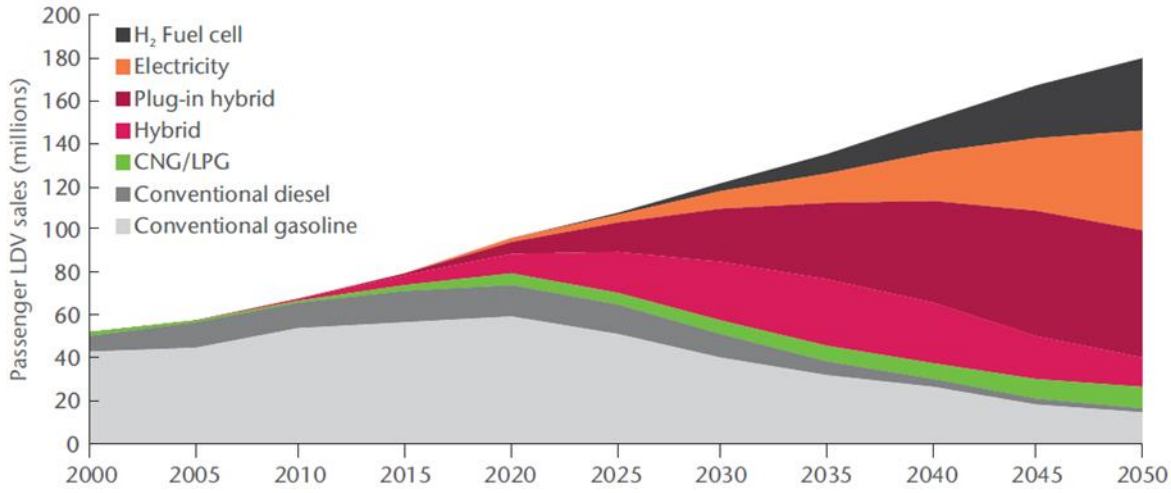

Figure 2. Annual light-duty vehicle sales by technology type, BLUE Map scenario.[13]

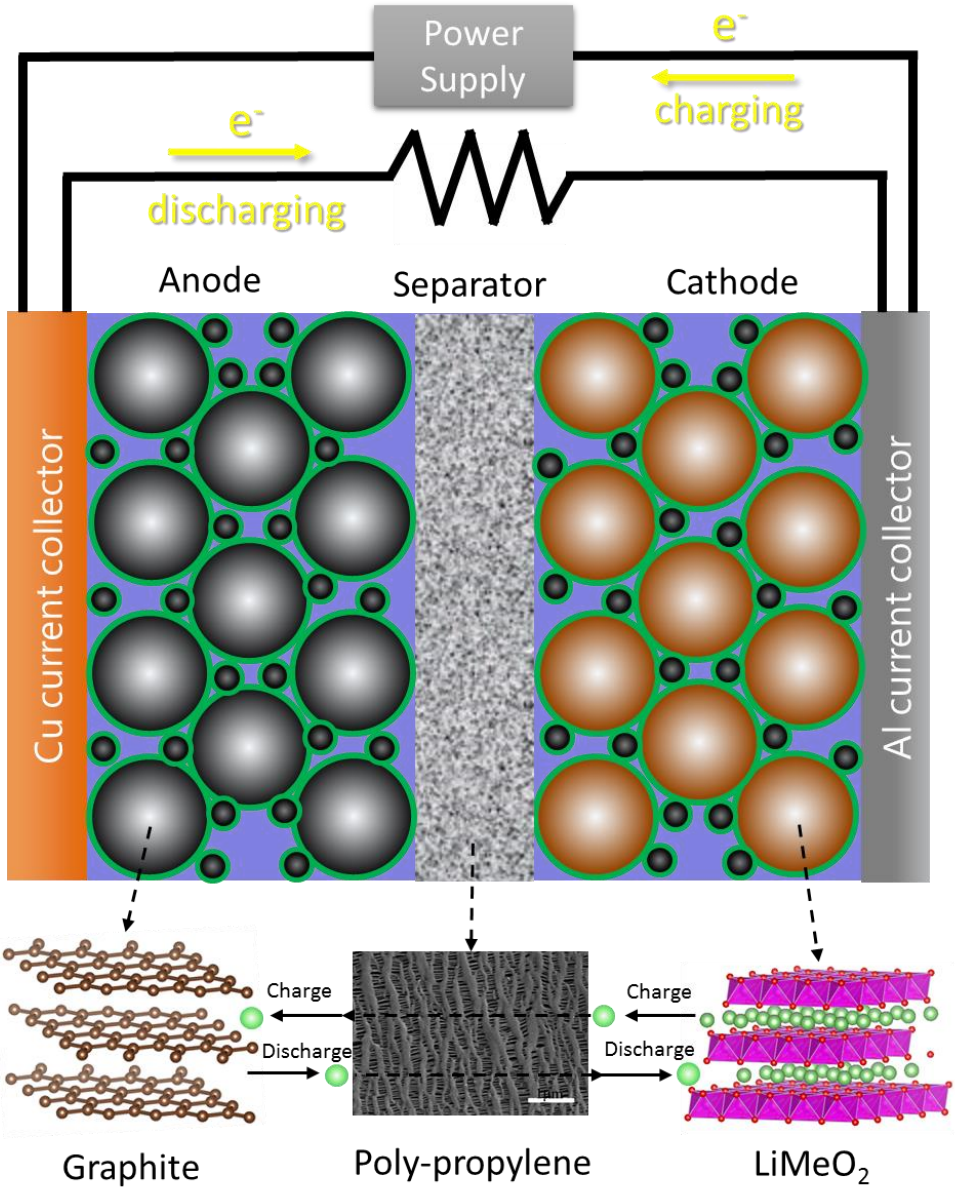

Figure 3. Schematic diagram of a lithium-ion cell consisting of (right) an intercalation cathode on an aluminum current collector, (middle) porous poly-propylene separator, and (right) a graphite anode on a copper current collector. Under images are microscale structure of these materials.

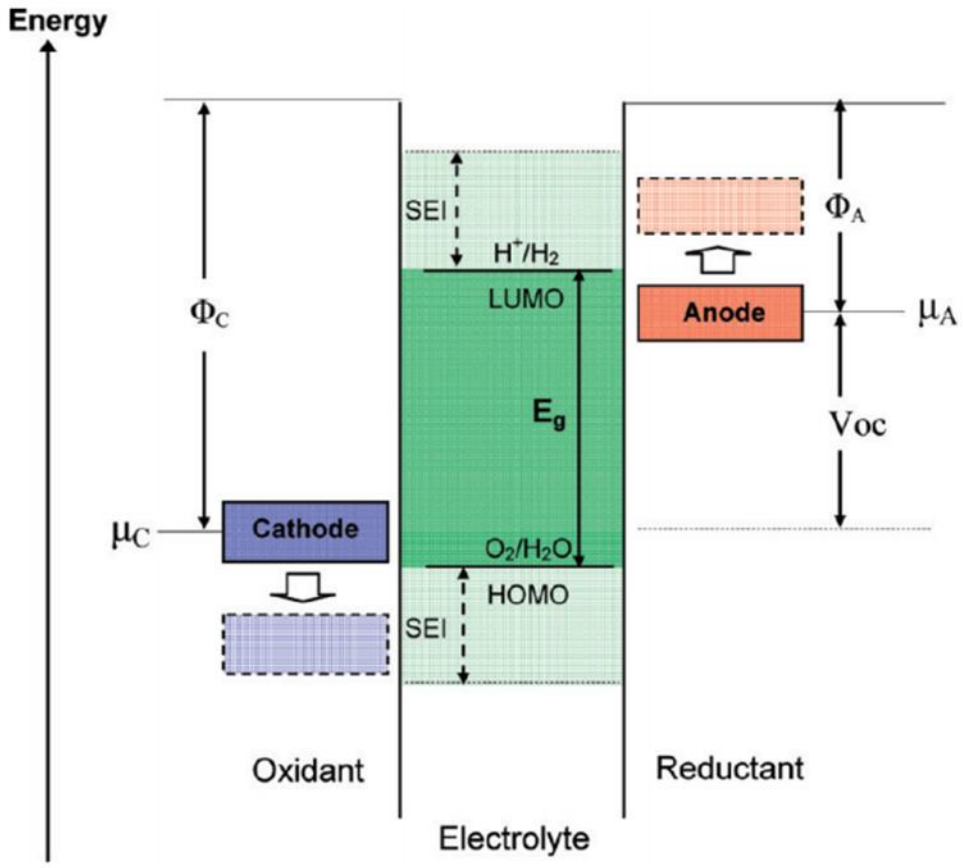

Figure 4. Schematic open-circuit energy diagram of an aqueous electrolyte. Φ_A and Φ_C are the anode and cathode work functions. E_g is the window of the electrolyte for thermodynamic stability. A μ_A > LUMO and/or a μ_C < HOMO requires a kinetic stability by the formation of an SEI layer. Reprinted with permission from ref. [96]. Copyright 2009 American Chemical Society.

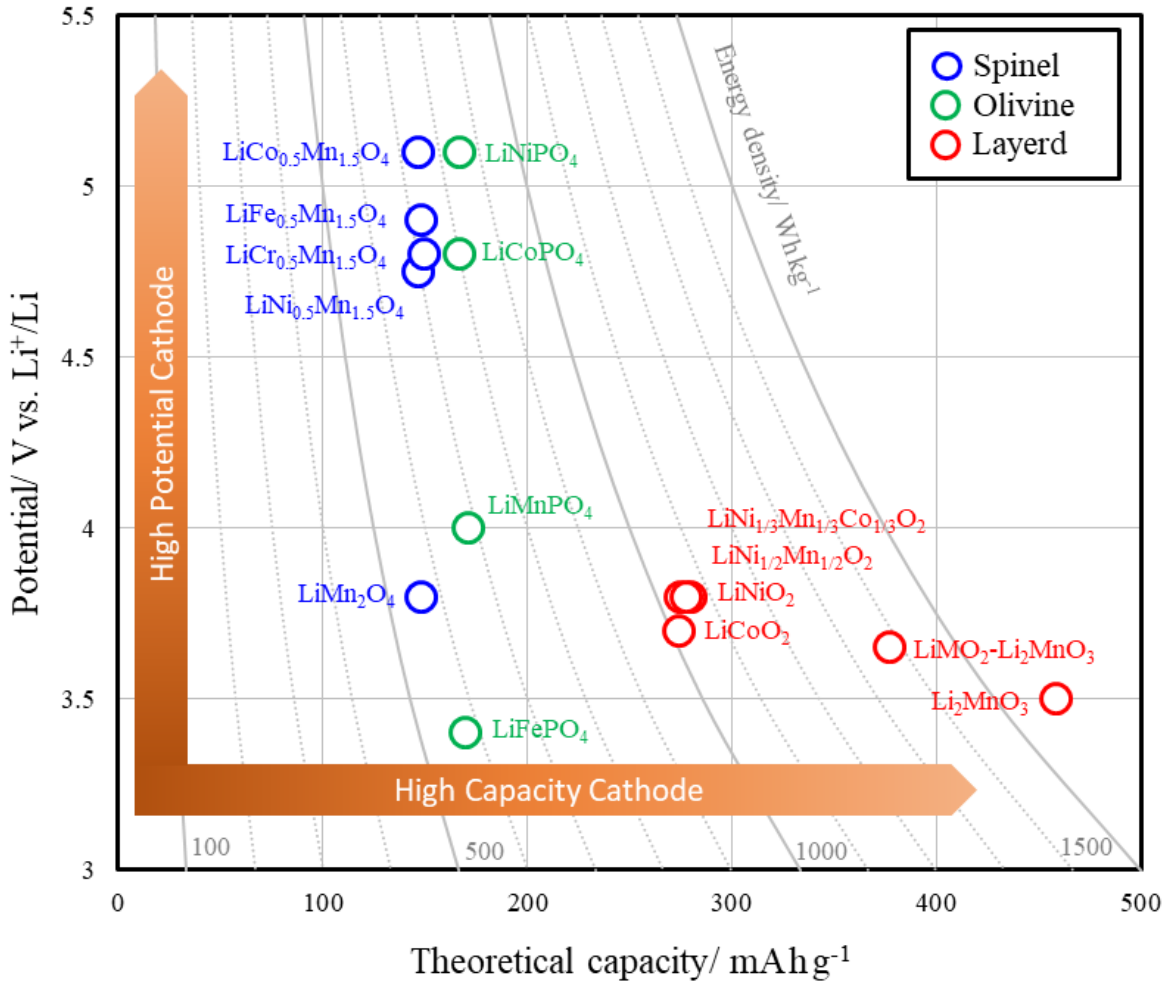

Figure 5. Relationship between operation potential and theoretical capacity of three major structural type of cathode materials.

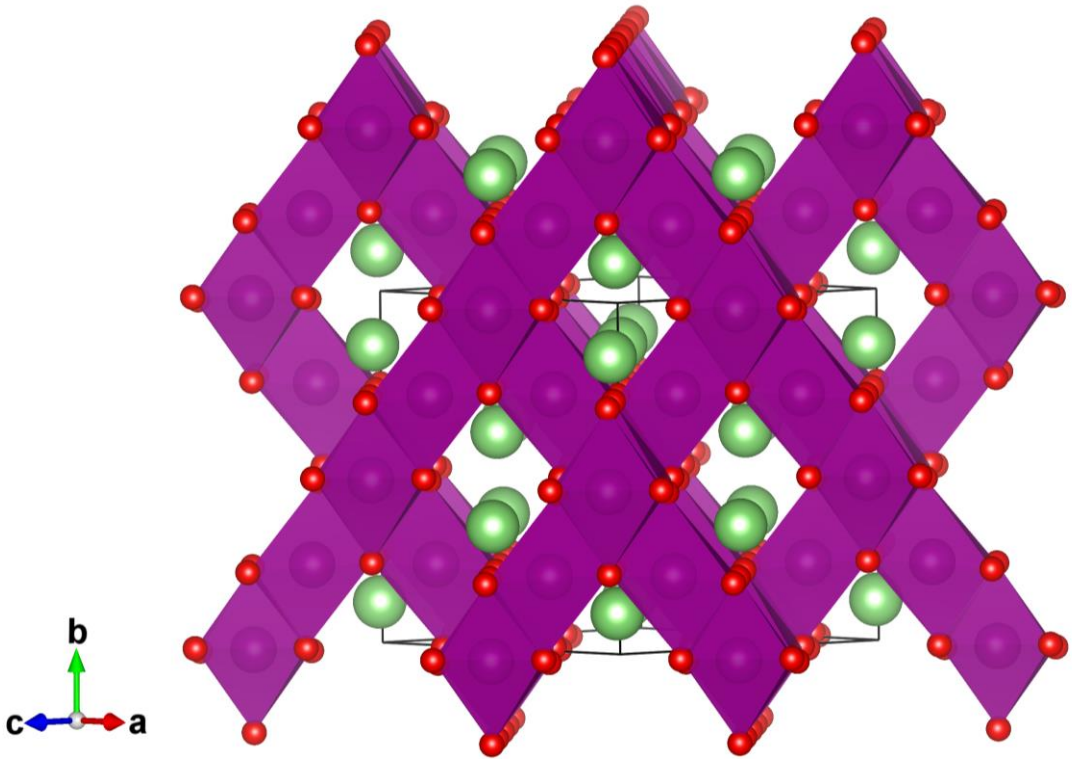

Figure 6. Crystalline structure of spinel $LiMn_2O_4$. Purple octahedron is MnO_8 unit. This figure is drawn by using VESTA package.[97]

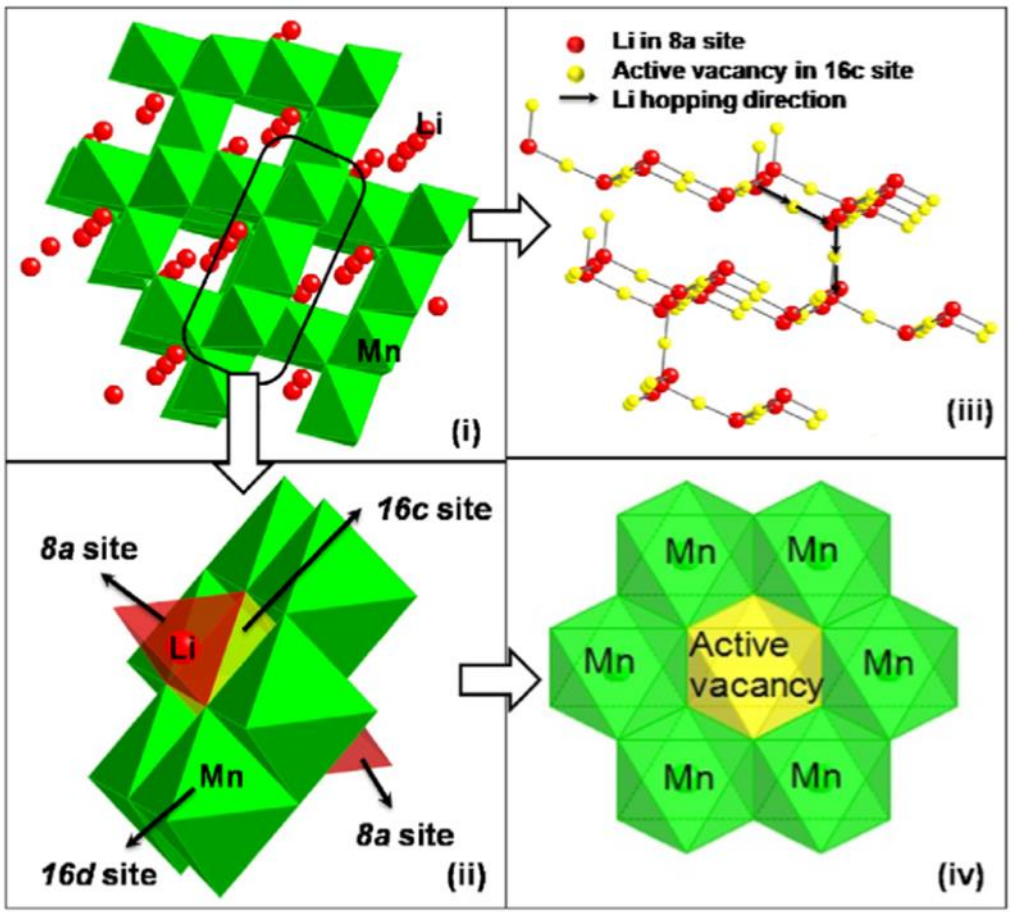

Figure 7. Crystalline structure of spinel LiMn2O4 and (b) its corresponding lithium diffusion pathways. Reprinted with permission from ref. [17]. Copyright 2010 Elsevier B.V.

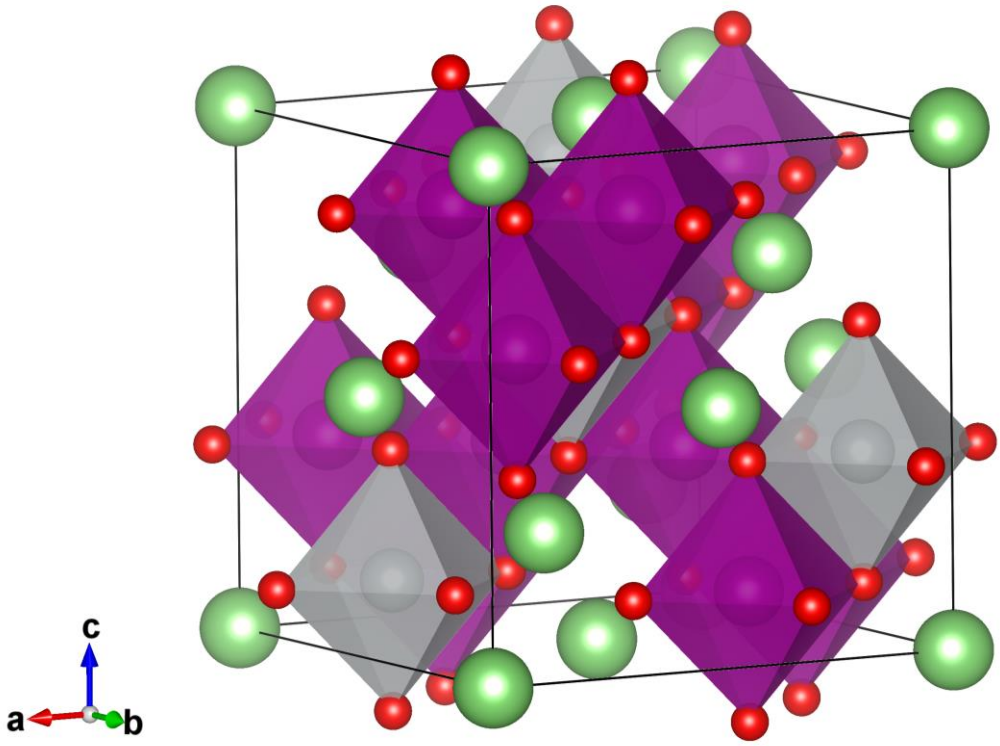

Figure 8. Crystalline structure of partly substituted high potential spinel $LiNi_{0.5}Mn_{1.5}O_4$ (space group: $P4_332$). This figure is drawn by using VESTA package.[97]

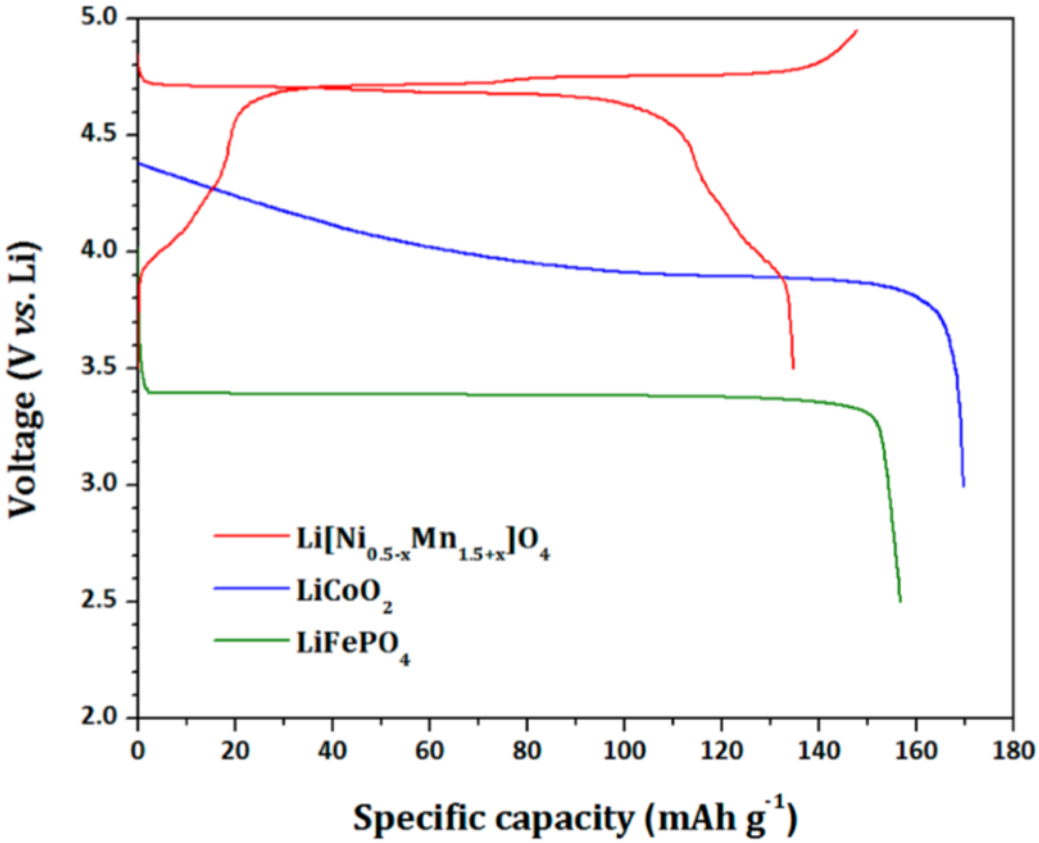

Figure 9. Comparison of charge/discharge voltage curves of $LiNi_{0.5-x}Mn_{1.5+x}O_4$ with those of $LiCoO_2$ and $LiFePO_4$. Reprinted with permission from ref. [27]. Copyright 2013 American Chemical Society.

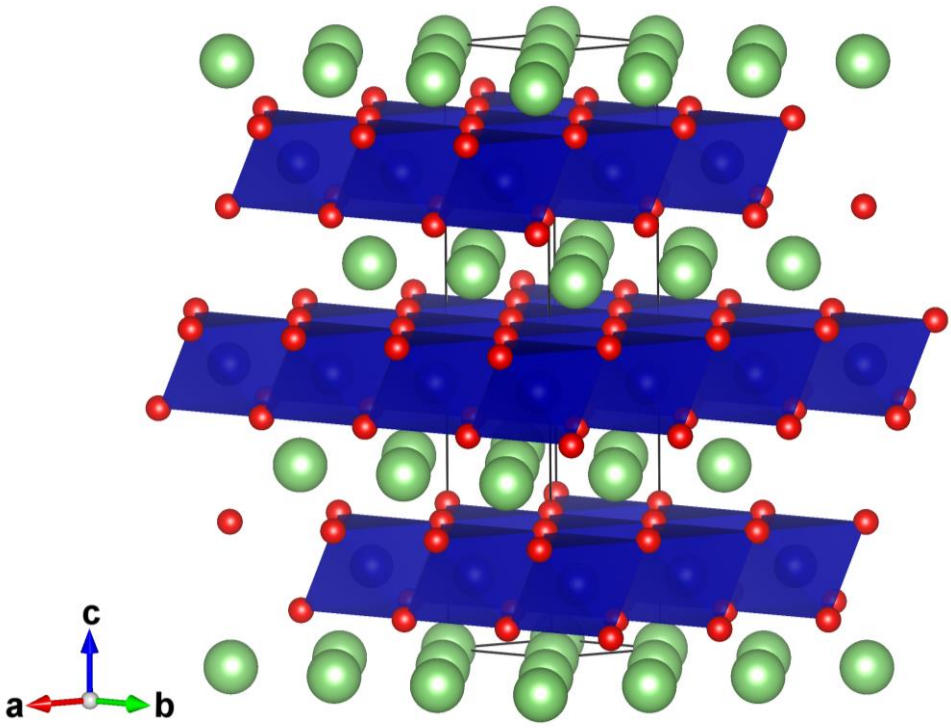

Figure 10. Crystalline structure of layered $LiCoO_2$. Blue octahedron is CoO_6 unit. This figure is drawn by using VESTA package.[97]

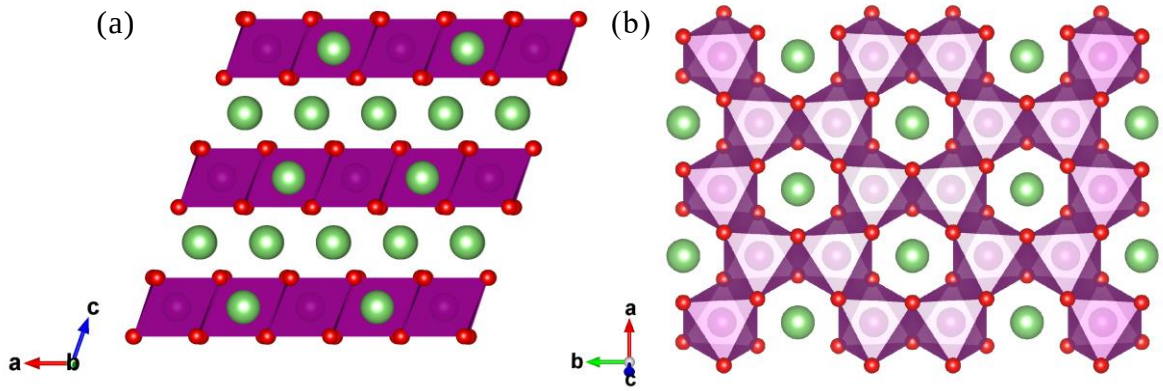

Figure 11. Crystalline structure of Li-rich manganese oxide (Li_2MnO_3) along (a) *a*-*b* plane and (b) *c*-axis (transition-metal layer). This figure is drawn by using VESTA package.[97]

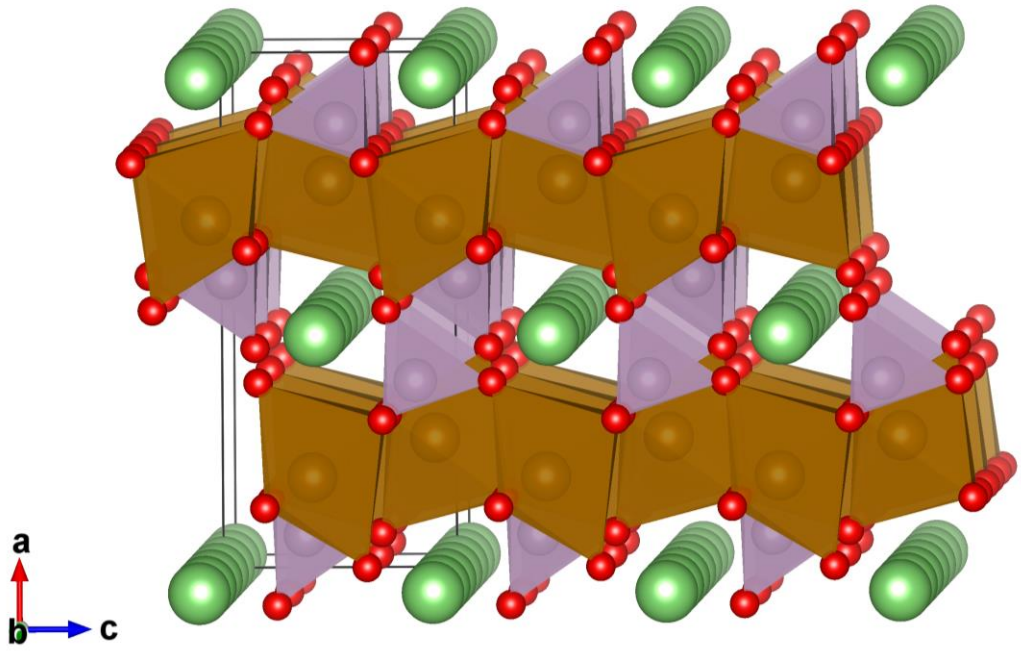

Figure 12. Crystalline structure of olivine $LiFePO_4$. Brown octahedron and gray tetrahedron are FeO_6 and PO_4, respectively. This figure is drawn by using VESTA package.[97]

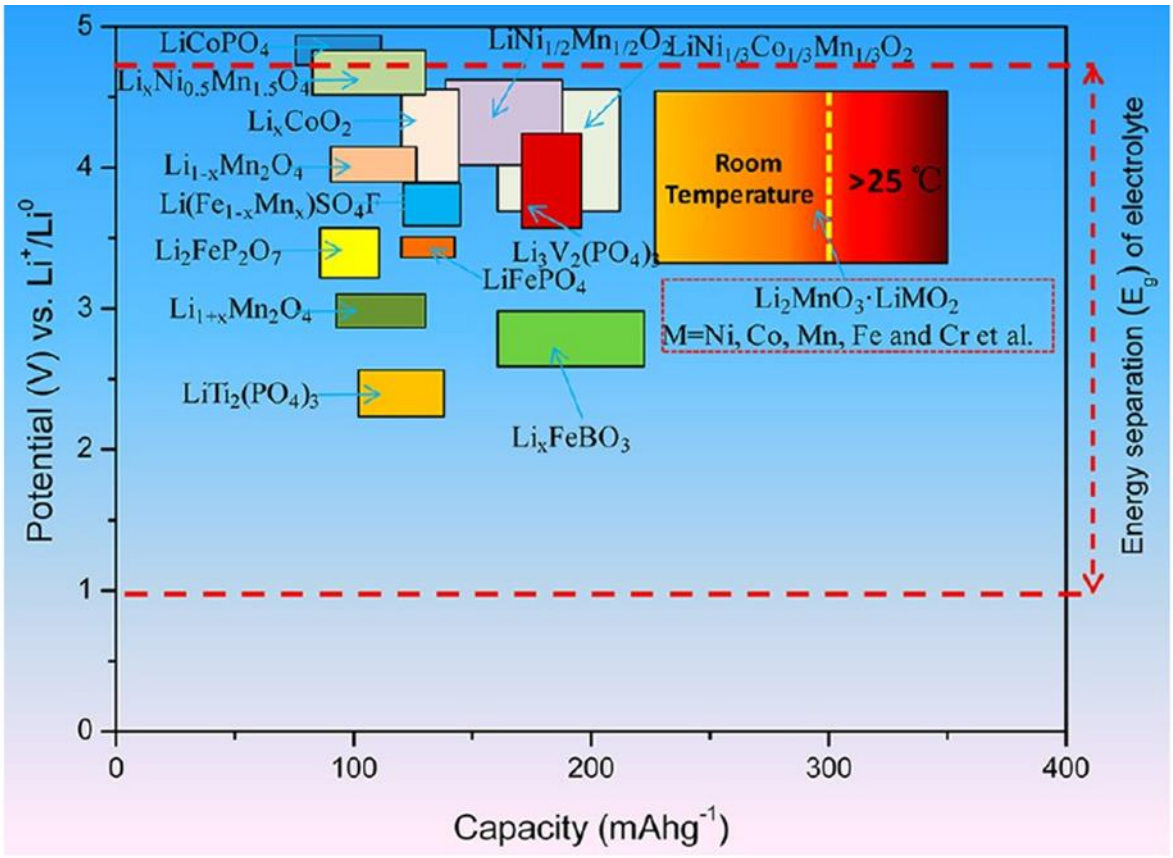

Figure 13. Available voltage and capacity of the main cathode materials for lithium-ion batteries. Reprinted with permission from ref. [45]. Copyright 2013 American Chemical Society.

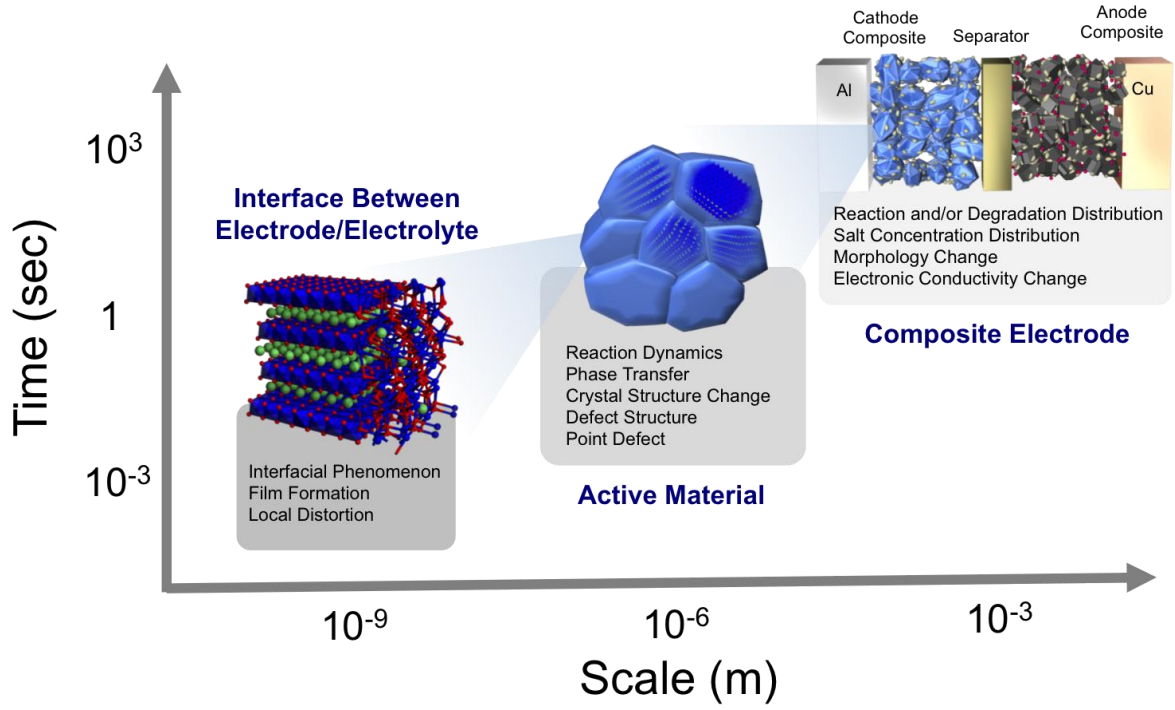

Figure 14. Elementary reactions in lithium-ion battery in each time and space scale.

References

[1] A. Yoshino, K. Sanechika, T. Nakajima, Japanese Patent 1989293, 1985.

[2] K. Mizushima, P. C. Jones, P. J. Wiseman, J. B. Goodenough, Mater. *Res. Bull.* 1980, *15*, 783.

[3] R. Yazami, P. Touzain, *J. Power Sources* **1983**, *9*, 365.

[4] R. Feng, U. von Sacken, J. R. Dahn, J. Electrochem. Soc. **1990**, *137*, 2009.

[5] Technology Roadmap: Electric and plug-in hybrid electric vehicles, International Energy Agency **2011**, 12.

[6] M. M. Thackeray, W. I. F. David, P. G. Bruce, J. B. Goodenough, *Mater. Res. Bull*. **1983**, *18*, 461.

[7] K. Takada, N. Aotani, K. Iwamoto, S. Kondo, *Solid State Ionics 1995*, *79*, 284.

[8] W. Li, J. C. Currie, *J. Electrochem. Soc.* **1997**, *144*, 2773.

[9] M. Broussely, Abstract No. 415, eleventh international meeting on lithium batteries, Monterey, California, USA, 23-28 June 2002.

[10] M. E. Spahr, P. Novák, B. Schnyder, O. Haas, R. Nesper, *J. Electrochem. Soc*. **1998**, *145*, 1113.

[11] T. Ohzuku, Y. Makimura, *Chem. Lett.* **2001**, *30*, 642.

[12] Z. Lu, D.D. MacNeil, J.R. Dahn, *Electrochem. Solid State Lett.* **2001**, *4*, A191.

[13] Technology Roadmap: Electric and plug-in hybrid electric vehicles, International Energy Agency **2011**, 14.

[14] T. Ohzuku, M. Kitagawa, T. Hirai, *J. Electrochem. Soc.* **1990**, *137*, 769.

[15] J. M. Tarascon, E. Wang, F. K. Shokoohi, W. R. McKinnon, S. Colson, *J. Electrochem. Soc.* **1991**, *138*, 2859.

[16] J. M. Tarascon, D. Guyomard, *J. Electrochem. Soc.* **1991**, *138*, 2864.

[17] B. Xu, S. Meng, *J. Power Sources* **2010**, *195*, 4971.

[18] M. Wakihara, G. Li, H. Ikuta, In:M. Wakihara, O. Yamamoto (Eds.), *Lithium Ion Batteries*, p.26, Kodansha, Tokyo; Wiley/VCH, Weinheim, 1998.

[19] L. Guohua, H. Ikuta, T. Uchida, M. Wakihara, *J. Electrochem. Soc.* **1996**, *143*, 178.

[20] G. Pistoia, G. Wang, *Solid State Ionics* **1993**, *66*, 135.

[21] D. Song, H. Ikuta, T. Uchida, M. Wakihara, *Solid State Ionics* **1999**, *117*, 151.

[22] Y. Terada, K. Yasaka, F. Nishikawa, T. Konishi, M. Yoshino, I. Nakai, *J. Solid. State. Chem.* **2001**, *156*, 286.

[23] T. Okumura, M. Shikano, H. Kobayashi, *J. Power Sources* **2013**, *244*, 544.

[24] T. Okumura, Y. Yamaguchi, H. Kobayashi, *Phys. Chem. Chem. Phys.* **2016**, *18*, 17827.

[25] A. Manthiram, K. Chemelewski, E.-S. Lee, *Energy Environ. Sci.* **2014**, *7*, 1339.

[26] J.-H. Kim, N. P. W. Pieczonka, L. Yang, *ChemPhysChem* **2014**, *15*, 1940.

[27] J. B. Goodenough, K.-S Park, *J. Am. Chem. Soc.* **2013**, *135*, 1167.

[28] J. Liu, A. Manthiram, *J. Phys. Chem. C* **2009**, *113*, 15073.

[29] G. Blasse, *Philips Res. Rep.* **1964**, *1*, 19.

[30] K. Akiyoshi, T. Ohzuku, N. Nakayama, Abstract 1149, The Electrochemical Society Meeting Abstrasts, Paris, France, April 27-May 2, 2003.

[31] Y. Idemoto, H. Narai, N. Koura, *J. Power Sources* **2003**, *125*, 119.

[32] J.-H. Kim, C. S. Yoon, S.-T. Myung, J. Prakash, Y.-K. Sun, *Electrochem. Solid-State Lett.* **2004**, *7*, A216.

[33] J.-H. Kim, S.-T. Myung, C. S. Yoon, S. G. Kang, Y.-K. Sun, *Chem. Mater.* **2004**, *16*, 906.

[34] K. Y. Chung, W.-S. Yoon, H. S. Lee, J. MacBreen, X.-Q. Yang, S. H. Oh, W. H. Ryu, J. L. Lee, W. I. Cho, B. W. Cho, *J. Power Sources* **2006**, *163*, 185.

[35] M. G. S. R. Thomas, W. I. F. David, J. B. Goodenough, *Mat. Res. Bull.* **1985**, *20*, 1137.

[36] J. R. Dahn, U. von Sacken, C. A. Michal, *Solid State Ionics* **1990**, *44*, 87.

[37] R. Kanno, H. Kubo, Y. Kawamoto, T. Kamiyama, F. Izumi, Y. Takeda, M. Takano, *J. Solid State Chem.* **1994**, *110*, 216.

[38] J. B. Goodenough, D. G. Wickham, W. J. Croft, *J. Phys. Chem. Solids* **1958**, *5*, 107.

[39] G. Dutta, A. Manthiram, J. B. Goodenough, J.-C. Grenier, *J. Solid State Chem.* **1992**, *96*, 123.

[40] J. Morales, C. Pérez-Vincente, J. L. Tirado, *Mat. Res. Bull.* **1990**, *25*, 623.

[41] W. Li, J. N. Reimers, J. R. Dahn, *Phys. Rev. B* **1992**, *46*, 3236.

[42] H. Arai, S. Okada, H. Ohtsuka, M. Ichimura, J. Yamaki, *Solid State Ionics* **1995**, *80*, 261.

[43] H. Arai, S. Okada, Y. Sakurai, J. Yamaki, *Solid State Ionics* **1998**, *109*, 295.

[44] W.-S. Yoon, K. Y. Chung, J. McBreen, X.-Q. Yang, *Electrochem. Commun.* **2006**, *8*, 1257.

[45] H. Yu, H. Zhou, *J. Phys. Chem. Lett.* **2013**, *4*, 1268.

[46] P. Rozier, J. M. Tarascon, *J. Electrochem. Soc.* **2015**, *162*, A2490.

[47] Z. Lu, J. R. Dahn, *J. Electrochem. Soc.* **2002**, *149*, A815.

[48] M. M. Thackeray, S. H. Kang, C. S. Johnson, J. T. Vaughey, R. Benedek, S. A. Hackney, *J. Mater. Chem.* **2007**, *17*, 3112.

[49] M. M. Thackeray, C. S. Johnson, J. T. Vaughey, N. Li, S. A. Hackney, *J. Mater. Chem.* **2005**, *15*, 2257.

[50] H. J. Yu, H. J. Kim, Y. R. Wang, P. He, D. Asakura, Y. Nakamura, H. Zhou, *Phys. Chem. Chem. Phys.* **2012**, *14*, 6584.

[51] H. J. Yu, H. Zhou, *J. Mater. Chem.* **2012**, *22*, 15507.

[52] H. J. Yu, Y. R. Wang, D. Asakura, E. Hosono, H. Zhou, *RSC Adv.* **2012**, *2*, 8797.

[53] D. Y. W. Yu, K. Yanagida, Y. Kato, H. Nakamura, *J. Electrochem. Soc.* **2009**, *156*, A417.

[54] A. K. Padhi, K. S. Nanjundaswamy, J. B. Goodenough, *J. Electrochem. Soc.* **1997**, *144*, 1188.

[55] H. Huang, S.-C. Yin, L. F. Nazar, *Electrochem. Solid-State Lett.* **2001**, *4*, A170.

[56] A. Yamada, S. C. Chung, K. Hinokuma, *J. Electrochem. Soc.* **2001**, *148*, A224.

[57] Y. Asari, Y. Suwa, T. Hamada, *Phys. Rev. B* **2011**, *84*, 134113.

[58] G. H. Li, H. Azuma, M. Tohda, *Electrochem. Solid State Lett.* **2002**, *5*, A135.

[59] S. Okada, S. Sawa, M. Egashira, J. Yamaki, M. Tabuchi, H. Kageyama, T. Konishi, A. Yoshino, *J. Power Sources* **2001**, *97-98*, 430.

[60] M. Cococcioni, C. A. Marianetti, D. Morgan, G. Ceder, *Phys. Rev. B* **2004**, *70*, 235121.

[61] Y. Feng, H. Zhang, L. Fang, Y. Ouyang, Y. Wang, *J. Mater. Chem. A* **2015**, *3*, 15969.

[62] P. Yu, B. N. Popov, J. A. Pitter, R. E. White, *J. Electrochem. Soc.* **1999**, *146*, 8.

[63] A. Funabiki, M. Inaba, Z. Ogumi, *J. Power Sources* **1997**, *68*, 227.

[64] K. Shaju, G. S. Rao, B. Chowdari, *J. Electrochem. Soc.* **2004**, *151*, A1324.

[65] W. Weppner, R. A. Huggins, *J. Electrochem. Soc.* **1977**, *124*, 1569.

[66] Q. Wang, H. Li, X. Huang, L. Chen, *J. Electrochem. Soc.* **2001**, *148*, A737.

[67] M. Levi, D. Aurbach, *J. Phys. Chem. B* **1997**, *101*, 4641.

[68] D. Guyomard, J. Tarascon, *J. Electrochem. Soc.* **1992**, *139*, 937.

[69] J. Backholm, P. Georén, G. A. Niklasson, *J. Appl. Phys.* **2008**, *103*, 023702.

[70] F. Lin, Y. Liu, X. Yu, L. Cheng, A. Singer, O. G. Shpyrko, H. L. Xin, N. Tamura, C. Tian, T.-C. Weng, X.-Q. Yang, Y. S. Meng, D. Nordlund, W. Yang, M. M. Doeff, *Chem. Rev.* **2017**, *117*, 13123.

[71] R. R. Chianelli, J. C. Scanlon, B. M. L. Rao, *J. Electrochem. Soc.* **1978**, *125*, 1563.

[72] D. Takamatsu, Y. Koyama, Y. Orikasa, S. Mori, T. Nakatsutsumi, T. Hirano, H. Tanida, H. Arai, Y. Uchimoto, Z. Ogumi, *Angew. Chem., Int. Ed.* **2012**, *51*, 11597.

[73] K. Yamamoto, T. Minato, S. Mori, D. Takamatsu, Y. Orikasa, H. Tanida, K. Nakanishi, H. Murayama, T. Masese, T. Mori, H. Arai, Y. Koyama, Z. Ogumi, Y. Uchimoto, *J. Phys. Chem. C* **2014**, *118*, 9538.

[74] Y. Orikasa, T. Maeda, Y. Koyama, H. Murayama, K. Fukuda, H. Tanida, H. Arai, E. Matsubara, Y. Uchimoto, Z. Ogumi, *J. Am. Chem. Soc.* **2013**, *135*, 5497.

[75] H. Liu, F. C. Strobridge, O. J. Borkiewicz, K. M. Wiaderek, K. W. Chapman, P. J. Chupas, C. P. Grey, *Science* **2014**, *344*, 1252817.

[76] H. Murayama, K. Kitada, K. Fukuda, A. Mitsui, K. Ohara, H. Arai, Y. Uchimoto, Z. Ogumi, E. Matsubara, *J. Phys. Chem. C* **2014**, *118*, 20750.

[77] K. Kitada, H. Murayama, K. Fukuda, H. Arai, Y. Uchimoto, Z. Ogumi, E. Matsubara, *J. Power Sources* **2016**, *301*, 11.

[78] R. E., II Gerald, R. J. Klingler, G. Sandí, C. S. Johnson, L. G. Scanlon, J. W. Rathke, *J. Power Sources* **2000**, *89*, 237.

[79] R. E., II Gerald, J. Sanchez, C. S. Johnson, R. J. Klingler, J. W. Rathke, *J. Phys.: Condens. Matter* **2001**, *13*, 8269.

[80] M. Letellier, F. Chevallier, C. Clinard, E. Frackowiak, J.-N. Rouzaud, F. Béguin, *J. Chem. Phys.* **2003**, *118*, 6038.

[81] M. Letellier, F. Chevallier, M. Morcrette, *Carbon* **2007**, *45*, 1025.

[82] B. Key, R. Bhattacharyya, M. Morcrette, V. Seznéc, J.-M. Tarascon, C. P. Grey, *J. Am. Chem. Soc.* **2009**, *131*, 9239.

[83] F. Chevallier, F. Poli, B. Montigny, M. Letellier, *Carbon* **2013**, *61*, 140.

[84] K. Shimoda, M. Murakami, D. Takamatsu, H. Arai, Y. Uchimoto, Z. Ogumi, *Electrochim. Acta* **2013**, *108*, 343.

[85] K. Ogata, E. Salager, C. J. Kerr, A. E. Fraser, C. Ducati, A. J. Morris, S. Hofmann, C. P. Grey, *Nat. Commun.* **2014**, *5*, 3217.

[86] K. Gotoh, M. Izuka, J. Arai, Y. Okada, T. Sugiyama, K. Takeda, H. Ishida, *Carbon* **2014**, *79*, 380.

[87] E. Salager, V. Sarou-Kanian, M. Sathiya, M. Tang, J.-B. Leriche, P. Melin, Z. Wang, H. Verin, C. Bassada, M. Deschamps, J.-M. Tarascon, *Chem. Mater.* **2014**, *26*, 7009.

[88] H. Jung, P. K. Allan, Y.-Y. Hu, O. J. Borkiewicz, X.-L. Wang, W.-Q. Han, L.-S. Du, C. J. Pickard, P. J. Chupas, K. W. Chapman, A. J. Morris, C. P. Grey, *Chem. Mater.* **2015**, *27*, 1031.

[89] W.-S. Yoon, M. Balasubramanian, X.-Q. Yang, J. McBreen, J. Hanson, *Electrochem. Solid-State Lett.* **2005**, *8*, A83.

[90] H. C. Shin, K. Y. Chung, W. S. Min, D. J. Byun, H. Jang, B. W. Cho, *Electrochem. Commun.* **2008**, *10*, 536.

[91] J. B. Leriche, S. Hamelet, J. Shu, M. Morcrette, C. Masquelier, G. Ouvrard, M. Zerrouki, P. Soudan, S. Belin, E. Elkaïm, F. Baudelet, *J. Electrochem. Soc.* **2010**, *157*, A606.

[92] X.-J. Wang, C. Jaye, K.-W. Nam, B. Zhang, H.-Y. Chen, J. Bai, H. Li, X. Huang, D. A. Fischer, X.-Q. Yang, *J. Mater. Chem.* **2011**, *21*, 11406.

[93] R. Oishi, M. Yonemura, Y. Nishimaki, S. Torii, A. Hoshikawa, T. Ishigaki, T. Morishima, K. Mori, T. Kamiyama, Nucl. Instr. And Meth. **2009**, *600*, 94.

[94] T. Kawaguchi, K. Fukuda, K. Tokuda, K. Shimada, T. Ichitsubo, M. Oishi, J. Mizuki, E. Matsubara, *J. Synchrotron Radiat.* **2014**, *21*, 1247.

[95] T. Kawaguchi, K. Fukuda, K. Tokuda, M. Sakaida, T. Ichitsubo, M. Oishi, J. Mizuki, E. Matsubara, *Phys. Chem. Chem. Phys.* **2015**, *17*, 14064.

[96] J. B. Goodenough, Y. Kim, *Chem. Mater.* **2010**, *22*, 587.

[97] K. Momma, F. Izumi, *J. Appl. Crystallogr.* **2011**, *44*, 1272.

Chapter 2. Understanding of Phase Transition Behavior for High-potential Cathode using In Situ and Ex Situ ^{6,7}Li NMR Spectroscopy

2.1. Introduction

A nickel-substituted lithium manganese spinel $LiNi_{0.5}Mn_{1.5}O_4$ is preferred candidate of high-voltage positive electrode materials. This material shows two distinct cubic structures depending on the Ni and Mn distribution.[1-6] In the Ni/Mn ordered structure, Ni^{2+} and Mn^{4+} ions occupy the 4*b* and 12*d* Wyckoff positions in the space group $P4_332$, respectively, while these ions randomly occupy the 16*d* position in the Ni/Mn disordered $Fd\bar{3}m$ structure. It is believed that the cation ordering is an important factor influencing battery performances, and several studies reported better cycling performance and rate capability for the disordered spinel,[1,2,4] whereas a recent study has suggested that the partially ordered spinel having integrated nanodomains of ordered and disordered structures shows better performances than each spinel does.[7] The disordered spinel is often prepared by the calcination at higher temperatures, which provides oxygen loss and is sometimes expressed as $LiNi_{0.5}Mn_{1.5}O_{4-\delta}$.[1,3,8] Alternatively, Cabana *et al.* suggested that the disordered spinel prepared at high temperatures systematically showed an excess of Mn, which was compensated by the formation of a secondary rocksalt phase but not by the creation of oxygen vacancies, *i.e.*, $LiNi_{0.5-\delta}Mn_{1.5+\delta}O_4$.[5,9]

A small difference in delithiation process has been reported between the two spinel structures.[1,2,4] The delithiation of the $P4_332$ spinel basically proceeds in separate two-phase reactions between $LiNi_{0.5}Mn_{1.5}O_4$ ($Li_{1.0}$ phase) and $Li_{0.5}Ni_{0.5}Mn_{1.5}O_4$ ($Li_{0.5}$)

at ~4.70 V, and between $Li_{0.5}Ni_{0.5}Mn_{1.5}O_4$ and $Ni_{0.5}Mn_{1.5}O_4$ ($Li_{0.0}$) at ~4.74 V. On the other hand, the $Fd\bar{3}m$ spinel shows a single-phase reaction (solid solution behavior) in the $Li_{1.0}$ phase at the initial stage of delithiation. Importantly, these phase transitions occur in a topotactic way, where the cubic lattice constant decreases from a = 8.17 ($Li_{1.0}$) to 8.09 Å ($Li_{0.5}$) and 8.00 Å ($Li_{0.0}$), respectively.[1,2,4,10] Such a small lattice mismatch (lattice strain) and a fast-three-dimensional Li diffusion path would expect good rate capability and cyclability. X-ray absorption fine structure (XAFS) studies at Ni/Mn K- and $L_{2,3}$-edges have revealed that Ni^{2+} ions in the $Li_{1.0}$ phase was oxidized to Ni^{3+} in the $Li_{0.5}$ phase and Ni^{4+} in the $Li_{0.0}$ phase, respectively, while the valence state of Mn^{4+} ions remained unchanged during delithiation.[11-15]

Solid-state nuclear magnetic resonance (NMR) spectroscopy is a useful technique for investigating the chemical environments on a specific element in the battery materials. In particular, the ^{6,7}Li magic-angle spinning (MAS) NMR technique has been widely applied for the chemical structure characterization of the pristine and delithiated positive electrode materials, because it gives direct information about mobile Li^+ ions.[16-32] Cabana *et al.* compared the ^{6}Li MAS NMR spectra of $LiNi_{0.5}Mn_{1.5}O_4$ synthesized at various temperatures.[5] They suggested the existence of minor peaks other than that corresponding to a regular Li environment, and the relative intensities of the minor peaks are temperature-dependent. The sample with the $P4_332$ structure synthesized at 700 °C seems to show a relatively narrow distribution with a least number of minor peaks, while that with the $Fd\bar{3}m$ structure calcined at lower and higher temperatures shows a much broader distribution. ^{6}Li MAS NMR spectra for the $Li_xNi_{0.5}Mn_{1.5}O_4$ samples prepared at various states of charge were also reported, which showed that the signal intensity decreased monotonously without any observable peak shifts or new resonances.[23] The authors concluded that the local electronic and atomic

environments of the Li ions remaining in the structure were not significantly perturbed by the removal of the nearby Li ions. However, this is surprising, since the in situ X-ray diffraction (XRD) and XAFS results have clearly shown the structural and electronic evolutions on phase transition.[2,13] This apparent inconsistency may come from undesirable reaction in disassembling the batteries because it is expected that the active materials at charged state are highly reactive with moisture and oxygen. In recent years, in situ (in operando) static NMR measurements have been applied to small homemade batteries under electrochemical operation.[33-43] This technique enables us to quantitatively evaluate the spectral (structural) changes in a single experiment in a nondestructive manner, despite giving worse spectral resolution compared to the ex situ MAS technique. We here examine the delithiation and lithiation behavior of ordered spinel $LiNi_{0.5}Mn_{1.5}O_4$ and disordered spinel $LiNi_{0.4}Mn_{1.6}O_4$ by using in situ ^{7}Li NMR and ex situ ^{6}Li MAS NMR spectroscopy to clarify the correlation between crystal structures (Ni/Mn ordering) and Li local environments.

2.2. Experimental

Sample Preparation: The $P4_332$-structured $LiNi_{0.5}Mn_{1.5}O_4$ was prepared by annealing the battery grade $LiNi_{0.5}Mn_{1.5}O_4$ powder ($Li_{1.002}Ni_{0.507}Mn_{1.496}O_{4.000}$, Toda Kogyo) at 700 °C for 48 h in air. Similarly, the $Fd\bar{3}m$-structured $LiNi_{0.4}Mn_{1.6}O_4$ was prepared by annealing the powder at 900 °C for 6 h. These structures were confirmed by X-ray diffraction. Energy-dispersive X-ray spectrometry (EDS) analyses on scanning electron microscope (SEM) showed the average Ni/Mn ratio of 0.48(1)/1.52(1) for the former particles and 0.36(2)/1.64(2) for the latters (total of Ni and Mn amount was fixed to 2.0), indicating that annealing at high temperature causes

the deviation of Ni/Mn ratio from the original one. A mixture of active material ($LiNi_{0.5}Mn_{1.5}O_4$ or $LiNi_{0.4}Mn_{1.6}O_4$), acetylene black (Denki kagaku Kogyo), polyvinylidene difluoride (PVDF, Kureha) with a weight ratio of 91:6:3 was spread with N-methylpyrrolidone (NMP) onto aluminum foil, and then dried at 80 °C under vacuum overnight to constitute a positive electrode. The SEM images of the electrodes were shown in Figure 1 (the average particle size; ~5 μm). The electrode for in situ NMR measurement was cut in the dimensions of 15 × 5 mm^2, which included ~15 mg of active material, while those for ex situ NMR and XRD. A foil of metallic lithium (0.2 mm in thickness, >99.9%, Honjo Metal) was used as a counter electrode. The electrolyte used in this study was 1 M $LiPF_6$ dissolved in anhydrous ethylene carbonate (EC) and ethyl methyl carbonate (EMC) with a volumetric ratio of 3:7 (Kishida Chemical). These components were assembled together with the Celgard 2500 separator and soaked in the electrolyte solution in an Ar-filled glovebox (<3.0 ppm oxygen), which were sealed in a silica-coated or aluminum-coated plastic bag cells for in situ or ex situ NMR measurements, respectively.

Electrochemical Measurements: The electrochemical measurements were performed at room temperature on an automatic cycling/data recording system (HJ1001SD8, Hokuto Denko). The cells were galvanostatically pre-cycled 3 times over the voltage range from 3.5 to 5.0 V at a rate of 0.2C (1C = 147 mA g^{-1}), and then charged again to 5.0 V at a rate of 0.1C with a 5.0 V constant voltage charging process and subsequently discharged to 2.0 V at a rate of 0.1C with a 2.0 V constant voltage discharging process for in situ NMR observation. A series of electrode samples for ex situ measurements were prepared in the same charge-discharge procedure and disassembled at desired states of charge and discharge. An electrode sample, which was soaked in the electrolyte solution for 48 h at room temperature but

electrochemically uncycled, was also prepared for reference. They were carefully disassembled in the glovebox and rinsed with dimethyl carbonate (DMC) to remove the electrolyte solution residue. These samples were used for ^{6}Li MAS NMR and XRD measurements. In situ ^{7}Li NMR and ^{6}Li MAS NMR spectra were acquired on a DD2 600 spectrometer (Agilent Technologies) at a magnetic field of 14.1 T.

***In situ ^{6,7}Li NMR measurements*:** In situ ^{7}Li NMR measurements were performed with a homemade wide-bore static probe, where a flat battery cell was vertically placed in the center of 10 mm diameter solenoidal coil.[39] A Hahn echo pulse sequence (π/2-τ-π-τ-acq) was used with a first pulse width of 2.0 μs, echo decay of 8 μs and a relaxation delay of 0.05 s. We confirmed that the very short relaxation delay of 0.05 s was sufficient to obtain the full of intensity of spinel phases at several states of charge/ discharge; the initial state (before charging), half-charged state, and discharged state at 2.0 V. The pulse irradiation offset frequency was set at the peak top position of $LiNi_{0.5}Mn_{1.5}O_4$ or $LiNi_{0.4}Mn_{1.6}O_4$ positive electrode material at the initial state during the in situ measurement. A total of 17916 scans was collected for each spectrum. It takes 15 min over which the acquired spectrum is averaged, corresponding to the change of 0.025Li per $LiNi_{0.5}Mn_{1.5}O_4$ in the 0.1C measurement. ^{6}Li MAS NMR measurements were performed with a wide-bore T3MAS probe (Agilent Technologies). The powder samples were packed into 1.2 mmϕ MAS ZrO_2 rotors with airtight caps, which were spun at a spinning rate of 40 or 60 kHz during the experiments. Although all the experiments were nominally carried out at room temperature, the practical temperatures of spinning samples at 40 and 60 kHz were estimated to be ~47 and ~67 ^{o}C, respectively, due to frictional heating, which were estimated based on a separate temperature calibration using ^{207}Pb NMR for $Pb(NO_3)_2$.[44] A rotor-synchronized Hahn echo sequence was used with a π/2 pulse width of 0.8 μs and a relaxation delay of 0.1

s. All spectra were referenced to 1 M LiCl solution at 0.0 ppm.

2.3. Results and Discussion

2.3.1. In Situ Observation of Li Structural Changes in Ordered and Disordered Spinel

Figure 2 shows the in situ ^{7}Li NMR spectra of Li//$LiNi_{0.5}Mn_{1.5}O_4$ cell along with an electrochemical profile charging from 3.5 to 5.0 V and subsequent discharging down to 2.0 V (Figure 2a). The charge and discharge capacities were 132 and 241 mA h g^{-1}, respectively, indicating that $Li_{0.1}Ni_{0.5}Mn_{1.5}O_4$ and $Li_{1.74}Ni_{0.5}Mn_{1.5}O_4$ remained as bulk composition in the electrode neglecting any contributions from electrolyte decomposition and impurities in the active material. Three signals were observed in the lowermost spectrum before charging (Figure 2b). Sharp peaks at ~0 and 268 ppm are assigned to $LiPF_6$ in the electrolyte solution and Li metal as counter electrode, respectively. A severely broadened signal centered at ~1600 ppm comes from $LiNi_{0.5}Mn_{1.5}O_4$ in the positive electrode. It should be noted that the peak position of $LiNi_{0.5}Mn_{1.5}O_4$ in the in situ spectra is not equal to its isotropic shift (938 ppm as shown below). This is due to the bulk magnetic susceptibility effect, which causes additional peak shifts for metallic/paramagnetic materials in the cell when the cell is flat-shaped and placed at nonmagic angle with respect to the applied magnetic field.[45,46] We also note that the much larger signal intensity of $LiNi_{0.5}Mn_{1.5}O_4$ compared to the other Li components is a consequence of the pulse optimization for the former (for example, the pulse irradiation offset and relaxation delay).

Figure 2b and 2c shows the drastic changes not only in intensity but also in peak position of $LiNi_{0.5}Mn_{1.5}O_4$ signal on charge-discharge process. We found the

appearance of a new peak at ~1200 ppm, which can be attributed to the $Li_{0.5}$ phase as in the previous XRD studies.[2,13] The observed lower frequency shift is ascribable to the change in paramagnetic shift due to the valence change from Ni^{2+} (electron spin S = 1) to Ni^{3+} (S = 1/2) on the phase transformation from $Li_{1.0}$ to $Li_{0.5}$ phase.[11,13,15]

Figure 3a and 3b shows the peak area ratio between the $Li_{1.0}$ and $Li_{0.5}$ phases along with charging profile. The peak area for each component was derived by the signal decomposition, which is shown in Supporting Information. We note that NMR spectroscopy is basically a quantitative analytical method, indicating that the changes in ^{7}Li signal intensity of the active material should be proportional to the charging or discharging capacities. However, it was found that the peak intensity of $LiNi_{0.5}Mn_{1.5}O_4$ immediately decreased at the onset of charging. The apparent intensity loss is larger than the consumed Li content estimated from the constant current density. This behavior corresponds to the build-up before voltage plateau at 4.73 V on the charging profile. Similar behavior has been also reported in the in situ NMR studies for $LiCoO_2$ and $Li_{1.08}Mn_{1.92}O_4$.[39,46] We suggested that the intensity loss can be ascribed to the signal decay before signal acquisition, since a severe electron-nuclear dipolar interaction induces a very rapid T_2 relaxation decay. The large intensity reduction at the very early delithiation stage is believed to be due to the localized nature of the electron on paramagnetic ions and its nearby Li^+ ions.[20,39] Although $LiNi_{0.5}Mn_{1.5}O_4$ has only divalent Ni^{2+} and tetravalent Mn^{4+} ions in its theoretical composition, the active material used in this study showed a small deviation from the stoichiometry (see Experimental Section), leading to the existence of a small amount of Mn^{3+} ion (< 3%). The $P4_332$ ordered spinel structure can accommodate a small deviation of the Ni/Mn ratio with the excess Mn atoms in 4b position.[3,5] $LiNi_xMn_{2-x}O_4$ ($0 < x < 0.5$) has a

Mn^{3+}/Mn^{4+} redox couple at ~4 V, where delithiation proceeds in a solid solution reaction.[47] Therefore, we believe that the apparent intensity loss in NMR spectra at the onset of charging comes from a solid solution reaction associated with the Mn^{3+}/Mn^{4+} redox reaction below 4.7 V.

At the first plateau of 4.73 V, the ^{7}Li peak intensity of the $Li_{1.0}$ phase decreased monotonously, and that of the $Li_{0.5}$ phase increased in parallel (Figure 3b). The peak separation between the signals for $Li_{1.0}$ and $Li_{0.5}$ phases was barely enough to evaluate each signal intensity, and a pseudo-isosbestic point observed in the spectra for $0.55 \leq x \leq$ ~0.8 in $Li_xNi_{0.5}Mn_{1.5}O_4$ is a clear indication of the two-phase reaction between these phases (Figure 4b). The second plateau at 4.76 V corresponds to a monotonous intensity decrease of the $Li_{0.5}$ phase, originating from the second two-phase reaction between $Li_{0.5}$ and $Li_{0.0}$ phases, where the $Li_{0.0}$ phase has no Li content and therefore no contributions in the ^{7}Li NMR spectra.

On discharging process to 3.5 V, the intensity variations were reversible (Figure 3c and 3d). The cell was further discharged down to 2.0 V. Figure 2b shows a broader, asymmetric signal at the end of discharging, indicating that $LiNi_{0.5}Mn_{1.5}O_4$ can accommodate further lithium with different environments. The previous studies have reported that excess lithium insertion into $LiNi_{0.5}Mn_{1.5}O_4$ leads to tetragonal $Li_2Ni_{0.5}Mn_{1.5}O_4$ ($Li_{2.0}$ phase).[6,8,10] A recent study pointed out that two voltage plateaus observed at ~2.7 V and ~2.1 V under Nonequilibrium condition correspond to two tetragonal phases, stable T1 phase and metastable T2 phase, respectively.[6] The pseudo-isosbestic points observed in the in situ NMR spectra for $1.0 \leq x \leq 1.74$ in $Li_xNi_{0.5}Mn_{1.5}O_4$ indicates the two-phase reaction between $Li_{1.0}$ and $Li_{2.0}$ phases, but it seems difficult to discriminate the two peaks for the two $Li_{2.0}$ phases, T1 and T2 (Figure 4d). Moreover, the broad signals of $Li_{1.0}$ and $Li_{2.0}$ phases had heavily superposed each

other, and it is difficult to decompose these two components without any assumptions. Here, we assumed that the last spectrum at 2.0 V ($Li_{1.74}Ni_{0.5}Mn_{1.5}O_4$ in bulk composition) was a mixture of $0.74Li_2Ni_{0.5}Mn_{1.5}O_4$ and $0.26LiNi_{0.5}Mn_{1.5}O_4$. Figure 3d shows the $Li_{1.0}$ phase decreasing in intensity along with the $Li_{2.0}$ phase increasing, confirming the two-phase reaction scheme between them. The sum of peak areas was largely deviated from the ideal line when excess lithium was inserted into $LiNi_{0.5}Mn_{1.5}O_4$. This is owing to the imperfect excitation of the broader signal of $Li_{2.0}$ phase, which shows multiple peaks with strong electron-nuclear dipolar interactions over wide frequency as mentioned below. We emphasize that us in situ ^{7}Li NMR measurement shows the changes in peak position as well as peak intensity on charge-discharge process, clearly suggesting the two-phase reactions between $Li_{1.0}$, $Li_{0.5}$, and $Li_{0.0}$ phases at the voltage window of 3.0-5.0 V and between $Li_{1.0}$ and $Li_{2.0}$ phases at 2.0-3.0 V, respectively.

The in situ ^{7}Li NMR spectra of Li//$LiNi_{0.4}Mn_{1.6}O_4$ cell are shown in Figure 5 along with the corresponding electrochemical profile (Figure 5a). $LiNi_{0.4}Mn_{1.6}O_4$ showed a much broader signal centered at ~1400 ppm (the lowermost spectrum in Figure 5b). This broad signal seems to move slightly to higher frequency before reaching to the ~4.7 V plateau, and then to lower frequency on further delithiation (Figure 6a). The slight positive shift below ~4.7 V can be attributed to the valence change of Mn^{3+} (S = 2) to Mn^{4+} (S = 3/2) in $LiNi_{0.4}Mn_{1.6}O_4$. Similar behavior has been reported for $Li_{1.08}Mn_{1.92}O_4$.[46] After the Mn^{3+}/Mn^{4+} redox reaction finished, the subsequent Ni^{2+}/Ni^{3+} redox reaction started, and the signal moved to lower frequency.

The intensity variations in $Li_xNi_{0.4}Mn_{1.6}O_4$ along with the charging and discharging profiles are shown in Figure 7. In this case, the $Li_xNi_{0.4}Mn_{1.6}O_4$ signal was fitted with a single bigaussian function with the peak position and width being

adjustable parameters. The good fitting with a single function is consistent with the observed continuous phase transition between $Li_{1.0}$ and $Li_{0.5}$ (Figure 8). Again, the peak intensity immediately decreased at the onset of charging (Figure 7a and 7b). The apparent intensity loss is larger than that observed in the ordered spinel $Li_xNi_{0.5}Mn_{1.5}O_4$, which may result from larger Mn^{3+} content in the disordered spinel $LiNi_{0.4}Mn_{1.6}O_4$. Below $x \approx 0.9$, the intensity monotonously decreased, although small intensity maximum was seen at $x \approx 0.5$ (Figures 5c and 7b). This apparent maximum seems to come from the signal narrowing at $x \approx 0.5$ (Figure S6b), which may be an indication of the completion of the continuous valence change from Ni^{2+} to Ni^{3+}, that is, $Li_{0.5}Ni_{0.4}Mn_{1.6}O_4$. On the discharging process, the intensity variations were reversible at the voltage window of 3.5-5.0 V (Figure 7c and 7d). Although the two-phase reaction between the $Li_{1.0}$ and $Li_{2.0}$ phases has been reported below 3.0 V,[6,8] it is very difficult to follow the reaction in the present spectra as they are overlapped with each other. Therefore, we only plotted the total intensity, which was again largely underestimated from the ideal line when excess lithium was inserted into $LiNi_{0.4}Mn_{1.6}O_4$. The reason for the deviation is attributable to the imperfect excitation of the broader signal of $Li_{2.0}$ phase.

2.3.2. Detailed Characterization of Li Environments in Ordered and Disordered Spinel

To examine the detailed local environment around Li ions, $LiNi_{0.5}Mn_{1.5}O_4$ and $LiNi_{0.4}Mn_{1.6}O_4$ electrode samples were also prepared by disassembling the cells at various charging and discharging states. Both the $P4_332$ and $Fd\bar{3}m$ samples were characterized by XRD, which confirmed the occurrence of $Li_{1.0}$, $Li_{0.5}$, $Li_{0.0}$, and $Li_{2.0}$

phases as shown in Figure 9 and 10. Figure 11 shows the spectral evolutions of ^{6}Li MAS NMR spectra for $LiNi_{0.5}Mn_{1.5}O_4$ electrodes, which were consistent with the above in situ NMR result, but more detailed structural information was provided. The spectrum of the soaked sample shows a sharp main signal at 938 ppm and a minor shoulder signal at 870 ppm (Figure 11a). The relative intensities of the 938 and 870 ppm signals including spinning sidebands were estimated to 96 and 4%, respectively. These signals belong to the $Li_{1.0}$ phase. According to the previous studies, they can be assigned to the Li ions in a crystallographic regular environment for $P4_332$ structure surrounded by $3Ni^{2+}/9Mn^{4+}$ ions, and in an irregular environment where the Li ion is surrounded by $2Ni^{2+}/10Mn^{3+,4+}$ ions or $3Ni^{2+}/9Mn^{3+,4+}$, respectively.[5,23,47,48] The latter environment was observed due to incomplete Ni/Mn ordering in the ordered spinel structure and/or small deviation from Ni/Mn stoichiometry related to the formation of trivalent Mn^{3+} ion. It is noted that the spectrum we obtained is similar in shape to that of $LiNi_{0.45}Mn_{1.55}O_4$ reported by Duncan *et al.*, supporting a small Ni deficiency in our sample.[47] The presence of the minor signal suggests that the $P4_332$ ordered spinel can accommodate a small amount of Ni/Mn disordering, which may be dispersed in the structure as nanoscale domains.[7,48] On the other hand, we believe that another minor signal at 710 ppm come from the impurity phase such as $Li_xNi_{1-x}O$[2,9] or $LiNiO_2$[23] (16% of total Li), because this signal shows a strong dipolar interaction different from the others, and still exists in the spectrum of the 258 mA h g^{-1} discharged sample (this signal is overlapped with the other peaks at 40 kHz MAS in Figure 11b; see also Figure 12d).[23] Charging to 15 mA h g^{-1} produced a small shift of the main signal to lower frequency (925 ppm), and a disappearance of the 870 ppm signal (Figure 11a). These features strongly suggest that Li ion was first deintercalated from the minor environment at 870 ppm where Mn^{3+} converted to Mn^{4+} during the initial raising the

potential to 4.73 V, which corresponds to 15 mA h g^{-1} charging. The 710 ppm signal also decreased in intensity, suggesting the partial delithiation from the impurity phase. The 62 mA h g^{-1} charged sample showed the $Li_{1.0}$ signal at ~920 ppm and a new sharp signal at 680 ppm. The latter can be explicitly attributed to the Li ions in the $Li_{0.5}$ phase. The phase transformation from $Li_{1.0}$ to $Li_{0.5}$ involves a valence change from Ni^{2+} to Ni^{3+}, leading to a new peak at lower frequency as shown in the above in situ NMR spectra. The existence of two separate signals from the $Li_{1.0}$ and $Li_{0.5}$ phases confirms a two-phase reaction. The $Li_{0.5}/Li_{1.0}$ phase ratio estimated from the ^{6}Li signal intensity was in excellent agreement with that from the Rietveld analyses (0.8/0.2 in phase ratio). The remnant Li signal from the $Li_{0.5}$ phase and a very small signal at ~525 ppm was observed in the spectrum of the 125 mA h g^{-1}-charged sample. Although the $Li_{0.0}$ phase is considered as Li-free phase in an ideal composition, we tentatively ascribed the latter signal to the Li environment residing in the $Li_{0.0}$ phase because the valence changes from Ni^{3+} (S = 1/2) to Ni^{4+} (S = 0) would lead to an additional peak shift to much lower frequency. Then, the actual Li content in the $Li_{0.0}$ phase was estimated to be ~0.01Li, that is, $Li_{\sim 0.01}Ni_{0.5}Mn_{1.5}O_4$ in chemical composition, on the basis of the relative intensity of the 525 and 680 ppm signals and the phase ratio obtained from the Rietveld analyses.

The spectrum of the 135 mA h g^{-1} discharged sample was almost identical to that of soaked sample, indicating the reversible lithium extraction-insertion reaction (Figure 11b). The minor signal at 952 ppm was also recovered. It should be noted that the main and minor peaks shift toward higher frequencies than those observed in the soaked one. This is because of the difference in actual sample temperature coming from frictional heating on rotating at 40 or 60 kHz, the latter gives higher sample temperature, leading to a peak shift to lower frequency (40 kHz MAS was selected to

avoid peak overlapping). On further discharging to 200 mA h g^{-1}, new signals were observed as well as the $Li_{1.0}$ signal. These new signals became prominent at 258 mA h g^{-1} discharging. We observed three isotropic shifts at 209, 307, and 943 ppm, all of which showed asymmetric spinning sideband manifolds, indicating their strong anisotropic electron-nuclear dipolar interactions. These signals should be assigned to the Li environments in the $Li_{2.0}$ phase, most probably in the T1 phase because the electrode sample was disassembled after long relaxation time reaching to ~2.7 V at open-circuit voltage.[6] A previous study has reported that the ^{6}Li MAS NMR spectra of lithium manganese oxides shift from 700-850 ppm for Mn^{4+}, to ~500 ppm for $Mn^{3.5+}$ (mixed valence), and to 36-143 ppm for Mn^{3+}-containing compounds.[19,21,23] Therefore, we tentatively consider that the two peaks at 209 and 307 ppm for $Li_{2.0}$ phase come from the Li environments close to Ni^{2+}/Mn^{3+} ions, and that at 943 ppm from the environments close to Ni^{2+}/Mn^{4+} in $Li_2Ni_{0.5}Mn_{1.5}O_4$, where 2/3Mn ions are trivalent and the other 1/3Mn ions are still tetravalent. Unfortunately, the crystal structure of this tetragonal phase has not yet been determined.[10] The determination of the crystal structure requires a high quality diffraction profile of the target phase, but it is beyond the scope of this study. Hence, we discuss its possible structure based on our NMR results. By an analogy to $LiMn_2O_4$ ($Fd\bar{3}m$), the Ni/Mn-disordered $LiNi_{0.5}Mn_{1.5}O_4$ ($Fd\bar{3}m$) is considered to transform into the Ni/Mn-disordered $Li_2Ni_{0.5}Mn_{1.5}O_4$ ($I4_1/amd$) on lithium insertion. The Ni/Mn-ordered structure ($P4_332$) has a lower symmetry than $Fd\bar{3}m$, suggesting that the space group of its counterpart tetragonal phase is also different (lower) in symmetry from $I4_1/amd$ (*e.g.*, $P4_32_12$, the subgroup of $P4_332$) and it would have three crystallographically distinct Li sites.

Figure 13 shows the ^{6}Li MAS NMR spectra for $LiNi_{0.4}Mn_{1.6}O_4$ electrodes disassembled at various charging and discharging states. The spectrum of the soaked

sample for $LiNi_{0.4}Mn_{1.6}O_4$ shows a broad feature (Figure 13a), which was very different from that for $LiNi_{0.5}Mn_{1.5}O_4$. Such a difference can be attributed to the difference in Li local environment in between $P4_332$- and $Fd\bar{3}m$-structured spinel phases, as well as the small difference in chemical composition (although the $Fd\bar{3}m$ structured $LiNi_{0.5}Mn_{1.5}O_4$ prepared at 800 °C for 30 min showed a similar spectrum to that of $LiNi_{0.4}Mn_{1.6}O_4$), indicating that ^{6}Li NMR spectroscopy is sensitive to the Ni/Mn ordering around Li ions.[5,47] The spectrum is similar in shape to that of $LiNi_{0.35}Mn_{1.65}O_4$ ($Fd\bar{3}m$) reported by Duncan *et al.*, suggesting that the Li ions experience several environments arising from different Ni/$Mn^{3+,4+}$ arrangements.[47] The peak maximum at ~820 ppm indicates the predominance of $2Ni^{2+}/10Mn^{4+,3+}$ and $1Ni^{2+}/11Mn^{4+,3+}$ arrangements in $LiNi_{0.4}Mn_{1.6}O_4$.[5] Additional signal at 700 ppm comes from the impurity phase, whose intensity was increased from 16% to 28% of total Li by the calcination at 900 °C for 6 h. The 15 mA h g^{-1}-charged sample showed a small positive shift of the spinel signal to 850 ppm, corresponding to the valence change of some Mn^{3+} to Mn^{4+}.[19,22] Charging to 60 mA h g^{-1} lead to a peak shift to lower frequency. This signal can be attributed to the Li ions in the $Li_{0.5}$ phase according to the supporting XRD measurements (Figures 14 and 8). These XRD results suggest that the phase transformation from $Li_{1.0}$ to $Li_{0.5}$ is a single-phase reaction in the $Fd\bar{3}m$ spinel, where the valence change occurs in the randomly 16*c*-occupying Ni ions from divalent to trivalent and the cell volume decreases continuously.[2,4,47] We note that the oxidation of Ni ion provides a negative frequency shift, while that of Mn ion provides a positive shift. In the 115 mA h g^{-1} charged sample, the peak position further shifted down to ~700 ppm. We believe that this signal comes from the remaining $Li_{0.5}$ phase, although some contributions from the impurity phase, as observed in the soaked and 15 mA h g^{-1} charged samples, may be included.

On the discharging process, the 115 mA h g^{-1} discharged sample showed a spectrum similar to that of soaked one (Figure 13b). The spectrum of the 228 mA h g^{-1} discharged sample shows a new broad signal at ~470 ppm, which can be attributed to the Li environments in the $Li_{2.0}$ phase. We note that the spectrum is very different from that of the $Li_{2.0}$ phase coming from $P4_332$ structure as shown above (see also Figure 12d). If we believe that the $Li_{2.0}$ phase coming from $Fd\bar{3}m$ structure adopts the space group $I4_1/amd$, the broad signal at ~470 ppm would be attributed to the 8*c* octahedral site in Wyckoff position, which was proposed for Li occupation in $Li_2Mn_2O_4$,[49] although an earlier study had suggested both the 4*a* tetrahedral and 8*c* octahedral sites.[50] The broad feature reflects the random occupation of Ni/Mn ions in 8*d* site.

2.4. Conclusions

We carried out an intensive characterization of ordered spinel $LiNi_{0.5}Mn_{1.5}O_4$ and disordered spinel $LiNi_{0.4}Mn_{1.6}O_4$ on charge-discharge process by using in situ (in operando) ^{7}Li NMR and ^{6}Li MAS NMR spectroscopy. The present study provided the fundamental information on how the Li environments in the active materials change during electrochemical delithiation and lithiation reaction as well as the crystal or electronic structures do. The in situ ^{7}Li monitoring of the ordered spinel on delithiation revealed the appearance and subsequent disappearance of a new signal from $Li_{0.5}Ni_{0.5}Mn_{1.5}O_4$, indicating the two-phase reaction processes among $Li_{1.0}Ni_{0.5}Mn_{1.5}O_4$, $Li_{0.5}Ni_{0.5}Mn_{1.5}O_4$, and $Li_{0.0}Ni_{0.5}Mn_{1.5}O_4$. In contrast, the disordered spinel did not show clear two-phase reaction process between $Li_{1.0}Ni_{0.4}Mn_{1.6}O_4$ and $Li_{0.5}Ni_{0.4}Mn_{1.6}O_4$, which is consistent with a continuous phase transition between them. The ^{7}Li intensity

variations revealed that both the ordered and disordered spinel phases had a single-phase reaction process at the onset of charging, which resulted from Mn^{3+}/Mn^{4+} redox reaction. Also, the in situ monitoring suggested that the Ni/Mn ordering in $P4_332$ and disordering in $Fd\bar{3}m$ were kept during charge-discharge process. ^{6}Li MAS NMR spectra of the electrode samples disassembled at various Li contents also supported the in situ result. The present results are in contrast with the previous study showing no significant evolution in peak position during delithiation.[23] We believe that their samples were subjected to moisture or oxygen before NMR measurements, which would decompose the unstable $Li_{0.5}$ phase (into, for example, Li_2CO_3 and Li-free transition-metal oxides) but the $Li_{1.0}$ phase was stable and alive. The application of in situ and ex situ NMR techniques has confirmed that the evolutions of Li local environments in the ordered and disordered spinel phases on charge-discharge process are different from each other and are consistent with those of their crystal and electronic structures. This underlines that the Li environments are strongly affected by the framework structures (bond angles, interatomic distances, and lattice parameters) and especially by the electronic structures (valence states) of the surrounding transition-metal ions.

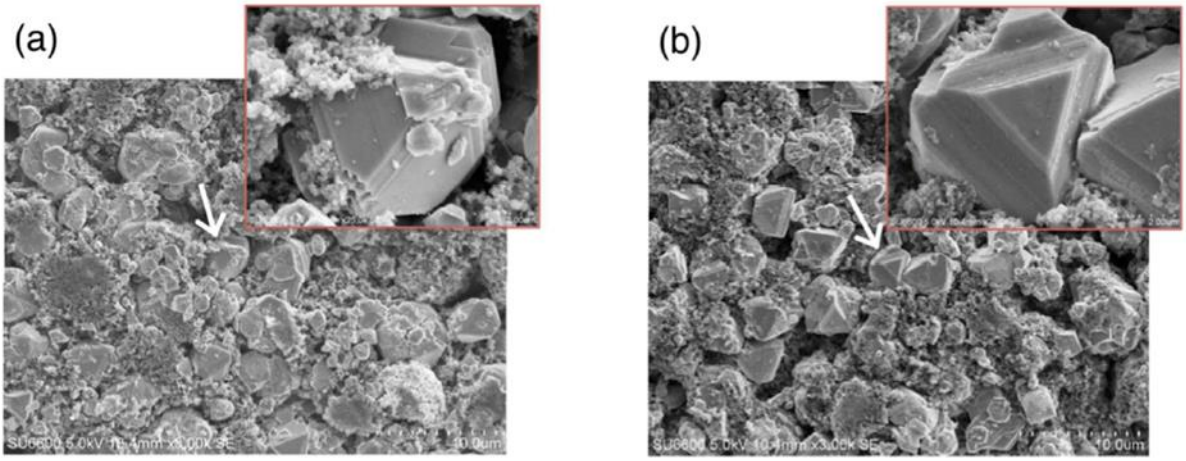

Figure 1. SEM images of (a) $LiNi_{0.5}Mn_{1.5}O_4$ ($P4_332$) and (b) $LiNi_{0.4}Mn_{1.6}O_4$ ($Fd\bar{3}m$) positive electrodes. A single particle marked with arrow is enlarged in the inset.

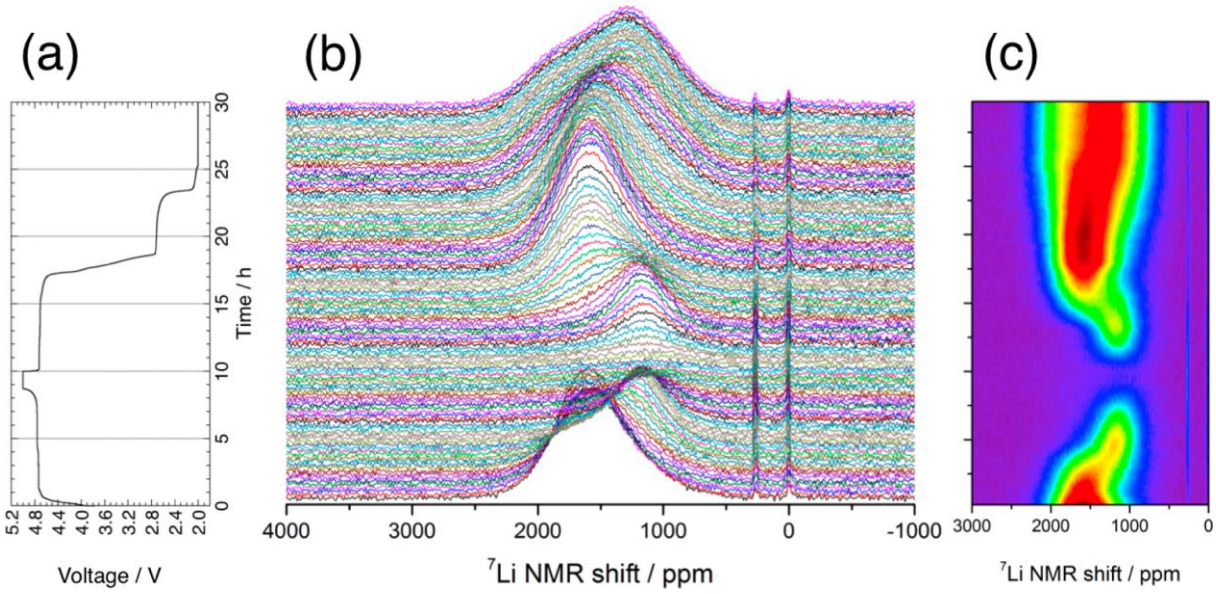

Figure 2. In situ ^{7}Li static NMR spectra of Li//$LiNi_{0.5}Mn_{1.5}O_4$ ($P4_332$ structure) cell. (a) Charge-discharge profile (0.1C rate) as a function of time, (b) stacked, and (c) contour plots of in situ ^{7}Li spectra.

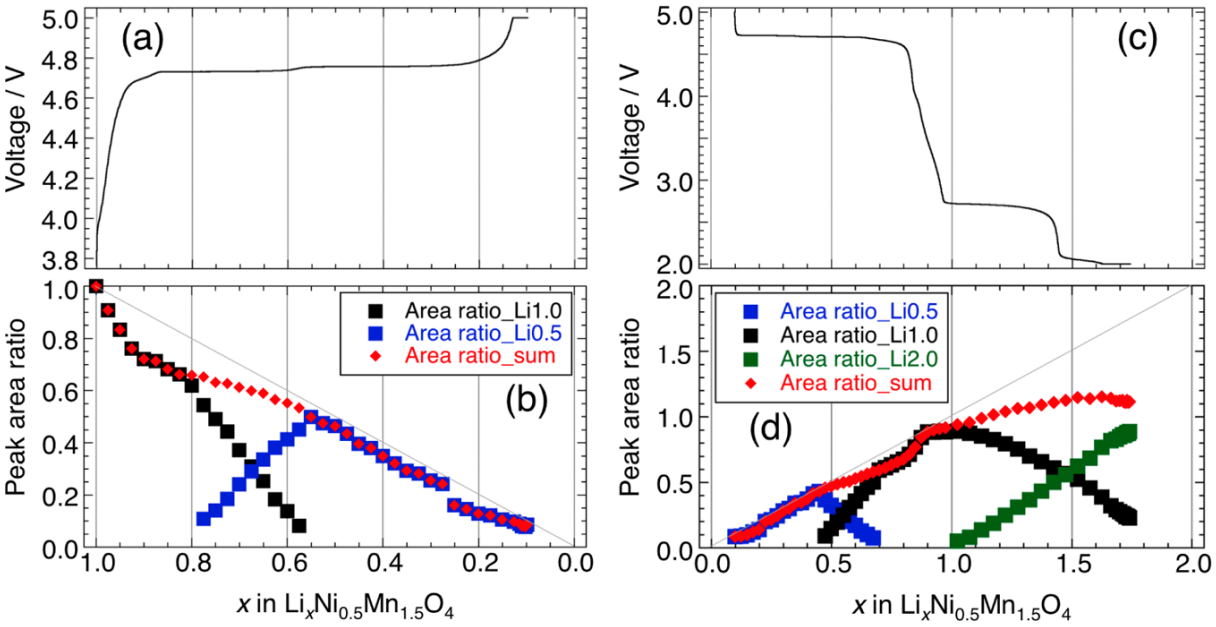

Figure 3. (a) Charging profile up to 5.0 V and (b) peak area ratio of the $Li_{1.0}$ and $Li_{0.5}$ phase components decomposed from in situ ^{7}Li spectra of the $LiNi_{0.5}Mn_{1.5}O_4$ electrode. (c) Discharging profile down to 2.0 V and (d) peak area ratio of the $Li_{0.5}$, $Li_{1.0}$, and $Li_{2.0}$ phase components.

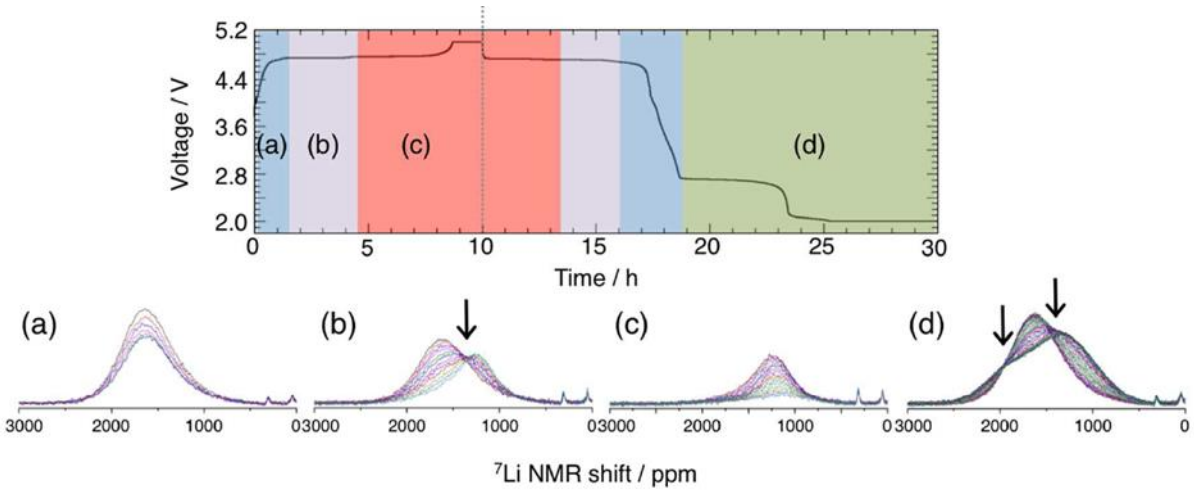

Figure 4. In situ ^{7}Li NMR spectra of $Li_xNi_{0.5}Mn_{1.5}O_4$ separated at different reaction stages with the corresponding charge-discharge profile; (a) single-phase reaction in $Li_{1.0}$ phase, (b) two-phase reaction between $Li_{1.0}$ and $Li_{0.5}$ phases, (c) two-phase reaction between $Li_{0.5}$ and $Li_{0.0}$ phases, and (d) two-phase reaction between $Li_{1.0}$ and $Li_{2.0}$ phases. Pseudo-isosbestic points are marked with arrows.

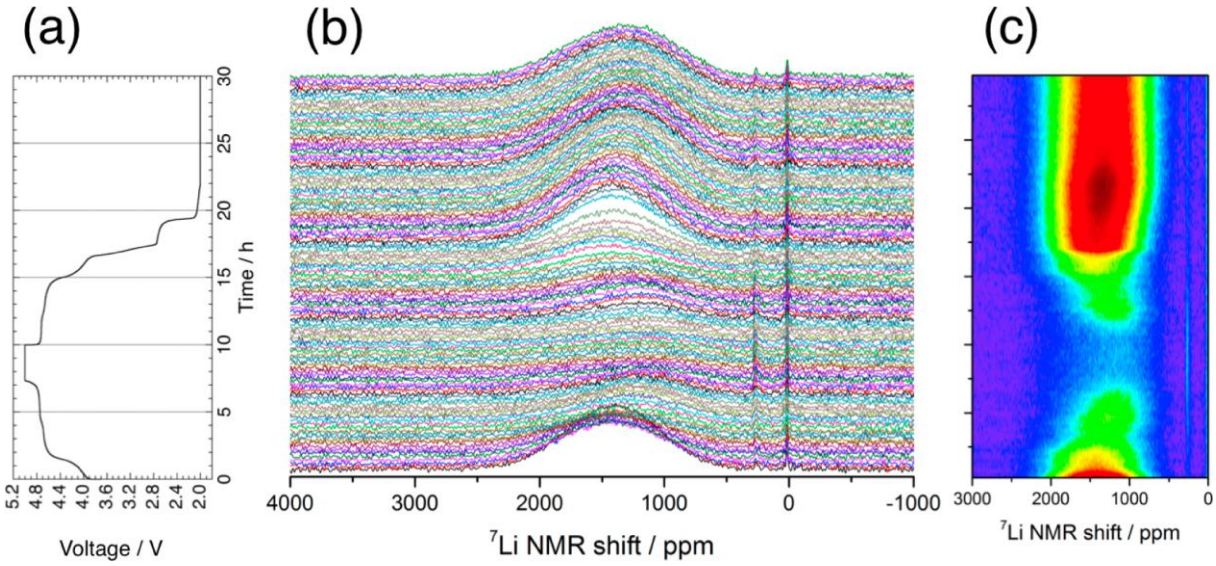

Figure. 5. In situ ^{7}Li static NMR spectra of Li//$LiNi_{0.4}Mn_{1.6}O_4$ ($Fd\bar{3}m$ structure) cell. (a) Charge-discharge profile (0.1C rate) as a function of time, (b) stacked, and (c) contour plots of in situ ^{7}Li spectra.

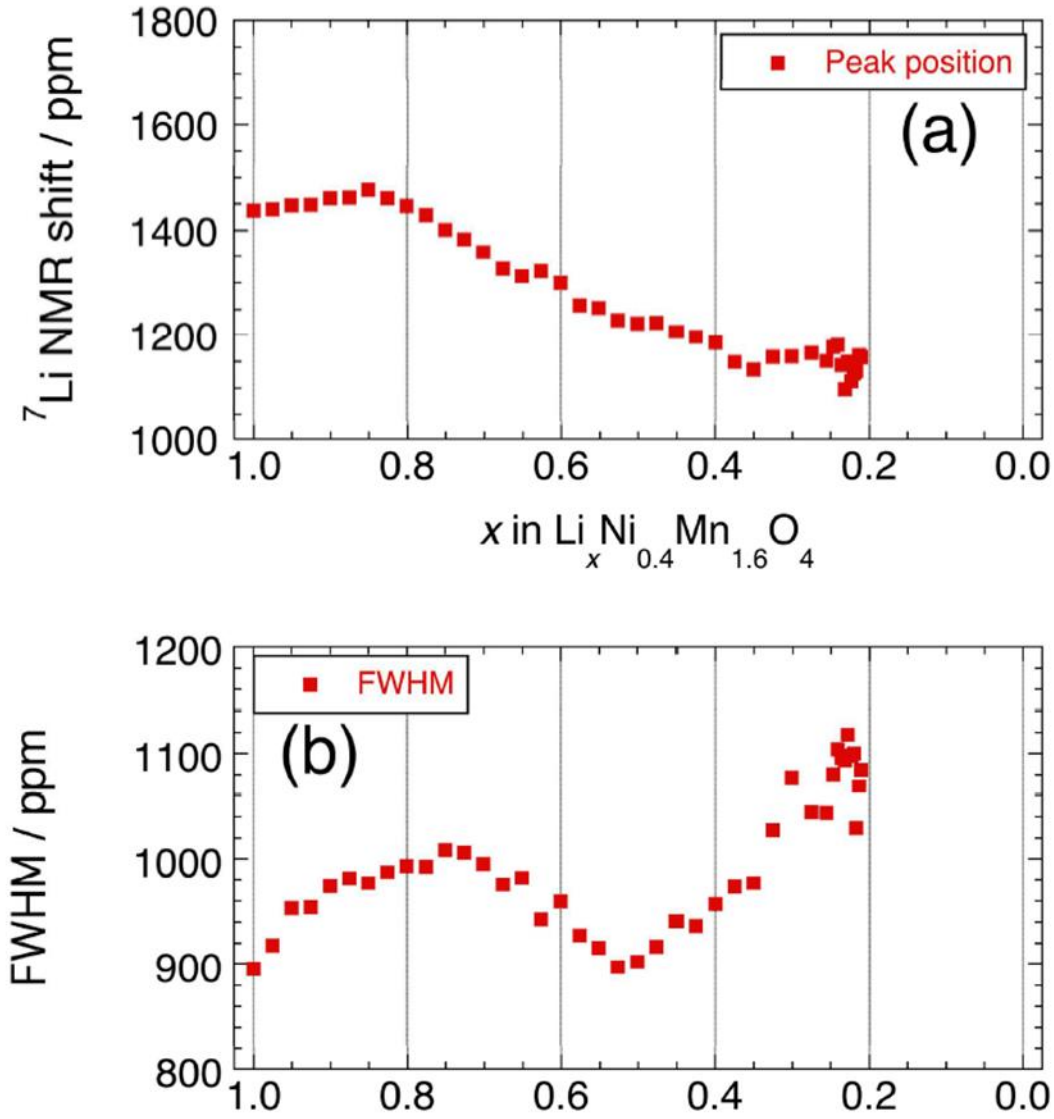

Figure 6. (a) Peak top positions and (b) peak widths extracted from in situ ^{7}Li spectra of the $LiNi_{0.4}Mn_{1.6}O_4$ electrode on charging process.

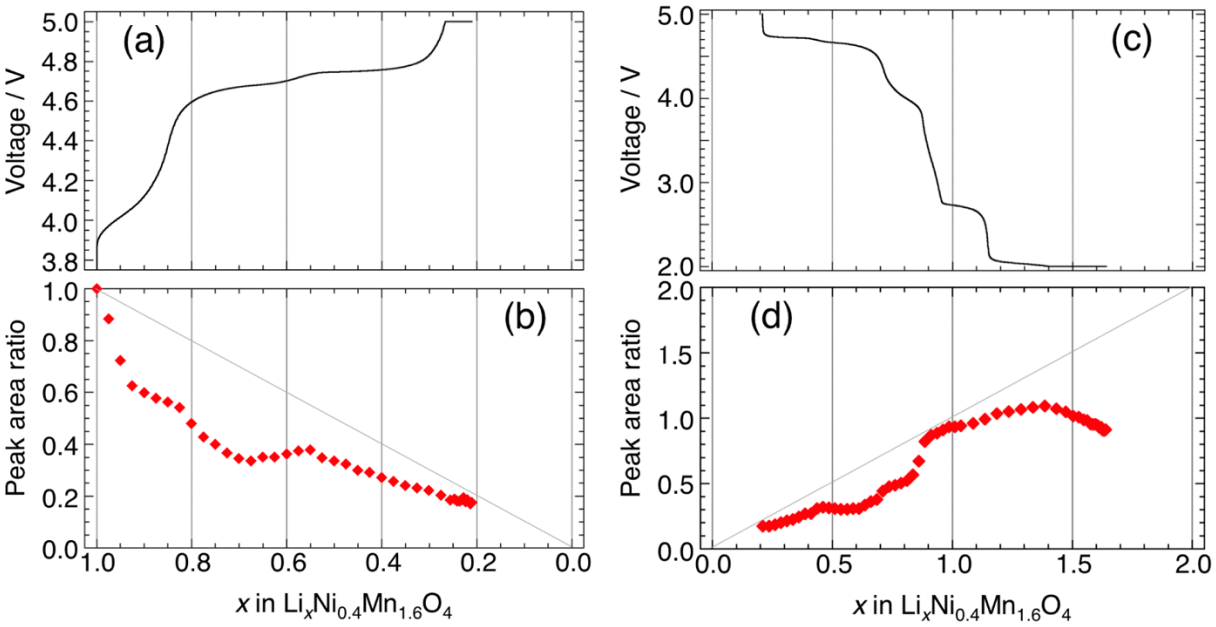

Figure 7. (a) Charging profile up to 5.0 V and (b) peak area extracted from in situ ^{7}Li spectra of the $LiNi_{0.4}Mn_{1.6}O_4$ electrode. (c) Discharging profile down to 2.0 V and (d) peak area variation.

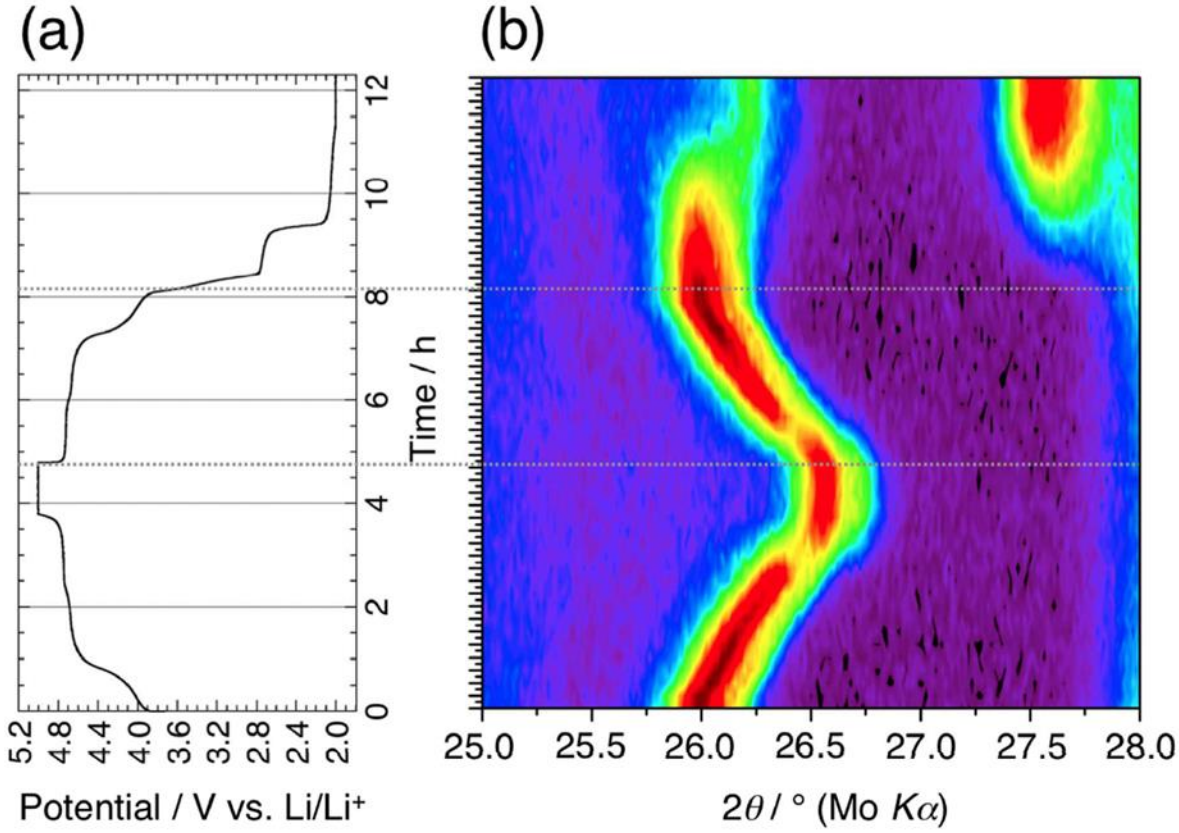

Figure 8. (a) Charge-discharge profile (0.2C rate) as a function of time, and (b) a contour plot of the in situ XRD profiles acquired with Mo Kα radiation in the 2θ range of 25.0^{o} - 28.0^{o}, corresponding to the 511/333 reflection.

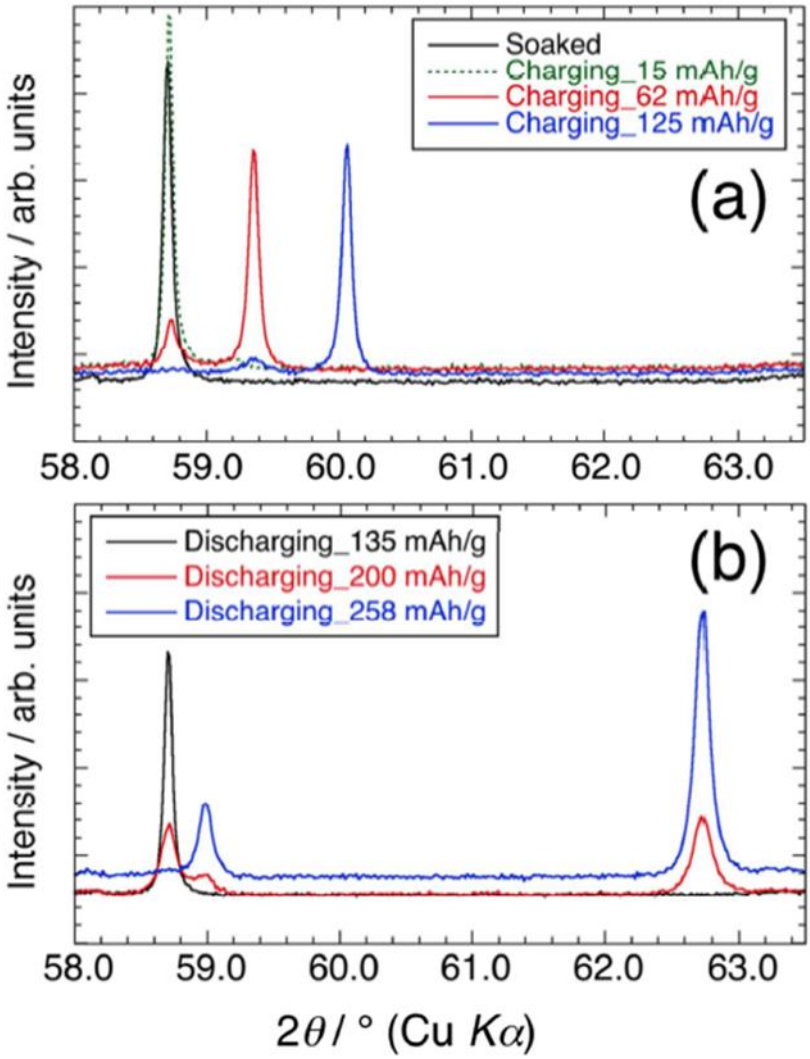

Figure 9. XRD profiles of the $LiNi_{0.5}Mn_{1.5}O_4$ electrodes disassembled on (a) charging process to 5.0 V, and (b) discharging process to 2.0 V. The 511/333 reflection for $P4_332$ and the 321 and 224 reflections for $I4_1/amd$ were shown.

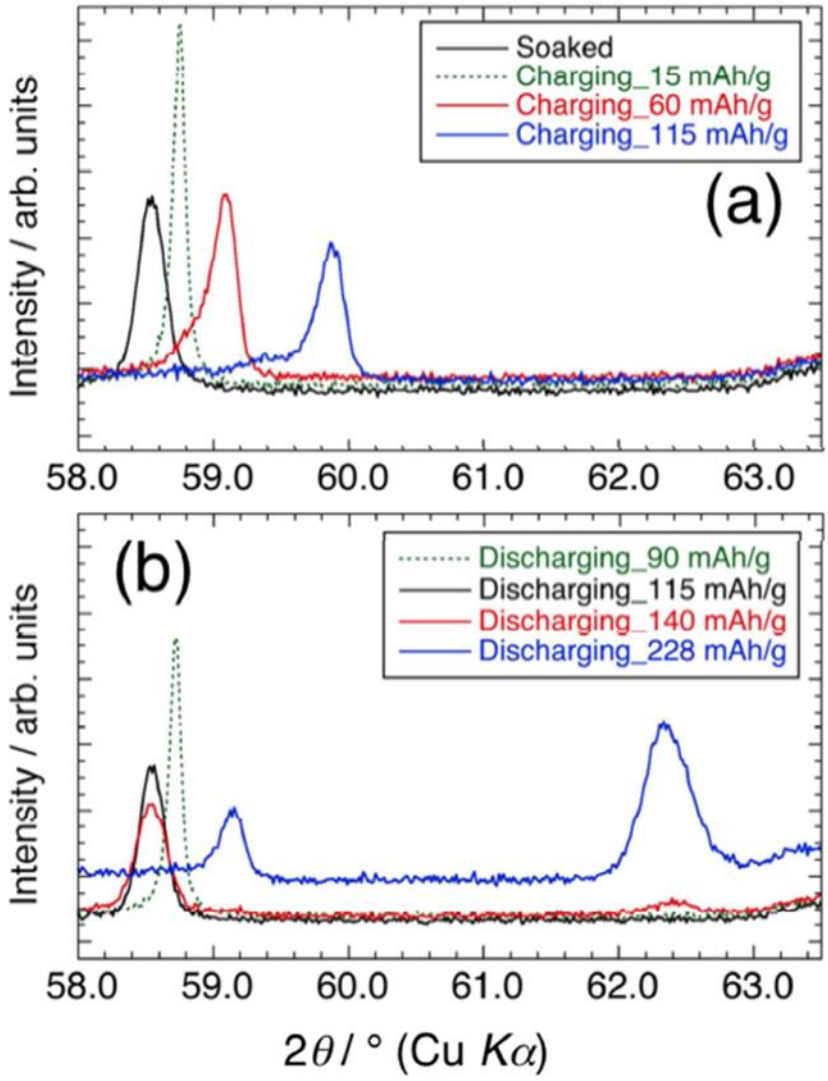

Figure 10. XRD profiles of the $LiNi_{0.4}Mn_{1.6}O_4$ electrode disassembled on (a) charging process to 5.0 V, and (b) discharging process to 2.0 V. The 511/333 reflection for $Fd\bar{3}m$ and the 321 and 224 reflections for $I4_1/amd$ were shown.

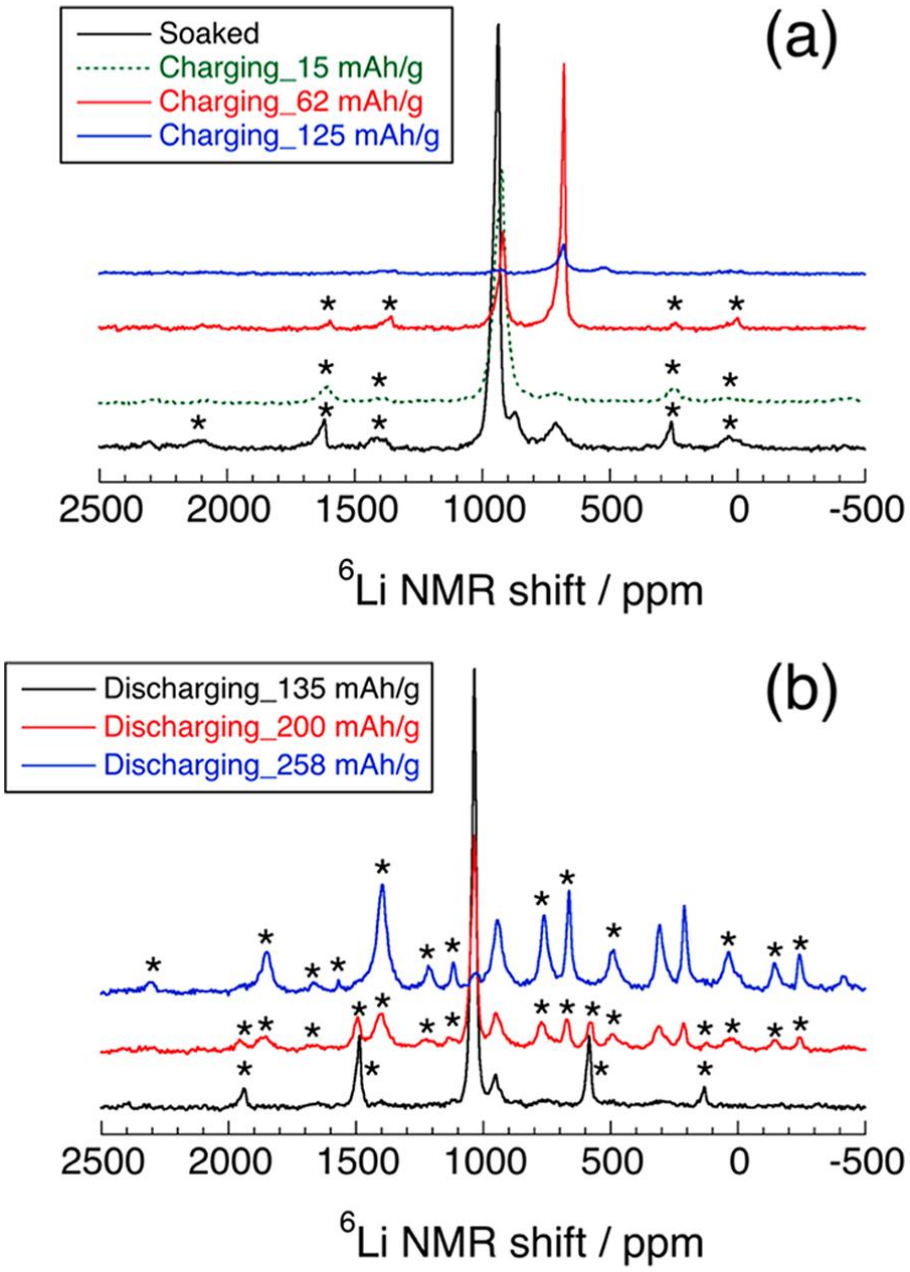

Figure. 11. ^{6}Li MAS NMR spectra of the $LiNi_{0.5}Mn_{1.5}O_4$ electrode disassembled on (a) charging process to 5.0 V, and (b) discharging process to 2.0 V. These were acquired at a MAS rate of 60 and 40 kHz, respectively. Asterisks indicate spinning sidebands. Spectra were normalized for sample weight and scan numbers and stacked upward for clarity.

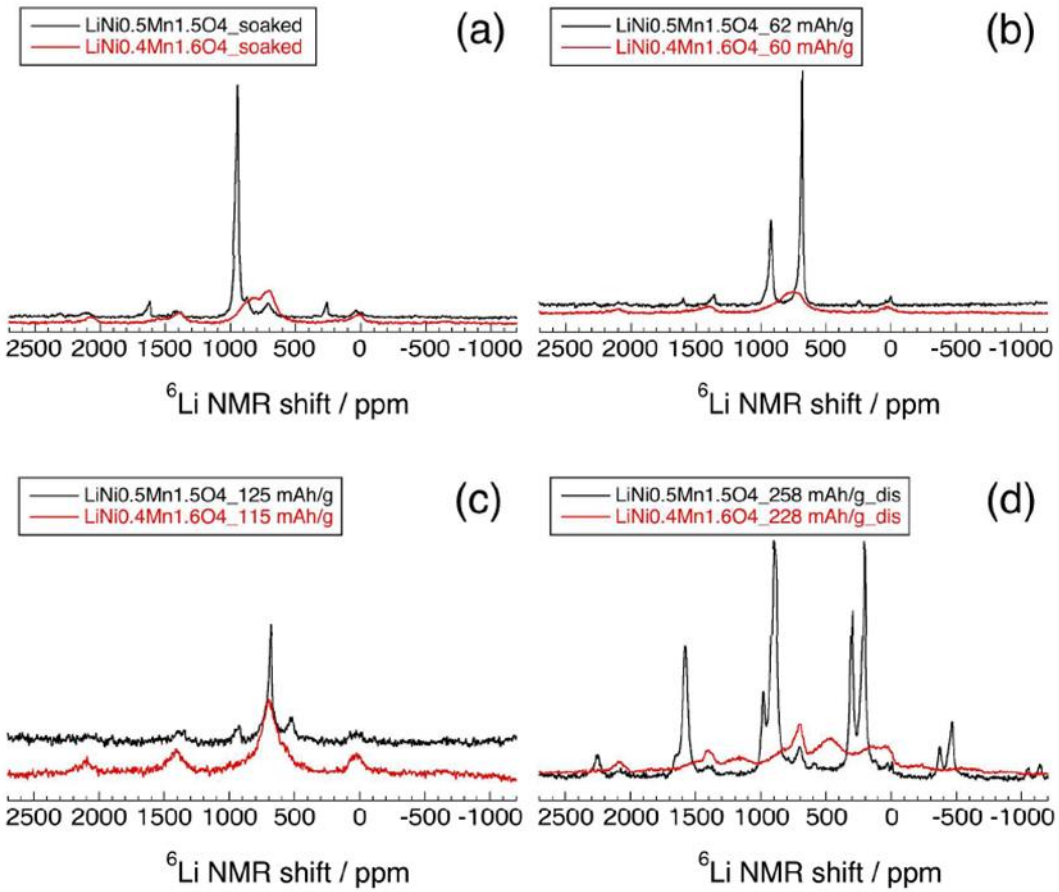

Figure 12. Comparison of the ^{6}Li MAS NMR spectra between the $LiNi_{0.5}Mn_{1.5}O_4$ and $LiNi_{0.4}Mn_{1.6}O_4$ electrodes disassembled at similar charging and discharging states; (a) soaked, (b) charging to ~62 mA h g^{-1}, (c) charging to 5.0 V, and (d) discharging to 2.0 V. They were acquired at a MAS rate of 60 kHz.

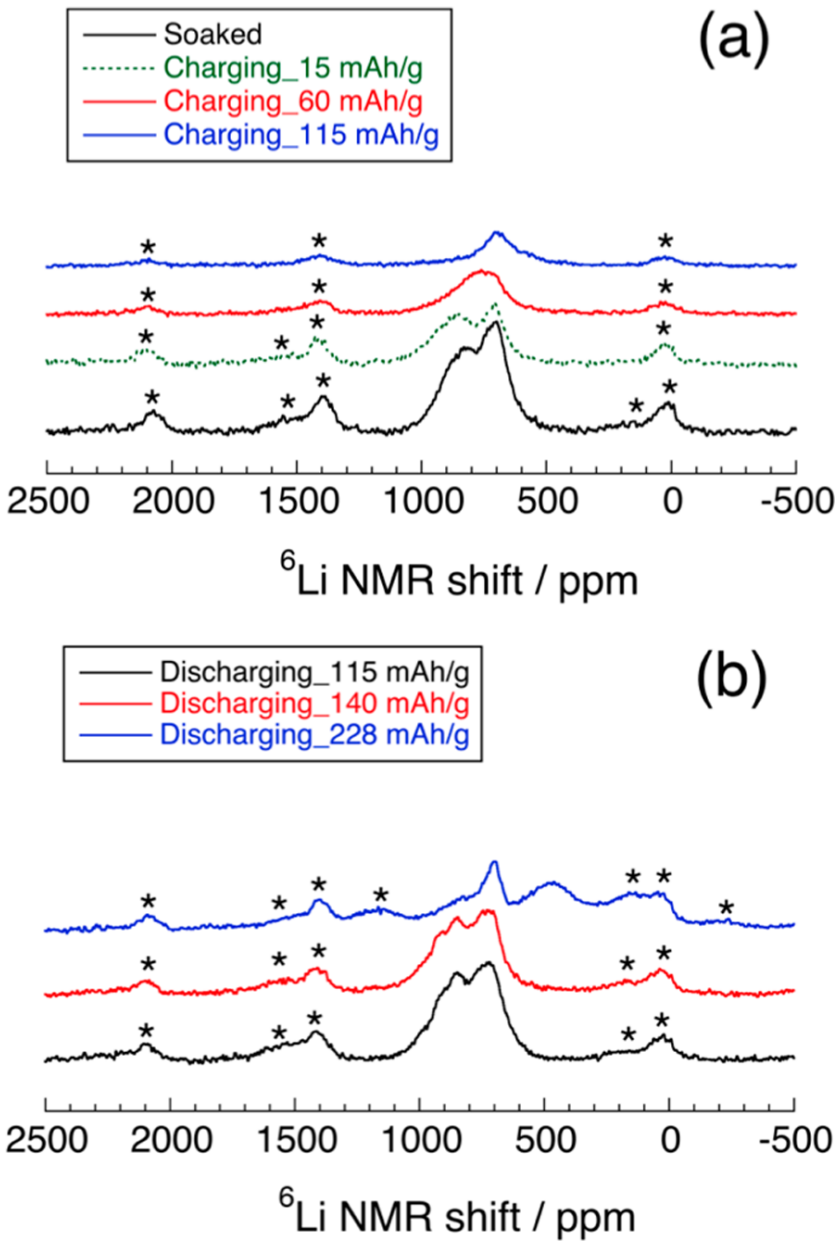

Figure 13. ^{6}Li MAS NMR spectra of the $LiNi_{0.4}Mn_{1.6}O_4$ electrode disassembled on (a) charging process to 5.0 V and (b) discharging process to 2.0 V. These were all acquired at a MAS rate of 60 kHz. Asterisks indicate spinning sidebands. Spectra were normalized for sample weight and scan numbers and stacked upward for clarity.

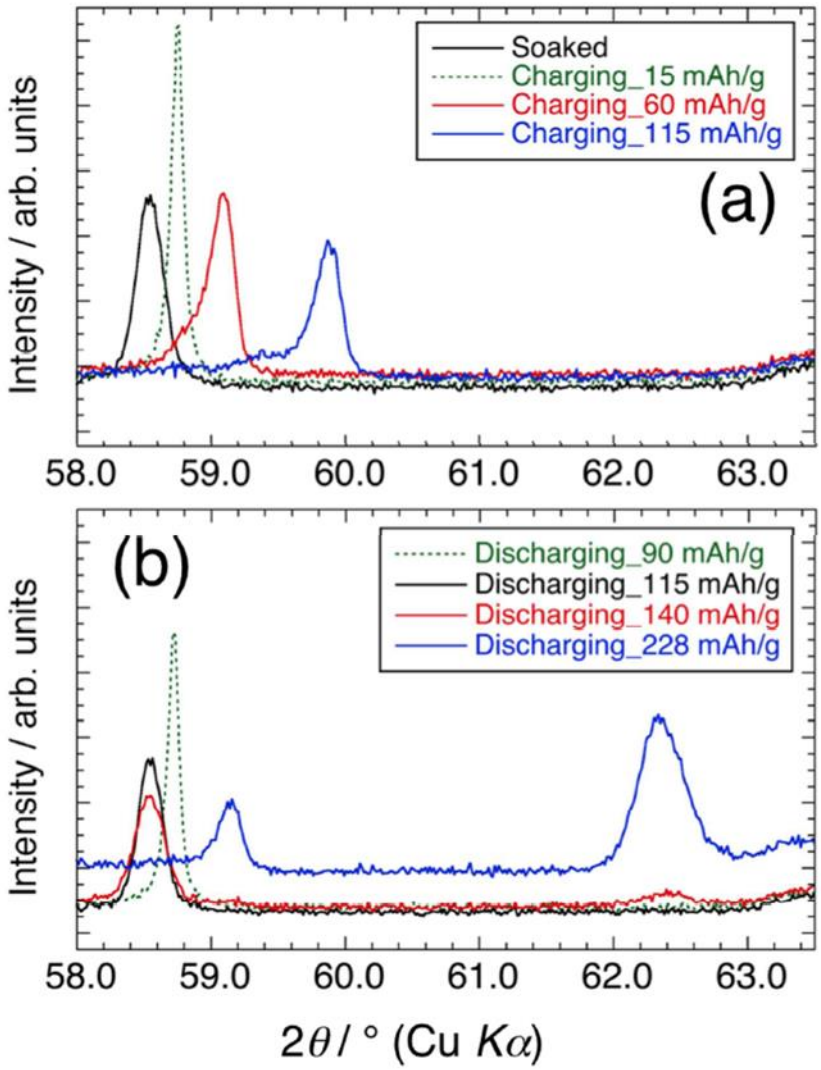

Figure 14. XRD profiles of the $LiNi_{0.4}Mn_{1.6}O_4$ electrode disassembled on (a) charging process to 5.0 V, and (b) discharging process to 2.0 V. The 511/333 reflection for $Fd\bar{3}m$ and the 321 and 224 reflections for $I4_1/amd$ were shown.

References

[1] J.-H. Kim, S.-T. Myung, C. S. Yoon, S. G. Kang, Y.-K. Sun, *Chem. Mater.* **2004**, *16*, 906.

[2] M. Kunduraci, G. G. Amatucci, *J. Electrochem. Soc.* **2006**, *153*, A1345.

[3] D. Pasero, N. Reeves, V. Pralong, A. R. West, *J. Elctrochem. Soc.* **2008**, *155*, A282.

[4] L. Wang, H. Li, X. Huang, E. Baudrin, *Solid State Ionics* **2011**, *193*, 32.

[5] J. Cabana, M. Casas-Cabanas, F. O. Omenya, N. A. Chernova, D. Zeng, M. S. Whittingham, C. P. Grey, *Chem. Mater.* **2012**, *24*, 2952.

[6] E.-S. Lee, K.-W. Nam, E. Hu, A. Manthiram, *Chem. Mater.* **2012**, *24*, 3610.

[7] J.-H. Kim, A. Huq, M. Chi, N. P. W. Pieczonka, E. Lee, C. A. Bridges, M. M. Tessema, A. Manthiram, K. A. Persson, B. R. Powell, *Chem. Mater.* **2014**, *26*, 4377.

[8] S. H. Park, S.-W. Oh, S. H. Kang, I. Belharouak, K. Amine, Y.-K. Sun, *Electrochim. Acta* **2007**, *52*, 7226.

[9] Q. Zhong, A. Bonakdarpour, M. Zhang, Y. Gao, J. R. Dahn, *J. Electrochem. Soc.* **1997**, *144*, 205.

[10] K. Ariyoshi, Y. Iwakoshi, N. Nakayama, T. Ohzuku, *J. Electrochem. Soc.* **2004**, *151*, A296.

[11] N. Hayakawa, T. Kawai, H. Sakai, A. Honda, T. Oyama, K. Yamanaka, C. Yogi, T. Ohta, *Hyomenkagaku* **2013**, *34*, 415 (in Japanese).

[12] T. Okumura, M. Shikano, H. Kobayashi, *J. Power Sources* **2013**, *244*, 544.

[13] H. Arai, K. Sato, Y. Orikasa, H. Murayama, I. Takahashi, Y. Koyama, Y. Uchimoto, Z. Ogumi, *J. Mater. Chem. A* **2013**, *1*, 10442.

[14] J. Rana, S. Glatthaar, H. Gesswein, N. Sharma, J. R. Binder, R. Chernikov, G.

Schumacher, J. Banhart, *J. Power Sources* **2014**, *255*, 439.

[15] J. Zhou, D. Hong, J. Wang, Y. Hu, X. Xie, H. Fang, *Phys. Chem. Chem. Phys.* **2014**, *16*, 13838.

[16] K. R. Morgan, S. Collier, G. Burns, K. Ooi, *J. Chem. Soc., Chem. Commun.* **1994**, 1719.

[17] C. Marichal, J. Hirschinger, P. Granger, M. Ménétrier, A. Rougier, C. Delmas, *Inorg. Chem.* **1995**, *34*, 1773.

[18] P. Mustarelli, V. Massarotti, M. Bini, D. Capsoni, *Phys. Rev. B* **1997**, *55*, 12018.

[19] Y. J. Lee, F. Wang, C. P. Grey, *J. Am. Chem. Soc.* **1998**, *120*, 12601.

[20] M. Ménétrier, I. Saadoune, S. Levasseur, C. Delmas, *J. Mater. Chem.* **1999**, *9*, 1135.

[21] Y. J. Lee, C. P. Grey, *Chem. Mater.* **2000**, *12*, 3871.

[22] Y. J. Lee, F. Wang, S. Mukerjee, J. McBreen, C. P. Grey, *J. Electrochem. Soc.* **2000**, *147*, 803.

[23] Y. J. Lee, C. Eng, C. P. Grey, *J. Electrochem. Soc.* **2001**, *148*, A249.

[24] Y. J. Lee, S.-H Park, C. Eng, J. B. Parise, C. P. Grey, *Chem. Mater.* **2002**, *14*, 194.

[25] C. P. Grey, N. Dupré, *Chem. Rev.* **2004**, *104*, 4493.

[26] A. R. Armstrong, N. Dupré, A. J. Paterson, C. P. Grey, P. G. Bruce, *Chem. Mater.* **2004**, *16*, 3106.

[27] L. S. Cahill, S.-C. Yin, A. Samoson, I. Heinmaa, L. F. Nazar, G. R. Goward, *Chem. Mater.* **2005**, *17*, 6560.

[28] C. Chazel, M. Ménétrier, L. Croguennec, C. Delmas, *Inorg. Chem.* **2006**, *45*, 1184.

[29] J. Cabana, S.-H. Kang, C. S. Johnson, M. M. Thackeray, C. P. Grey, *J. Electrochem. Soc.* **2009**, *156*, A730.

[30] C. Sirisopanaporn, R. Dominko, C. Masquelier, A. R. Armstrong, G. Mali, P. G. Bruce, *J. Mater. Chem.* **2011**, *21*, 17823.

[31] K. Shimoda, H. Sugaya, M. Murakami, H. Arai, Y. Uchimoto, Z. Ogumi, *J. Electrochem. Soc.* **2014**, *161*, A1012.

[32] M. Murakami, Y. Noda, Y. Koyama, K. Takegoshi, H. Arai, Y. Uchimoto, Z. Ogumi, *J. Phys. Chem. C* **2014**, *118*, 15375.

[33] R. E., II Gerald, R. J. Klingler, G. Sandí, C. S. Johnson, L. G. Scanlon, J. W. Rathke, *J. Power Sources* **2000**, *89*, 237.

[34] R. E., II Gerald, J. Sanchez, C. S. Johnson, R. J. Klingler, J. W. Rathke, *J. Phys.: Condens. Matter* **2001**, *13*, 8269.

[35] M. Letellier, F. Chevallier, C. Clinard, E. Frackowiak, J.-N. Rouzaud, F. Béguin, *J. Chem. Phys.* **2003**, *118*, 6038.

[36] M. Letellier, F. Chevallier, M. Morcrette, *Carbon* **2007**, *45*, 1025.

[37] B. Key, R. Bhattacharyya, M. Morcrette, V. Seznéc, J.-M. Tarascon, C. P. Grey, *J. Am. Chem. Soc.* **2009**, *131*, 9239.

[38] F. Chevallier, F. Poli, B. Montigny, M. Letellier, *Carbon* **2013**, *61*, 140.

[39] K. Shimoda, M. Murakami, D. Takamatsu, H. Arai, Y. Uchimoto, Z. Ogumi, *Electrochim. Acta* **2013**, *108*, 343.

[40] K. Ogata, E. Salager, C. J. Kerr, A. E. Fraser, C. Ducati, A. J. Morris, S. Hofmann, C. P. Grey, *Nat. Commun.* **2014**, *5*, 3217.

[41] K. Gotoh, M. Izuka, J. Arai, Y. Okada, T. Sugiyama, K. Takeda, H. Ishida, *Carbon* **2014**, *79*, 380.

[42] E. Salager, V. Sarou-Kanian, M. Sathiya, M. Tang, J.-B. Leriche, P. Melin, Z.

Wang, H. Verin, C. Bassada, M. Deschamps, et al. *Chem. Mater.* **2014**, *26*, 7009.

[43] H. Jung, P. K. Allan, Y.-Y. Hu, O. J. Borkiewicz, X.-L. Wang, W.-Q. Han, L.-S. Du, C. J. Pickard, P. J. Chupas, K. W. Chapman, et al. *Chem. Mater.* **2015**, *27*, 1031.

[44] A. Bielecki, D. Burum, *J. Magn. Reson. A* **1995**, *116*, 215.

[45] N. M. Trease, L. Zhou, H. J. Chang, B. Y. Zhu, C. P. Grey, *Solid State Nucl. Magn. Reson.* **2012**, *42*, 62.

[46] L. Zhou, M. Leskes, A. J. Ilott, N. M. Trease, C. P. Grey, *J. Magn. Reson.* **2013**, *234*, 44.

[47] H. Duncan, B. Hai, M. Leskes, C. P. Grey, G. Chen, *Chem. Mater.* **2014**, *26*, 5374.

[48] S. Ivanova, E. Zhecheva, R. Stoyanova, D. Nihtianova, S. Wegner, P. Tzvetkova, S. Simova, *J. Phys. Chem. C* **2011**, *115*, 25170.

[49] A. S. Wills, N. P. Raju, C. Morin, J. E. Greedan, *Chem. Mater.* **1999**, *11*, 1936.

[50] W. I. F. David, M. M. Thackeray, L. A. de Picciotto, J. B. Goodenough, *J. Solid State Chem.* **1987**, *67*, 316.

Chapter 3. Elucidating of Fast Reaction Mechanism for High-potential Cathode using Time-resolved XRD

3.1. Introduction

Phase transition dynamics of electrode materials during charging and discharging is of great interest in the field of material science as well as in terms of practical battery performance such as rate capability. For lithium-ion battery application, the phase transition behavior of lithium iron phosphates $LiFePO_4$ (LFP) and nickel-substituted lithium manganese spinel $LiNi_{0.5}Mn_{1.5}O_4$ (LNMO) is intensively studied as they show good rate capability despite that they undergo two-phase reactions associated with large lattice volume changes (ca. 7% and 6%) during charging and discharging.[1-3] For LFP, high charging and discharging rates are attained only with nanosized materials and the behavior of this material showing moderate potential (3.4 V vs. Li/Li^+) have been analyzed with operando X-ray diffraction (XRD) and X-ray absorption spectroscopy (XAS) techniques with high time resolutions[4-6] that directly capture the changes of crystal structures and the oxidation states of the electrode materials, respectively. Operando synchrotron-beam aided analysis has demonstrated[7-10] that there are a variety of solid-solution intermediates between the end members (Li-rich $Li_{1-\alpha}FePO_4$ and Li-poor $Li_{\beta}FePO_4$ phases) during fast charging/discharging, in contrast to the two-phase coexistence of the Li-rich and Li-poor phases proposed by the ex situ analysis.[11,12] The existence of these intermediate states (metastable phases and solid-solutions) have been reported also based on theoretical calculations[13-15] and is expected to mitigate the lattice strain at the phase boundary in between the Li-rich and Li-poor

phases and hence assist fast charging and discharging. Though the physical origin of such intermediate states is hardly evaluated by operando XRD and XAS that offer averaged information, the detailed XRD profile analysis by Liu *et al.*[8] suggests that they are at the phase boundary. The existence of the phase boundary (phase transition front) in a single particle has been evidenced in chemically delithiated micron-sized LFP particles by transmission electron microscopy (TEM) observation.[16,17] It is expected that the excess energy required for single-phase transition is proportional to the particle volume (the cube of its size) while that for two-phase transition is proportional to the area of the phase boundary (the square of its size), implying that the two-phase transition pathway is preferred for large particles.

For the LNMO electrodes, there emerge three phases in the charge-discharge processes, namely $Li_{1.0}Ni_{0.5}Mn_{1.5}O_4$ (Li1), $Li_{0.5}Ni_{0.5}Mn_{1.5}O_4$ (Li1/2), and $Ni_{0.5}Mn_{1.5}O_4$ (Li0), and there are two regions of two-phase coexistence with their redox potential values close to each other (4.70 V (Li1/Li1/2) and 4.74 V (Li1/2/Li0) vs. Li/Li^+).[6,18-22] As the micron-sized LNMO particles show high rate capability,[23,24] it is expected that the existence of possible intermediate states between the stable phases (namely Li1, Li1/2, and Li0) is captured by operando analytical methods with high time resolutions. In such large particles, the phase transition front could be captured in electrochemically delithiated/lithiated samples, which has not been reported to our knowledge.

In this study, we report the phase transition behavior of the LNMO electrodes captured by operando TR-XRD measurement using synchrotron radiation X-ray. Micron-sized LNMO particles of the disordered type (space group $Fd\bar{3}m$) were used. It is shown that minor diffraction components appearing in the transition states, in addition to those of the thermodynamically stable phases, are originated from solid-solution domains at the phase transition front of $Li_xNi_{0.5}Mn_{1.5}O_4$ as suggested by ex

situ TEM observation of LNMO particles. The transition behavior accompanied with continuous lithium composition changes is demonstrated.

3.2. Experimental

Preparing the Cell: $LiNi_{0.5}Mn_{1.5}O_4$ (LNMO) (Toda Kogyo Co.) powder used as an active material has primary and secondary particle sizes of around 1 and 5-10 μm, respectively. Its disordered structure was confirmed by neutron diffraction at SPICA at J-PARC, Ibaraki, Japan.[21] The working electrode consisted of LNMO (80 wt%), acetylene black (10 wt%) and polyvinylidene difluoride (PVDF) binder (10 wt%), coated on aluminum current foil. After coating, the foil was dried at 80 ^oC for a few hours, and then pressed by a roll press (600 kgf). The thickness of the electrode layer was as thin as around 20 μm to minimize the effect of kinetics derived from the ion transportation in the electrolyte contained in the composite electrode.[31]

The electrochemical measurements of the electrode were employed using aluminum-pouch-type cells, which consisted of the working electrode (25 mm by 15 mm), metallic lithium as counter and reference electrodes, 1 mol dm^{-3} $LiPF_6$ in a 3:7 mixture of ethylene carbonate (EC) and ethyl methyl carbonate (EMC) as an electrolyte, and a polyolefin film as a separator. The cell was assembled in an Ar-filled glove box. The electrochemical charge and discharge tests were performed at room temperature and the potential range was between 3.5 and 5.0 V. The cell was controlled by a potentiostat (SP300, Bio-Logic). The cell capacity was preliminarily checked by 0.1 C rate (ca. 15 mA g^{-1}). The cell composition prior to the measurement from fully charged or discharged state was controlled also by a slow charge/discharge process of 0.1 C.

***Nonequilibrium Structural Analysis*:** The operando TR-XRD measurements were

conducted in a transmission mode at beam lines BL28XU and BL46XU at SPring-8, Hyogo, Japan. The incident X-ray of 12.4 keV (0.100 nm wavelength) was used with a beam size of 0.5 mm by 0.5 mm. The diffraction pattern was measured using a 2D hybrid pixel array detector PILATUS 100K (DECTRIS Ltd.). To realize a high time resolution to capture the dynamic behavior, we measured the diffractions in the region around the 115 diffraction of LNMO, in which region the diffraction signals from other cell components such as aluminum are absent. The profile was measured in 0.5 s with the interval of another 2.0 s while the electrochemical charge and discharge tests were employed at rate of 0.5, 1, or 5 C. This indicates that the composition change during a single XRD pattern measurement was less than 0.2%.

***Morphological Analysis*:** The TEM was employed using HF-3300EH (Hitachi High-Technologies Corporation) with Gatan GIF (Gatan Inc.) operated at 300 kV for initial $LiNi_{0.5}Mn_{1.5}O_4$ powder and a $Li_{0.25}Ni_{0.5}Mn_{1.5}O_4$ electrode obtained by 1 C charging. The $Li_{0.25}Ni_{0.5}Mn_{1.5}O_4$ sample was obtained by disassembling the cell shortly after the charging process was terminated. The electrode was sliced in a thickness of 100 nm using a focused ion beam (FIB, NB5000 FIB-SEM dualbeam system, Hitachi High-Technologies Corporation) with Ga ion at an accelerating voltage of 40-2 kV and then an Ar ion beam (Gatan PIPS Model 691, Gatan Inc.) at an accelerating voltage of 1 kV was applied to the sliced sample to remove the FIB damages formed on the both surfaces of the particle. The thickness of the sample for TEM observation was finally ca. 50 nm. ED analysis and EELS were also performed to analyze the particle morphology, crystal structure, and intraparticle distribution of the reacting material. The SEM was employed using SU8000 (Hitachi High-Technologies Corporation) at an accelerating voltage of 5 kV.

3.3. Results and Discussion

3.3.1. Intermediate States Suggested by Asymmetric Diffraction Profiles

Figure 1a shows the operando TR-XRD profiles of the LNMO electrode during charging from the fully discharged state and the following full discharging, both at 1 C rate (146 mA g^{-1}). The corresponding potential profiles are shown in Figure 2. A capacity of approximately 110 mA h g^{-1} was obtained with the electrode utilization of 80%. In the XRD profiles, there are three peaks corresponding to the Li0, Li1/2, and Li1 phases, with continuous peak shifts for the Li1 phase at the beginning of charging and the end of discharging, which is in agreement with the reported behavior of the disorder-type LNMO.[25] The lattice constants (0.8093 nm and 0.8011 nm for the Li1/2 and Li0 phases) obtained from the diffraction peaks are also in good agreement with the literature.[3]

The XRD profile can apparently be represented by the two-phase coexistence model, however, it is noticed from the detailed observation of the profile that the peak shapes corresponding to both the starting and produced phases are asymmetric. Figure 1b shows an example of profile fitting results taken from the TR-XRD measurements in the transition state between the Li1/2 and Li0 phases. When two symmetric peak profiles of Gaussian functions are assumed for these phases, the experimentally observed intensity in between the two peaks is larger than the calculated intensity. Such phenomena were generally observed in other profiles including the transition between the Li1 and Li1/2 phases, and the diffraction intensity increase to lead asymmetric diffraction profiles was always found in between the main peaks (see Figure 3). These results suggest us that there are minor diffractions with intermediate d values, in

addition to those for the thermodynamically stable Li1, Li1/2, and Li0 phases. This is in contrast to the profiles near the single-phase region of the Li1, Li1/2, and Li0 phases where a single symmetric Gaussian function can well describe the profiles.

To describe the asymmetric diffraction profiles observed in the transition between the stable phases, two additional diffraction components were added to those for the stable phases, assuming that all four partial profiles are described with the symmetrical Gaussian functions. As shown in Figure 1c, good agreement between the experimental and calculated profiles is obtained. Such good fits were obtained also in other profiles recorded during the TR-XRD measurement. Here we assume that two additional intermediates have spinel structures similar to the thermodynamically stable phases and that the apparent d values obtained in the XRD measurement can be translated as the lattice constants of the additional cubic spinels. Figure 4 shows the lattice constant variation obtained from the peak centers of the partial diffraction profiles. The lattice constants of the stable phases are nearly invariant except for the solid solution region of the Li1 phase whereas the lattice constants for the additional components, which are always in between those of the stable phases, change in the course of charging (delithiation) and discharging (lithiation). This suggests us that the additional components originate in intermediates between the starting and produced phases. The diffraction centers and hence the lattice constants of the additional components nearly continuously change to fill the gaps between the stable phases, implying the solid-solution nature of the intermediates to facilitate fast phase transitions, as has been found for the LFP electrode.[8,26] The full-width at half-maximum (FWHM) values of the partial diffraction profiles for the stable phases are generally low and increase on the appearance or the disappearance of the phase, whereas the FWHM values of the additional components are relatively high as shown in Figure 5. This may be the reason

why such minor diffractions have not been reported so far. No previous report on the minor diffractions by ex situ XRD measurements suggests that they are gradually lost during the relaxation. Assuming that the diffraction intensity of $Li_xNi_{0.5}Mn_{1.5}O_4$ is unchanged for all the x value, the normalized peak area can be correlated to the amount (or molar ratio) of the stable phases and the intermediates. The normalized peak area and hence the molar ratio of the intermediates is at their maximum in the middle of transitions between the stable phases as shown in Figure 6.

3.3.2. Origin of Intermediate States

There are two possible models accounting for the presence of the intermediate states in the reaction process as shown in Figure 7. Model A shown as "particle-by-particle model" is that several solid-solution intermediates between the stable phases are simultaneously present while the phase transition is so fast that the composition in each single particle seems essentially uniform.[27] Here various states in different particles result in the minor diffractions. Model B shown as "concurrent process model" is that the reaction simultaneously proceeds in all the particles and there is a phase transition front in a single particle[28] and mixed states in the particle including the phase transition front are captured by XRD. On the analogy of the micron-sized LFP particles in which the domino-cascade type fast phase transition proposed for the nanosized particles can hardly occur,[29] Model B (concurrent process model) seems more probable for micron-sized LNMO particles used in this experiment. If the reaction proceeds as shown in Model B and the movement of the phase transition front is relatively slow, ex situ TEM measurement could reveal the two-phase coexistence in a single particle. That is, we expect that the TEM analysis provides supportive physical information on

the phase transition front suggested by the XRD measurement.

The TEM analysis was then performed. The electron diffraction (ED) patterns of the pristine LNMO particles show that they have a spinel structure with a lattice constant of 0.82 nm as shown in Figure 8, being consistent with the result from the synchrotron XRD, and indicate that they are of primary particles (single crystals). The scanning electron microscopy (SEM) images of the pristine and the charged samples show that facetted primary LNMO particles with a few microns in size are kept during the charging process as shown in Figure 9. Figure 10a shows a TEM image of a $Li_{0.25}Ni_{0.5}Mn_{1.5}O_4$ sample obtained from the cell disassembled just after the 1 C charging process was finished. Compared to the homogeneous morphology of the pristine LNMO particle, there are cracks, stripes, lattice defects, and regions of different contrast in this charged sample, suggesting that these particles contain multiple phases. The ED patterns of a single primary particle of the $Li_{0.25}Ni_{0.5}Mn_{1.5}O_4$ sample show that all regions have the same spinel structures and the lattice constants are consistent with the Li1/2 and Li0 phases obtained by the XRD measurements (see Figure 11). As the small difference in the lattice constant between these two phases is hard to distinguish by the ED patterns, we tried to distinguish the domains of the two phases by the presence (Li1/2 phase) and absence (Li0 phase) of lithium using electron energy loss spectroscopy (EELS). Figures 10b and 10c shows intensity profiles of EELS spectra obtained from regions A and B in a single primary particle of the $Li_{0.25}Ni_{0.5}Mn_{1.5}O_4$ sample shown in Figure 10a. There is no lithium in region A whereas the presence of lithium is detected in region B. We employed several TEM-EELS measurements in different particles to find the coexistence of lithium-containing and lithium-absent regions in single particles and the results show that the bright and dark regions in the TEM images, respectively, correspond to the lithium-absent and lithium-

containing regions by means of EELS. This indicates that the Li1/2 and Li0 phases coexist in single particles of the electrochemically obtained $Li_{0.25}Ni_{0.5}Mn_{1.5}O_4$ sample and that the phase transition front exists in between these two phases. Although the sample taken from the disassembled cell is in the relaxed state and not in the transition state, the result obtained here strongly suggests that the two phases coexist in micronsized primary particles during battery operation and that the phase transition of $LiNi_{0.5}Mn_{1.5}O_4$ proceeds with Model B. Model A can be excluded also by the fact that the profile corresponding to the single phase region, especially that at Li1/2, is well described with a single symmetric Gaussian function with small profile broadening as shown in Figure 3, showing that particle-by-particle composition distribution is limited. Note that possible strain effect at the phase transition front can contribute to the asymmetric peak profile as shown in Figure 1, nevertheless, such strain appearing only the intermediate states is consistent with the phase transition with lattice mismatches shown in Model B. Note also that this behavior is totally different from that in LNMO nanoparticles that show the solid-solution-type phase transition at C/4 rate.[30]

3.3.3. Phase Transition Dynamics at High and Low Rates

The asymmetric profile captured by operando TR-XRD is thus considered to be the reflection of the diffractions from the stable phases and from the domains at the phase transition front appeared in the transition states that could mitigate the lattice strain at the phase boundary and facilitate fast phase transition of the LNMO electrodes. Assuming the Vegard's law, this lattice constant change can be correlated to the lithium content change in the intermediate domain at the phase transition front that presumably fill the gap of the lithium content, as well as that of the volume, between the starting

and produced phases. Namely, an XRD profile containing diffractions from stable phases and intermediates can be interpreted to give a picture of a solid-solution domain spatially existing at the phase boundary between the stable phases as depicted in Figure 12.

To examine the effect of the charge-discharge rate on the phase transition behavior, the behavior at higher rate of 5 C was similarly analyzed with the operando TR-XRD method. Reflecting the good rate capability of this material, the capacity at 5 C rate was 94 mA h g^{-1} in the potential plateau region at 4.7 V with the material utilization of 64% as shown in Figure 2. Again, each diffraction profile can mostly be expressed with diffraction components corresponding to stable phases and intermediates. The lattice constants of the Li1 and Li1/2 phases obtained from the diffraction centers are nearly unchanged except for the solid-solution region in the Li1 phase whereas that for the Li0 phase gradually shifts approaching to the Li1/2 phase, being different from the behavior at 1 C rate (see Figure 13). This is particularly so for the discharging process with no apparent minor diffraction, showing reaction asymmetry between charging and discharging of the LNMO electrode at high rates. Other intermediates behave so that the gap between the thermodynamically stable phases can be filled. The asymmetry is obvious in the normalized peak areas of the components during the phase transitions as shown in Figure 14. The FWHM values are relatively low for the thermodynamically stable phases, however, those of the Li0 phase, especially on discharging, are as high as those observed for the minor components as shown in Figure 15. At lower rates, on the other hand, it is deduced that the intermediate states are gradually lost during the relaxation, because the products after full relaxation have been reported to consist of only the Li1, Li1/2, and Li0 phases.[20,25] As expected, a lower rate test at 0.5 C results in the same transition behavior as 1 C but low intensities for the intermediates as shown

in Figure 16. This indicates that the transition mechanism shown in Model B is valid at lower rates, though the contribution of the intermediates depends on the rate.

Up to here the phase transitions are expressed by representative lattice constants of the thermodynamically stable phases and intermediates, however, the observed broad XRD profiles can actually be correlated to the diverging lattice constants (and hence lithium contents), which shows the solid-solution nature of the intermediates. Based on this, the lattice constant distribution and the corresponding distribution (population) of the lithium content were evaluated from the diffraction profiles. The population profiles of the lattice constant shown in Figure 17 were estimated from the *operando* TR-XRD profiles as follows. Assuming the peak broadening comes only from the diverging d value, a XRD profile with normalized area intensity, $f(2\theta)$, is considered as a distribution function of 2θ. Therefore, the XRD profile can be converted to a distribution function of lattice constant,

$$p(a)da = f(2\theta)d(2\theta), \tag{3.1}$$

where

$$a = \frac{\sqrt{h^2+k^2+l^2}\lambda}{2sin\theta}, \tag{3.2}$$

(h, k, l) = (1, 1, 5) and λ = 0.100 nm in this study. The fitted XRD profiles with Gaussian functions, instead of the raw profiles, were used for smoothing. The population x of the lattice constant smaller than y is estimated as,

$$x = \Pr(a < y) = \int_{-\infty}^{y} p(a)da, \quad \textbf{(3.3)}$$

where Pr denotes probability.

The obtained results are shown in Figure 17. The population in the horizontal axis shows the degree of the reaction process and hence the location of the phase transition front in an averaged single particle. Apart from the solid-solution region in the Li1 phase, S-inverse-shaped profiles with dominant Li0, Li1/2, and Li1 regions are apparent for 1 C rate, as expected. At 5 C rate, the behavior is similar to that at 1 C rate between the Li1 and Li1/2 phases while there is a considerable shift of the lithium content in the Li0 phase. This indicates that, at faster rate with larger overvoltage applied to the system, the solid-solution-type reaction with homogenized lithium content, namely Model A, is preferred over the two-phase reaction with the movement of the phase transition front. The phase transition route dependency on the charge–discharge rate has also been found in LFP.[7] Note that the asymmetric behavior shown in Figure 13, 14, and 15 is not appreciable in Figure 17, in which the information of the diffraction profiles is obscured, however, the asymmetric profile changes at around the Li0 phase (the end of charging and the beginning of discharging) is obvious as depicted in Figure 18.

This asymmetric behavior between the Li0 and Li1/2 phases, in which the solid-solution-type behavior is pronounced on discharging more than charging, can be correlated to the previously reported behavior that the phase transition kinetics between the Li1 and Li1/2 phases is faster than that between the Li1/2 and Li0 phases.[21,22] For the LNMO electrode, the reaction potential values for the subsequent phase transitions are so close that both transitions can proceed under high rate conditions with sufficient overpotential. For charging, it is suggested that the first transition from the Li1 phase

to the Li1/2 one is nearly completed until the second transition from the Li1/2 to the Li0 starts, because the former kinetics is faster than the latter. So, the transition proceeds largely in a stepwise manner. For discharging, it is probable that the first transition from the Li0 phase to the Li1/2 one and the second transition from the Li1/2 to the Li1 simultaneously proceed due to the kinetic relationship described above. These behaviors are characteristically shown at high population region (*ca.* 1.0 to 0.7) in Figures 17c and 17d. Accordingly, it is expected that, on high rate discharging, the transition from the Li0 phase to the Li1/2 one is much accelerated to avoid the formation of three-phase coexistence in a single particle that can have large stress, and to result in the kinetically more favorable solid-solution pathway.

3.4. Conclusions

Charge-discharge reaction dynamics of micron-sized particles of $LiNi_{0.5}Mn_{1.5}O_4$ (LNMO) are investigated by TR-XRD, TEM, and EELS. Operando TR-XRD reveals that there are intermediate states in the two-phase coexistence region of $LiNi_{0.5}Mn_{1.5}O_4$, namely between Li1 and Li1/2 and between Li1/2 and Li0, while symmetric diffraction profiles are observed in single-phase regions. Good agreement between the experimental and calculated profiles is obtained when two additional diffraction components are added to those for the thermodynamically stable phases. TEM-EELS analysis shows the two-phase coexistence in primary particles, suggesting that the origin of the intermediate states is ascribed to the solid-solution domain at the phase transition front. For the Li1 and Li1/2 phases, the lattice changes observed at 5 C rate are similar to that observed at 1 C rate. However, the Li0 phase shows lattice constant

changes in a solid-solution manner at 5 C rate whereas the lattice constant is invariant at 1 C rate. This can be attributed to the transition kinetics between Li1/2 and Li0 being slower than that between Li1 and Li1/2. Namely, when the required current flow exceeds a certain limit corresponding to the maximum speed of the phase front movement, a kinetically more favorable solid-solution pathway is preferred between the Li1/2 and Li0 phases.

Two-phase reaction with a volume change and a lattice misfit is very common among the phase transitions of electrode materials during the charging and discharging, and the phase transition dynamics is likely to be affected by factors such as particle size and crystallinity of the materials. The operando XRD measurements with the detailed peak-profile analysis demonstrated in the present study can contribute to elucidation of the phase transition dynamics in single particles with consideration of the factors, and thus to further development of high-rate capable batteries.

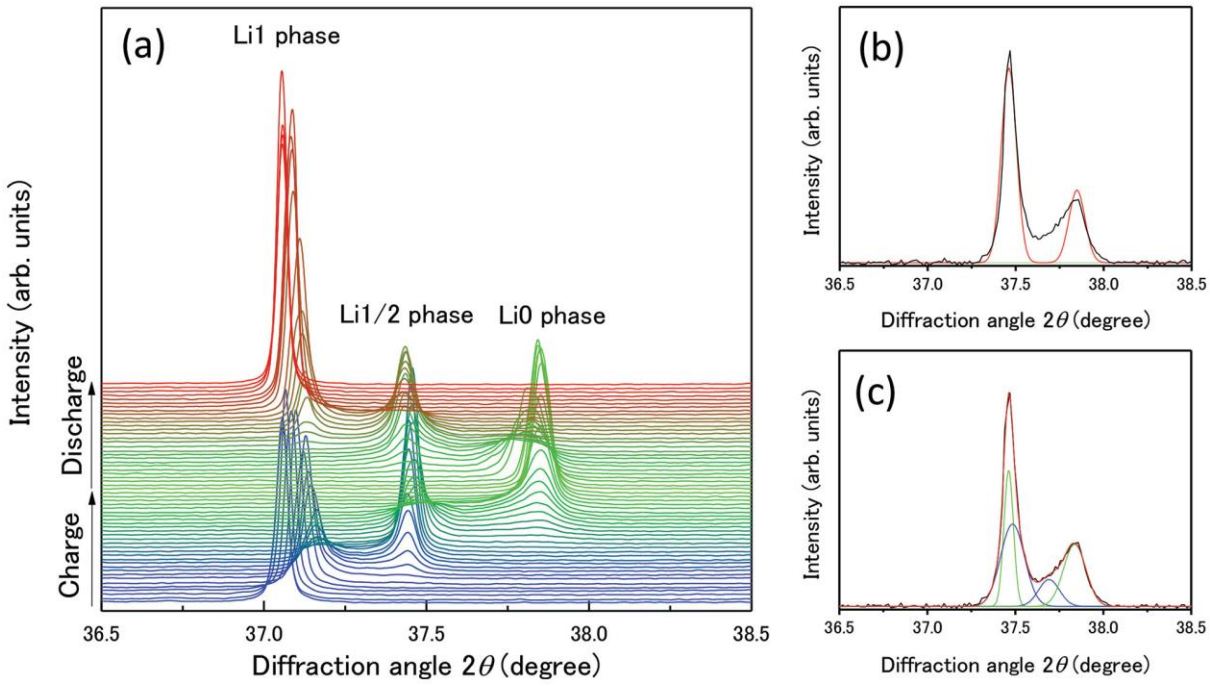

Figure 1. (a) Operando TR-XRD profiles of 115 diffractions in a $LiNi_{0.5}Mn_{1.5}O_4$ electrode at rate of 1 C (146 mA g^{-1}), (b) an XRD profile during phase transition between Li1/2 and Li0 phases fitted based on the conventional two-phase reaction model, and c) that fitted with Li1/2 and Li0 phases with additional two minor components.

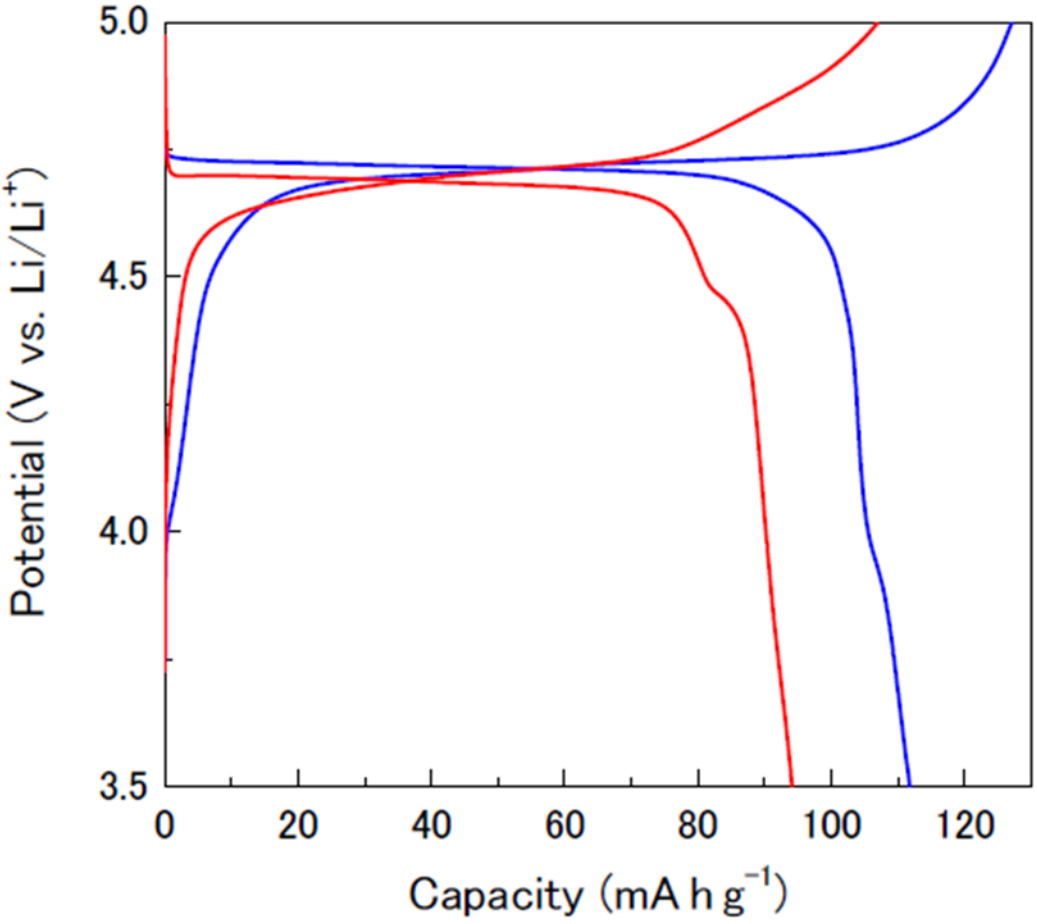

Figure 2. Potential profiles of $LiNi_{0.5}Mn_{1.5}O_4$ electrodes with 1 C rate (146 mA g^{-1}; blue lines) and 5 C rate (730 mA g-1; red lines).

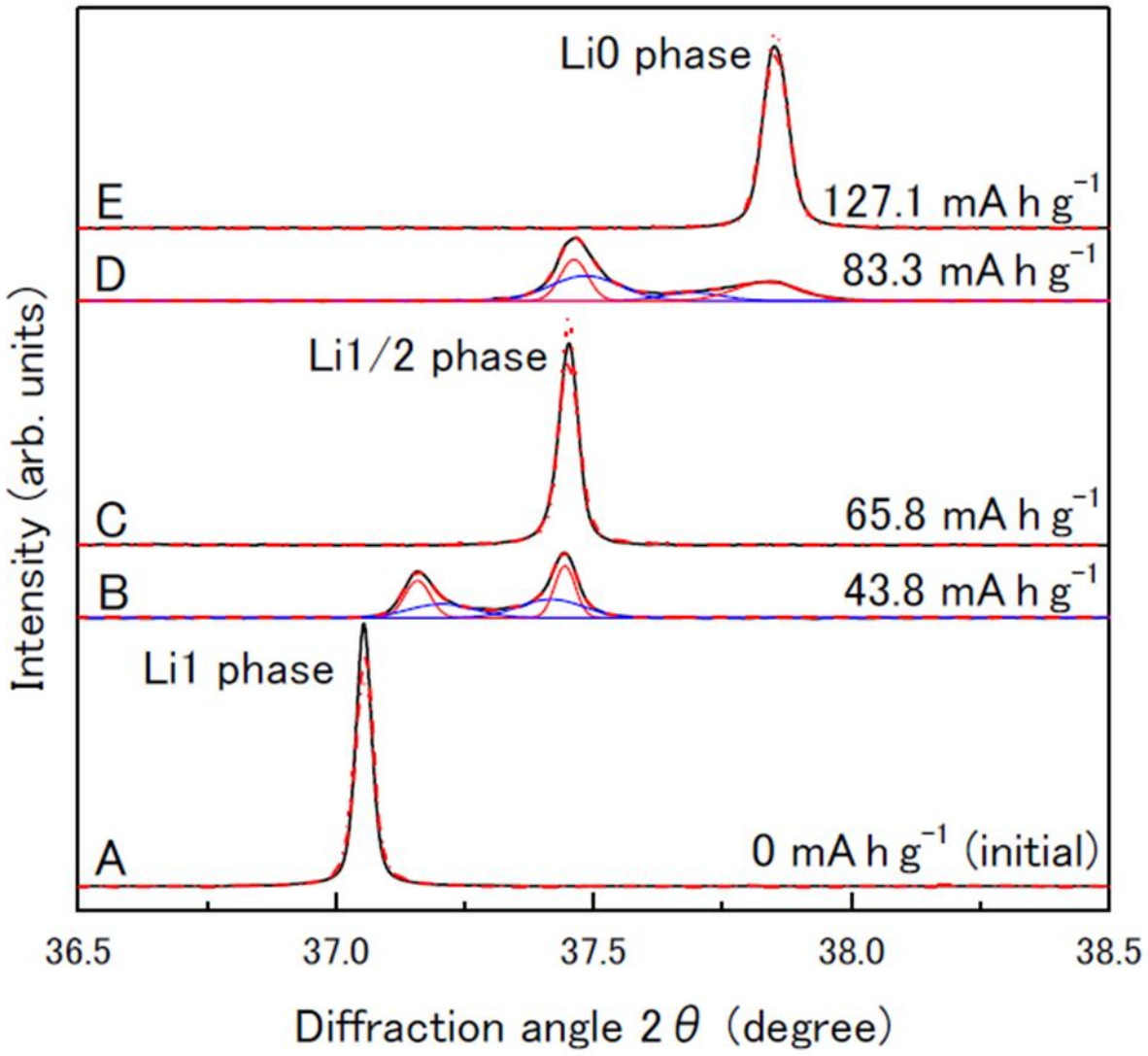

Figure 3. Examples of XRD profiles of a LiNi0.5Mn1.5O4 electrode in 1 C charging. The profiles A, C and E are fitted with a single symmetric Gaussian function, while B and D are fitted with four Gaussian functions; two for the starting and produced phases and two for additional intermediates.

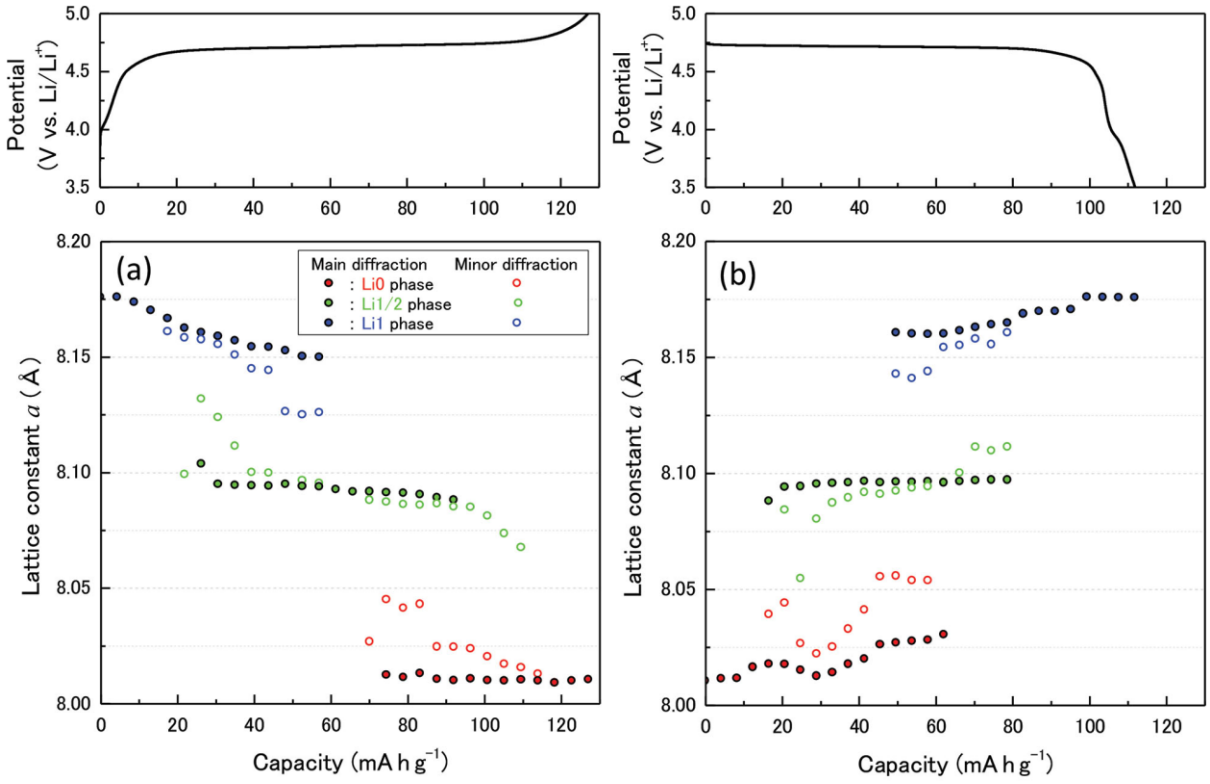

Figure 4. Variation of lattice constants of a $LiNi_{0.5}Mn_{1.5}O_4$ electrode obtained from peak centers of partial diffraction profiles with the corresponding electrode potential profiles during (a) charging and (b) discharging at rate of 1 C.

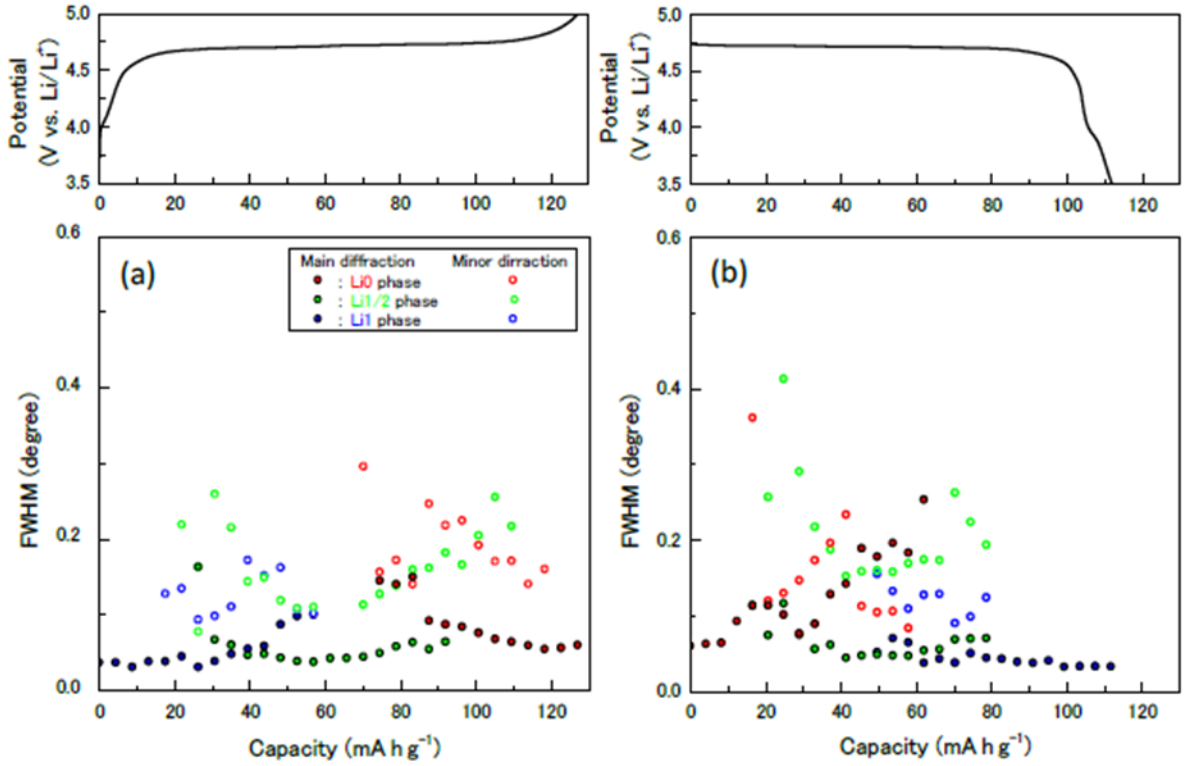

Figure 5. Variation of FWHM of partial diffraction profiles of a $LiNi_{0.5}Mn_{1.5}O_4$ electrode with the corresponding electrode potential profiles during (a) charging and (b) discharging at rate of 1 C.

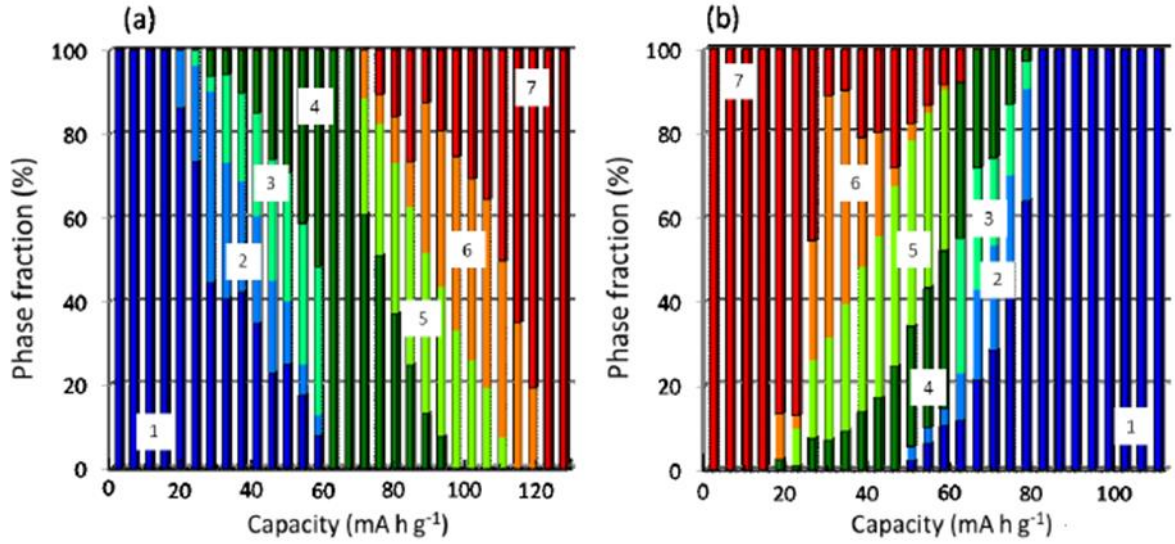

Figure 6. Variation of phase ratio of $LiNi_{0.5}Mn_{1.5}O_4$ during (a) charging and (b) discharging at rate of 1 C. The bars 1-7 correspond to Li1 diffractions, minor ones by Li1, minor ones by 1/2 toward Li1, Li1/2 ones, minor ones by 1/2 toward Li0, minor ones by Li0 and Li0 ones, respectively.

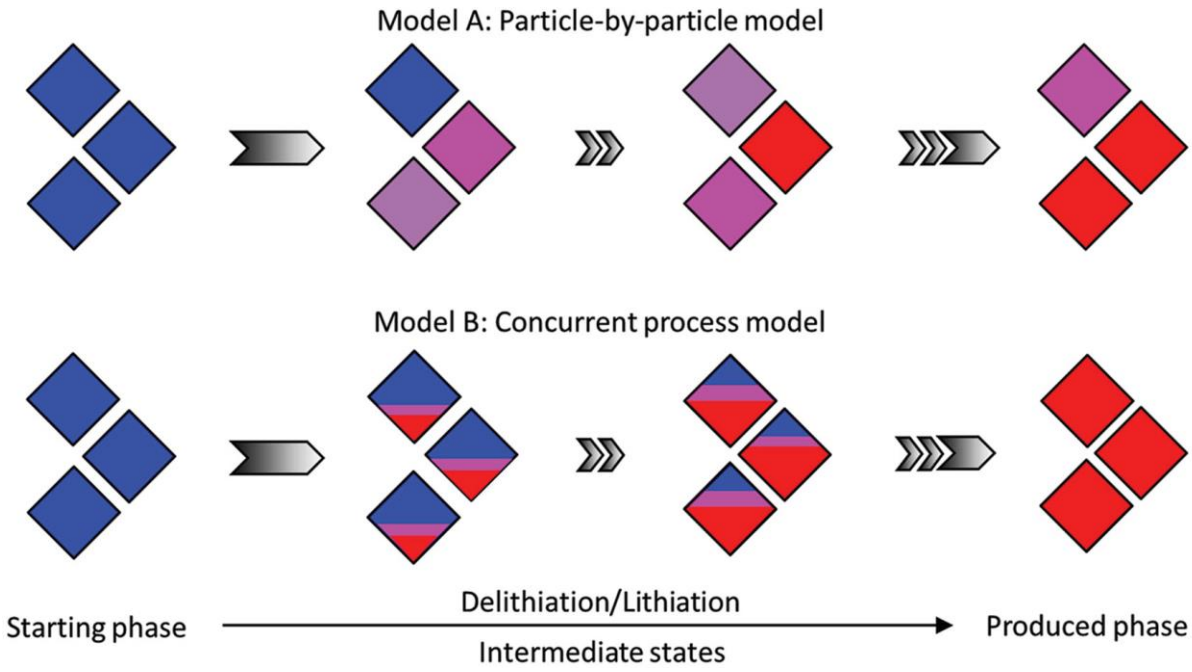

Figure 7. Phase transition models with intermediate states during delithiation/lithiation. Model A (particle-by-particle model): several solid-solution intermediates between the starting and produced phases are simultaneously present and the composition in each single particle is essentially uniform. Model B (concurrent process model): the reaction simultaneously proceeds in all the particles and there is a phase transition front in a single particle.

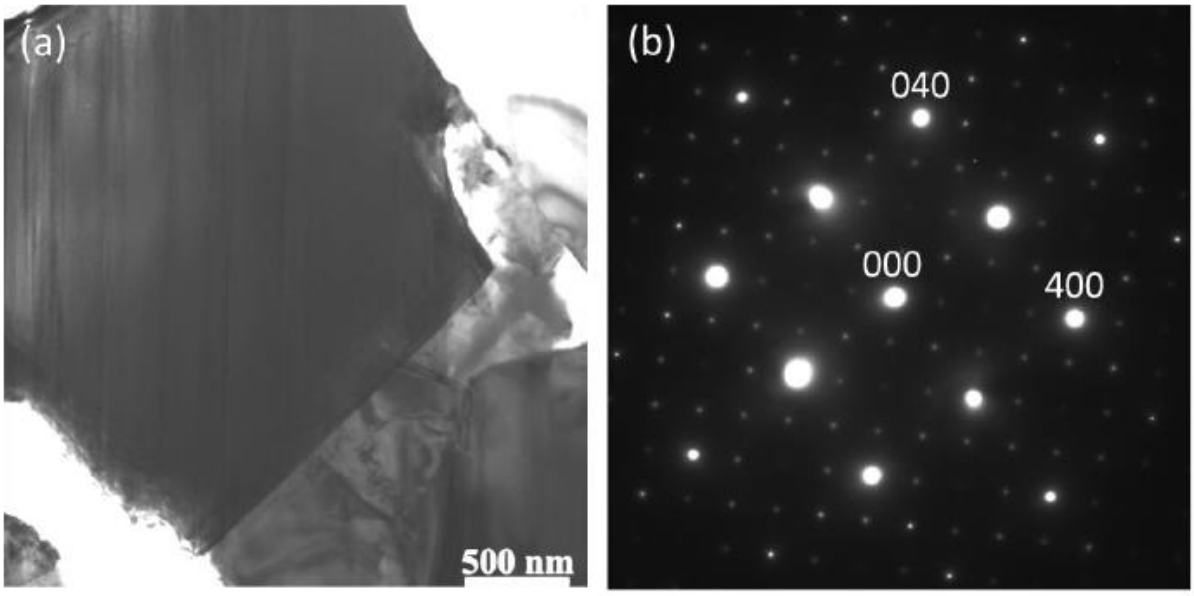

Figure 8. (a) TEM image and (b) ED pattern along [001] zone axis of a pristine $LiNi_{0.5}Mn_{1.5}O_4$ particle. The lattice constant obtained by ED is 0.82 nm.

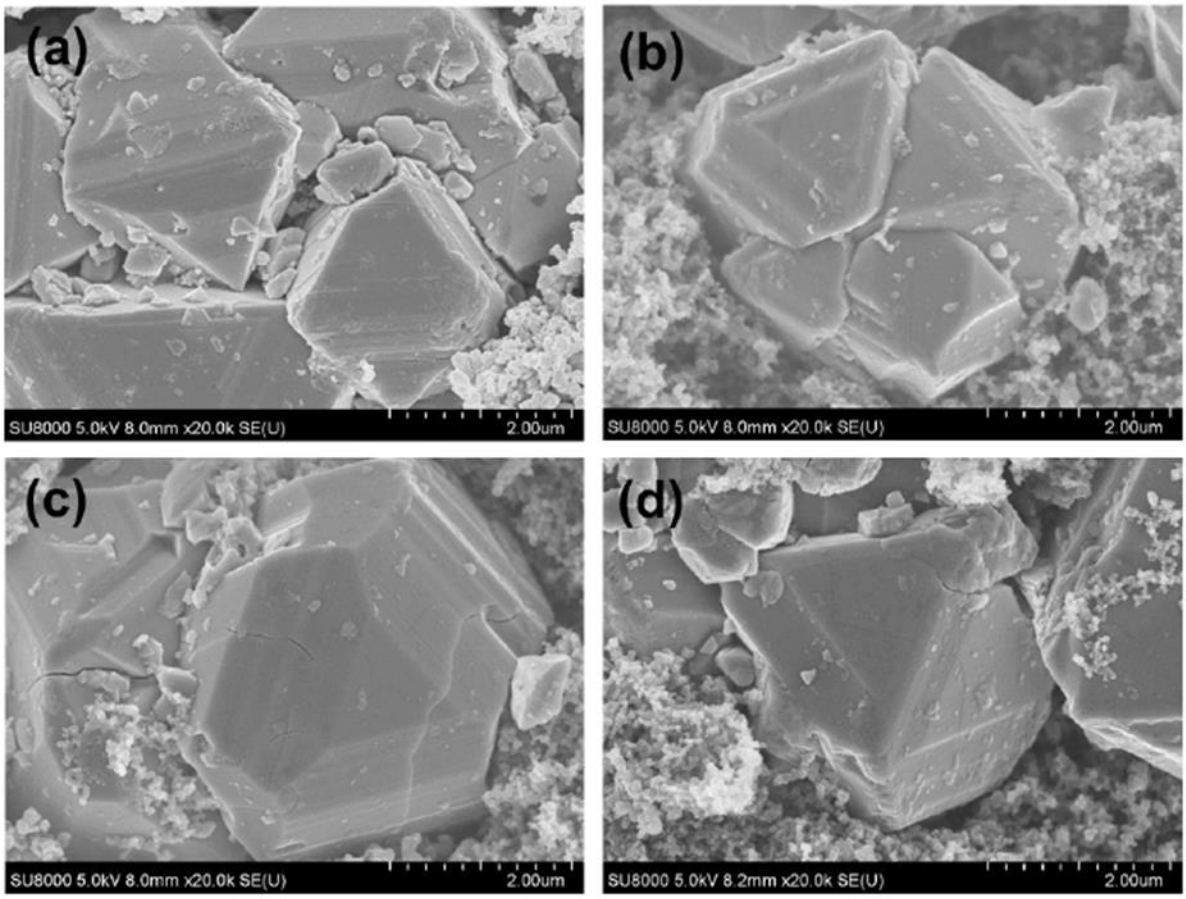

Figure 9. SEM images of (a) pristine $LiNi_{0.5}Mn_{1.5}O_4$ electrode, (b) a $Li_{0.5}Ni_{0.5}Mn_{1.5}O_4$ electrode, (c) a $Li_{0.25}Ni_{0.5}Mn_{1.5}O_4$ electrode and (d) a $Li_{0.0}Ni_{0.5}Mn_{1.5}O_4$ electrode. The charged electrode samples were obtained by 1 C rate charging.

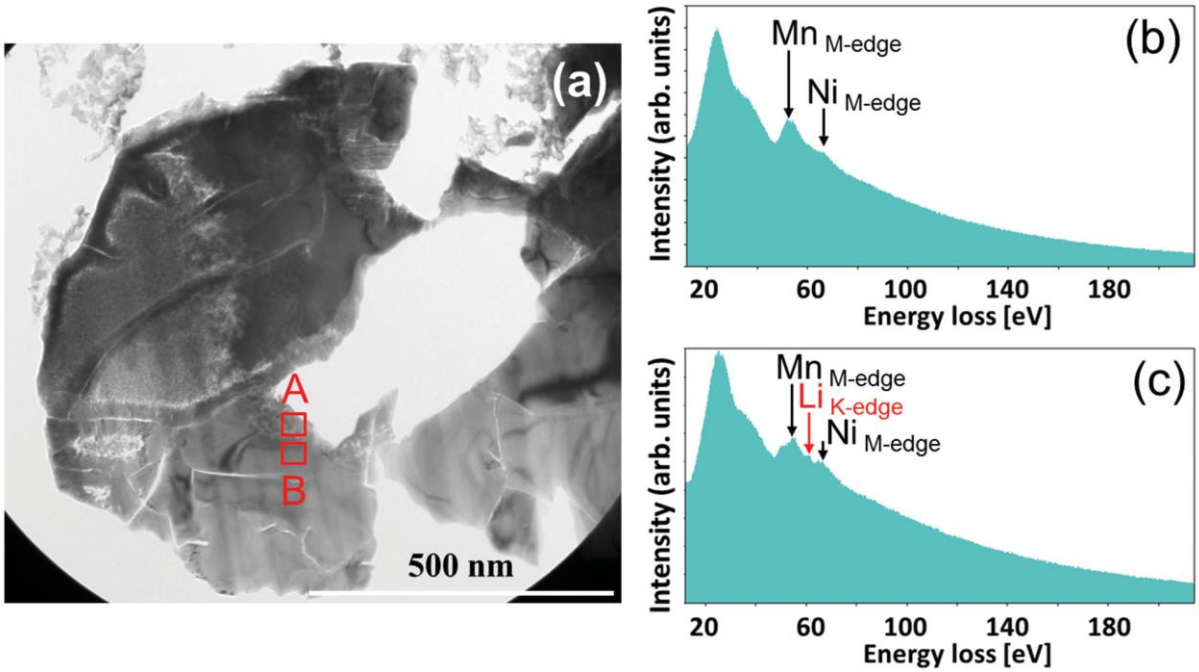

Figure 10. (a) TEM image of a $Li_{0.25}Ni_{0.5}Mn_{1.5}O_4$ electrode sample obtained by 1 C rate charging (b) and (c) intensity profiles of EELS spectra in regions A and B shown in the TEM image.

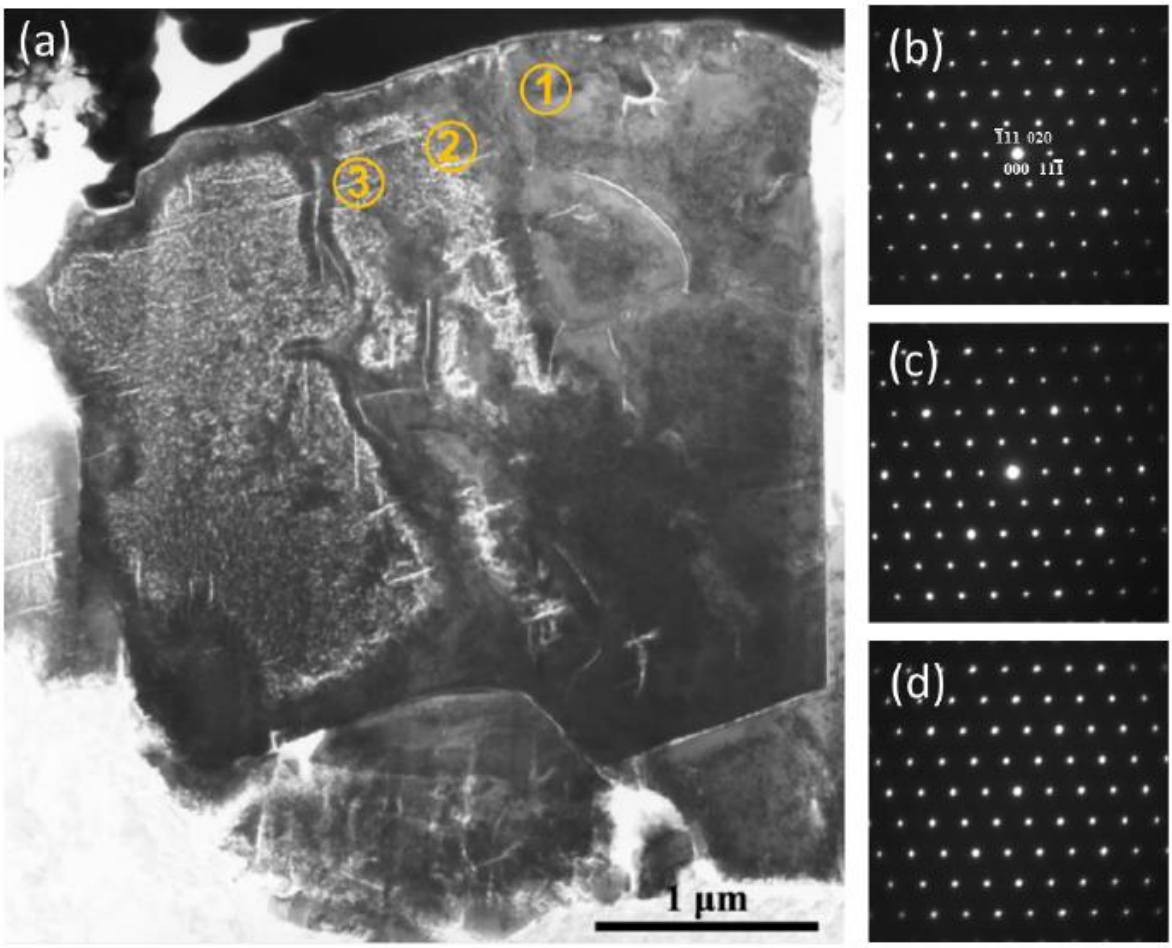

Figure 11. (a) TEM image of a $Li_{0.25}Ni_{0.5}Mn_{1.5}O_4$ electrode obtained by 1 C rate charging. (b), (c) and (d) ED patterns along [101] zone axis in regions 1, 2 and 3 shown in the TEM image. The ED patterns are well indexed by the spinel structure.

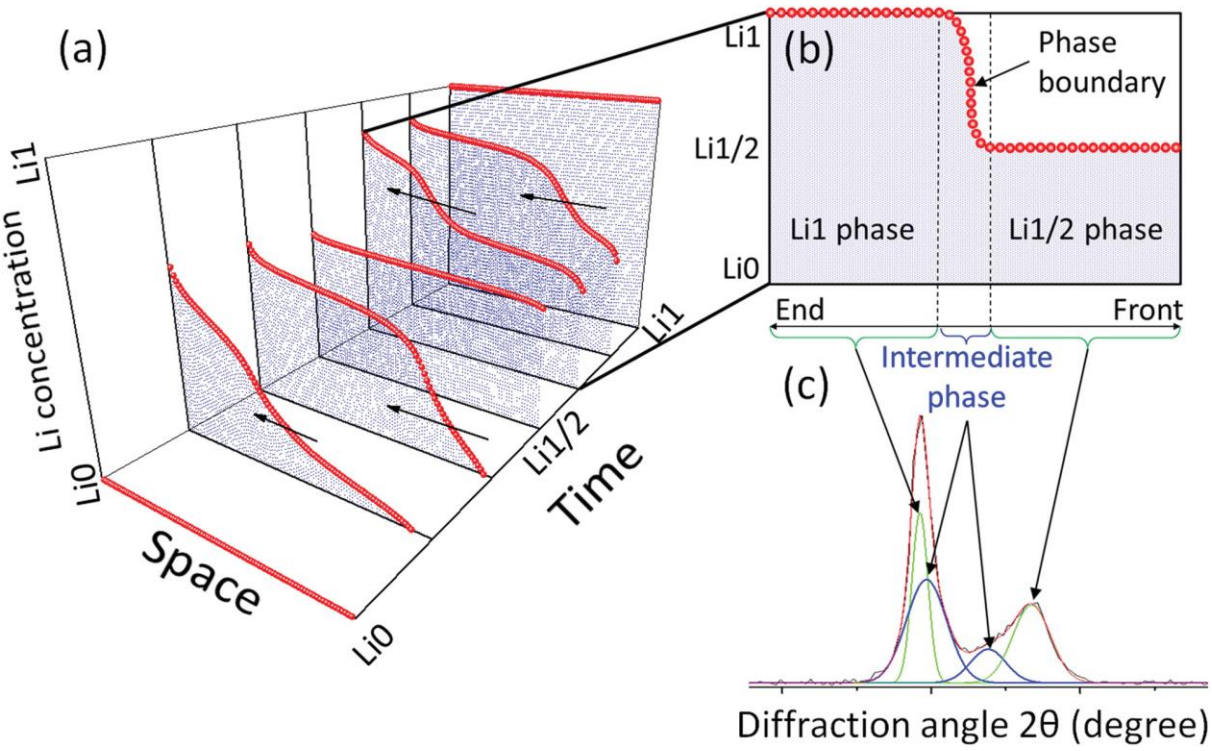

Figure 12. Reaction scheme with (a) temporal transition of moving phase transition front, (b) example of the state at phase transition between Li1 and Li1/2, and (c) associated XRD profile.

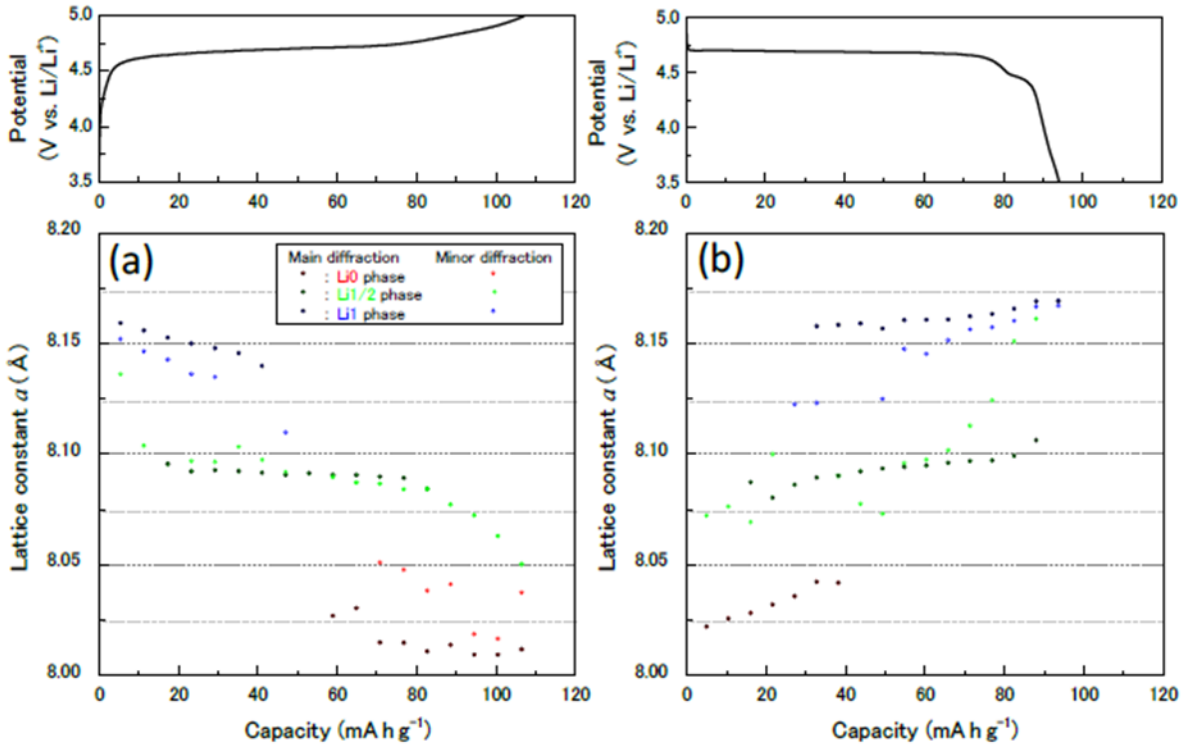

Figure 13. Variation of lattice constants of a $LiNi_{0.5}Mn_{1.5}O_4$ electrode obtained from peak centers of partial diffraction profiles with the corresponding electrode potential profiles during (a) charging and (b) discharging at rate of 5 C.

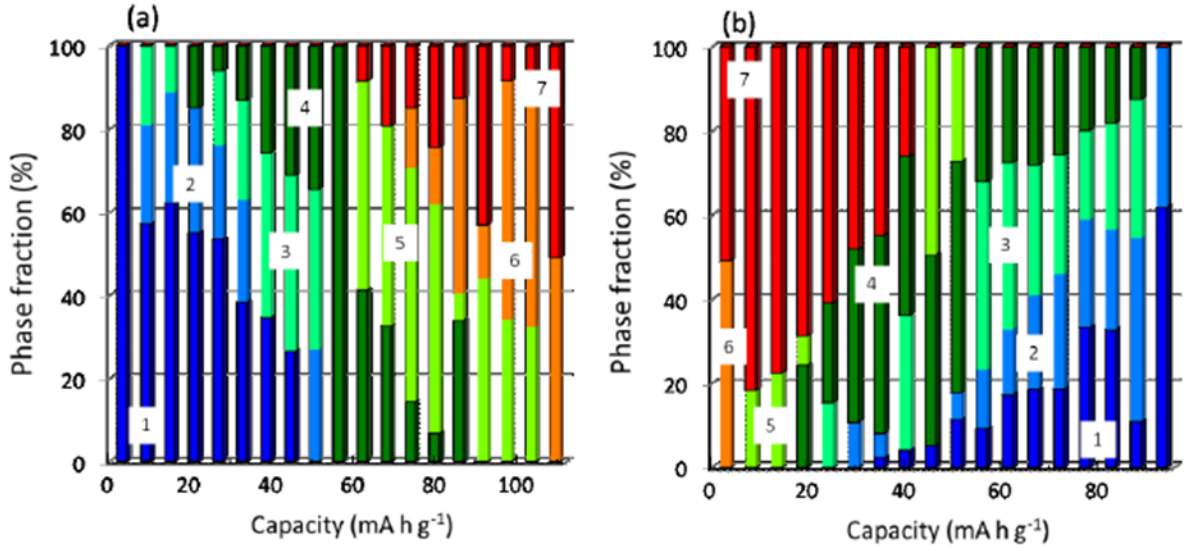

Figure 14. Variation of normalized peak area of $Li_xNi_{0.5}Mn_{1.5}O_4$ during (a) charging and (b) discharging at rate of 5 C. The notations of elements 1-7 are the same as those of Figure 6.

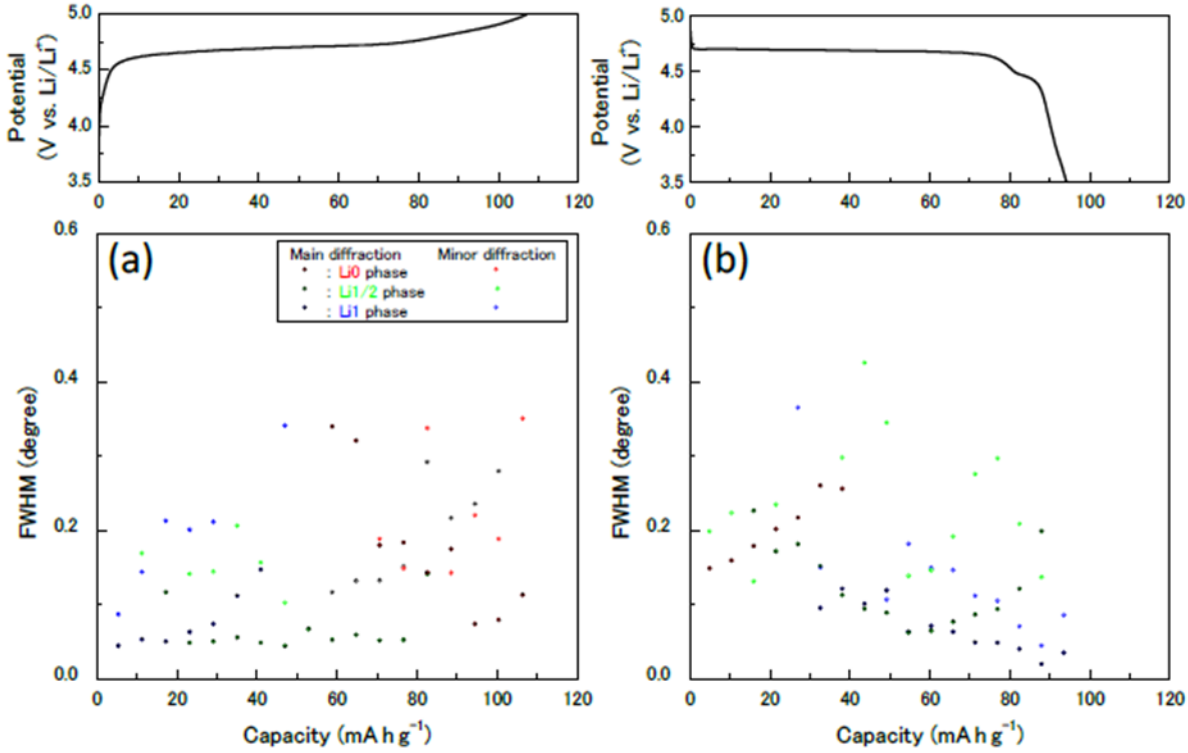

Figure 15. Variation of FWHM of partial diffraction profiles of a LiNi0.5Mn1.5O4 electrode with the corresponding electrode potential profiles during (a) charging and (b) discharging at rate of 5 C.

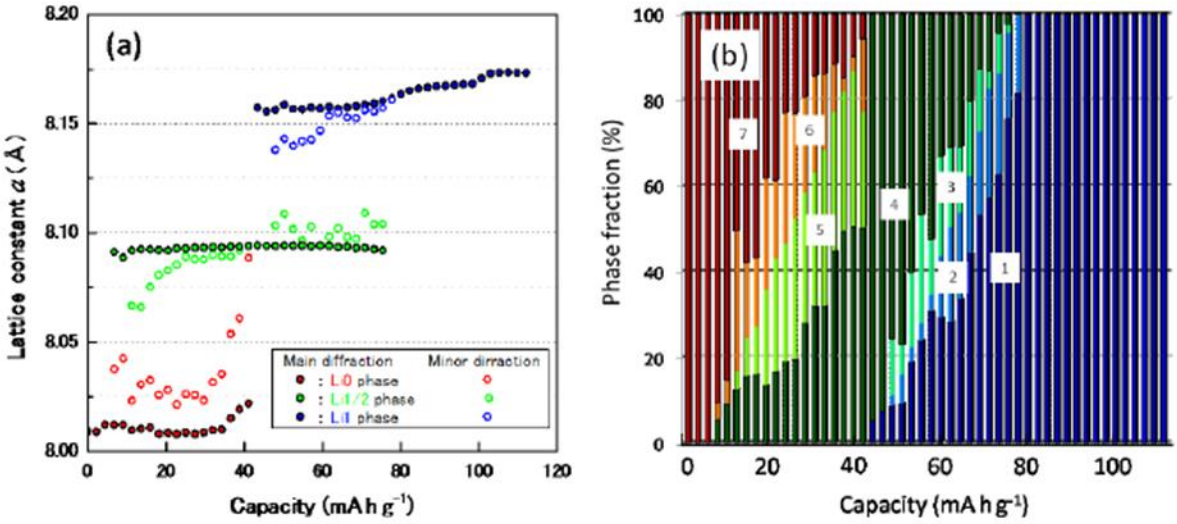

Figure 16. Variation of (a) lattice constant, and (b) normalized peak area of $Li_xNi_{0.5}Mn_{1.5}O_4$ during discharging at rate of 0.5 C. The notations of elements 1-7 are the same as those of Figure 6.

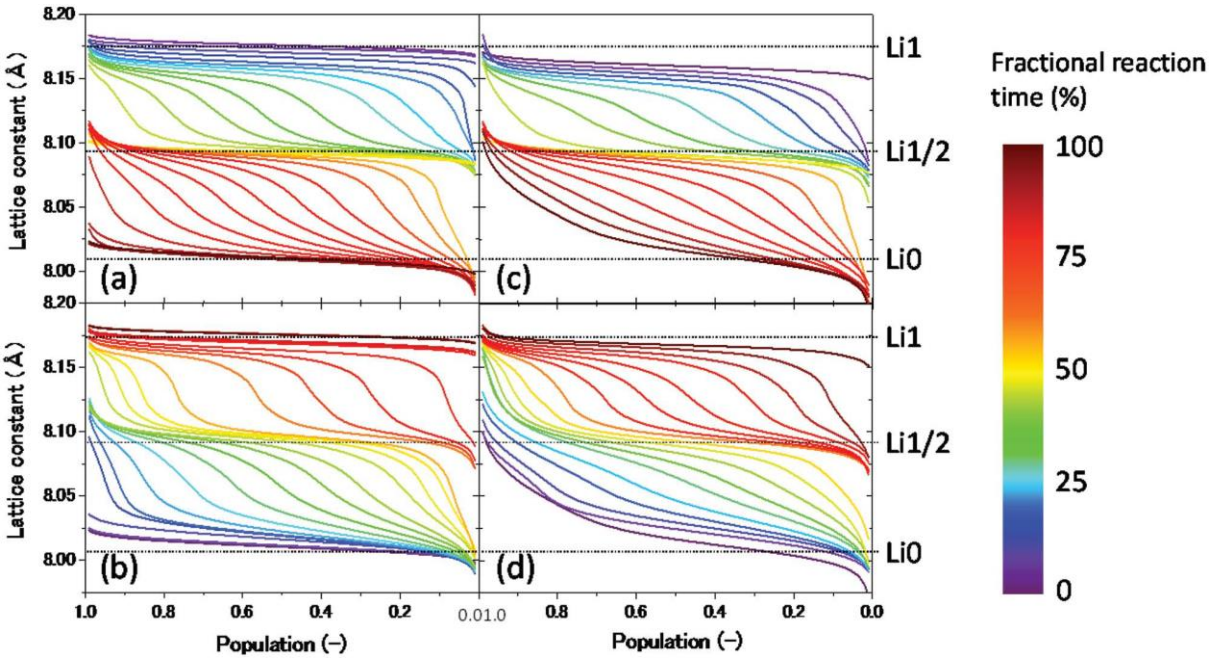

Figure 17. Lattice constant population profiles of $LiNi_{0.5}Mn_{1.5}O_4$ electrodes for (a) 1 C rate charging, (b) 1 C rate discharging, (c) 5 C rate charging, and (d) 5 C rate discharging. The Li1, Li1/2, and Li0 means the lattice constant at these phases correspond to peak centers of partial diffraction profiles.

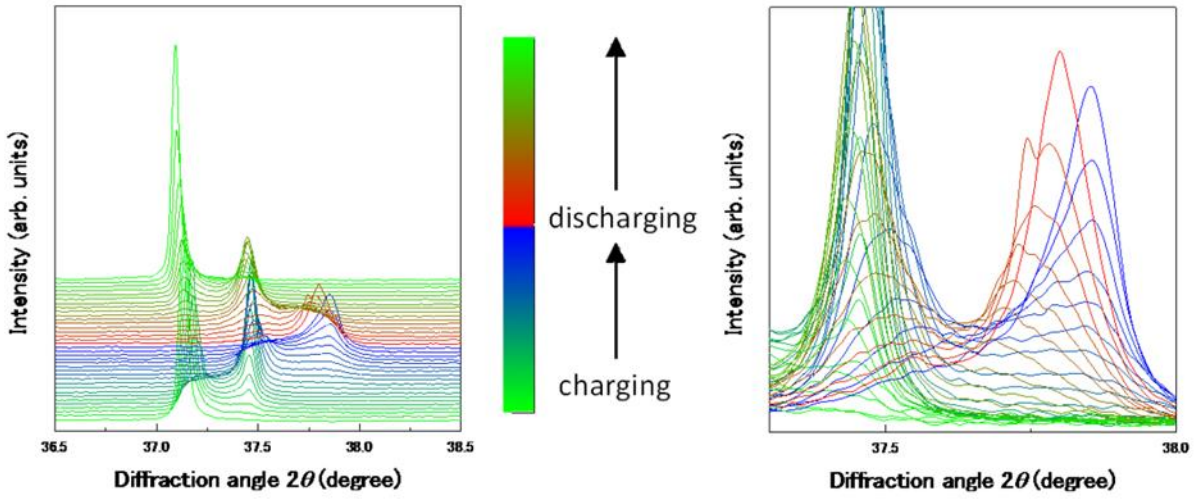

Figure 18. (a) Operando TR-XRD profiles of $LiNi_{0.5}Mn_{1.5}O_4$ at rate of 5 C, and (b) extended Figure near the Li0 phase.

Reference

[1] R. Malik, A. Abdellahi, G. Ceder, *J. Electrochem. Soc.* **2013**, *160*, A3179.

[2] J.-H. Kim, S.-T. Myung, C. S. Yoon, S. G. Kang, Y.-K. Sun, *Chem. Mater.* **2004**, *16*, 906.

[3] M. Kunduraci, G. G. Amatucci, *J. Electrochem. Soc.* **2006**, *153*, A1345.

[4] Q. Liu, H. He, Z. Li, Y. Liu, Y. Ren, W. Lu, J. Lu, E. A. Stach, J. Xie, *ACS Appl. Mater. Interfaces* **2014**, *6*, 3282.

[5] J. Wang, Y. K. Chen-Wiegart, J. Wang, *Nat. Commun.* **2014**, *5*, 4570.

[6] Y. Orikasa, T. Maeda, Y. Koyama, T. Minato, H. Murayama, K. Fukuda, H. Tanida, H. Arai, E. Matsubara, Y. Uchimoto, Z. Ogumi, *J. Electrochem. Soc.* **2013**, *160*, A3061.

[7] Y. Orikasa, T. Maeda, Y. Koyama, H. Murayama, K. Fukuda, H. Tanida, H. Arai, E. Matsubara, Y. Uchimoto, Z. Ogumi, *J. Am. Chem. Soc.* **2013**, *135*, 5497.

[8] H. Liu, F. C. Strobridge, O. J. Borkiewicz, K. M. Wiaderek, K. W. Chapman, P. J. Chupas, C. P. Grey, *Science* **2014**, *344*, 1252817.

[9] X. Zhang, M. van Hulzen, D. P. Singh, A. Brownrigg, J. P. Wright, N. H. van Dijk, M. Wagemaker, *Nano Lett.* **2014**, *14*, 2279.

[10] Y. Li, F. El Gabaly, T. R. Ferguson, R. B. Smith, N. C. Bartelt, J. D. Sugar, K. R. Fenton, D. A. Cogswell, A. L. D. Kilcoyne, T. Tyliszczak, M. Z. Bazant, W. C. Chueh, *Nat. Mater.* **2014**, *13*, 1149.

[11] A. K. Padhi, K. S. Nanjundaswamy, J. B. Goodenough, *J. Electrochem. Soc.* **1997**, *144*, 1188.

[12] A. S. Andersson, J. O. Thomas, *J. Power Sources* **2001**, *97-98*, 498.

[13] F. Zhou, C. A. Marianetti, M. Cococcioni, D. Morgen, G. Ceder, *Phys. Rev. B* **2004**, *69*, 201101.

[14] P. Bai, D. A. Cogswell, M. Z. Bazant, *Nano Lett.* **2011**, *11*, 4890.

[15] D. A. Cogswell, M. Z. Bazant, *ACS Nano* **2012**, *6*, 2215.

[16] G. Chen, X. Song, T. J. Richardson, *Electrochem. Solid-State Lett.* **2006**, *9*, A295.

[17] A. Nakamura, S. Furutsuki, S. Nishimura, T. Tohei, Y. Sato, N. Shibata, A. Yamada, Y. Ikuhara, *Chem. Mater.* **2014**, *26*, 6178.

[18] K. Dokko, M. Mohamedi, N. Anzue, T. Itoh, I. Uchida, *J. Mater. Chem.* **2002**, *12*, 3688.

[19] R. Alcántara, M. Jaraba, P. Lavela, J. L. Tirado, *Electrochim. Acta* **2002**, *47*, 1829.

[20] J.-H. Kim, C. S. Yoon, S.-T. Myung, J. Prakash, Y.-K. Sun, *Electrochem. Solid-State Lett.* **2004**, *7*, A216.

[21] H. Arai, K. Sato, Y. Orikasa, H. Murayama, I Takahashi, Y. Koyama, Y. Uchimoto, Z. Ogumi, *J. Mater. Chem. A.* **2013**, *1*, 10442.

[22] I. Takahashi, H. Murayama, K. Sato, T. Naka, K. Kitada, K. Fukuda, Y. Koyama, H. Arai, E. Matsubara, Y. Uchimoto, Z. Ogumi, *J. Mater. Chem. A* **2014**, *2*, 15414.

[23] K. Amine, H. Tukamoto, H. Yasuda, Y. Fujita, *J. Electrochem. Soc.* **1996**, *143*, 1607.

[24] K. Amine, H. Tukamoto, H. Yasuda, Y. Fujita, *J. Power Sources* **1997**, *68*, 604.

[25] L. Wang, H. Li, X. Huang, E. Baudrin, *Solid State Ionics* **2011**, *193*, 32.

[26] Y. Orikasa, T. Maeda, Y. Koyama, H. Murayama, K. Fukuda, H. Tanida, H. Arai, E. Matsubara, Y. Uchimoto, Z. Ogumi, *Chem. Mater.* **2013**, *25*, 1032.

[27] F. Omenya, B. Wen, J. Fang, R. Zhang, Q. Wang, N. A. Chernova, J. Schneider-Haefner, F. Cosandey, M. S. Whittingham, *Adv. Energy Mater.* **2015**, *5*, 1401204.

[28] W. C. Chueh, F. E. Gabaly, J. D. Sugar, N. C. Bartelt, A. H. McDaniel, K. R. Fenton, K. R. Zavadil, T. Tyliszczak, W. Lai, K. F. McCarty, *Nano Lett.* **2013**, *13*, 866.

[29] C. Delmas, M. Maccario, L. Croguennec, F. L. Cras, F. Weill, *Nat. Mater.* **2008**, *7*, 665.

[30] A. Singer, A. Ulvestad, H. Cho, J. W. Kim, J. Maser, R. Harder, Y. S. Meng, O. G. Shpyrko, *Nano Lett.* **2014**, *14*, 5295.

[31] X. Ma, B. Kang, G. Ceder, *J. Electrochem. Soc.* **2010**, *157*, A925.

Chapter 4. Structural Refinement of High-capacity Cathode using Neutron and X-ray Joint Analysis

4.1. Introduction

In recent years, solid solutions of lithium-rich layered oxide materials (LLOs) especially lithium-rich manganese oxide (Li_2MnO_3) and other layered transition metal (TM) oxide ($LiMeO_2$, Me = Co, Ni, Al etc.) have been investigated for use as cathode materials in lithium-ion batteries because they show specific capacities (280 mA h g^{-1}) higher than those of $LiMeO_2$. Among the various Li_2MeO_3 compounds being explored, Li_2MnO_3 has been examined particularly intensively.[1-3] On the other hand, about a decade ago, Lu *et al.* investigated the structures and battery properties of $Li[Ni_xLi_{1/3-2x/3}Mn_{2/3-x/3}]O_2$ materials, which are solid solutions of $Li(Li_{1/3}Mn_{2/3})O_2$ [Li_2MnO_3], and $Li(Ni_{1/2}Mn_{1/2})O_2$, (1-2x: 2x; see Figure 1) and found that they show better electrochemical performances than does $Li(Li_{1/3}Mn_{2/3})O_2$, especially at x = 1/3 to 5/12.[4] In addition to this study, other efforts have also been made to improve the performance of such Li-rich materials.[5] Recently, the combined use of X-ray and neutron diffraction analyses allowed us to determine the structural parameters of such complex crystals with precision. In addition, to analyze the structural defects, the FAULTS program created by Casas-Cabanas[6] *et al.* is helpful because it simultaneously allows for Rietveld refinement and stacking fault analysis based on DIFFaX.[7]

In this study, we prepared five $Li_2(Ni_xMn_{1-x})O_{3(-\delta)}$ (x = 0, 1/20, 1/10, 1/6, and 1/4) specimens and scrutinized their structures as well as with their structural defects complementarily using a general Rietveld program, Z-Rietveld[8] (for the joint analysis),

and the FAULTS program (for the stacking fault analysis). The results of quantitative analysis for these five specimens are listed in Table 1. It was assumed that the metal atomic sites (Li and TM layers in the Li_2MnO_3 structure; see below for structural details) are all filled with atoms, that is, they do not have any vacancies. We prepared the starting materials so as to form $Li_2(Ni_xMn_{1-x})O_3$ pseudobinary compounds; however, as can be seen from Table 1 and Figure 1, the resultant materials were formed away from the Li_2MnO_3-Li_2NiO_3 pseudobinary line.

4.2. Experimental

Sample Preparation: $Li_2(Ni_xMn_{1-x})O_{3(-\delta)}$ (x = 0, 1/20, 1/10, 1/6, and 1/4) were synthesized by a solid-state reaction of $LiOH \cdot H_2O$, $NiCO_3$, and $MnCO_3$ at a molar ratio of 2.1: x: 1 - x as precursors. These starting materials were thoroughly mixed by milling in acetone for 2 h and then dried at 100 ºC. The precursors were pelletized at 5 MPa and calcined at 450 ºC for 24 h. They were powdered and pressed again to form new pellets, which were then annealed at 900 ºC for 12 h in the air. The heating and cooling rates were both 300 ºC h^{-1}.

A mixture of the active material, acetylene black (Denki Kagaku Kogyo), and polyvinylidene difluoride (PVDF, Kureha) with a weight ratio of 80:10:10 was spread onto an aluminum foil with N-methylpyrrolidone (NMP) and then dried at 80 °C under vacuum overnight to constitute a positive electrode. The electrode was pressed to a typical thickness of 30-35 μm. Metallic lithium foil (0.2 mm in thickness, > 99.9%, Honjo Metal) was used as counter and reference electrodes. These components were assembled together with the s polyolefin separator and soaked in the electrolyte solution in an Ar-filled glovebox, which were sealed in an aluminum-coated laminate-

type cell. The electrolyte used in this study was 1 M $LiPF_6$, which was dissolved in anhydrous ethylene carbonate (EC) and ethyl methyl carbonate (EMC) with a volumetric ratio of 3:7 (Kishida Chemical). The electrochemical measurements were performed at room temperature on an automatic cycling and data recording system (HJ1001SD8, Hokuto Denko).

Structural Refinements: Synchrotron diffraction experiments were performed using a large-diameter Debye-Scherrer camera with an imaging plate on the BL02B2 beamline at the Japan Synchrotron Radiation Research Institute (JASRI/Spring-8).[9] The neutron powder diffraction data were obtained using a time-of-flight powder diffractometer (BL09 beamline, SPICA) at the Japanese Proton Accelerator Research Complex (J-PARC).[10] Inductively coupled plasma atomic emission spectroscopy (for metals) and iodometric redox titration (for oxygen) analyses were used to determine the compositions of the synthesized products (Table 1).

4.3. Results and Discussion

4.3.1. Estimate Amount of Cation Mixing

Figure 2 shows the first cycle charge-discharge profiles of the $Li_2(Ni_xMn_{1-x})O_{3(-\delta)}$ (x = 0, 1/20, 1/10, and 1/4) specimens. As can be seen in Figure 2, their specific capacities are not sufficiently high; however, the dependence of the specific capacity on the Ni composition is almost similar to that reported by Beaulieu[4,11] *et al.*, which is that replacing Mn with Ni lowers the potential of the charge plateau and leads to higher charge-discharge capacities.

Figure 3 shows the synchrotron diffraction patterns obtained for the four $Li_2(Ni_xMn_{1-x})O_{3(-\delta)}$ (x = 0, 1/10, 1/6, and 1/4) materials. The diffraction patterns are

almost similar, suggesting that the pseudobinary compounds are all isostructural with Li_2MnO_3. Li_2MnO_3 is known, as shown in Figure 4, to have a monoclinic structure (space group $C2/m$) consisting of three kinds of *ABC*-stacked atomic layers as well as the compounds $LiMO_2$ (space group $R\bar{3}m$)[12] (M: transition metal). However, 33% of the atoms in the TM layer of Li_2MnO_3 are of Li and not of Mn, in contrast to the case for the $LiMnO_2$ structure. The Li atoms in the TM layer occupy the 2*b* sites of $C2/m$; on the other hand, the remaining 67% Mn atoms are located at the 4*g* sites. These two kinds of atoms form an ordered arrangement in the TM plane (see Figure 4). The structures were analyzed by the Z-Rietveld code for neutron-synchrotron joint analysis, in order to determine the precise atomic positions and site occupancies of Li, Mn, and Ni first, without considering the stacking faults. The structure refinement results are presented in Table 2 and Figure 5. Almost all the diffraction peaks were in good agreement with the calculated ones generated using single sets of the profile parameters (*U*, *V*, and *W* for the synchrotron diffractions and σ and γ for the neutron diffractions).[8] This strongly indicated that the peaks of the synthesized samples were from a single phase of the monoclinic Li_2MnO_3 structure, that is, the structure of $Li[Li_{0.2}Mn_{0.6}Ni_{0.2}]O_2$ reported by Jarvis[13] *et al.*, who used the electron diffraction technique to conclude that this material is composed of a solid solution of Li_2MnO_3 and $LiMO_2$ domains with $C2/m$ monoclinic symmetry. During the analyses, no atomic mixing between the metal and oxygen layers was assumed; however, all possible metal-atom occupation (mixing) configurations among the 2*c*, 4*h* (both in the Li layer), 2*b*, and 4*g* (both in the TM layer) sites were examined, because it is known that the Li and Mn atoms at the 2*b* and 4*g* sites show a partially disordered atomic arrangement in Li_2MnO_3 (i.e., cation mixing in the TM layer).[2,3,14] These examinations revealed that the Li layers are composed exclusively of Li atoms, whereas the TM layers comprise

the atoms of the three metals (Li, Ni, and Mn), which are largely mixed among the 2*b* and 4*g* sites. As seen in Table 3, the Mn atoms prefer the 4*g* site; on the other hand, the Li and Ni atoms tend to selectively occupy the 2*b* site. This suggests that the 4*g* site tends to favor the higher-valence cations than does the 2*b* site. This cation mixing in the TM layers was also confirmed by high-angle annular dark field (HAADF)-scanning transmission electron microscopy (STEM) observations (Figure 6).

4.3.2. Estimate Amount of Stacking Faults

Next, we elucidated the stacking faults in the $Li_2(Ni_xMn_{1-x})O_{3(-\delta)}$ specimens. In the diffraction profiles, fairly intense diffuse peaks related to the stacking faults can be observed, especially at the bottom of the 020, 110, and $\bar{1}11$ reflections (see Figure 3). This result is similar to that reported for the Li_2MnO_3 crystal.[2,3,13-15] The Li_2MnO_3 crystal is composed of periodic *ABC* stacking of three different atomic layers, namely, the TM, O, and Li layers, along the *c*-axis direction, as shown below (also see Figure 4):

A *B* *C* *A* *B* *C* *A* *B* *C* *A* *B* *C*

·····—O—TM—O—Li—O—TM—O—Li—O—TM—O—Li—····· (1)

Here, this type of layer stacking can be regarded as a structure consisting of *ABC* stacking of slabs formed by four –O–TM–O–Li– atomic layers. Stacking faults are generated in such layered materials by the glide translation of the atomic planes in the *a*-*b* plane. Furthermore, the topologically possible stacking faults can be described fully using three different stacking vectors, [0, 0, 1], [1/2, -1/6, 1] (both as cubic-type stacking), and [1/6, -1/6, 1] (as a hexagonal-type stacking), in the monoclinic (*C*2/*m*)

cell (see Figures 7-1 and 7-2) and by their combinations (multiplications). During the FAULTS Rietveld refinement process, it was assumed that the stacking faults were allowed only between the interslabs indicated by the arrows and were never generated within the slabs in ill. 1. The probabilities of translation from one slab to the next by these stacking vectors can be represented by the three α parameters, α_{11}, α_{12}, and α_{13}. The parameter α_{11} is the probability for the normal cubic-type stacking found in the perfect Li_2MnO_3 crystal, whereas α_{12} is that for another cubic-type stacking fault related to the ordered atomic arrangement in the TM layers. When $\alpha_{11} = 1$, $\alpha_{12} = 0$, and $\alpha_{13} = 0$, this crystal has no stacking faults. If the TM layer has a completely disordered (random) atomic arrangement, there is no difference between α_{11} and α_{12} (see Figure 7-2).

As can be seen in the diffraction patterns (Figure 3), the superstructure reflections consist of sharp and diffuse peaks (see the inset profiles with the backgrounds), which demonstrates that these materials comprise two kinds of domains with different crystallinities. This can be attributed to the existence of highly ordered domains that have perfectly ordered atomic arrangements and no stacking faults as well as disordered domains with the atomic mixing and stacking faults mentioned above, as has been reported for Li_2MnO_3.[2,3,13-15]

Figure 8 shows that the compositional dependencies of parameters α_{11}, α_{12}, and α_{13} for the imperfect domains, as well as the fraction of perfect (/imperfect) domains as obtained by the FAULTS analysis (the Rietveld analysis results are also shown in Figure 9). As can be seen in Figure 8a, the α_{13} parameters, which indicated the formation of hexagonal stacking faults, were almost zero; on the other hand, the cubic stacking faults generated by [1/2, -1/6, 1] (α_{12}) were 20%. These stacking faults in the imperfect domains tended to decrease as the Ni concentration was increased; on the

other hand, the fraction of the imperfect domains increased with the increase in the Ni concentration. The volume ratio of the perfect and imperfect domains is shown in Figure 8b. Because the defects in the specimen were diluted by the perfect domains, when applying this average correction to Figure 8a, we could obtain the modified α parameters, as shown in Figure 8c. As seen in this figure, the $Li_2(Ni_xMn_{1-x})O_{3(-\delta)}$ compounds contain a significant number of stacking faults; however, the average fraction of the stacking faults remains almost unchanged, irrespective of the Ni concentration.

Finally, we show the relationship between the electrochemical behavior and the structural features of the $Li_2(Ni_xMn_{1-x})O_{3(-\delta)}$ specimens. Pure Li_2MnO_3 does not show any property, because manganese is only at a +4 state in this material. It is simply expected that, as soon as Ni is introduced in the material, redox can occur and electrochemical properties are improved. However, in the case of the $Li_2(Ni_xMn_{1-x})O_{3(-\delta)}$ crystals, it is essential that the Li ions in the TM layers are used as effectively as those in the Li layers, in order to ensure superior electrochemical performance; in other words, the Li ions need to smoothly migrate within as well as across the layers during the charging-discharging processes. In Li_2NiO_3 in which non-reactive Mn^{4+} of Li_2MnO_3 is all replaced with Ni^{4+}, its capacity is expected to be almost the same to Li_2MnO_3. As expected, the specific capacity of Li_2NiO_3 is no more than 240 mA h g^{-1}.[16] While on the other hand, in Li_2MoO_3 in which Mn is all substituted with reactive Mo, its capacity is expected to be significantly increased compared with Li_2MnO_3. But actually, the specific capacity of Li_2MoO_3 is no more than 230 mA h g^{-1}.[17] Furthermore, in Li_2RuO_3 in which Mn is all exchanged with reactive Ru, its capacity is expected to be considerably increased. But actually, the specific capacity is no more than 270 mA h g^{-1}.[18] These mean that, even if non-active Mn is replaced by active transition metals,

the resultant materials do not show much improvement in capacity. Assuming that only the two-electron reaction of $Ni^{2+} \leftrightarrow Ni^{4+}$ contributes to increase of the specific capacity, it corresponds to increase of 125 mA g^{-1}, for example, for $Li_2(Mn_{0.75}Ni_{0.25})O_3$; however, as can be seen in Figure 2, the capacity increases more than expected. This difference is deemed to be provided by the formation of Li percolation paths. In these crystals, every metal atom in the Li and TM layers has 12 metal (Li or Mn/Ni) atoms as the second nearest neighbors (see Figures 4 and 10). When the Li ions jump into the positions of their 12 neighboring metal atoms, they have to pass through the potential barrier formed by the six obstructing atoms (two O ions and four Li/Mn ions) located around each jumping axis (see Figures 11 and 12). In a perfect crystal, when a conducting Li ion moves continuously to the neighboring Li positions, it necessarily encounters the potential barrier formed by the contribution of one or two Mn/Ni ions, as seen in Figures 11 and 12, within two jumping steps. Of the Li, Mn, Ni, and O obstructing atoms, the Mn atoms make it the most difficult for the migrating Li atoms to slip through the barriers; this is because they are tetravalent cations (Mn^{4+}), forming a significantly large Coulomb potential so as to cut off the paths.[19] Then, when these Mn^{4+} ions are replaced by low-valence cations such as Li^+ or Ni^{2+}, it is expected that the conducting Li ions can move to the neighboring positions more easily.

4.4. Conclusions

The significant number of stacking faults and cation mixing in $Li_2(Ni_xMn_{1-x})O_{3(-\delta)}$ can cause an exchange of the Mn^{4+}/Ni^{2+} and Li^+ positions in the TM layer. Figures 11 and 12 show several of an enormous number of metal-atom chains in the $Li_2(Ni_xMn_{1-}$

$_x)O_{3(-\delta)}$ crystals. When the transition metals on the chain in Figure 11 are replaced by Li atoms, this chain acts as a Li-percolation path; when the obstructing high-valence Mn^{4+} cations around the chains in Figures 11 and 12 are replaced by low-valence cations (Li^+ or Ni^{2+}), these chains become smoother Li percolation paths. In the synthesized $Li_2(Ni_xMn_{1-x})O_{3(-\delta)}$ specimens, as the Ni content was increased, the number of lower-valence Ni ions increased instead of the number of the higher-valence Mn ions. Furthermore, the degree of atomic mixing became more significant (see Table 3). These phenomena resulted in an increase in the number of longer and smoother percolation paths. It is, therefore, deemed that the replacement of Mn with Ni results in active Li ions and increases the charge-discharge capacity (see Figure 2). In other words, the idea of Lee[19] *et al.* of facilitating smooth Li percolation is topologically realized in the $Li_2(Ni_xMn_{1-x})O_{3(-\delta)}$ compounds, and we believe that the interchanging of the atomic positions of Li and Mn/Ni is one of the major reasons for the compounds exhibiting performances better than that of Li_2MnO_3. Assuming that the partially delithiated Li_2MnO_3, $Li_{2-y}(Ni_xMn_{1-x})O_3$, keeps the *C*2/*m* monoclinic structure with delithiation, Li atoms in the lattice are simply substituted by vacancies. This replacement is expected to facilitate the Li diffusion in the lattice, because the vacancy decreases the Coulomb potential on the percolation paths compared with Li^+. It is reported that the spinel structures are generated in the charging process of Li_2MnO_3,[20] which are presumed to decrease the capacity. Therefore, it is very likely that such unnecessary structures are generated also in $Li_{2-y}(Ni_xMn_{1-x})O_3$. Suppressing the spinel formation and stabilizing the original monoclinic structure will be an essential issue to obtain higher capacities and cyclabilities.

By introducing Ni ions into Li_2MnO_3 structure, the additional Ni redox reactions can be available, which would contribute to the observed capacities for $Li_2(Ni_xMn_{1-}$

$_x)O_{3(-\delta)}$. We stress that in addition to these redox reaction mechanisms, the disordered arrangement within the TM layer, which fosters the formation of longer and smoother Li percolation path, contributes to the better electrochemical performances.

Table 1. Results of quantitative analyses of the $Li_2(Ni_xMn_{1-x})O_{3(-\delta)}$ specimens. The metal sites in these crystals were assumed to have no vacancies.

#	targeted composition		obtained composition
1	Li_2MnO_3	$Li[Li_{1/3}Mn_{2/3}]O_2$	$Li[Li_{0.328}Mn_{0.672}]O_{1.969}$
2	$Li_2(Mn_{19/20}Ni_{1/20})O_3$	$Li[Li_{1/3}Mn_{19/30}Ni_{/1/30}]O_2$	$Li[Li_{0.310}Mn_{0.655}Ni_{0.035}]O_{1.950}$
3	$Li_2(Mn_{9/10}Ni_{1/10})O_3$	$Li[Li_{1/3}Mn_{3/5}Ni_{/1/15}]O_2$	$Li[Li_{0.302}Mn_{0.626}Ni_{0.072}]O_{1.955}$
4	$Li_2(Mn_{5/6}Ni_{1/6})O_3$	$Li[Li_{1/3}Mn_{5/9}Ni_{1/9}]O_2$	$Li[Li_{0.283}Mn_{0.595}Ni_{0.123}]O_{1.935}$
5	$Li_2(Mn_{3/4}Ni_{1/4})O_3$	$Li[Li_{1/3}Mn_{1/2}Ni_{1/6}]O_2$	$Li[Li_{0.250}Mn_{0.557}Ni_{0.194}]O_{1.927}$

Table 2. Structural parameters of $Li_2(Ni_xMn_{1-x})O_{3(-\delta)}$ (x=0, 1/10, 1/6, and 1/4) refined by the Z-Rietveld program using both neutron and synchrotron diffraction data. The standard deviations are shown within the parentheses. The stacking probabilities, α_{11}, α_{12}, and α_{13}, were determined by the FAULTS program using the synchrotron diffraction data only, while using the structural parameters, g, x, y, z, and B obtained from the above-mentioned joint analyses.

x=0: a = 4.9252(1) Å, b = 8.5284(2) Å, c = 5.0203(1) Å, β = 109.2928(1)°;
R_{wp} = 7.90%, R_e = 1.09% (for ND+SR),
R_{wp} = 4.20%, R_p = 3.00%, R_B = 9.29%, and R_{Fobs} = 9.87% (for ND), and
R_{wp} = 10.46%, R_p = 7.46%, R_B = 6.45%, and R_{Fobs} = 6.12% (for SR).

atom	site	g	x	y	z	B (Å^2)
Li (1)	2*b*	0.7464	0	1/2	0	0.469
Mn (1)	2*b*	0.2536	0	1/2	0	0.469
Ni (1)	2*b*	—	—	—	—	—
Li (2)	2*c*	1	0	0	1/2	1.52
Li (3)	4*h*	1	0	0.6551(2)	1/2	1.52(1)
Li (4)	4*g*	0.1188	0	0.16625(2)	0	0.469
Mn (2)	4*g*	0.8812(2)	0	0.16625	0	0.469(6)
Ni (2)	4*g*	—	—	—	—	—
O (1)	4*i*	0.968(1)	0.2221(1)	0	0.22603(9)	0.511(6)
O (2)	8*j*	0.993	0.25232(7)	0.32355(4)	0.22284(5)	0.511

R =12.1%, χ^2=163.3.

α_{11}	α_{12}	α_{13}
0.7253(7)	0.2629	0.0118(1)

x=1/10: a = 4.9352(2)Å, b = 8.5460(3)Å, c = 5.0254(2)Å, β = 109.2876 (4)°;
R_{wp} = 4.70%, R_e = 1.21% (for ND+SR),
R_{wp} = 3.56%, R_p = 2.70%, R_B = 7.81%, and R_{Fobs} = 8.13% (for ND), and
R_{wp} = 5.97%, R_p = 4.31%, R_B = 4.71%, and R_{Fobs} = 5.47% (for SR).

atom	site	g	x	y	z	B (Å^2)
Li (1)	2*b*	0.645	0	1/2	0	0.675
Mn (1)	2*b*	0.227(1)	0	1/2	0	0.675
Ni(1)	2*b*	0.127(1)	0	1/2	0	0.675
Li (2)	2*c*	1	0	0	1/2	1.62
Li (3)	4*h*	1	0	0.6606(3)	1/2	1.62(1)
Li (4)	4*g*	0.131	0	0.16640	0	0.675
Mn (2)	4*g*	0.824	0	0.16640(5)	0	0.675(9)
Ni(2)	4*g*	0.044	0	0.16640	0	0.675
O (1)	4*i*	0.976(1)	0.2212(2)	0	0.2265(1)	0.602(8)
O (2)	8*j*	0.978	0.2497(1)	0.32396(6)	0.22302(8)	0.602

R =7.46%, χ^2=41.6.

α_{11}	α_{12}	α_{13}
0.7811(10)	0.2120	0.0069(1)

x=1/6: a = 4.9467(1)Å, b = 8.5626(2)Å, c = 5.0316(1) Å, β = 109.3033(4)°;
R_{wp} = 4.05%, R_e = 1.02% (for ND+SR),
R_{wp} = 3.25%, R_p = 2.44%, R_B = 7.09%, and R_{Fobs} = 7.49% (for ND), and
R_{wp} = 5.58%, R_p = 4.18%, R_B = 4,99%, and R_{Fobs} = 5.53% (for SR).

atom	site	g	x	y	z	B (Å^2)
Li (1)	2b	0.565	0	1/2	0	0.715
Mn (1)	2b	0.261(1)	0	1/2	0	0.715
Ni(1)	2b	0.174(1)	0	1/2	0	0.715
Li (2)	2c	1	0	0	1/2	1.39
Li (3)	4h	1	0	0.6646(2)	1/2	1.39(1)
Li (4)	4g	0.141	0	0.16671	0	0.715
Mn (2)	4g	0.762	0	0.16671(5)	0	0.715(7)
Ni(2)	4g	0.097	0	0.16671	0	0.715
O (1)	4i	0.969(1)	0.2185(1)	0	0.2264(1)	0.537(6)
O (2)	8j	0.967	0.2494(1)	0.32266(4)	0.22346(7)	0.537

R =7.63%, χ^2=41.0.

α_{11}	α_{12}	α_{13}
0.7976(9)	0.1981	0.0043(1)

x=1/4: a = 4.945 (2) Å, b = 8.558(3) Å, c = 5.028(2) Å, β = 109.2607(4)°;
R_{wp} = 4.72%, R_e = 1.08% (for ND+SR),
R_{wp} = 3.58%, R_p = 2.68%, R_B = 9.04%, and R_{Fobs} = 9.10% (for ND), and
R_{wp} = 6.05%, R_p = 4.56%, R_B = 5.35%, and R_{Fobs} = 6.32% (for SR).

atom	site	g	x	y	z	B (Å^2)
Li (1)	2b	0.500	0	1/2	0	0.86
Mn (1)	2b	0.236(2)	0	1/2	0	0.86
Ni(1)	2b	0.259(1)	0	1/2	0	0.86
Li (2)	2c	1	0	0	1/2	0.70
Li (3)	4h	1	0	0.6512(2)	1/2	0.70(2)
Li (4)	4g	0.124	0	0.16789	0	0.86
Mn (2)	4g	0.716	0	0. 16789(6)	0	0.86(1)
Ni(2)	4g	0.160	0	0.16789	0	0.86
O (1)	4i	0.991(2)	0.2215(2)	0	0.2286(2)	0.52(1)
O (2)	8j	0.949	0.2497(2)	0.32320(6)	0.22274(9)	0.52

R =7.88%, χ^2=54.8.

α_{11}	α_{12}	α_{13}
0.8024(8)	0.1931	0.0045(1)

Table 3. Site Occupancies of the Metal Atoms in the TM Layer of $Li_2(Ni_xMn_{1-x})O_{3(-\delta)}$ (x = 0, 1/10, 1/6, and 1/4), As Determined by the Joint Neutron and Synchrotron Analyses.

	$x = 0$		$x = 1/10$		$x = 1/6$		$x = 1/4$	
atom	2b	4g	2b	4g	2b	4g	2b	4g
Li (1)	0.7464	0.1188	0.645	0.131	0.565	0.141	0.500	0.124
Mn (1)	0.2536	0.8812(2)	0.227(1)	0.824	0.261(1)	0.762	0.236(2)	0.716
Ni (1)	-	-	0.127(1)	0.044	0.174(1)	0.097	0.259(1)	0.160

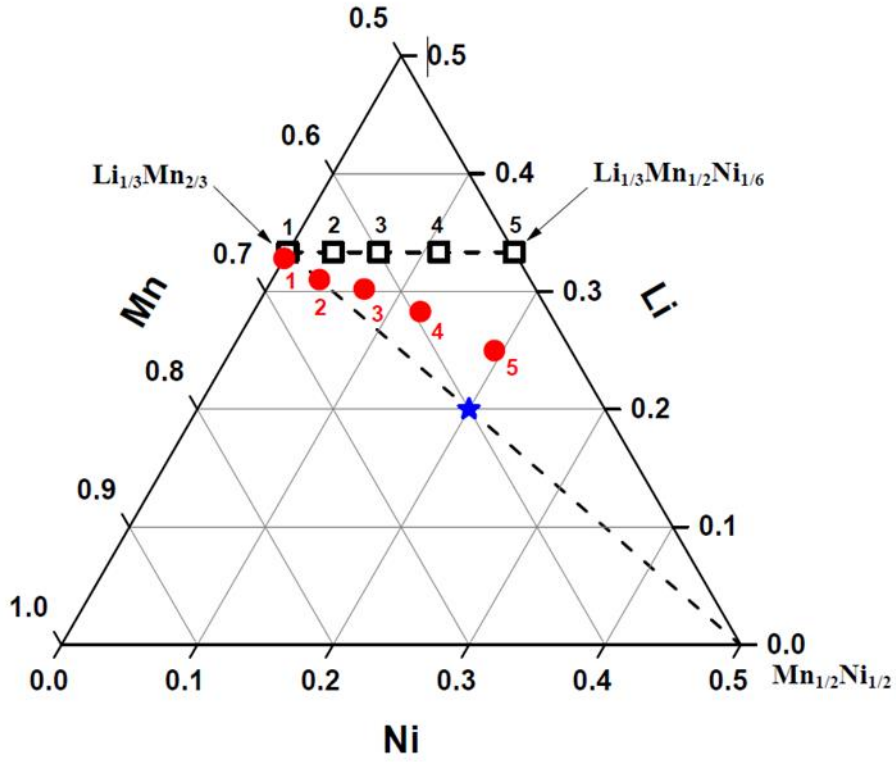

Figure 1. Metal atom present in the TM layer in $Li[Li_mMn_nNi_{1-m-n}]O_{2(-\varepsilon)}$ as represented using a ternary diagram. The open squares represent the preparation compositions; on the other hand, the red dots represent the compositions obtained from the quantitative analyses. The star in the graph represents the composition $Li[Li_{0.2}Mn_{0.6}Ni_{0.2}]O_2$.

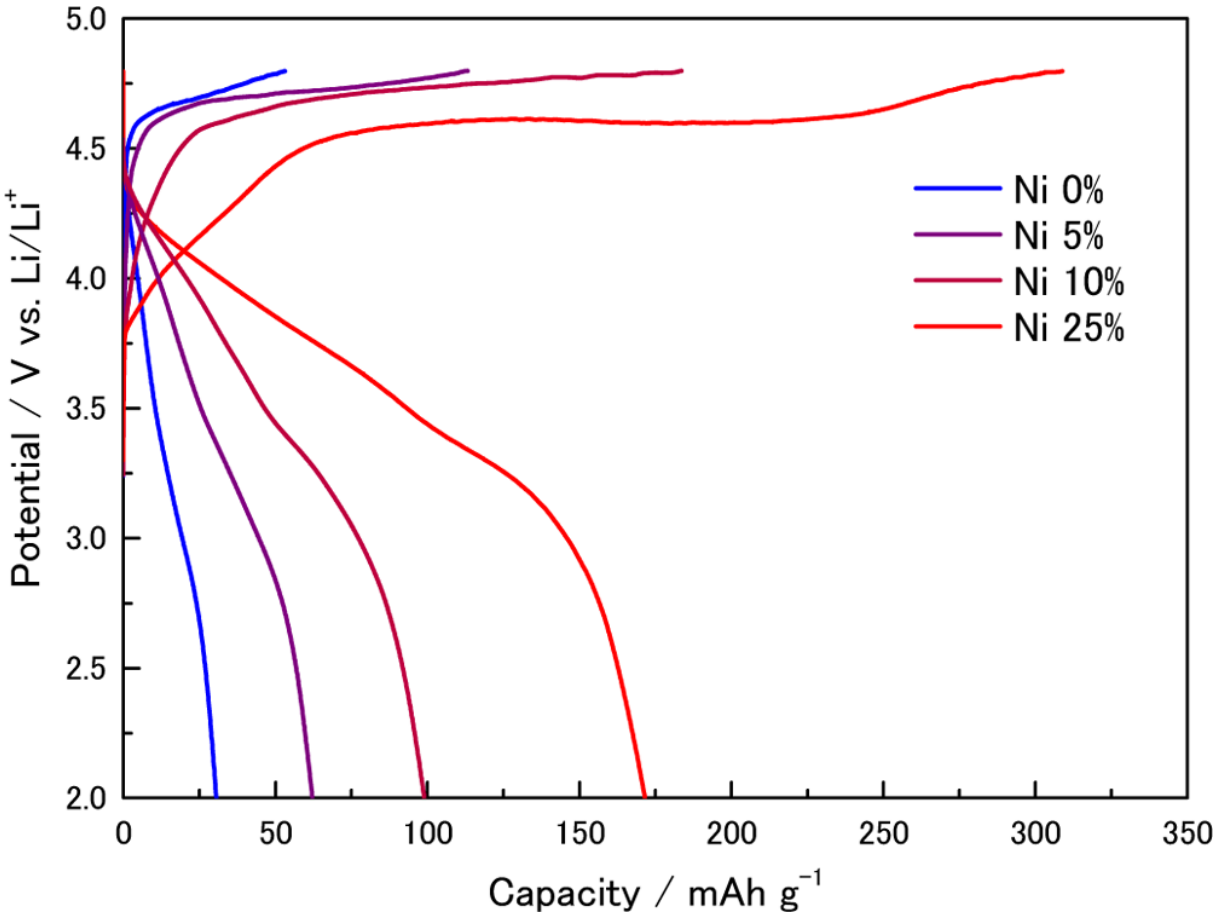

Figure 2. First charge−discharge curves of $Li_2(Ni_xMn_{1-x})O_{3(-\delta)}$ (x = 0, 1/20, 1/10, and 1/4) between 2.0 and 4.8 V (vs Li/Li^+) at a rate of 10 mA g^{-1} as measured at room temperature.

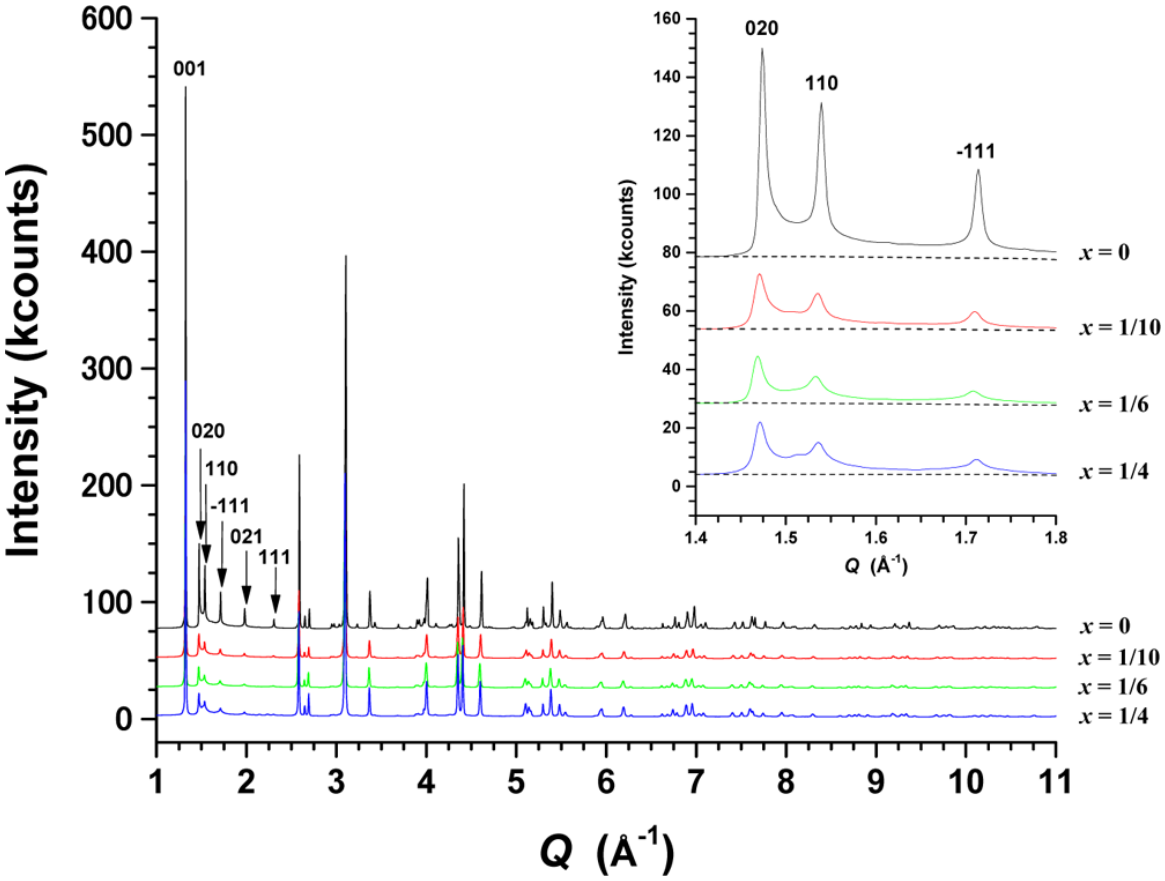

Figure 3. Synchrotron diffraction patterns of $Li_2(Ni_xMn_{1-x})O_{3(-\delta)}$ (x = 0, 1/10, 1/6, and 1/4). The arrows indicate the positions of the 020, 110, $\bar{1}11$, 021, and 111 superstructure reflections. The insets show magnified images of the low-angle parts; fairly intense diffuse peaks from the stacking faults can be seen, especially at the bottoms of the 020, 110, and $\bar{1}11$ superstructure reflections (the background profiles are represented by the broken lines).

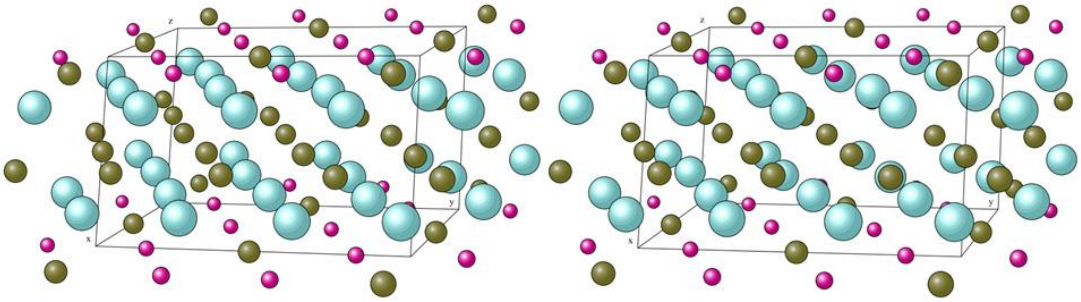

Figure 4. Stereographic view of ideally ordered Li_2MnO_3 as depicted by the intersection technique (Li: dark green, O: aqua, Mn: pink). The unit cell of this crystal (contoured with thin lines) is composed of cubic-stacked, TM, O, Li, and O layers. These layers are parallel to the *a*-*b* plane (base plane) of the cell. The TM layer consists of Li atoms at the 2*b* site and Mn atoms at the 4*g* site; the Li layer is composed exclusively Li atoms located at the 2*c* and 4*h* sites.

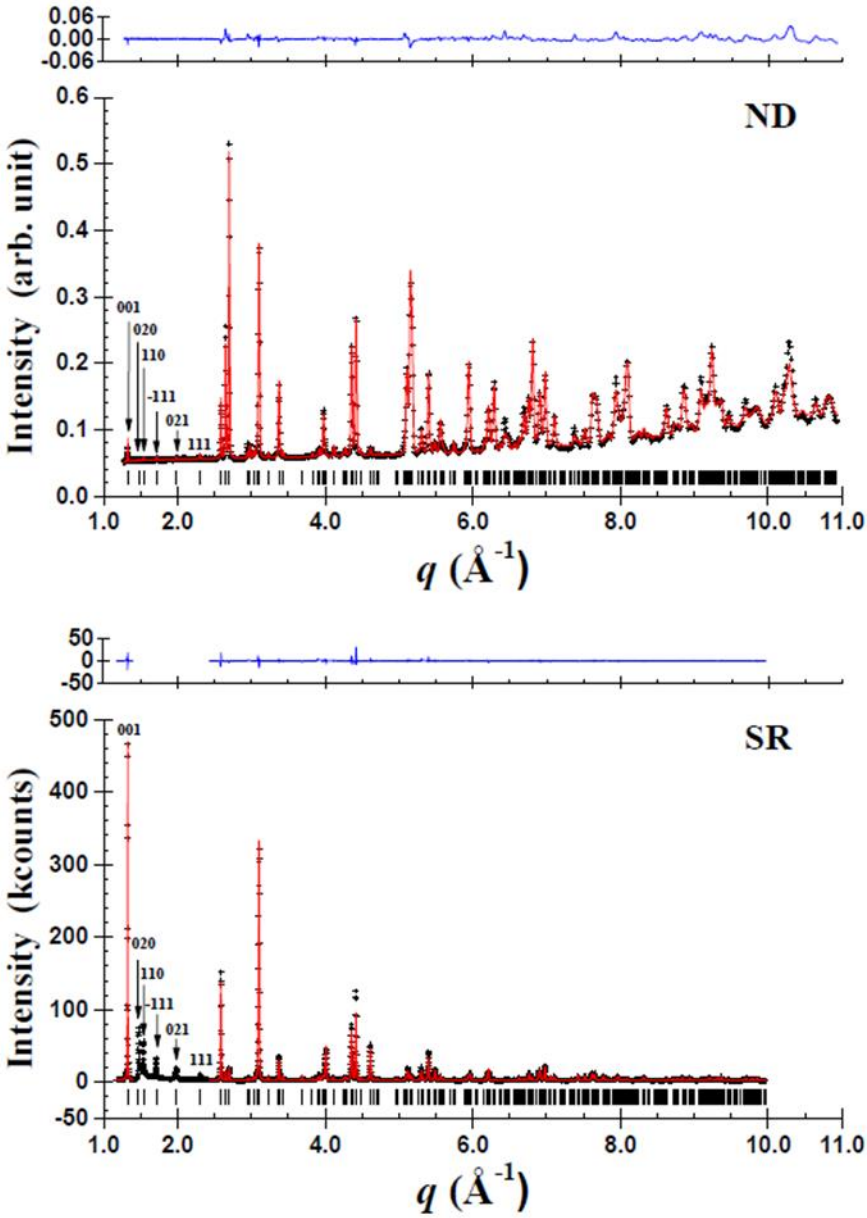

Figure 5-1. Observed (+) and calculated (red line) neutron (ND) and synchrotron (SRD) diffraction profiles acquired at room temperature for $Li_2(Ni_xMn_{1-x})O_{3(-\delta)}$ (x=0), whose structure was refined by the joint Rietveld method ($q = 4\pi\sin\theta/\lambda$). The difference curves (observed minus calculated, blue lines) appear at the top of the figures; under the profiles, the reflection markers are indicated by spikes. The 020, 110, $\bar{1}11$, 021, and 111 peaks were excluded from SRD data for the analysis.

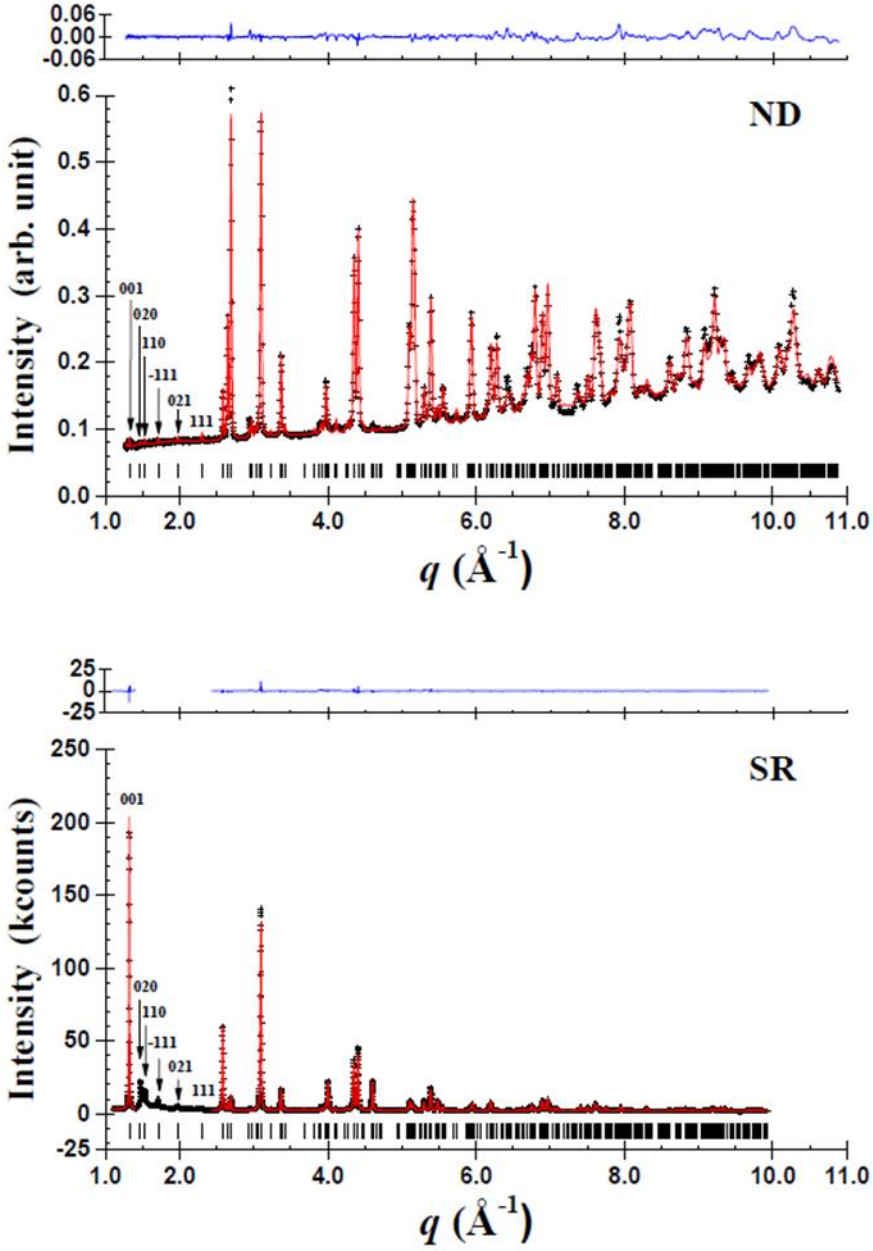

Figure 5-2. Observed (+) and calculated (red line) neutron (ND) and synchrotron (SRD) diffraction profiles acquired at room temperature for $Li_2(Ni_xMn_{1-x})O_{3(-\delta)}$ (x=1/10).

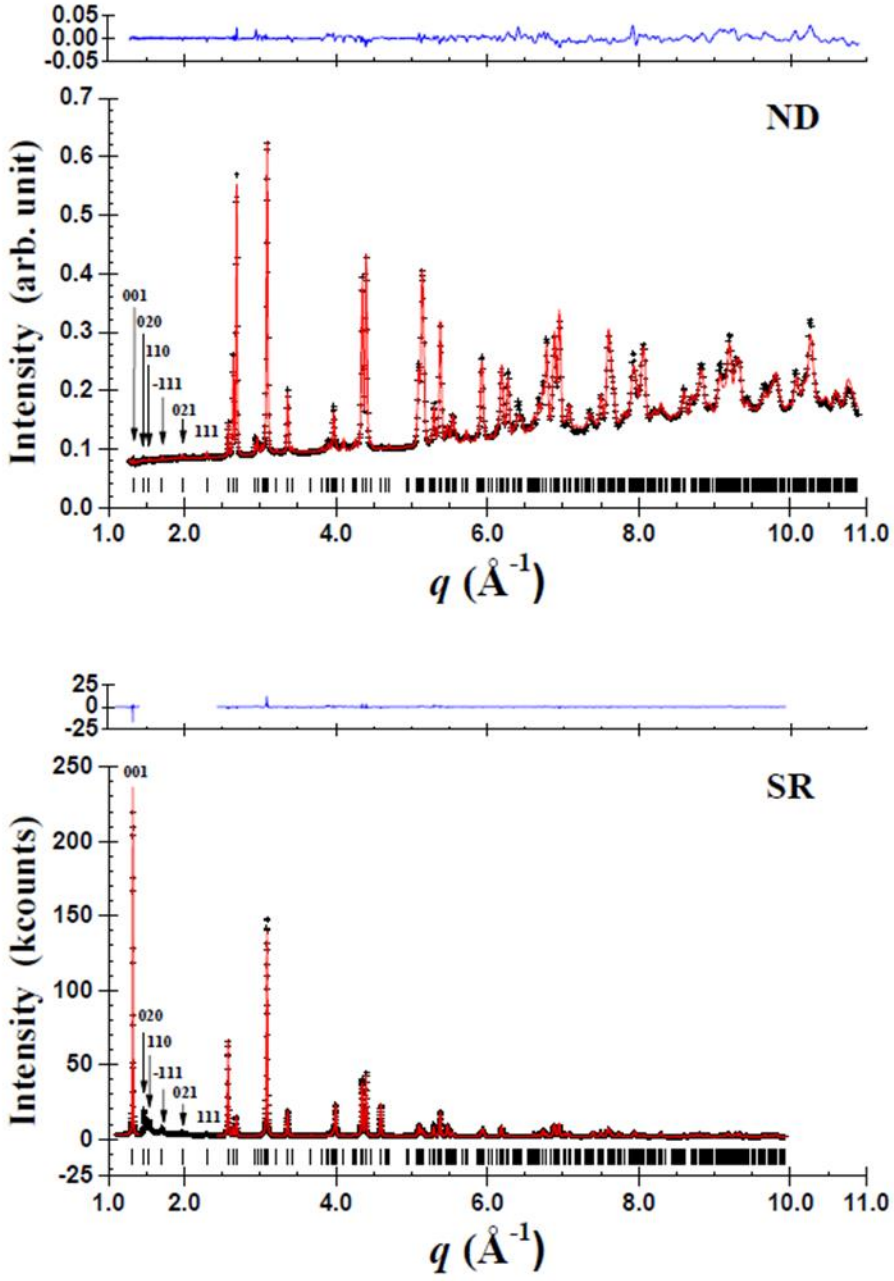

Figure 5-3. Observed (+) and calculated (red line) neutron (ND) and synchrotron (SRD) diffraction profiles acquired at room temperature for $Li_2(Ni_xMn_{1-x})O_{3(-\delta)}$ (x=1/6).

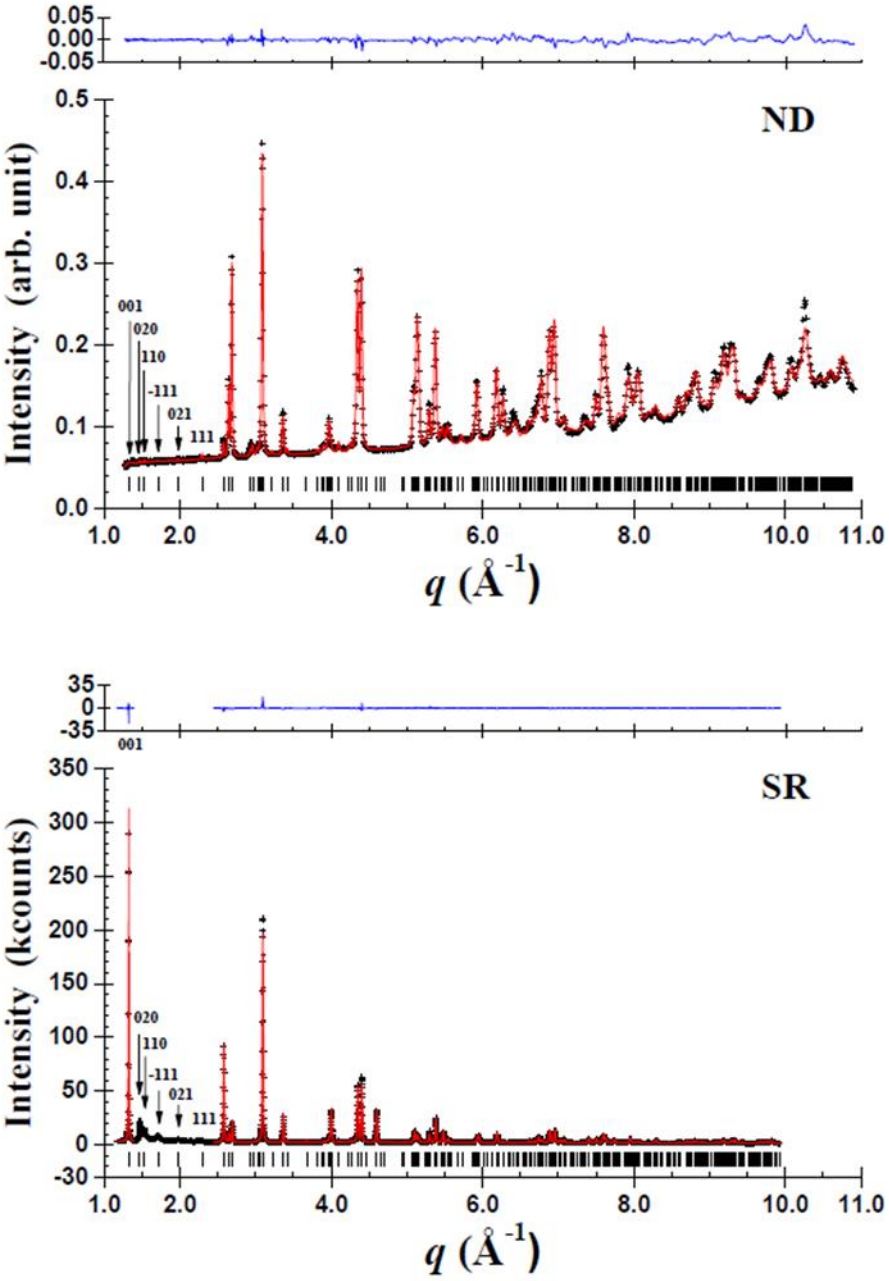

Figure 5-4. Observed (+) and calculated (red line) neutron (ND) and synchrotron (SRD) diffraction profiles acquired at room temperature for $Li_2(Ni_xMn_{1-x})O_{3(-\delta)}$ (x=1/4).

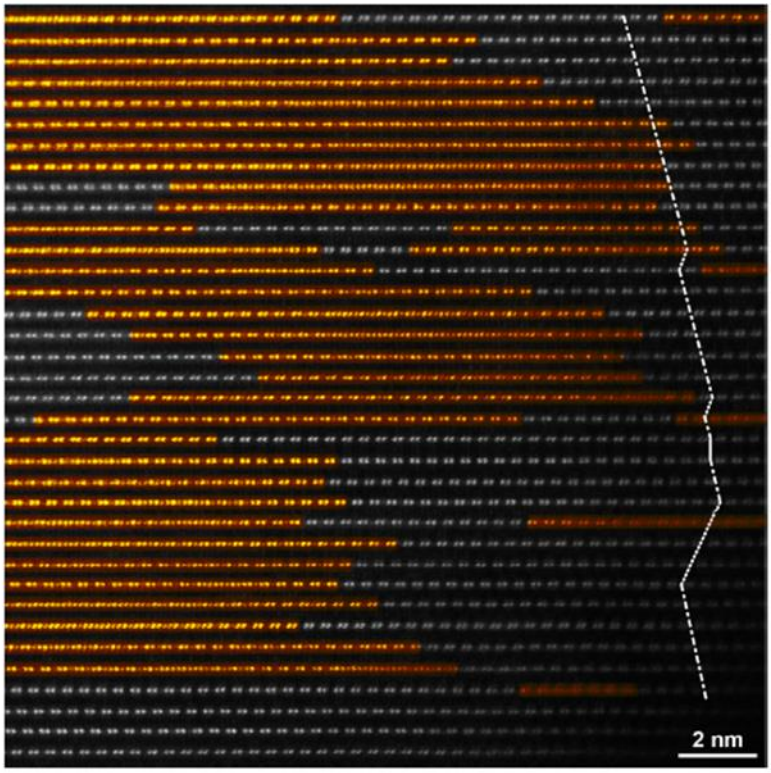

Figure 6. HAADF STEM image of the $Li_2(Ni_xMn_{1-x})O_{3(-\delta)}$ (x=1/4) compound synthesized at 900 ºC. The bright spots indicate the positions of the Mn/Ni atomic columns in $Li_2(Ni_xMn_{1-x})O_{3(-\delta)}$ (x=1/4) viewed along the [100], [110], and [$1\bar{1}0$] zone axes, which are indicated by the solid, dashed, and dashed-dotted lines, respectively.

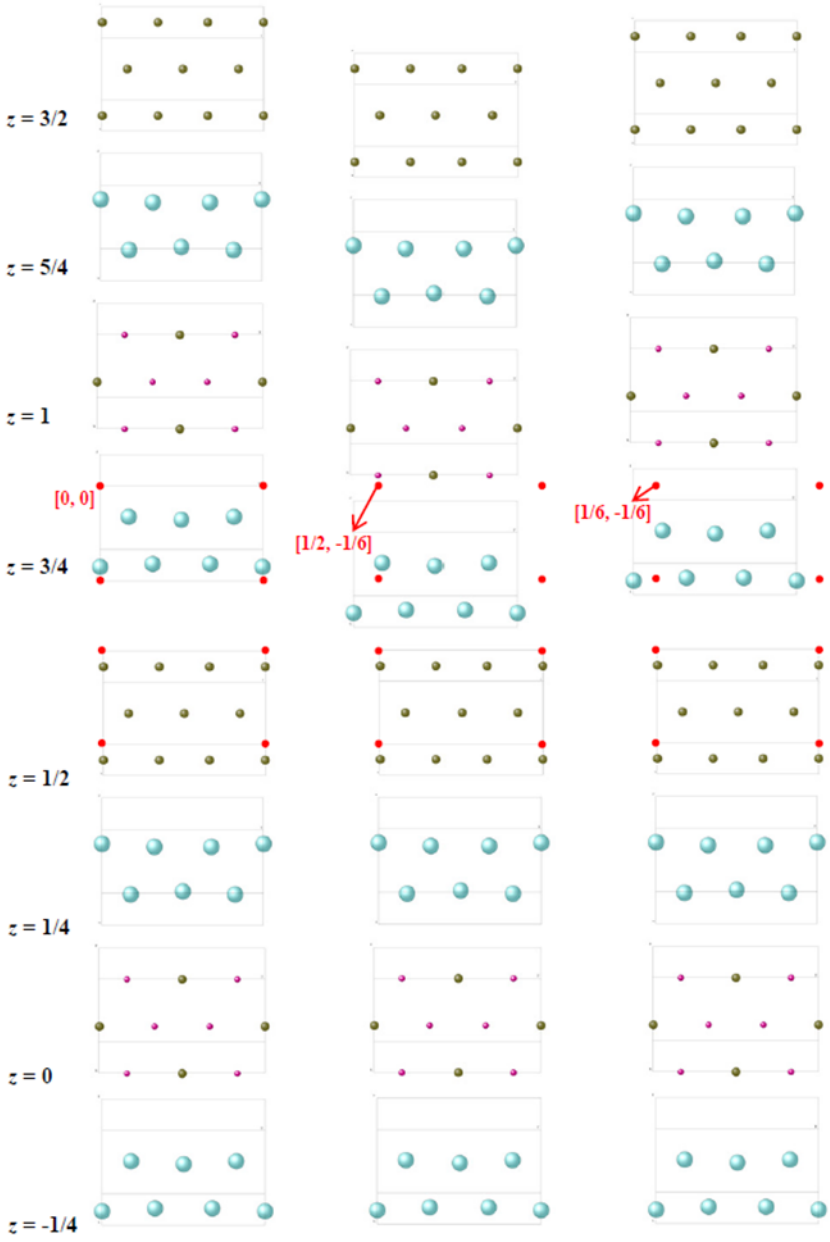

Figure 7-1. Layer stacking structures of Li_2MnO_3 (Li: dark green, O: aqua, Mn: pink). Slabs, which consist of four atomic layers, can slip by the translation vector, [0, 0], [1/2, -1/6], or [1/6, -1/6], producing stacking faults in the crystal. The thin lines represent the unit cells while the red dots indicate the alignment points of the upper and lower slabs.

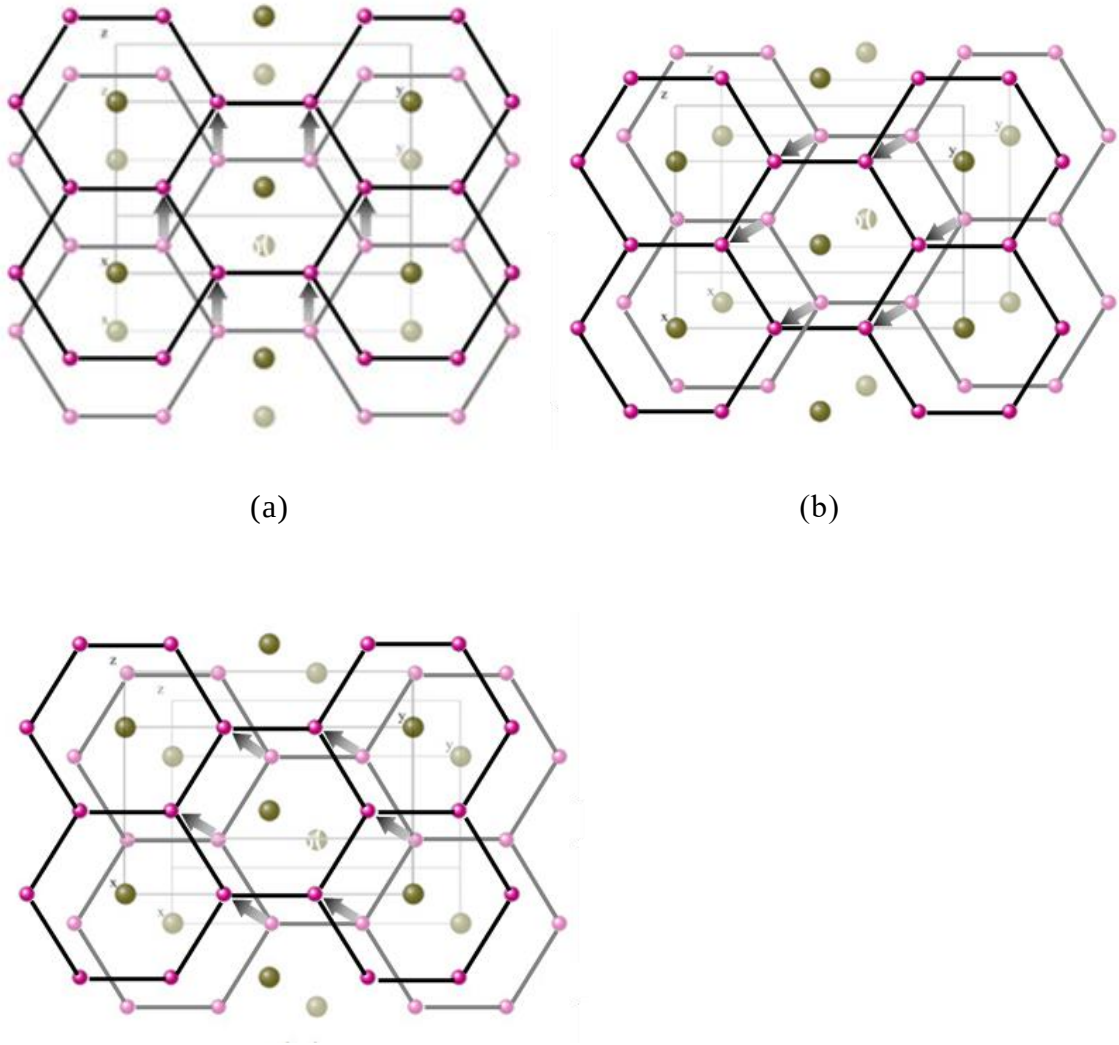

Figure 7-2. Stacking structures of the upper (z=1) and lower (z=0) TM layers in Li_2MnO_3 (Li: dark green, O: aqua, Mn: pink; the lower layers are depicted as half tone images). The upper layer is shifted by the translation vector, (a) [0, 0, 1], (b) [1/2, -1/6, 1], or (c) [1/6, -1/6, 1], which produces three kinds of atomic configurations. Notice that, when the 2*b* and 4*f* sites on the TM layer are occupied completely at random by Li and TM atoms (see Figure 4), the atomic configurations of (a) and (b) coincide with each other.

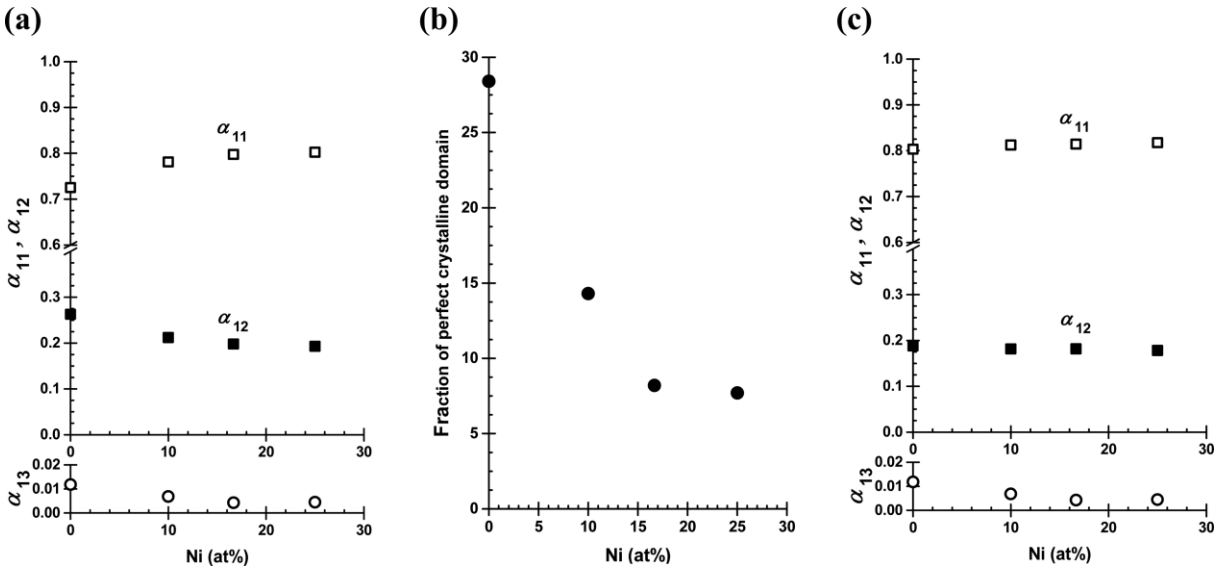

Figure 8. (a) Translation probabilities for the three kinds of stacking faults, α_{11}, α_{12}, and α_{13} and (b) the fractions of the perfect crystalline domains as obtained from the FAULTS analyses for $Li_2(Ni_xMn_{1-x})O_{3(-\delta)}$ (x = 0, 1/10, 1/6, and 1/4). (c) The translation probabilities in panel a as averaged (corrected) by the domain fraction shown in panel b. The standard deviations as estimated by the least-squares refinements were smaller than the marks. The labels of the horizontal axes of these graphs show the Ni concentrations, x, of the $Li_2(Ni_xMn_{1-x})O_{3(-\delta)}$ specimens.

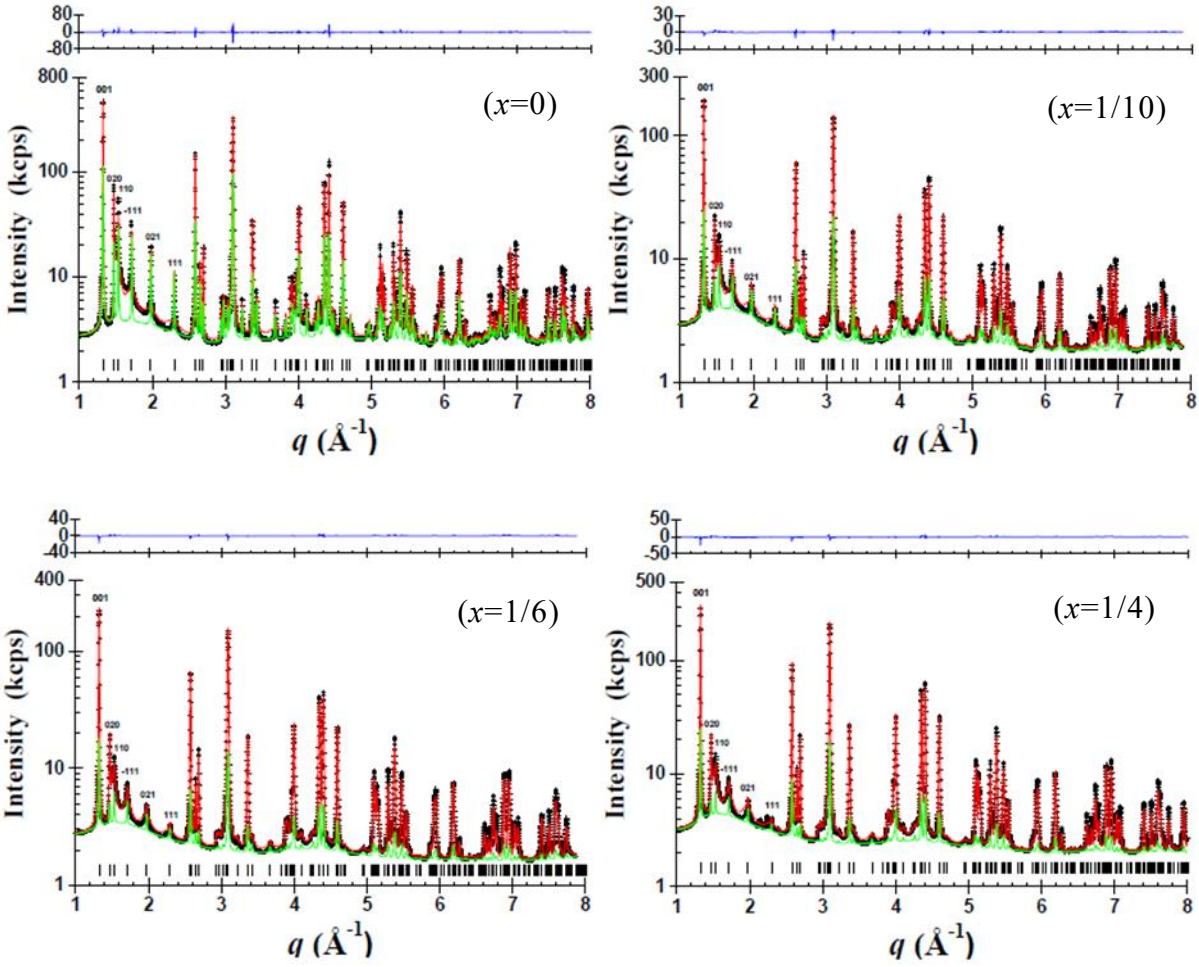

Figure 9. Observed (+) and calculated (red line) X-ray diffraction profiles of $Li_2(Ni_xMn_{1-x})O_{3(-\delta)}$ (x=0, 1/10, 1/6, and 1/4) synthesized at 900 °C for 12 h on a logarithmic scale. A difference curve (observed minus calculated, blue line) appears at the top of the figure; under the diffraction profiles, the reflection markers are indicated by spikes. The background profile is shown by a green line. Some of the peaks on the low-angle side are labeled with their Miller indices.

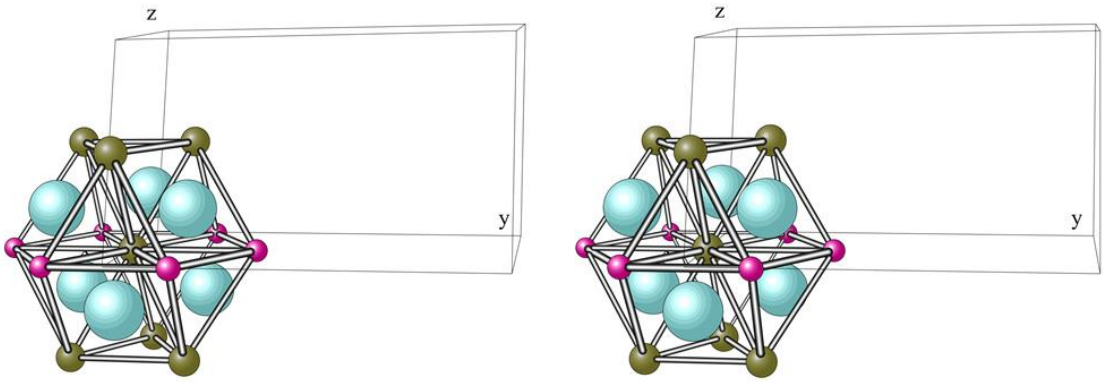

Figure 10. Nearest O atoms (aqua) and second-nearest metal atoms (TM: pink/Li: green) around a Li atom in the TM layer in $Li_2(Ni_xMn_{1-x})O_{3(-\delta)}$ crystals as depicted using the intersection technique; the metal atoms are linked by bars. All the other metal atoms in the crystals are also coordinated by 18 atoms (six oxygen and twelve metal atoms).

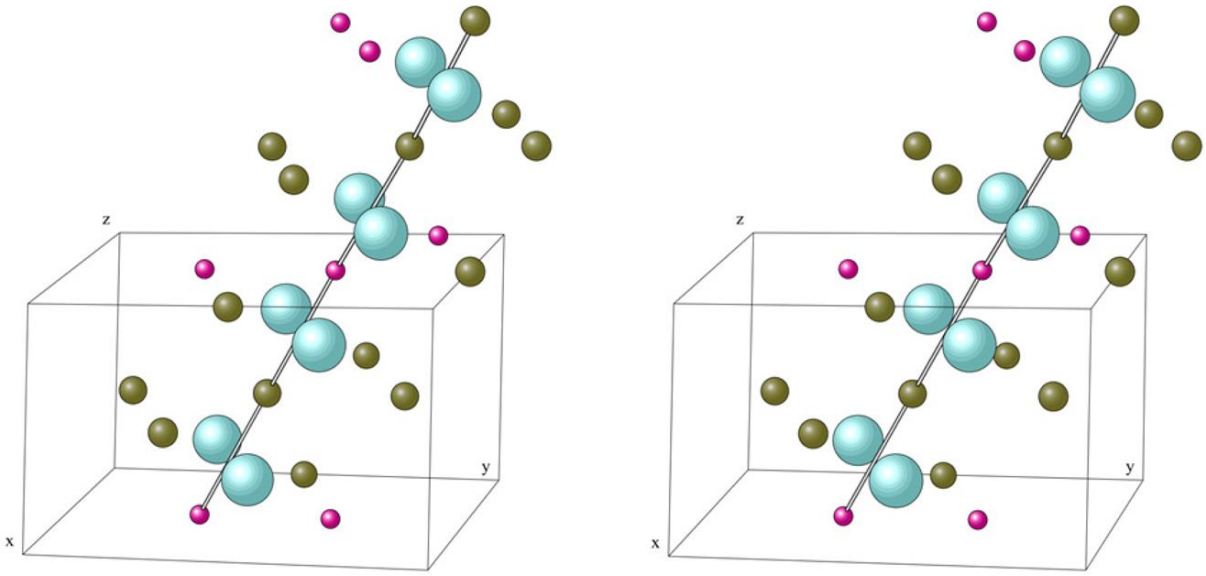

Figure 11. Stereo graphic of a Li-Mn chain (connected by bars) and the obstructing atoms located along the chain in a perfectly ordered Li_2MnO_3 crystal (cross-eyed stereo viewing: Li, dark green; O, aqua; and Mn, pink). This chain can be a smooth Li percolation path in the $Li_2(Ni_xMn_{1-x})O_{3(-\delta)}$ crystal as well (even along the *c*-axis direction, as shown in this figure), when the Mn/Ni atoms in the chain are replaced by Li atoms and the obstructing Mn^{4+} ions are substituted by Li^+ or Ni^{2+} ions.

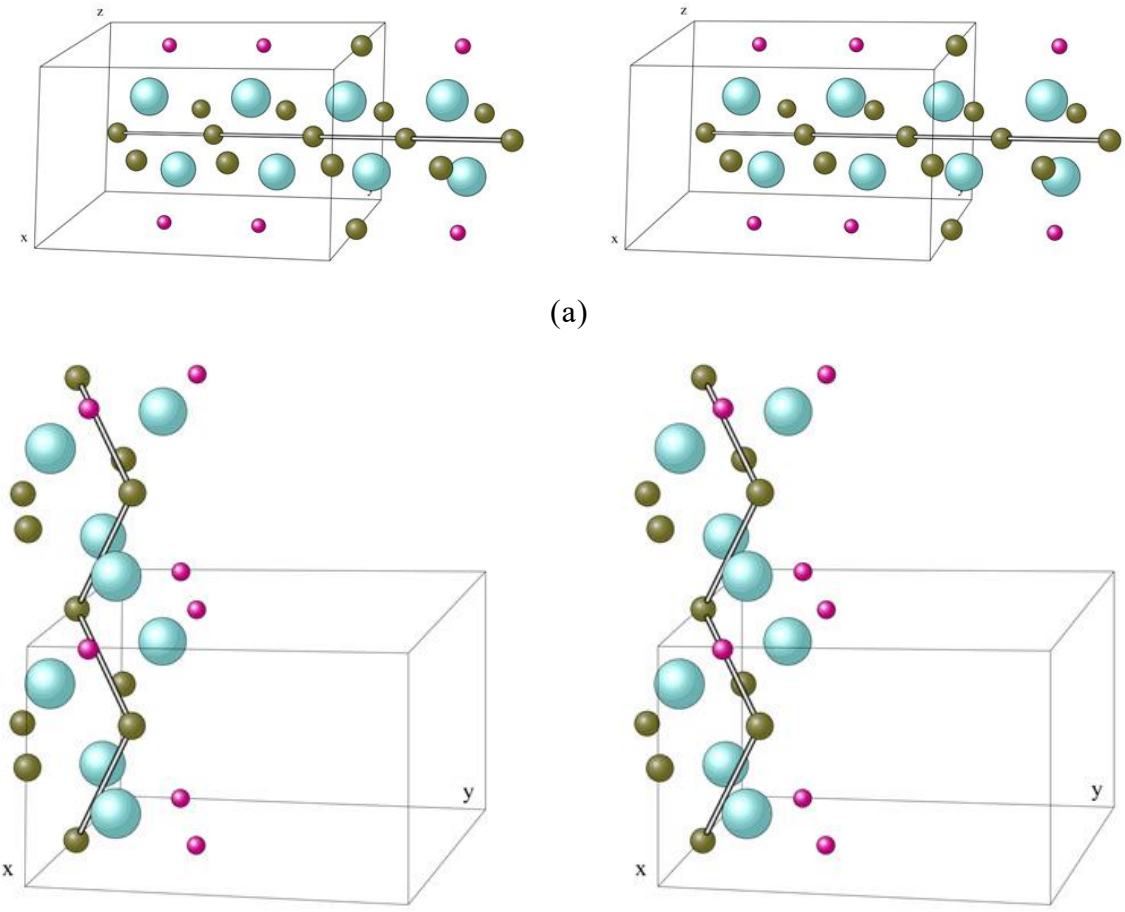

Figure 12. Li-Li chains (connected by bars) located (a) in the Li layer and (b) across the Li and TM layers with their obstructing atoms along the chains in the perfectly ordered Li_2MnO_3 crystal (cross-eyed viewing / Li: dark green, O: aqua, and Mn: pink).

References

[1] D. Y. W. Yu, K. Yanagida, Y. Kato, H. Nakamura, *J. Electrochem. Soc.* **2009**, *156*, A417.

[2] A. Boulineau, L. Croguennec, C. Delmas, F. Weill, *Solid State Ionics* **2010**, *180*, 1652.

[3] T. Matsunaga, H. Komatsu, K. Shimoda, T. Minato, M. Yonemura, T. Kamiyama, S. Kobayashi, T. Kato, T. Hirayama, Y. Ikuhara, H. Arai, Y. Ukyo, Y. Uchimoto, Z. Ogumi, *Chem. Mater.* **2016**, *28(12)*, 4143.

[4] Z. Lu, L. Y. Beaulieu, R. A. Donaberger, C. L. Thomas, J. R. Dahn, *J. Electrochem. Soc.* **2002**, *149*, A778.

[5] B. Song, H. Liu, Z. Liu, P. Xiao, M. O. Lai, L. Lu, *Sci. Rep.* **2013**, *3*, 3094.

[6] M. Casas-Cabanas, J. Rodríguez-Carvajal, M. R. Palacín, *Z. Kristallogr. Suppl.* **2006**, *2006*, 243.

[7] M. M. J. Treacy, J. M. Newsam, M. W. Deem, *Proc. R. Soc. London, Ser. A* **1991**, *433*, 499.

[8] R. Oishi, M. Yonemura, Y. Nishimaki, S. Torii, A. Hoshikawa, T. Ishigaki, T. Morishima, K. Mori, T. Kamiyama, *Nucl. Instrum. Methods Phys. Res., Sect. A* **2009**, *600*, 94.

[9] E. Nishibori, M. Takata, K. Kato, M. Sakata, Y. Kubota, S. Aoyagi, Y. Kuroiwa, M. Yamakata, N. Ikeda, *J. Phys. Chem. Solids* **2001**, *62*, 2095.

[10] M. Yonemura, K. Mori, T. Kamiyama, T. Fukunaga, S. Torii, M. Nagao, Y. Ishikawa, Y. Onodera, D. S. Adipranoto, H. Arai, Y. Uchimoto, Z. Ogumi, *J. Phys.: Conf. Ser.* **2014**, *502*, 012053.

[11] A. Boulineau, L. Croguennec, C. Delmas, F. Weill, *Chem. Mater.* **2009**, *21*, 4216.

[12] P. Strobel, B. Lambert-Andron, *J. Solid State Chem.* **1988**, *75*, 90.

[13] K. A. Jarvis, Z. Deng, L. F. Allard, A. Manthiram, P. J. Ferreira, *Chem. Mater.* **2011**, *23*, 3614.

[14] K. Kubota, T. Kaneko, M. Hirayama, M. Yonemura, Y. Imanari, K. Nakane, R. Kanno, *J. Power Sources* **2012**, *216*, 249.

[15] C. H. Lei, J. G. Wen, M. Sardela, J. Bareño, I. Petrov, S.-H. Kang, D. P. Abraham, *J. Mater. Sci.* **2009**, *44*, 5579.

[16] http://www.kri-inc.jp/ts/dept/pdf/nano-h_4-4.pdf.

[17] 3rd Euro-Mediterranean Conference on Materials and Renewable Energies EMCMRE-3, Marrakech-Morocco, November 2-6, 2015.

[18] Y. Yao, X. Bie, C. Wang, Y. Wei, G. Chen, F. Du, *J. Mater. Chem. A* **2015**, *3*, 18273.

[19] J. Lee, A. Urban, X. Li, D. Su, G. Hautier, G. Ceder, *Science* **2014**, *343*, 519.

[20] P. J. Phillips, J. Bareno, Y. Li, D. P. Abraham, R. F. Klie, *Adv. Energy Mater.* **2015**, *5*, 1501252.

Chapter 5. Observation of Anion-redox Behavior for High-capacity Cathode using Hard X-Ray Photoelectron Spectroscopy

5.1. Introduction

Lithium-rich manganese-based layered oxides (LLOs), commonly described as a composite $x\mathrm{Li_2MnO_3}$ $(1\text{-}x)\mathrm{LiMO_2}$ (M = Ni, Co, *etc.*), is well known that LLOs show a characteristic irreversible voltage plateau at ca. 4.5 V *vs.* $\mathrm{Li/Li^+}$ in the initial charging process, which is considered to come from the activation of the nominally inactive $\mathrm{Li_2MnO_3}$ component in the materials.[1,2] Much attention has been paid to the origin of this plateau because it is the key behavior explaining extra capacities in LLOs. The previous papers have related it to $\mathrm{O_2}$ gas release behavior, which should be accompanied by structural rearrangement.[3,4] The $\mathrm{O_2}$ release was evidenced by the gas chromatography (GC) or differential electrochemical mass spectrometry (DEMS) analyses.[5-9] The oxygen loss from the material is consistent with a large irreversible capacity observed in the initial cycle, but the quantification of the released $\mathrm{O_2}$ is not so straightforward.[5,7,10] As an alternative approach, the oxygen deficiency has been shown from X-ray diffraction data analyzed by the Rietveld method.[4,11,12] These studies have confirmed that the oxygen is more or less extracted from the structure. On the other hand, the first-principles calculations have suggested that the oxidation of oxygen anions without $\mathrm{O_2}$ release could explain the plateau profile.[13,14] These theoretical studies indicate that the redox reaction of oxygen in lattice should be considered. Recently, we have reported evidence of peroxide formation in $\mathrm{Li_{1.16}Ni_{0.15}Co_{0.19}Mn_{0.50}O_2}$ at a charged state by using soft X-ray absorption

spectroscopy (XAS) at the O K-edge.[15] However, the detailed oxidation behavior of the oxygen in lattice is not yet well understood during the charge-discharge process.

X-ray photoelectron spectroscopy (XPS) is one of the unique techniques for obtaining chemical state information on a specific element in the battery materials. This technique is especially surface-sensitive, which usually has a probing depth of <*ca.* 5 nm using a conventional X-ray source (Al Kα radiation of 1.49 keV, for example), and is suitable for the chemical characterization of the solid electrolyte interphase (SEI) comprising light elements (Li, C, O, and F) deposited on the electrode surface.[16-18] Recently, Tarascon and coworkers used this technique to identify the oxidation of oxygen anions in positive electrode materials.[19,20] They suggested the formation of peroxide species in $Li_2Ru_{1-y}Mn_yO_3$ and $Li_2Ru_{1-y}Sn_yO_3$ charged at 4.6 V from the O 1s XPS spectra with the aid of electron paramagnetic resonance (EPR) spectroscopy. More recently, Han *et al.* have compared the oxidation state of lattice oxygen among chemically delithiated and re-lithiated Li_2MnO_3, $Li_{1.14}Ni_{0.136}Co_{0.136}Mn_{0.544}O_2$, $LiNi_{0.5}Co_{0.2}Mn_{0.3}O_2$, and $LiCoO_2$ samples and suggested that the peroxide species were uniquely formed in the former two materials.[21,22] However, because of its surface-sensitive nature, it is often the case that the O 1s XPS spectra were largely affected by electrolyte degradation products such as Li_2CO_3, which makes it difficult to validate the formation of peroxide species in the bulk. XPS measurements using synchrotron X-ray radiation are advantageous to probe the chemical state information from the deeper inside of the material (the probing depth of <*ca.* 50 nm),[23] which enables us to focus on the lattice structure of the LIB active materials buried beneath the surface-deposited products. In this study, we have investigated the oxidation/reduction behaviors of lattice oxygen and transition metals in a lithium-rich manganese-based layered oxide $Li[Li_{0.25}Ni_{0.20}Mn_{0.55}]O_{1.93}$ during the irreversible initial charge-discharge

cycle by using hard X-ray photoelectron spectroscopy (HAX-PES). A possible structural modification occurring during the charge-discharge cycles has also been examined for the material disassembled on the fifth cycle.

5.2. Experimental

Sample Preparation: $Li[Li_{0.25}Ni_{0.20}Mn_{0.55}]O_{1.93}$ was synthesized by a solid-state reaction at 900 °C for 12 h with the starting materials $LiOH \cdot H_2O$, Ni_2CO_3 (Wako Pure Chemical Industries), and $MnCO_3$ (Kojundo Chemical Laboratory). Li_2MnO_3 ($Li[Li_{0.33}Mn_{0.67}]O_2$) was also prepared at 900 °C by the same procedure as a reference material. From the scanning electron microscopic observation, the average particle size of $Li[Li_{0.25}Ni_{0.20}Mn_{0.55}]O_{1.93}$ was estimated to be *ca.* 5 mm, which consisted of small crystallites of *ca.* 200 nm in diameter. The chemical composition $Li[Li_{0.25}Ni_{0.20}Mn_{0.55}]O_{1.93}$ was determined from the inductively coupled plasma-atomic emission spectrometry (ICP-AES, ICPS-8100, Shimadzu) and the iodometric titration measurements that estimate the average oxidation states of the transition metals using 0.03 M $Na_2S_2O_3$ solution. The materials were also characterized by X-ray diffraction and indexed to *C*2/*m* (Figure 1).

A mixture of the active material ($Li[Li_{0.25}Ni_{0.20}Mn_{0.55}]O_{1.93}$ or Li_2MnO_3), acetylene black (Denki Kagaku Kogyo) and polyvinylidene difluoride (PVDF, Kureha) with a weight ratio of 80 : 10 : 10 was spread onto an aluminum foil with N-methylpyrrolidone (NMP) and then dried at 80 °C under vacuum overnight to constitute a positive electrode. The electrode was pressed to a typical thickness of 30-35 mm. A foil of metallic lithium (0.2 mm in thickness, >99.9%, Honjo Metal) was used as counter and reference electrodes. These components were assembled together with a

Celgard 2500 separator and soaked in the electrolyte solution in an Ar-filled glovebox, which were sealed in an aluminum-coated laminate-type cell. The electrolyte used in this study was 1 M $LiPF_6$, which was dissolved in anhydrous ethylene carbonate (EC) and ethyl methyl carbonate (EMC) with a volumetric ratio of 3 : 7 (Kishida Chemical).

Electrochemical Measurements: The electrochemical measurements were performed at room temperature on an automatic cycling and data recording system (HJ1001SD8, Hokuto Denko). The cells were galvanostatically cycled between 4.8 and 2.0 V vs. Li/Li^+ at a current rate of 10 mA g^{-1}. A series of delithiated/re-lithiated samples were prepared for HAX-PES measurements by disassembling the cell at desired states of charge and discharge (Tables 1 and 2). They were carefully disassembled in the glove box and rinsed with dimethyl carbonate (DMC) to remove the electrolyte residue.

HAX-PES: The HAX-PES spectra were acquired at room temperature at BL28XU at SPring-8 (Hyogo, Japan). The electrode samples were placed onto a sample holder in the glove box and then transferred to an ultra-high vacuum sample chamber ($<5 \times 10^{-6}$ Pa) without exposing them to air. The incident photon energy was 7.94 keV. The detection depth was estimated to be ca. 50 nm from thickness-controlled oxidized Si wafers. The photoelectron analyzer was a VG Scienta EW4000. The pass energy was set to 200 eV. The binding energies of all the spectra were calibrated with respect to the lattice oxygen peak of $Li[Li_{0.25}Ni_{0.20}Mn_{0.55}]O_{1.93}$ (529.4 eV relative to the C 1s signal from acetylene black at 284.5 eV) and Li_2MnO_3 (529.5 eV) in O 1s spectra, respectively. These values were carefully determined by applying a dual beam charge neutralizer (low energy electrons and Ar^+ ions) on an in-house photoelectron spectrometer PHI5000 VersaProbe II (monochromated Al Kα radiation; 1486.6 eV, ULVAC-PHI.Inc). The spectra were analyzed after the Shirley-type background

subtraction.

First-Principles Calculations: First-principles calculations were performed based on the spin-polarized density functional theory (DFT) using the CASTEP code[24] to obtain essential information about the electronic structure of LLOs from a theoretical point of view. The generalized gradient approximation with the Hubbard U correction (GGA+*U*) for Ni and Mn 3d states (U_{eff} = 4.5 eV) was employed. The Perdew-Burke-Ernzerhof potential was used for the exchange-correlation term.[25] The plane-wave cut-off energy was set to 550 eV. The *k* point sampling for the Brillouin zone integration was done according to the Monkhorst-Pack scheme with a grid spacing of <0.04 $Å^{-1}$.[26] The model structure was constructed to reflect a minimal structural domain in the real material, which was prepared from a 2 × 1 × 2 supercell of the Li_2MnO_3 (*C*2/*m*) structure with $4Li^+$ ions in a transition-metal layer ($LiMn_2$ layer) substituted by $2Ni^{2+}$ ions, making the composition $Li_{28}Ni_2Mn_{16}O_{48}$ in the cell (the chemical composition in the simulation is different from that in the experiments for simplification). Atomic positions and cell parameters were fully relaxed until the residual forces and stresses acting on each atom were less than 0.03 eV $Å^{-1}$ and 0.05 GPa, respectively. Delithiated structures ($Li_{24}Ni_2Mn_{16}O_{48}$ and $Ni_2Mn_{16}O_{48}$) were also simulated for the Bader charge analysis.[27,28]

5.3. Results and Discussion

5.3.1. Chemical States in $Li[Li_{0.25}Ni_{0.20}Mn_{0.55}]O_{1.93}$ During the First Charge-Discharge Cycle

Figure 2 shows the charge-discharge profiles of $Li[Li_{0.25}Ni_{0.20}Mn_{0.55}]O_{1.93}$ for the first and fifth cycles. The sampling points for HAX-PES measurements are marked on

the figure. On the first charging process, a voltage slope is observed below 4.5 V, and a plateau is above 4.5 V, which is characteristic of the charging profile of LLOs.[29,30] This plateau is irreversible and is not observed on the first discharging process and subsequent charge-discharge cycles. The charging and discharging capacities are 309 and 172 mA h g^{-1} for the first cycle and 218 and 215 mA h g^{-1} for the fifth cycle, respectively. These capacities are much higher than that of Li_2MnO_3 prepared under the same conditions (Figure 3).

Figure 4a shows the Mn $2p_{3/2}$ HAX-PES spectra for the first cycle. Mn ions are mainly tetravalent in the pristine $Li[Li_{0.25}Ni_{0.20}Mn_{0.55}]O_{1.93}$ (sample #1) on the basis of the chemical shift references in the previous studies.[31,32] The main peak remains almost unchanged on the charging to 4.8 V (Sps. #2-6), indicating that the tetravalent Mn ions have no contributions to charge compensation on the initial charging process. They remain unchanged during the discharging down to 3.5 V (Sps. #7 and 8), but there is an increase in intensity at lower energy between 639.0 and 641.0 eV at 2.0 V (Sp. #9). This indicates the increase of lower-valence components (Mn^{2+} and Mn^{3+}) in a voltage window between 3.5 and 2.0 V. Some researchers also reported a similar reduction in the Mn oxidation state during discharging,[11,19,33,34] suggesting the participation of the Mn redox reaction in the subsequent charge-discharge cycles. On the other hand, we found a different oxidation behavior of Mn ions in Li_2MnO_3, where the increase of lower-valence components is shown on the charging process (especially, Sp. #2 in Figure 5 and 6). Carroll *et al.* reported this unusual behavior for $Li_{1.2}Ni_{0.2}Mn_{0.6}O_2$ by using XPS and electron energy loss spectroscopy (EELS).[35] They suggested that the Mn reduction on the charging process was a consequence of the charge compensation for oxygen vacancy formation. Therefore, our results imply that the O_2 gas release is rather suppressed in $Li[Li_{0.25}Ni_{0.20}Mn_{0.55}]O_{1.93}$ than in Li_2MnO_3.

Figure 4b shows the Ni $2p_{3/2}$ photoelectron spectra for the first cycle. The pristine sample consists of divalent and trivalent Ni ions (Sp. #1), although the chemical shifts for the divalent, trivalent, and tetravalent Ni references were very close to each other.[36] The shoulder at the higher energy side increases in intensity during the voltage slope. This means the increase in the amount of tetravalent Ni ions up to 4.5 V (Sps. #2-4). In the plateau region, the peak shape is almost unchanged, indicating that Ni ions do not contribute to the charge compensation at this stage (Sp. #6). The high valence Ni ions are reduced to be divalent down to 3.5 V (Sps. #7 and 8). The peak position is unchanged in the voltage window between 3.5 and 2.0 V (Sp. #9). Similar behaviors were also reported in the previous XPS and XAS studies.[35,37-39] We note that the Li 1s spectra show a monotonous decrease in intensity during the charging process up to 4.8 V (Figure 7), indicating that the above spectral changes in Mn and Ni ions cannot explain the charge compensation in the voltage plateau region.

The O 1s photoelectron spectra are shown in Figure 8. The prominent peak at 529.4 eV is assigned to the lattice oxide ions (O^{2-}) in the pristine material (Sp. #1). The broader signal centered at 532.7 eV comes from the surface-deposited oxygen species. On delithiation, a shoulder signal arises at *ca.* 530.6 eV, the higher energy side of the oxide peak (Sps. #2-6). According to the previous studies, this signal corresponds to the more oxidized oxygen state than O^{2-} ions in the material, *i.e.*, peroxide-like O^{-} ions (here, the term "peroxide" does not necessarily mean the molecular unit O_2^{2-} as in Li_2O_2).[19,40-42] They are also visible in the Li_2MnO_3 electrodes (Sps. #2 and 3 in Figure 9). We here emphasize that this O^{-} signal is clearly visible and enhanced in the HAX-PES spectra rather than in the "surface-sensitive" in-house XPS spectra used in the previous studies,[19-22] which strongly suggests that they are formed in the lattice structure and are not from the surface-deposited oxygenated product such as Li_2O_2. We

note that the in-house XPS O 1s spectrum with Ar^+ sputtering also gives clear evidence of the O^- species in the bulk (Figure 10). Figure 11 represents the evolution of O^- ions relative to total lattice oxygen $[O^-]/[O^- + O^{2-}]$ in $Li[Li_{0.25}Ni_{0.20}Mn_{0.55}]O_{1.93}$. The details of the peak decomposition procedures are described in Figure 12. The amount of O^- species monotonously increases up to 33% at 4.8 V and then slightly decreases down to 2.0 V. A very recent XPS study on $Li_{1.2}Ni_{0.13}Co_{0.13}Mn_{0.54}O_2$, as well as $Li_2Ru_{1-x}M_xO_3$ and $Li_2Ir_{1-x}M_xO_3$, has reported that *ca.* 40% of lattice oxygen was converted to the peroxide species in the voltage plateau region,[43] which is consistent with our result. Our result also shows that the O^- species are formed on the voltage slope during charging and seem to exist even at 2.0 V (Figure 11). This suggests that the charge compensation is achieved not only by Ni ions but also by O anions in the slope region during the charging process. We therefore believe that the O^- species formed in the slope region is attached to the Ni ions, and the cation-anion dual charge compensation mechanism works at this stage. On the other hand, the O^- species formed in the plateau region can be related to the Mn ions, which are in the Li_2MnO_3- or $Li_2(Ni,Mn)O_3$-like domain assuming a nano-level composite structural model[1,2] in $Li[Li_{0.25}Ni_{0.20}Mn_{0.55}]O_{1.93}$.

Considering the chemical composition of $Li[Li_{0.25}Ni_{0.20}Mn_{0.55}]O_{1.93}$, the initial Ni oxidation state is +2.1, and therefore, it can deliver a capacity of *ca.* 130 mA h g^{-1} when it is oxidized to +4 during the charging up to 4.8 V. At the end of charge, 33% of the lattice oxygen (*i.e.*, 0.63O) change to the O^- species (Figure 11, Sp. #6), corresponding to an additional charge of 208 mA h g^{-1} by considering the O^{2-}/O^- couple. Therefore, the total capacity can be 338 mA h g^{-1}. This is slightly higher but reasonably close to the actual charging capacity of 309 mA h g^{-1}. At the end of discharge, the capacities recovered by Ni^{2+}/Ni^{4+} and O^{2-}/O^- couples are ca. 130 and 76 mA h g^{-1}, respectively,

the sum of which is again slightly higher than the actual discharging capacity of 172 mA h g^{-1} including the partial contributions from the Mn reduction. The small differences (overestimates) partly come from the assumption that all the Ni^{2+} ions change to Ni^{4+} without any electric isolation of active material particles and/or from the uncertainty in peak decomposition for the O 1s spectra. It is also suggested that the irreversible capacity during the first charge-discharge cycle is caused by the irreversible O^{2-}/O^{-} redox reaction as shown in Figure 11.

To gain some insight into the charge compensation mechanism in the LLO system, we calculated the electronic density of states (DOS) of a Li_2MnO_3-$Li(Ni,Mn)O_2$ composite-type model structure. The model structure was prepared in a simple fashion from a 2 × 1 × 2 supercell of the Li_2MnO_3 ($C2/m$) structure with $4Li^+$ ions in a $LiMn_2$ layer substituted by $2Ni^{2+}$ ions and 2 vacancies being a $Ni_{1/2}Mn_2$ layer as shown in Figure 13. This model gives atomic column images of –Li–Mn–Mn– arrangement as in Li_2MnO_3 and –M–M–M– as in $LiMO_2$ along the b axis, which were observed in the previous studies using scanning transmission electron microscopy (STEM).[38,44,45] The calculated DOS spectra show that the valence band just below the Fermi level is governed by Ni 3d and O 2p states in the $Ni_{1/2}Mn_2$ layer, indicating the contribution from both Ni and O ions for charge compensation during the voltage slope region. After the charge compensation by the Ni^{2+}/Ni^{4+} couple is finished, it is suggested that the oxidation of O anions from the $LiMn_2$ layer is also being involved as expected on the voltage plateau. The charge compensation can be evaluated based on the Bader charge analysis (Table 3). The average charges of Ni and Mn ions in $Li_{28}Ni_2Mn_{16}O_{48}$ are +1.26 and +2.08, respectively. They are smaller than their corresponding formal charges (+2 and +4), indicating their strong covalent bonding with oxygen. The charge of Ni ions increases but that of Mn ions remains almost constant when Li ions are extracted from

the model structure. The charge of O anions attached to Ni ions significantly decreases in $Li_{24}Ni_2Mn_{16}O_{48}$, but the O anions attached to Mn ions become a more oxidized state in $Ni_2Mn_{16}O_{48}$.

Based on the combined results of Mn 2p, Ni 2p, and O 1s spectra and qualitative understandings from the DFT calculations, the charge compensation mechanism is summarized as follows. The oxidation of Ni ions (Ni^{2+}/Ni^{4+}) and O anions (O^{2-}/O^{-}) occurs in the voltage slope region up to 4.5 V. Then, the oxidation of O anions (O^{2-}/O^{-}) only contributes to the charge compensation in the voltage plateau region. The oxygen loss as a gas release from this material seems less significant than that from Li_2MnO_3. On the discharging process, the reduction of Ni ions and O anions occurs down to 3.5 V and that of Mn ions starts below 3.5 V.

Because qualitative or quantitative gas detection measurements such as DEMS were not carried out, it is still unclear whether or not there is some participation of oxygen loss for charge compensation in this material. On the other hand, the present study shows the significant role of the redox reaction of the lattice oxygen (O^{2-}/O^{-}), suggesting that the Ni ions in the structure suppress the O_2 gas release at the voltage plateau. According to the previous studies, it is expected that a more electronegative cation is preferably hybridized to the ligand, the activated oxygen species.[19,20,34] Here, the Ni^{4+} ion at charged states has a larger electronegativity and has a preference to hybridize with the activated oxygen species over Mn^{4+} ions.[34] The present study supports the suggestion given by the previous studies that strong hybridization of Ni^{4+} and O^{-} species would stabilize the lattice structure preventing the O_2 release as evidenced by the fact that the Mn oxidation state remains tetravalent during the voltage plateau, while Li_2MnO_3 shows Mn valence reduction originating from the substantial O_2 release from the structure.[35]

5.3.2. Chemical States in $Li[Li_{0.25}Ni_{0.20}Mn_{0.55}]O_{1.93}$ During the Fifth Charge-Discharge Cycle

Next, we examine the structural stability on charge-discharge cycling. Figure 14a shows the Mn $2p_{3/2}$ HAX-PES spectra for the fifth charge-discharge cycle. The sample disassembled at 2.0 V after the fourth cycle (Sp. #10) shows a similar spectrum to that disassembled at 2.0 V after the first cycle (Sp. #9 in Figure 4a). On the charging process, the decrease of lower-valence Mn^{2+} and Mn^{3+} components and concomitant increase of Mn^{4+} state are observed above 3.5 V (Sps. #12 and 13). This spectral change is reversible (Sps. #14-16). The increased discharging capacity below 3.5 V for the fifth cycle compared with that for the first cycle (Figure 2) is attributable to the increasing participation of the Mn redox reaction for charge compensation. On the other hand, the oxidation state of Ni ions remains divalent during the fifth charge-discharge cycle (Figure 14b).

Figure 15 shows the O 1s spectra for the fifth cycle. Unfortunately, the signal at higher energy (>*ca.* 531.0 eV), mainly attributable to the surface-deposited lithium carbonate Li_2CO_3, is significant for the samples disassembled below 3.5 V. Based on the peak decomposition (Figure 16), we found that the O^- species still exist in the material, but they are almost constant in amount on the fifth cycle (Figure 17).

Considering that the Li 1s spectra for the fifth cycle still show the reversible delithiation/re-lithiation behavior (Figure 7b), the charge compensation is satisfied only by the Mn redox reaction on the fifth cycle. It is a very confusing result, because the previous XAS studies (bulk-sensitive) reported that the Ni ions act as a charge compensator even after the first cycle.[15,38,39] Therefore, we believe that the Ni ions

become inactive over (at least) 50 nm thickness from the surface, which is a probing depth of HAX-PES measurements, while they are still active in the deeper inside of the particles. This is probably related to structural rearrangement (deterioration) on the surface and sub-surface region. Recent STEM observations have revealed the formation of spinel- or rocksalt-like structural domains on the particle surface of LLOs after the charge-discharge cycles.[44,46-49] Therefore, the Ni 2p HAX-PES spectra of the cycled materials represent the electrochemically inactive Ni ions stabilized in the sub-surface Li-poor spinel- or rocksalt-like domains, which do not act as a charge-compensating ion on the charge-discharge cycles. The oxygen anions also have no more contribution to charge compensation in the sub-surface region, although it is possible that they are redox active in the bulk.[15,37,39] It is noteworthy that the formation of the spinel- or rocksalt-like domains suggests the oxygen loss from the surface. This indicates that both the mechanisms (oxygen loss and oxidation of the lattice oxygen) are important for the delithiation of the LLO positive electrode materials, and their contributions would be dependent on the chemical composition. The former mechanism would be dominant in Li_2MnO_3, but the latter becomes more important in Ni-containing LLOs.

5.4. Conclusions

We have investigated the oxidation/reduction behaviors of oxygen and transition metals in a Li-rich manganese-based layered oxide $Li[Li_{0.25}Ni_{0.20}Mn_{0.55}]O_{1.93}$ by using hard X-ray photoelectron spectroscopy. The Ni oxidation state increased in the voltage slope region of the first charging process, while it remained unchanged in the plateau

region. In the re-lithiated material, the Ni oxidation state reverted to divalent. Tetravalent Mn ions did not contribute to the charge compensation for the first charging process but were partially reduced on the discharging to 2.0 V. Then, the low-valence Mn ions participated in the delithiation/lithiation process on the subsequent cycles. It was clearly shown that the O^- species were formed in the material. The cation-anion dual charge compensation was suggested in the voltage slope region with the aid of theoretical calculations. We emphasize that HAX-PES is an excellent technique to understand the contribution of the lattice oxygen in charge compensation, because it enables us to get chemical state information on the lattice structure buried beneath the surface-oxygenated products due to its deeper probing depth than in-house XPS.

The Ni ions in the LLO lattice structure are considered to increase the capacity delivered by a (partially) reversible O^{2-}/O^- redox couple. This is related to the suppression of O^2 release due to the strong covalent bonding between Ni^{4+} and O^- ions in the $LiMO_2$- and Li_2MO_3-like domains. As a result, the discharging capacity exceeds 200 mA h g^{-1}. The O_2 release, if any, would come from the Li_2MnO_3 domain in the LLO lattice structure. Therefore, the homogeneous Ni incorporation into the lattice, that is a shift from the “composite” to “solid solution” structure, may be a key factor to design a fully reversible anion redox system.

Furthermore, we suggested the structural rearrangement occurring in the sub-surface region in the cycled material. During the fifth charge-discharge cycle, the O^- species were found to be electrochemically inactive. The divalent Ni ions were also inactive, but the oxidation state of Mn ions reversibly changed. It is very confusing because Ni and O ions were important redox-active elements in the first cycle. We therefore consider that structural deterioration that occurred in the cycled material is related to the formation of spinel- or rocksalt-like domains over the sub-surface region

(*ca.* 50 nm thickness) of the particles.

Table 1. Delithiated/re-lithiated samples of $Li[Li_{0.25}Ni_{0.20}Mn_{0.55}]O_{1.93}$ prepared for HAX-PES measurements.

	Sampling point	Potential / V	Capacity / mAh/g	Li content *x* in $Li_xNi_{0.20}Mn_{0.55}O_{1.93}$
1st cycle	①	OCV	0.0	1.25
	②	4.24	32.4	1.15
	③	4.45	51.5	1.09
	④	4.58	88.7	0.98
	⑤	4.61	227.6	0.56
	⑥	4.80	308.8	0.31
	⑦	4.00	–32.2	0.41
	⑧	3.50	–93.2	0.60
	⑨	2.00	–171.5	0.83
5th cycle	⑩	2.00	0.0	0.76
	⑪	3.39	21.7	0.69
	⑫	4.03	118.0	0.40
	⑬	4.80	217.6	0.10
	⑭	4.20	–21.4	0.16
	⑮	3.65	–82.4	0.35
	⑯	2.00	–214.6	0.75

Table 2. Delithiated/re-lithiated samples of Li_2MnO_3 prepared for HAX-PES measurements.

	Sampling point	Potential / V	Capacity / mAh/g	Li content x in $Li_xMn_{0.67}O_2$
1st cycle	①	OCV	0.0	1.33
	②	4.72	32.4	1.24
	③	4.80	56.8	1.17
	④	3.26	–15.2	1.21
	⑤	2.00	–32.5	1.26
5th cycle	⑥	2.00	0.0	1.24
	⑦	3.40	14.6	1.20
	⑧	4.15	28.3	1.16
	⑨	4.80	40.7	1.12
	⑩	3.75	–6.0	1.14
	⑪	3.26	–14.5	1.16
	⑫	2.00	–36.5	1.23

Table 3. Average bader charges calculated for the model structures.

Model composition	Li	Ni	Mn	O
$Li_{28}Ni_2Mn_{16}O_{48}$	+0.89	+1.26	+2.08	$-1.27^a/-1.26^b$
$Li_{24}Ni_2Mn_{16}O_{48}$	+0.89	+1.40	+2.09	$-1.15^a/-1.22^b$
$Ni_2Mn_{16}O_{48}$	—	+1.48	+2.11	$-0.92^a/-0.72^b$

[a] The charge for the O anions bonded with Ni ions (Ni-O-Mn). [b] The charge for the O anions bonded with Mn ions (Mn-O-Mn).

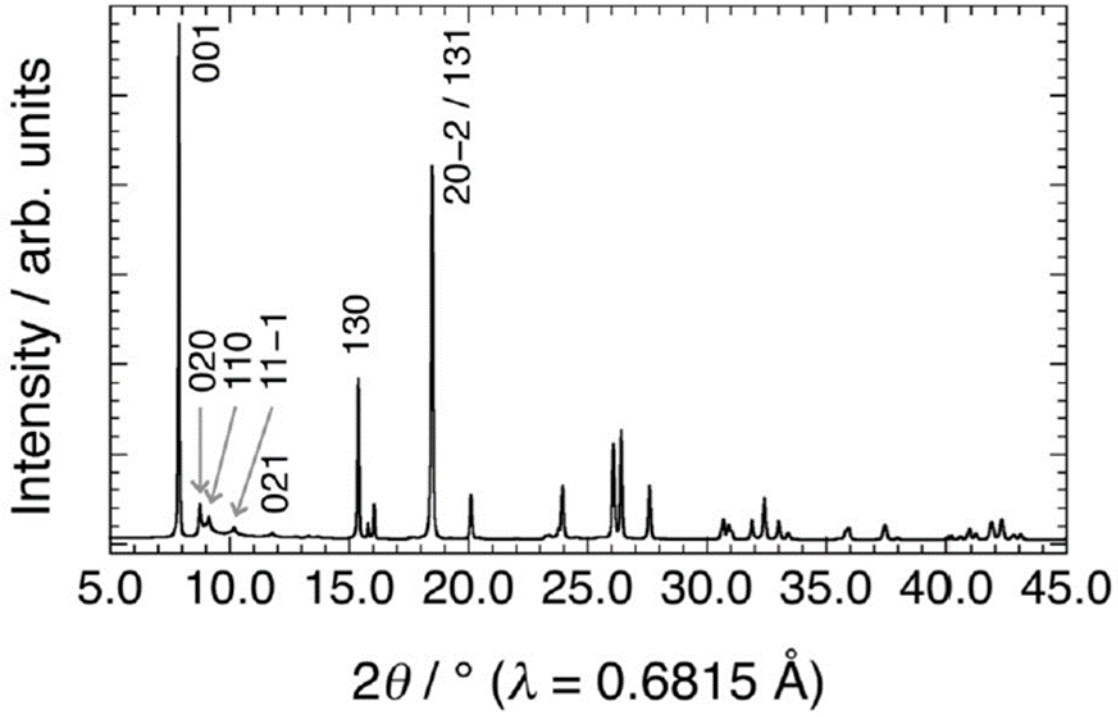

Figure 1. X-ray diffraction profile of the pristine $Li[Li_{0.25}Ni_{0.20}Mn_{0.55}]O_{1.93}$ sample, which is indexed with *C*2/*m*, and the refined lattice parameters are a = 4.951 Å, b = 8.558 Å, and c= 5.028 Å, β= 109.213° respectively.

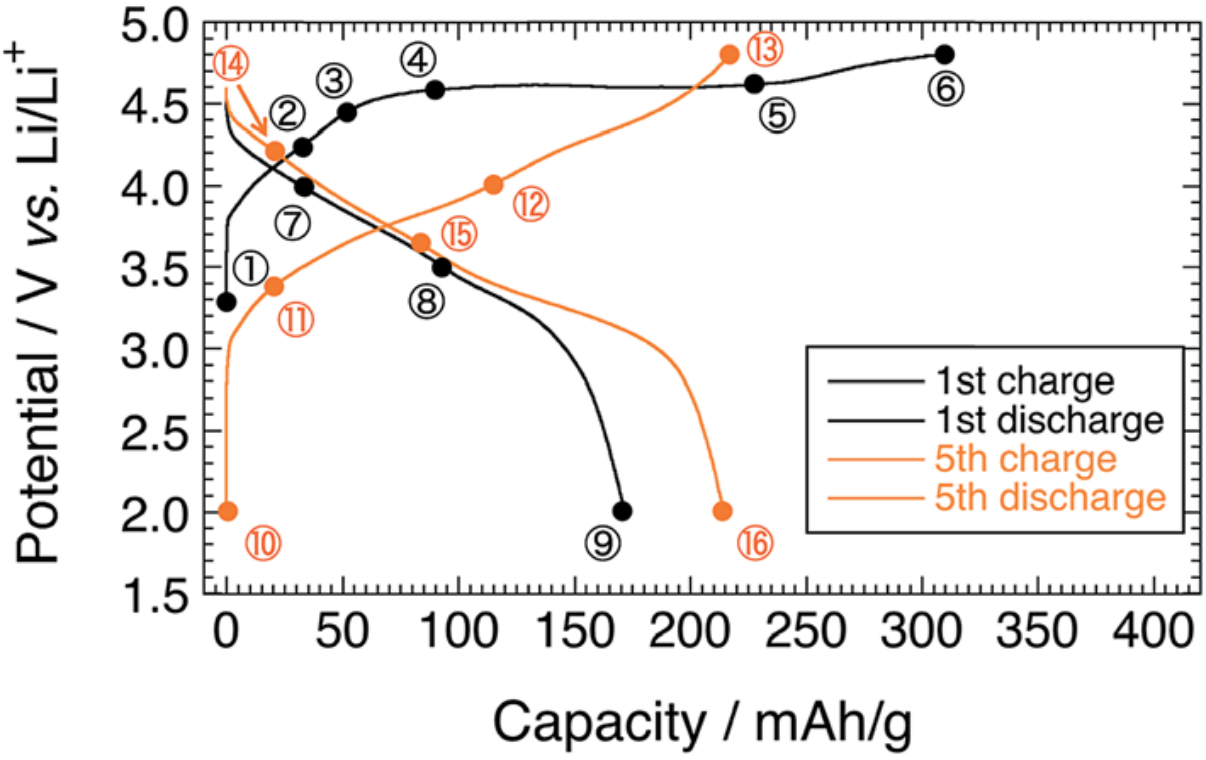

Figure 2. Charge-discharge profiles of the $Li[Li_{0.25}Ni_{0.20}Mn_{0.55}]O_{1.93}$ electrode for the first and fifth cycles. Sampling points for HAX-PES measurements are marked on the figure.

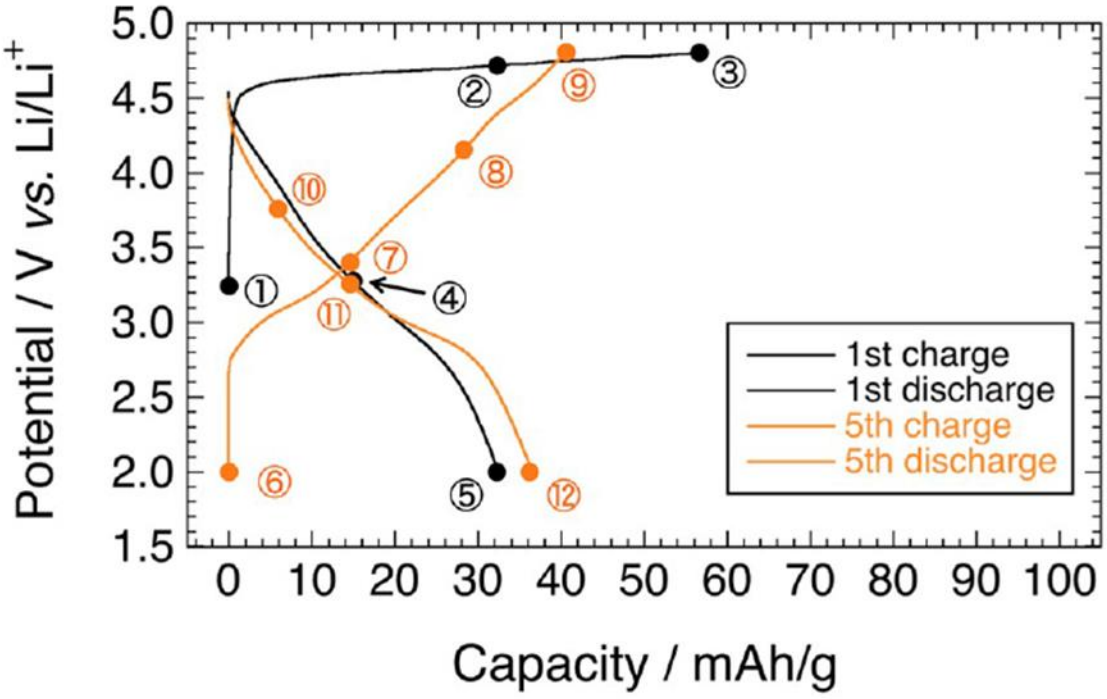

Figure 3. Charge-discharge profiles of Li_2MnO_3 electrodes for the first and fifth cycles. Sampling points for HAX-PES measurements are marked on the figure.

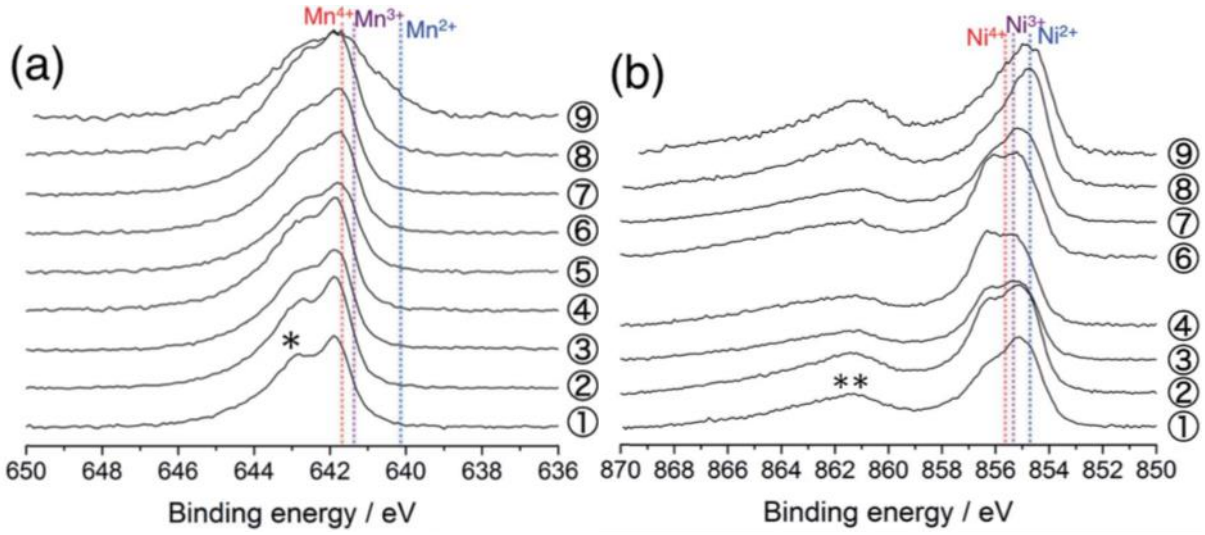

Figure 4. (a) Mn $2p_{3/2}$ and (b) Ni $2p_{3/2}$ photoelectron spectra of $Li[Li_{0.25}Ni_{0.20}Mn_{0.55}]O_{1.93}$ electrodes for the 1st cycle. The sampling points are cited from Fig. 1. The point #5 is excluded in (b) due to the acquisition failure. An asterisk in (a) and a double asterisk in (b) indicate the multiplet splitting and satellite peak, respectively. The vertical lines show the reference positions from ref. 33 and 38 rescaled with the acetylene black peak position at 284.5 eV in C 1s spectra.

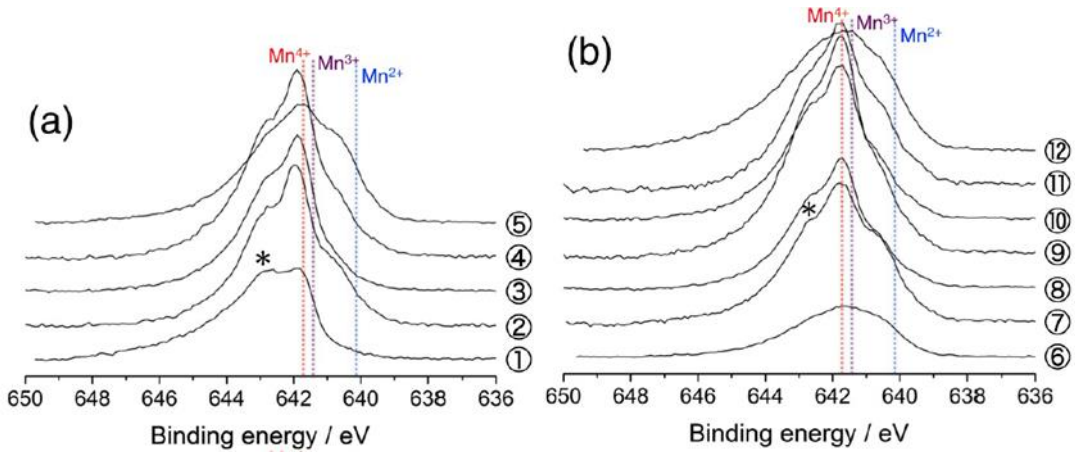

Figure 5. Mn $2p_{3/2}$ photoelectron spectra of Li_2MnO_3 electrodes for (a) the first and (b) fifth cycles. The sampling points are cited from Figure 1. Asterisks in (a) and (b) indicate the multiplet splitting. The vertical lines show the reference positions from ref. 33 in the main text rescaled with the acetylene black peak position at 284.5 eV in C 1s spectra.

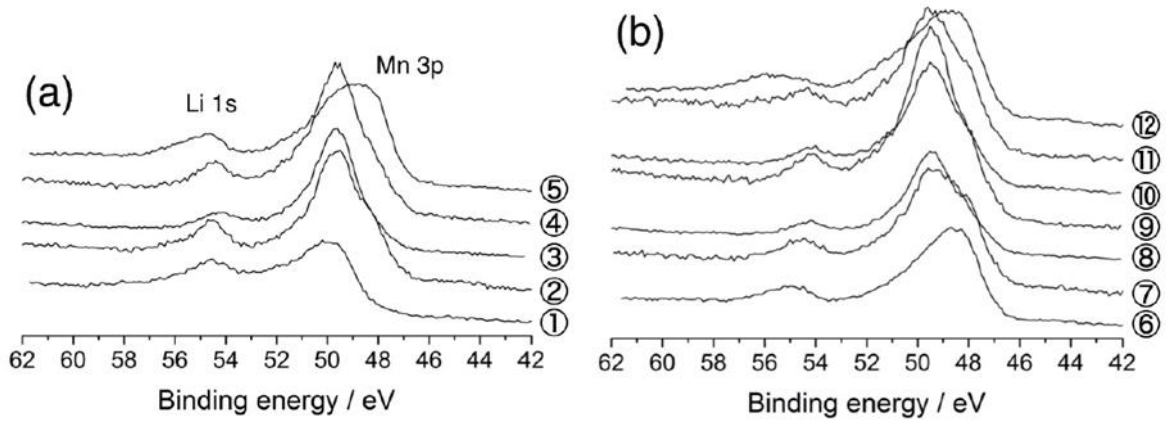

Figure 6. Li 1s and Mn 3p photoelectron spectra of Li_2MnO_3 electrodes for (a) the first and (b) fifth cycles. The sampling points are cited from Figure 1.

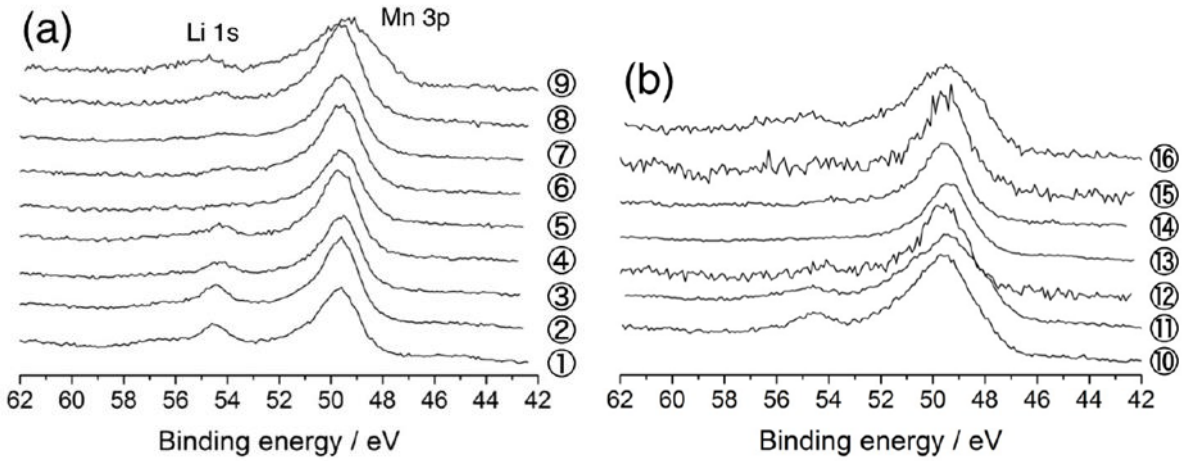

Figure 7. Li 1s and Mn 3p photoelectron spectra of $Li[Li_{0.25}Ni_{0.20}Mn_{0.55}]O_{1.93}$ electrodes for (a) the first and (b) fifth cycles. The sampling points are cited from Figure 2.

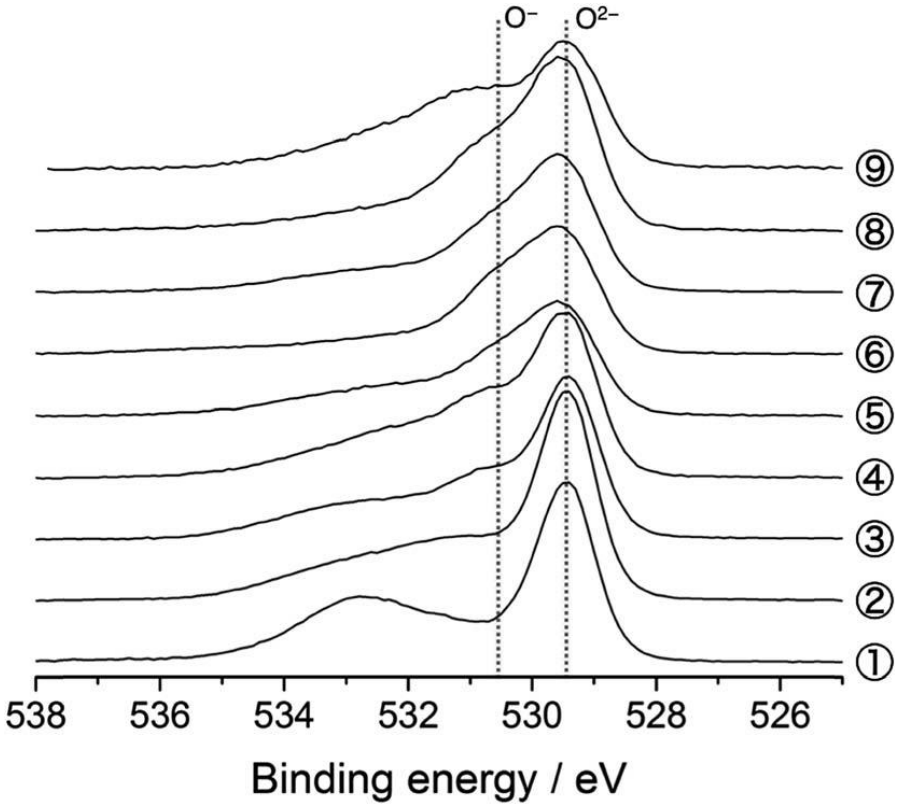

Figure 8. O 1s photoelectron spectra of $Li[Li_{0.25}Ni_{0.20}Mn_{0.55}]O_{1.93}$ electrodes for the first cycle. The sampling points are cited from Figure 2.

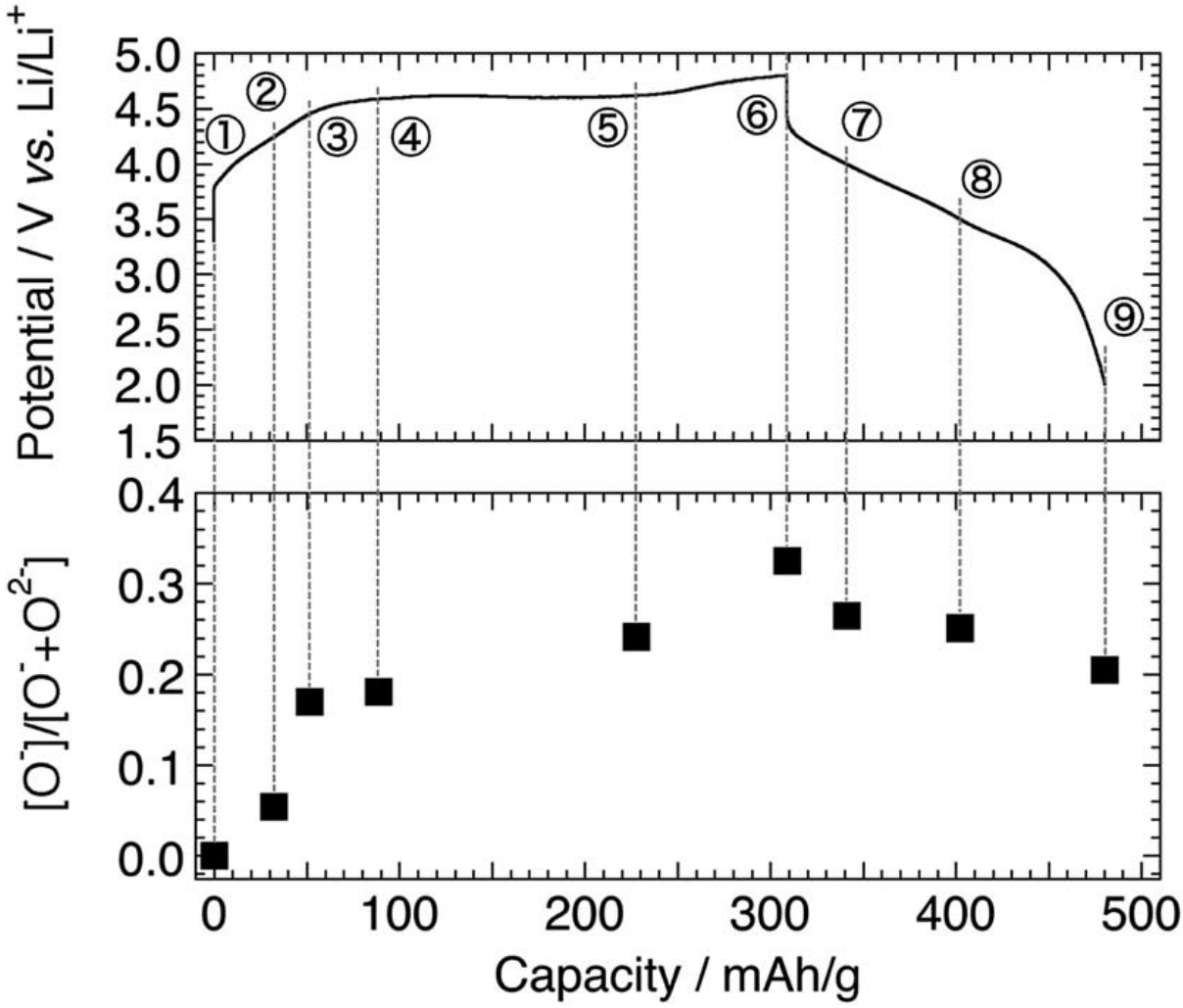

Figure 11. Intensity ratio of $[O^-]/[O^- + O^{2-}]$ in $Li[Li_{0.25}Ni_{0.20}Mn_{0.55}]O_{1.93}$ electrodes for the first cycle. The sampling points are cited from Figure 2.

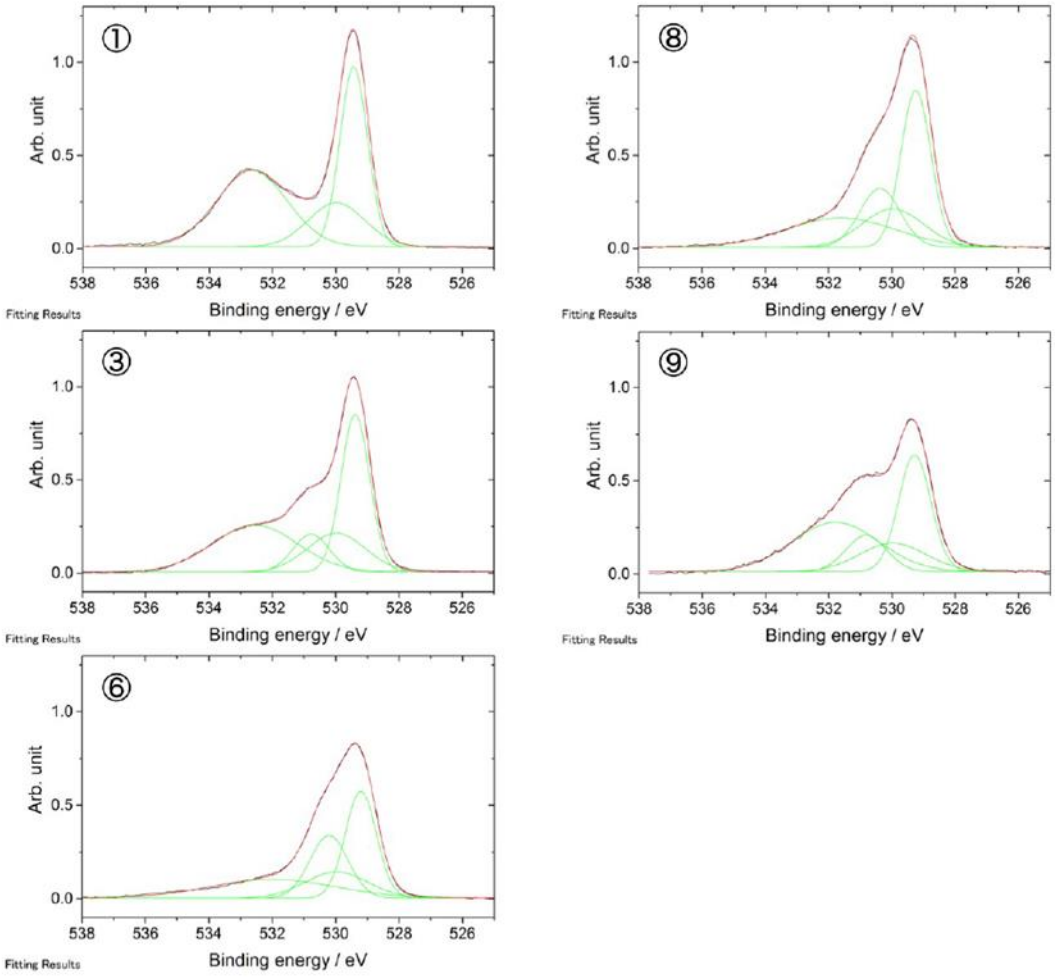

Figure 12. Examples of the O1s spectral decomposition for the first cycle. The sampling points are cited from Figure 2.

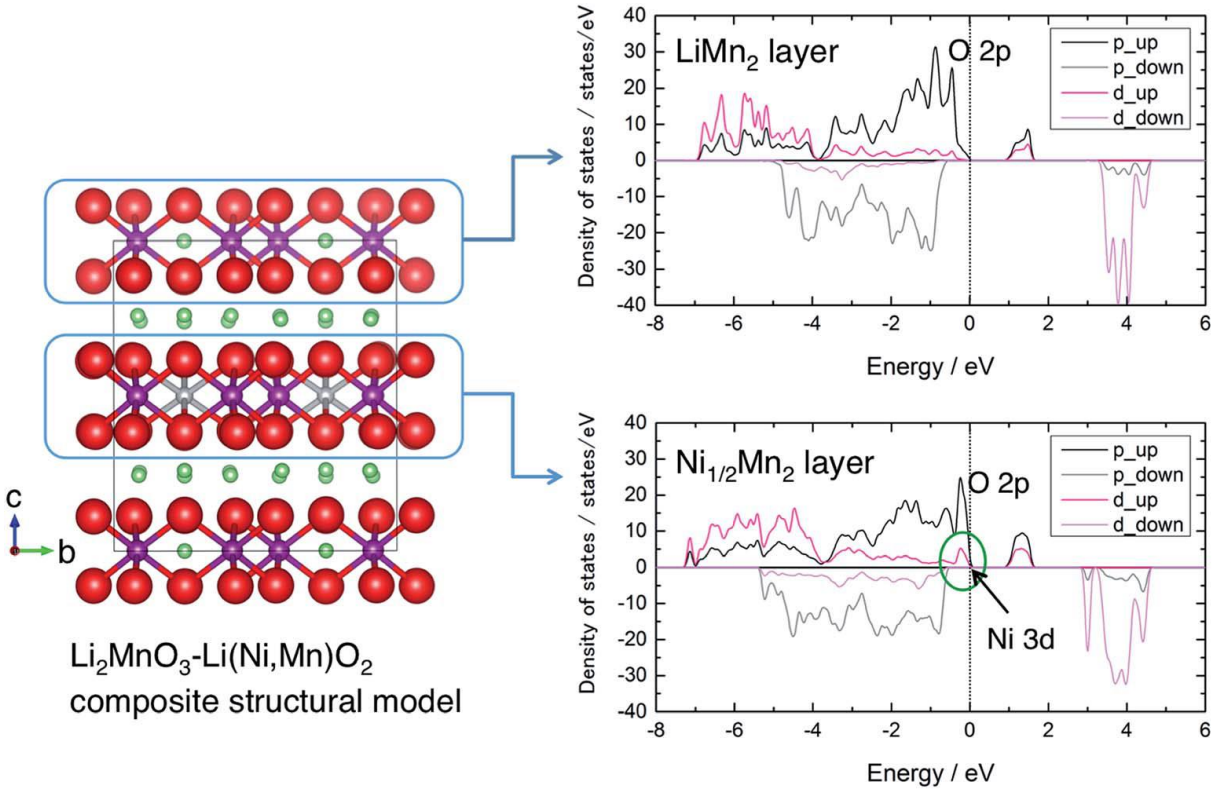

Figure 13. A Li_2MnO_3-$Li(Ni,Mn)O_2$-like composite structural model and calculated density of states of the $LiMn_2$ layer (Li_2MnO_3-like domain) and $Ni_{1/2}Mn_2$ layer ($Li(Ni,Mn)O_2$-like domain). O: red sphere, Mn: purple sphere, Ni: gray sphere, and Li: green sphere. The p and d components are almost exclusively dominated by O 2p and Ni/Mn 3d states, respectively. The "up" and "down" denote majority and minority spin states, respectively.

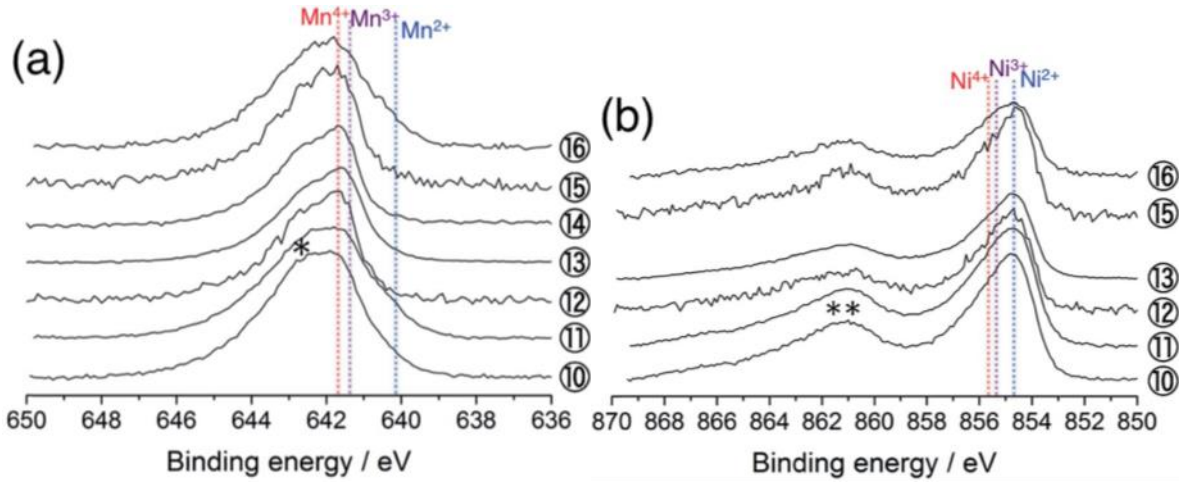

Figure 14. (a) Mn $2p_{3/2}$ and (b) Ni $2p_{3/2}$ photoelectron spectra of $Li[Li_{0.25}Ni_{0.20}Mn_{0.55}]O_{1.93}$ electrodes for the fifth cycle. The sampling points are cited from Figure 2. The point #14 is excluded in (b) due to the acquisition failure. An asterisk in (a) and a double asterisk in (b) indicate the multiplet splitting and satellite peak, respectively. The vertical lines show the reference positions from ref. 33 and 38 rescaled with the acetylene black peak position at 284.5 eV in C 1s spectra.

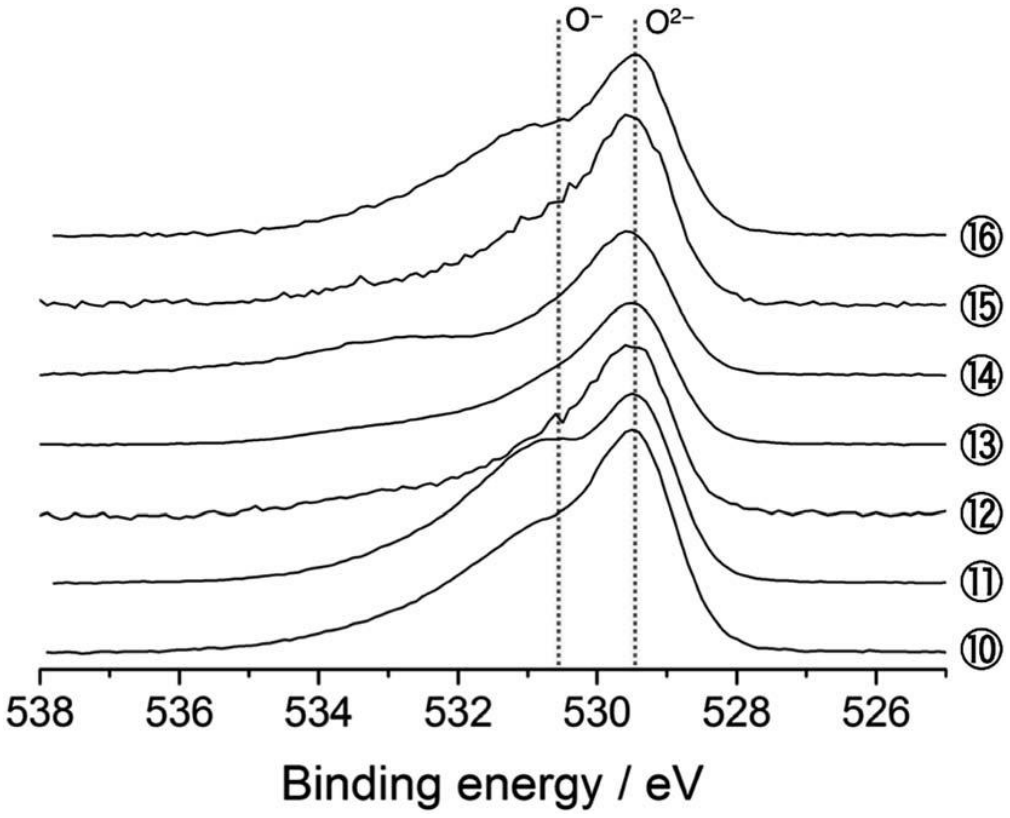

Figure 15. O 1s photoelectron spectra of $Li[Li_{0.25}Ni_{0.20}Mn_{0.55}]O_{1.93}$ electrodes for the fifth cycle. The sampling points are cited from Figure 2.

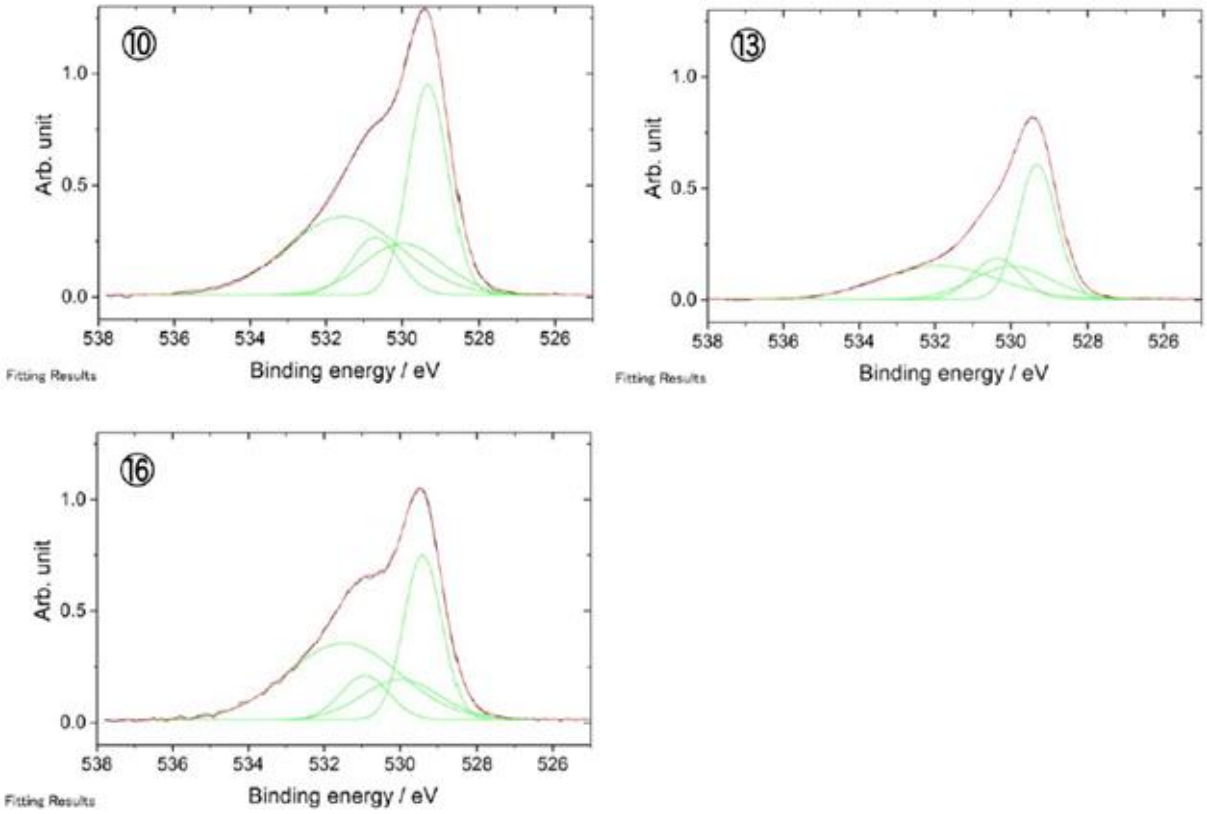

Figure 16. Examples of the O1s spectral decomposition for the fifth cycle. The sampling points are cited from Figure 2.

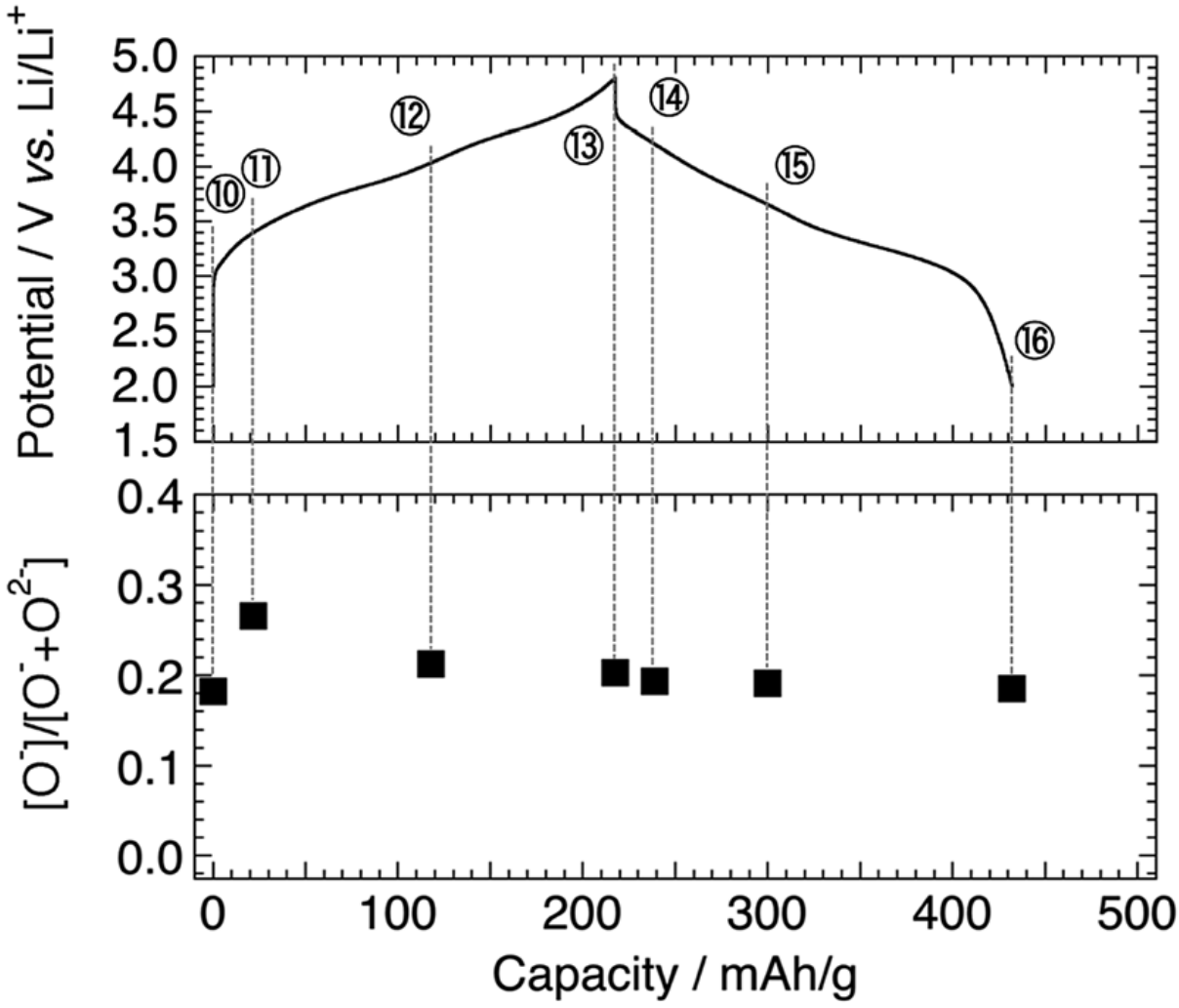

Figure 17. Intensity ratio of $[O^-]/[O^- + O^{2-}]$ in $Li[Li_{0.25}Ni_{0.20}Mn_{0.55}]O_{1.93}$ electrodes for the fifth cycle. The sampling points are cited from Figure 2.

References

[1] M. M. Thackeray, S.-H. Kang, C. S. Johnson, J. T. Vaughey, R. Benedek, S. A. Hackney, *J. Mater. Chem.* **2007**, *17*, 3112.

[2] H. Yu, H. Zhou, *J. Phys. Chem. Lett.* **2013**, *4*, 1268.

[3] Z. Lu, J. R. Dahn, *J. Electrochem. Soc.* **2002**, *149*, A815.

[4] N. Tran, L. Croguennec, M. Ménétrier, F. Weill, Ph. Biensan, C. Jordy, C. Delmas, *Chem. Mater.* **2008**, *20*, 4815.

[5] D. Y. W. Yu, K. Yanagida, Y. Kato, H. Makamura, *J. Electrochem. Soc.* **2009**, *156*, A417.

[6] A. R. Armstrong, M. Holzapfel, P. Novák, C. S. Johnson, S.-H. Kang, M. M. Thackeray, P. G. Bruce, *J. Am. Chem. Soc.* **2006**, *128*, 8694.

[7] F. La Mantia, F. Rosciano, N. Tran, P. Novák, *J. Electrochem. Soc.* **2009**, *156*, A823.

[8] P. Lanz, H. Sommer, M. Schulz-Dobrick, P. Novák, *Electrochim. Acta* **2013**, *93*, 114.

[9] E. Castel, E. J. Berg, M. El Kazzi, P. Novák, C. Villevieille, *Chem. Mater.* **2014**, *26*, 5051.

[10] M. Jiang, B. Key, Y. S. Meng, C. P. Grey, *Chem. Mater.* **2009**, *21*, 2733.

[11] N. Yabuuchi, K. Yoshii, S.-T. Myung, I. Nakai, S. Komaba, *J. Am. Chem. Soc.* **2011**, *133*, 4404.

[12] J. Kikkawa, T. Akita, M. Tabuchi, K. Tatsumi, M. Kohyama, *J. Electrochem. Soc.* **2011**, *158*, A760.

[13] Y. Koyama, I. Tanaka, M. Nagao, R. Kanno, *J. Power Sources* **2009**, *189*, 798.

[14] R. Xiao, H. Li, L. Chen, *Chem. Mater.* **2012**, *24*, 4242.

[15] M. Oishi, C. Yogi, I. Watanabe, T. Ohta, Y. Orikasa, Y. Uchimoto, Z. Ogumi, *J. Power Sources* **2015**, *276*, 89.

[16] A. M. Andersson, D. P. Abraham, R. Haasch, S. MacLaren, J. Liu, K. Amine, *J. Electrochem. Soc.* **2002**, *149*, A1358.

[17] L. Bodenes, R. Dedryvère, H. Martinez, F. Fischer, C. Tessier, J.-P. Pérès, *J. Electrochem. Soc.* **2012**, *159*, A1739.

[18] R. A. Quinlan, Y.-C. Lu, Y. Shao-Horn, A. N. Mansour, *J. Electrochem. Soc.* **2013**, *160*, A669.

[19] M. Sathiya, K. Ramesha, G. Rousse, D. Foix, D. Gonbeau, A. S. Prakash, M. L. Doublet, K. Hemalatha, J.-M. Tarascon, *Chem. Mater.* **2013**, *25*, 1121.

[20] M. Sathiya, G. Rousse, K. Ramesha, C. P. Laisa, H. Vezin, M. T. Sougrati, M.-L. Doublet, D. Foix, D. Gonbeau, W. Walker, A. S. Prakash, M. Ben Hassine, L. Dupont, J.-M. Tarascon, *Nat. Mater.* **2013**, *12*, 827.

[21] S. Han, B. Qiu, Z. Wei, Y. Xia, Z. Liu, *J. Power Sources* **2014**, *268*, 683.

[22] S. Han, Y. Xia, Z. Wei, B. Qiu, L. Pan, Q. Gu, Z. Liu, Z. Guo, *J. Mater. Chem. A* **2015**, *3*, 11930.

[23] G. Panaccione, K. Kobayashi, *Surf. Sci.* **2012**, *606*, 125.

[24] S. J. Clark, M. D. Segall, C. J. Picard, P. J. Hasnip, M. J. Probert, K. Refson, M. C. Payne, *Z. Kristallogr.* **2005**, *220*, 567.

[25] J. P. Perdew, K. Burke, M. Ernzerhof, *Phys. Rev. Lett.* **1996**, *77*, 3865.

[26] H. J. Monkhorst, J. D. Pack, *Phys. Rev. B: Condens. Matter Mater. Phys.* **1976**, *13*, 5188.

[27] R. Bader, Atoms in Molecules: *A Quantum Theory*, Oxford University Press, New York, **1990**.

[28] G. Henkelman, A. Arnaldsson, H. Jónsson, *Comput. Mater. Sci.* **2006**, *36*, 354.

[29] M. M. Thackeray, C. S. Johnson, J. T. Vaughey, N. Li, S. A. Hackney, *J. Mater. Chem.* **2005**, *15*, 2257.

[30] T. Ohzuku, M. Nagayama, K. Tsuji, K. Ariyoshi, *J. Mater. Chem.* **2011**, *21*, 10179.

[31] M. Oku, K. Hirokawa, S. Ikeda, *J. Electron Spectrosc. Relat. Phenom.* **1975**, *7*, 465.

[32] E. Regan, T. Groutso, J. B. Metson, R. Steiner, B. Ammundsen, D. Hassell, P. Pickering, *Surf. Interface Anal.* **1999**, *27*, 1064.

[33] C. Gan, H. Zhan, X. Hu, Y. Zhou, *Electrochem. Commun.* **2005**, *7*, 1318.

[34] S. Hy, J.-H. Cheng, J.-Y. Liu, C.-J. Pan, J. Rick, J.-F. Lee, J.-M. Chen, B. J. Hwang, *Chem. Mater.* **2014**, *26*, 6919.

[35] K. J. Carroll, D. Qian, C. Fell, S. Calvin, G. M. Veith, M. Chi, L. Baggetto, Y. S. Meng, *Phys. Chem. Chem. Phys.* **2013**, *15*, 11128.

[36] H. Arai, M. Tsuda, K. Saito, M. Hayashi, K. Takei, Y. Sakurai, *J. Solid State Chem.* **2002**, *163*, 340.

[37] H. Koga, L. Croguennec, M. Ménétrier, P. Mannessiez, F. Weill, C. Delmas, S. Belin, *J. Phys. Chem. C* **2014**, *118*, 5700.

[38] X. Yu, Y. Lyu, L. Gu, H. Wu, S.-M. Bak, Y. Zhou, K. Amine, S. N. Ehrlich, H. Li, K.-W. Nam, X.-Q. Yang, *Adv. Energy Mater.* **2014**, *4*, 1300950.

[39] A. Ito, Y. Sato, T. Sanada, M. Hatano, H. Horie, Y. Ohsawa, *J. Power Sources* **2011**, *196*, 6828.

[40] S. L. Qiu, L. Lin, J. Chen, M. Strongin, *Phys. Rev. B: Condens. Matter Mater. Phys.* **1990**, *41*, 7467.

[41] J.-C. Dupin, D. Gonbeau, P. Vinatier, A. Levasseur, *Phys. Chem. Chem. Phys.* **2000**, *2*, 1319.

[42] R. Younesi, M. Hahlin, F. Björefors, P. Johansson, K. Edström, *Chem. Mater.* **2013**, *25*, 77.

[43] D. Foix, M. Sathiya, E. McCalla, J.-M. Tarascon, D. Gonbeau, *J. Phys. Chem. C* **2016**, *120*, 862.

[47] A. Boulineau, L. Simonin, J.-F. Colin, E. Canévet, L. Daniel, S. Patoux, *Chem. Mater.* **2012**, *24*, 3558.

[45] H. Yu, R. Ishikawa, Y.-G. So, N. Shibata, T. Kudo, H. Zhou, Y. Ikuhara, *Angew. Chem., Int. Ed.* **2013**, *52*, 5969.

[46] A. Ito, K. Shoda, Y. Sato, M. Hatano, H. Horie, Y. Ohsawa, *J. Power Sources* **2011**, *196*, 4785.

[47] A. Boulineau, L. Simonin, J.-F. Colin, C. Bourbon, S. Patoux, *Nano Lett.* **2013**, *13*, 3857.

[48] C. Genevois, H. Koga, L. Croguennec, M. Ménétrier, C. Delmas, F. Weill, *J. Phys. Chem. C* **2015**, *119*, 75.

[49] P. Yan, A. Nie, J. Zheng, Y. Zhou, D. Lu, X. Zhang, R. Xu, I. Belharouak, X. Zu, J. Xiao, K. Amine, J. Liu, F. Gao, R. Shahbazian-Yassar, J.-G. Zhang, C.-M. Wang, *Nano Lett.* **2015**, *15*, 514.

Chapter 6. Elucidating of Transition-metal Migration Behavior for High-capacity Cathode using Operando XAS and Resonant X-ray Diffraction Spectroscopy

6.1. Introduction

Solid solutions of lithium-rich layered oxide materials (LLOs) especially lithium-rich manganese oxide (Li_2MnO_3) and other layered transition metal (TM) oxide ($LiMeO_2$, Me = Co, Ni, Al etc.) are the most featured active material for the cathode of LIBs.[1,2] A high capacity of over 280 mA h g^{-1} and comparatively stable cyclability have been reported for these solid-solution cathodes.[3] It was currently proposed that not only the involvement of introduced transition metal but also oxygen redox reaction[4-8] are its reaction mechanism.

It has also been reported that transition metal migration occurs in these materials during the first charging process when the lithium in the transition metal layer is extracted, by a scanning transmission electron microscopy (STEM) study.[9] However, it is still unclear when the transition metals migrate to which crystallographic sites. Actually, the electrochemical delithiation and lithiation processes in the first cycling process can greatly alter the whole battery behavior. For example, Ito et al. reported that a gradual charge process can reduce the irreversible capacity loss in the first charge and discharge cycle.[10-12] Elucidating the phenomena in the first cycle is therefore of great importance to realize the solid-solution cathodes. The changes in the crystal structure during the first cycle have been studied by the Rietveld analysis of synchrotron radiation or neutron radiation diffraction.[13,14] Consequently, the

disappearance of the superlattice peak is believed to be related to the rearrangement in the transition metal layer [$Li_{1/3}Mn_{2/3}$][15] and/or the formation of a stacking fault along with *c*-axis.[16] Such rearrangement in the transition metal layer presumably affects the evolution of the high capacity, temperature dependence of the performance,[15] and voltage fading phenomenon.[17] A previous X-ray absorption spectroscopy (XAS) study reported that manganese remains tetravalent and the redox reactions proceed by the valence changes of the other transition metals (*e.g.*, Ni, Co) and oxygen.[18] The combination studies of scattering and spectroscopy are complementary each other; however, it is desirable to use single analysis with both site selectivity (like scattering) and element selectivity (like spectroscopy) to understand the reaction mechanism in detail. Therefore, we attempted to semi-quantitatively comprehend the transition metal migration in Ni-substituted Li_2MnO_3 as a simple model of Li_2MeO_3 solid-solution cathodes by performing resonant X-ray diffraction spectroscopy (RXDS) analysis[19] in which element selectivity and site selectivity are respectively obtained by resonant scattering. For this purpose, operando XAS were first employed to understand the average valence changes of the constituent transition metal during the whole first cycle. Then, the RXDS analyses were further performed in the selected important conditions.

6.2. Experimental

Sample Preparation: The Ni-substituted Li_2MnO_3 was prepared by a solid-phase calcination method. The samples were prepared for contained TM ratio of $Mn_{1-x}Ni_x$ (x = 0, 0.05, 0.1, 0.25, 0.333, 0.5, 0.75, and 1). The precursors of $LiOH{\cdot}H_2O$ (Wako), $NiCO_3$ (Wako), and $MnCO_3$ (Kojundo Chemical Lab.) were mixed by zirconia ball milling in acetone for 2 h. The resulting precursors were dried at 373 K, pelletized at

5 MPa, and calcined at 1173 K for 12 h in air. As described in Section 6.3.1, the Li_2MnO_3 structure ($C2/m$) is retained in x = 0-0.25. Further increase of Ni contents resulted in the absence of the superlattice peaks and appearance of an impurity phase. Hence, we selected samples of $x \leq 0.25$ and further examined as follows. The chemical composition was analyzed by inductively coupled plasma-atomic emission spectrometry (ICP-AES, ICPS-8100, Shimadzu). The average oxidation states of the TM were determined from the iodometric titration measurements using 0.03 mol dm^{-3} $Na_2S_2O_3$ solution. Then, the oxygen contents of the materials were estimated from the ICP-AES and iodometric titration results. The chemical compositions for samples with x = 0, 0.05, 0.1, and 0.25 were determined to be $Li_{1.33}Mn_{0.67}O_{1.97}$, $Li_{1.31}Mn_{0.66}Ni_{0.04}O_{1.95}$, $Li_{1.30}Mn_{0.63}Ni_{0.07}O_{1.96}$, and $Li_{1.25}Mn_{0.56}Ni_{0.19}O_{1.93}$, respectively. These sample are here after denoted as Ni0%, Ni5%, Ni10%, and Ni25%, respectively.

Electrochemical Measurements: The charging and discharging reactions (electrochemical Li extraction-insertion) were operated in a three-electrode cell sealed with an aluminum-coated laminate. The working electrode consisting of the active material, acetylene black (Denki Kagaku Kogyo), and polyvinylidene difluoride (PVDF, Kureha) with a weight ratio of 8:1:1. The constituent mixture slurry with an N-methylpyrrolidone (NMP) solvent was spread onto an aluminum foil current corrector and dried at 353 K under vacuum for 12 h. A foil of 0.2 mm-thick metallic lithium (Honjo Metal) was used as a counter and reference electrode. All the potential values were measured versus the lithium reference electrode (vs Li/Li^+). The three electrodes were separated with a polyolefin separator. 1 mol dm^{-3} of $LiPF_6$ dissolved in anhydrous ethylene carbonate (EC) and ethyl methyl carbonate (EMC) with a volumetric ratio of 3:7 (Kishida Chemical) was used as the electrolyte in this study. The electrochemical cell was assembled in an Ar-filled glove box (<3.0 ppm oxygen). Electrochemical

measurements were performed at 298 K on an automatic cycling/data recording system (HJ1001SD8, Hokuto Denko). The cells were galvanostatically cycled ranging from 2.0 to 4.8 V at a rate of 10 mA g^{-1}. The electrode samples for ex situ measurements (X-ray diffraction (XRD), diffraction anomalous fine structure (DAFS) and electron energy loss (EEL) spectroscopy) were prepared in the same charge and discharge procedure and disassembled at desired states of charging and discharging.

XRD and Rietveld Refinements: XRD patterns were obtained using a diffractometer (SmartLab, Rigaku) with Cu Kα radiation in laboratory and also at BL02B2 in SPring-8, Hyogo, Japan. The XRD measurements performed in laboratory were obtained between 10 and 90° in 2θ at a scan rate of 1° min^{-1} equipped with a Johansson-type incident monochromator and a high-speed one-dimensional X-ray detector (D/teX Ultra, Rigaku). The synchrotron XRD measurements were performed using a large-diameter Debye-Scherrer camera with an imaging plate. The incident X-ray of 10.0 keV (0.124 nm wavelength) was used. The neutron powder diffraction data were obtained using a time-of-flight powder diffractometer (BL09 beamline, SPICA) at the Japanese Proton Accelerator Research Complex (J-PARC). The Rietveld analysis was performed by JANA[20] using XRD patterns obtained in SPring-8. Details on the refinement of crystalline structures were reported in the previous paper.[21]

STEM and EEL Spectroscopy: The atomic configuration of the sample was directly observed using an aberration-corrected (CEOS GmbH) STEM (JEM-2400FCS, JEOL Ltd.) operated at 200 kV. EEL spectra were obtained using an EEL spectrometer (Tridiem ERS, Gatan, Inc.) attached to a Wien filter monochromated aberration-corrected STEM (JEM-2400FCS, JEOL Ltd.) operated at 200 kV. EEL spectra were recorded in STEM mode, using 0.3 eV per channel. The convergence and collection semiangles were 33 and 43 mrad, respectively. Background signals of EEL spectra were

subtracted by power law fitting.

Operando XAS Measurements: In operando XAS measurements were performed by the three-electrode cell with charging and discharging at the Ni and Mn K-edges in the transmission geometry at beamline BL28XU in SPring-8 (Hyogo, Japan). Two ionization chambers were located upstream and downstream of the sample. The energy of the obtained XAS spectra was calibrated using the standard Ni and Mn foil for Ni K-edge (8.3328 keV) and Mn K-edge (6.5390 keV), respectively. The Ni and Mn K-edge spectra were measured in quick sequence with 1.5 min per spectrum and the interval of the two measurements was approximately 11 min. Since the electrochemical charge and discharge tests were conducted at the rate of 0.1C, the composition change during each measurement was less than 0.025% of the theoretical capacity.

RXDS Measurements: The RXDS measurements were conducted at beamline BL28XU, SPring-8, Japan. Transmitted XAS measurement was used for the absorption correction of the DAFS spectra. A two-dimensional Pilatus detector (Dectris Co., Ltd.) was mounted onto an arm of a multi-axis goniometer and was used to measure the diffraction profile. The DAFS spectra of Ni25% were measured from the 001 and $\bar{2}02$ diffraction peaks for Ni K-edge (8325.0-8365.0 eV) and Mn K-edge (6535.0-6575.0 eV), where the exposure time was set to over 100,000 photons to ensure accurate statistical precision. The pellet sample was rotated on the axis perpendicular to the sample surface to decrease the particle orientation. The observed diffraction peaks were integrated and then the peak intensity was determined by least-squares fitting using Toraya's split pseudo-Voigt peak function with a linear background.

The obtained DAFS spectra were analyzed by the logarithmic dispersion relation method described in detail in our previous paper.[22] The absolute values (in $-gf''$ unit) of the intensity of the DAFS spectra reflects the quantity of the selected ions in the

selected sites. The occupancy of Ni and Mn ions in the Li layer ($O_{Ni\ in\ Li}$ and $O_{Mn\ in\ Li}$) and that in the TM layer were calculated as follows

$$O_{Ni\ in\ Li} = \frac{I_{Ni\ in\ Li}}{I_{Ni\ in\ TM} + I_{Ni\ in\ Li}} g_{Ni}$$

$$O_{Mn\ in\ Li} = \frac{I_{Mn\ in\ Li}}{I_{Mn\ in\ TM} + I_{Mn\ in\ Li}} g_{Mn}$$

where $I_{Ni\ in\ Li}$ and $I_{Ni\ in\ TM}$ are the peak intensity maximum of the Ni K-edge DAFS spectra of the Li and TM layers, $I_{Mn\ in\ Li}$ and $I_{Mn\ in\ TM}$ are the peak intensity maximum of the Mn K-edge DAFS spectra of Li and TM layers, g_{Ni} and g_{Mn} are the concentration of Ni and Mn ions in the sample, respectively. Since the anomalous scattering between 001 and $\bar{2}02$ was negatively correlated, DAFS spectra of Li layer was calculated from the sum of F_{001}" and $F_{\bar{2}02}$". DAFS spectra of TM layer was also calculated from the difference of F_{001}" and $F_{\bar{2}02}$".

6.3. Results and Discussion

6.3.1. Crystal Structure

The crystal structure of the prepared samples was analyzed by XRD. The XRD pattern (obtained by Cu Kα X-ray source) of Ni0%, Ni3%, Ni25%, Ni50%, Ni75%, and Ni100% are shown in Figure 1. The XRD pattern of Li_2MnO_3 (Ni0%) is identical with that reported in the previous work.[23] The crystal structure of Li_2MnO_3 has Li and TM ion layers, in which the TM ion layers has an ordered atomic arrangement of Li ions at the 2*b* site and Mn ions at the 4*g* site in the space group *C*2/*m*. The changes in the XRD

pattern with the increasing Ni content can be typically seen at the 2θ region between 63.0 and 66.0°. In this region, $13\bar{3}$, 202 and $33\bar{1}$ peaks are observed at 2θ = 64.6, 64.7 and 65.6°. Though there are small peak angle shifts with the increasing nickel content, no appearance of impurity phases was observed for Ni25%, suggesting that Ni ions are introduced into the Li_2MnO_3 framework and that the superlattice structure represented by the *C*2/*m* space group is kept until Ni25%. We selected Ni25% to understand the activation behavior of the Li-rich system.

Rietveld refinement results were described in chapter 4.[21] We confirmed the substitution of Ni ions in the Li_2MnO_3 structure for Ni25%. Table 1 shows the structural parameters obtained from the Rietveld refinement of the XRD and neutron diffraction pattern. The composition obtained from the ICP-AES and the iodometric titration measurements was used for the refinement. The best refinement was obtained for the space group of *C*2/*m* with Ni ions occupying the 2*b* (replacing Li ion) and 4*g* (replacing Mn ion) sites with the occupancy of 0.259(1) and 0.160, as shown in Table 1. The hard X-ray photoemission spectroscopy (HAX-PES) measurement of this sample[24] indicates that it contains Ni^{2+} (with minor Ni^{3+}) and Mn^{4+}, which agree with the result of the chemical composition analysis.

Furthermore, the atomic alignments of Ni25% were directly analyzed by high-angle annular dark-field (HAADF) STEM and EEL spectroscopy. HAADF STEM can yield images in which the brightness can be directly correlated to the atomic number Z (it is approximately proportional to the square of Z). Figure 2a shows a typical HAADF STEM image obtained from Ni25%. The bright contrasts show the positions of TM (Mn and Ni) atomic columns in the sample. The EEL spectra obtained from the TM layer (Figure 2b) showed peaks around 650, 660, 860, and 880 eV. The former two and later two peaks are Mn-$L_{2,3}$ and Ni-$L_{2,3}$ edges, respectively. The EEL suggest that Ni is

homogeneously substituted in the TM layer regardless of the degree of ordering in the superlattice.

6.3.2. Electrochemical Behavior of Ni Introduced Li_2MnO_3

Figure 3 shows the charging and discharging curves in the first cycle and the corresponding dQ/dV curves obtained at a rate of 10 mA g^{-1}. The first charge and discharge capacity of Li_2MnO_3 were 90 and 45 mA h g^{-1}, respectively. The observed charging and discharging behaviors matched with previous reports of the Li_2MnO_3 electrodes.[25] The charging and discharging capacities increased with the increase the Ni contents and they reached 375 and 190 mA h g^{-1} for Ni25%.

The dQ/dV curves typically show how the discharging process is enhanced by Ni substitution for Mn in the Li_2MnO_3 structure, with some peak intensities at 3.4, 3.75, and 4.1 V (vs Li/Li^+) apparently increasing with the Ni content. Croy *et al.* reported that the dQ/dV curves of a Ni-Mg-substituted Li_2MnO_3 cathode have hysteresis peaks at 4.3 and 3.4 V in charging and discharging processes,[26] which is also confirmed in our results. Ni25% showed a stable cycle capacity as shown in Figure 4. The discharge capacity in 20th cycle was over 200 mA h g^{-1}. The cyclability of Li_2MnO_3 is almost unstable operating at room temperature.[8,25,27] It is suggested that the Ni substitution activates the inactive Li_2MnO_3 phase and stabilizes the crystal structure during the charging and discharging reactions.

6.3.3. Element-Selective Analysis by XAS

The XAS measurements were performed to understand the change of the

electronic structure and the local structure of Ni and Mn during the first charging and discharging processes of Ni25%. The obtained Ni K-edge spectra and the edge energy at μt = 1 are shown in Figure 5.

The changes of the Ni K-edge XAS spectra are divided into four regions in Figure 5f. At the beginning of the charging process where the potential in the charge curve change from 3.0 to 4.5 V (vs Li/Li^+), the edge energy of the Ni K-edge XAS spectra showed constant shifts to higher energy to 8344.0 eV, which is caused by the oxidation of Ni ions.[28] The degree of edge shift towards higher energy slightly decreased during 4.5- 4.7 V (vs Li/Li^+) as shown in Figure 5b. It is suggested that the multiple reactions occurred simultaneously for charge compensation. In the latter half of charging, the potential was stable at around 4.7 V and, the edge energy stayed at 8344.6 eV without significant changes, suggesting that the Ni oxidation state was unchanged as shown in Figure 5f. At the end of charging where the charge potential shifted from 4.7 to 4.8 V (vs Li/Li^+), the edge energy shifted to lower values from 8344.6 to 8344.1 eV as shown in Figure 5c. The low energy shift of the edge energy at the end of the charging process have also been reported in the previous study of Li-rich layer cathode materials.[18] This low energy shift can be ascribed to the reduction of Ni ions, although the charging (Li extraction) reaction proceeds. Some species other than Ni ions should be oxidized to compensate the charge changes of the electrode.

In the discharging process, the Ni K-edge energy changed almost linearly from 8344.1 to 8342.6 eV as shown in Figure 2d. The final edge energy after discharging (8342.6 eV) was slightly lower than that before charging (8342.9 eV). In addition, the spectrum shapes were not identical as shown in Figure 5a; there was a shoulder peak at 8335.5 eV in the spectrum before charging whereas such a peak was not observed after discharging. Since this shoulder peak reflects the coordination environments of

Ni ions,[29,30] this result suggests the irreversible change of the coordination environments surrounding Ni ions.

The obtained Mn K-edge XAS spectra of Ni25% in the first charging and discharging cycle are shown in Figure 6. The spectra did not show any clear shift in the edge energy, reflecting the unchanged oxidation state of the Mn ions during the charging and discharging processes.[18] It has been that, in addition to that of nickel, the oxidation of oxygen (O^{2-} to O^{-} species) contributes to the charge compensation of the electrode, which has been shown by using XPS, ESR, XAS, and HAX-PES.[4,8,24] The shape of Mn K-edge XAS spectra changed in the pre-edge and jump-edge regions during the first charging and discharging processes as shown in Figure 6e,f, which suggests the change of the coordination environments of Mn ions during the charging and discharging processes.

6.3.4. Site-Selective Analysis by RXDS

Diffraction anomalous near-edge structure (DANES) spectra obtained from the RXDS analysis corresponds to X-ray absorption near-edge structure spectra, which reflects the electric and local structures of the observed elements at certain crystal graphical sites in a semi-quantitative manner,[22] and therefore, is suitable to analyze the behavior of Ni and Mn ions in our sample during charging and discharging.

The Ni K-edge DANES spectra are shown in Figure 7. The different spectra in the Li and TM layers indicate the different coordination environments of Ni ions; the DANES spectrum in the Li layer was basically of the same shape as that in the previous report about the simulated data by Yabuuchi *et al.*[30] As there was no negative shift in the energy of the Ni ions in the TM layer during charging, the reduction of the Ni ions

at the end of charging observed in the XAFS measurement can be related to the migration of Ni to the Li layer. That is, Ni ions are reduced to Ni^{2+} to be accommodated to the Li layer. Thus, the migration of the Ni ions in the Li layer suggests that it selectively occurred at the end of the charging region (4.7-4.8 V). During the discharging process, Ni ions in the Li layer are irreversible atoms due to only partly re-migrated to the TM layer. Throughout the first cycling, the Ni ions in the Li layer do not contribute to charge transfer since there is no energy shift in the DANES spectra, though their coordination environment seems to change to some extent.

Figure 8 shows the Mn K-edge DANES spectra in the TM and Li layers. The analysis result of the initial powder sample is not obtained in the Li layer site. The Mn K-edge XAFS results suggested that the coordination environment of the Mn ions is changed during the charging and discharging processes. The interlayer migration is confirmed at charging to 4.8 V as shown in Figure 8c. Furthermore, more than 10% of the Mn ions once migrated to the Li layer. Although the DANES spectra in the Li layer is slightly not clear at charging to 4.8 V, the edge jumping can certainly be confirmed as shown in Figure 9. Then they almost re-migrate to the TM layer at the end of discharging. The edge energy of the Mn K-edge DANES spectrum in the TM layer did not show significant changes, indicating that their oxidation states remained unchanged.

The average cation valence and the occupancy of the transition metal in each site at each potential are shown in Table 2. The trends in the cation migration in Table 2 are extracted and shown in Figure 10. On the basis of these changes in the electron structure and site occupancy of each transition metal, the unique electrochemical characteristics of the Li-rich cathodes can be elucidated, as shown in the following.

Before the charging process, the Ni ions are mainly located in the TM layers. The oxidation states of Ni ions in both Li and TM layers are mostly 2+. Mn ions are located

only in the TM layer with the oxidation state of 4+. During charging to 4.32 V (before irreversible plateau region), Ni ions in the TM layer are oxidized while the oxidation states of Mn ions are unchanged, and no appreciable migration of Ni and Mn ions occurs. During the charging to 4.7 V, Mn ions migrate to the Li layer. Ni ions also migrate to the Li layer with a reduction during the end of charging region to 4.7-4.8 V. Above 4.3 V to the end of charging, the oxidation of O ions to O^- ions occurs described in chapter 5.[24]

During discharging to 4.0 V, Ni and Mn ions continue migrating to the Li layers and the Ni ions remaining in the TM layer are reduced. The oxidation state of Mn ions remaining in the TM layer do not significantly change. During discharging to 3.5 V, Ni and Mn ions re-migrate to the TM layer. During the discharging to 2.0 V, Ni and Mn ions further re-migrate to the TM layer and all the Mn ions return to the TM layer while 3.5% of the Li layer is still occupied by the Ni ions as shown in Figure 10. During the discharging process, the reduction of O^- is also observed, however, the amount of O^{2-} produced by the reduction is smaller than that before charging.[24] The reduction of the Ni ion unit in the TM layer mainly contributes to the charge compensation of the electrode in the discharging processes.

Figure 11 shows a schematic illustration of the reaction mechanism of Ni25% during first charging and discharging processes. The increase in the charge-discharge capacity and cycle stability by the Ni substitution indicates the important role of the transition metal substitution in the solid-solution cathode. The irreversible change of the crystal structure of the Li-rich manganese materials during charging and discharging processes causes the degradation of the capacity and the energy of the LIBs containing it.[31] The irreversible changes of the crystal structure during the charging and discharging processes are clearly observed in the disappearance of the superlattice

peaks in the XRD and in the change of potential profiles as shown in the previous report.[32] It should be noted that the role of the transition metal ions in Ni25% is significantly different from that of $LiNi_{1/3}Co_{1/3}Mn_{1/3}O_2$, a layered active material also containing Ni and Mn ions. For $LiNi_{1/3}Co_{1/3}Mn_{1/3}O_2$, Mn ions stays in the TM layer and stabilize the layered structure[31] while the Ni ions undergo the oxidation state changes (between 2+ and 4+) for charge compensation of the electrode.[33] In contrast, Mn ions migrate to the Li layer for Ni25%. Nevertheless, since Mn ions can re-migrate to the TM layer, it seems that Mn ions contribute to minimize the irreversible Ni migration to the Li layer and enhance the reversibility of the electrode. However, irreversible capacity of approximately 180 mA h g^{-1} was also confirmed at the first charging process. Given that the previous reports, their capacity loss is assigned to oxygen loss in the structure.[32] Therefore, the effective utilization of oxygen in the material is inadequate with the substitution of only Ni.

Here, we try to assign the reversible capacity to each redox element. The main contribution is by nickel with their capacity of 132 mA h g^{-1}. Most of the rest redox component is oxygen with their capacity of approximately 70 mA h g^{-1}. Interestingly, since this can be correlated to the amount of the Mn ions that migrate to the Li layer with one-electron charge transfer, it is deduced that the oxygen oxidation and manganese migration simultaneously occur, and it seems that the oxygen bound to the MnO_6 units in the Li layer is oxidized.

Finally, based on our results, we would like to suggest ideas to improve the cycling performance of the Li-rich cathodes containing Ni and Mn ions. It has been shown that Ni migration to the Li layer leads to the irreversible change of the crystal structure and deactivates the redox reaction of the Ni ions, both of which cause the deterioration of the battery performances. Therefore, it is desirable for obtaining high

capacity to suppress this Ni migration to the Li layer either by material chemistry or by a sophisticated charging process. The latter method can be related to the suppressed irreversibility of the Li-rich material by a gradual charging sequence reported by Ito *et al.*[10,11] Further RXDS analysis will clarify the behavior and roles of the TMs in these materials and contribute to the realization of the optimized electrode materials.

6.4. Conclusions

In this work, to understand the role of the TM-substituted Li_2MnO_3 phase in solid-solution cathode, the reaction mechanism during charging and discharging processes of Ni-substituted Li_2MnO_3 was investigated by element- and site-selective analyses of the electronic and the local structures using XAS and RXDS. The substitutions of the Ni ion activate Li_2MnO_3 for the extraction and insertion of the Li ions. The Ni ions in the TM layer have contributions for charge compensation during the charging and discharging processes. A part of the Ni ions migrates to the Li layer during the charging and discharging processes. The migration is an irreversible reaction. The Ni ions in the Li layer do not contribute to the charge compensation of the electrode. In contrast, the oxidation states of the Mn ions in the TM layer is unchanged during the charging and discharging processes. A part of the Mn ions migrates to the Li layer as well as the Ni ions, however, all the Mn ions migrated to the Li layer re-migrate to the TM layer during the discharging processes. The Ni and Mn ions in the Li layer suppress the irreversible changes of the crystal structure of $Li_2Mn_{1-x}Ni_xO_3$, which leads to the increase of the charging and discharging capacities and cyclability. Remigration of the Mn ions to form the Li vacancy also contributes to the increase of the discharge capacity. The analysis of reaction mechanisms by combination of XAS and RXDS

clarify the new aspect of the layered cathode that shows complex structure changes during the charging and discharging processes. We believe that our results will be very useful for designing new cathodes for LIBs having high capacity and cyclability.

Table 1. The average cation valence and the occupancy of the transition metal at each potential of Ni25%.

	Li in Li_xMeO_3	**Capacity mAh g^{-1}**	**Average Oxidation State of Ni**	**Cation mixing ratio in Li layer**	
				Ni	Mn
pristine	1.95	-	2.3	1.4	0
4.32 V	1.76	51	3.4	1.7	0
4.8 V	0.65	358	3.7	2.9	8.9
4.0 V	0.77	35	3.2	4.1	10.7
3.5 V	1.0	96	2.4	3.8	4.4
2.0 V	1.34	191	2.0	3.2	0

Table 2. Rietveld Refinement of Ni25%

atom	site	x	y	z	occupancy
Li	2b	0	1/2	0	0.500
Mn					0.236(2)
Ni					0.259(1)
Li	2c	0	0	1/2	1
Mn					0
Ni					0
Li	4h	0	0.6512(2)	1/2	1
Mn					0
Ni					0
Li	4g	0	0.16789	0	0.124
Mn					0.716
Ni					0.160
O	4i	0.2215(2)	0	0.2286(2)	0.991(2)
O	8j	0.2497(2)	0.32320(6)	0.22274(9)	0949

[a] a: 4.945(2) Å, b: 8.558(3) Å, c: 5.028(2) Å, β: 109.2607(4)°, R_{wp}: 4.72%, R_e: 1.08%.

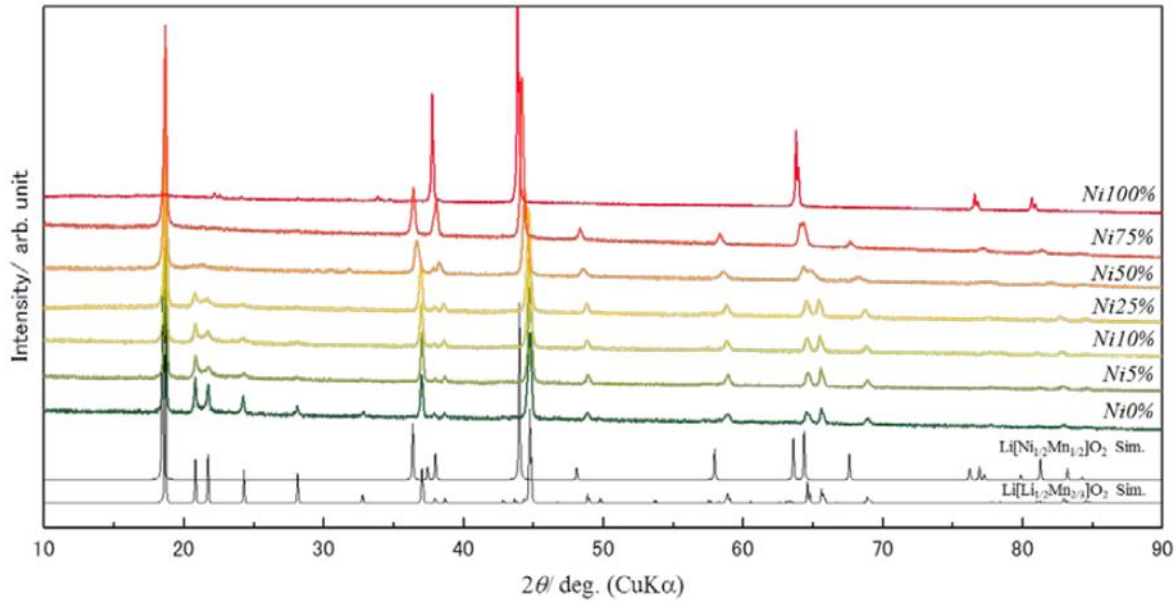

Figure 1. The XRD pattern (obtained by Cu Kα X-ray source) of Ni0%, Ni5%, Ni10%, Ni25%, Ni50%, Ni75% and Ni100%.

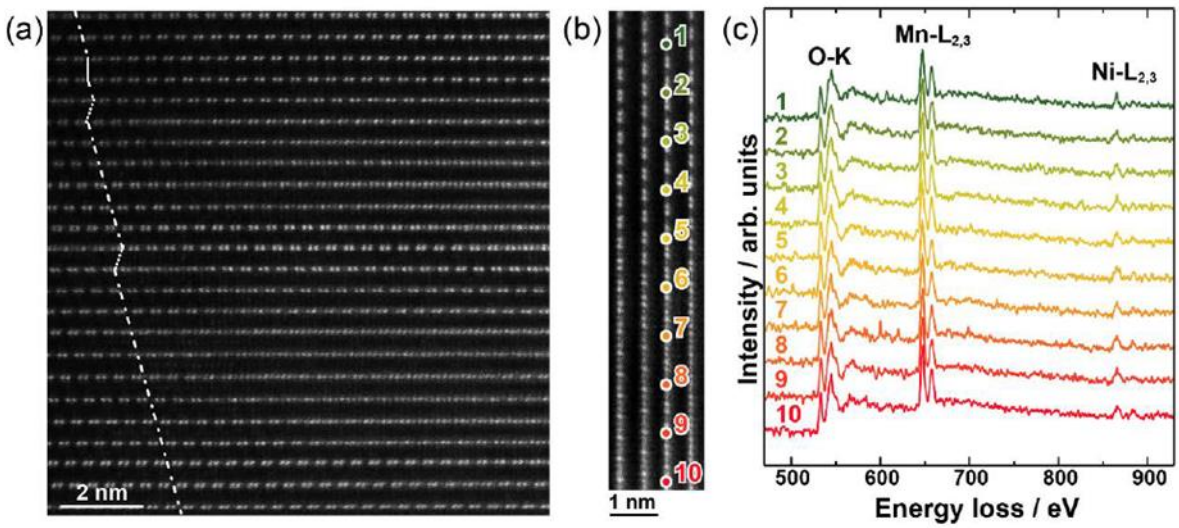

Figure 2. (a) HAADF STEM image of Ni25% viewed along the [100], [110], and [1$\bar{1}$0] zone axes, which are indicated by the solid, dashed, and dashed-dotted lines, respectively. (b) ADF STEM image with line profile step positions numbered (6-7: cation mixing in the TM layer). (c) O-K, Mn-L2,3 and Ni-L2,3 edge EEL spectra obtained from numbered points in (b).

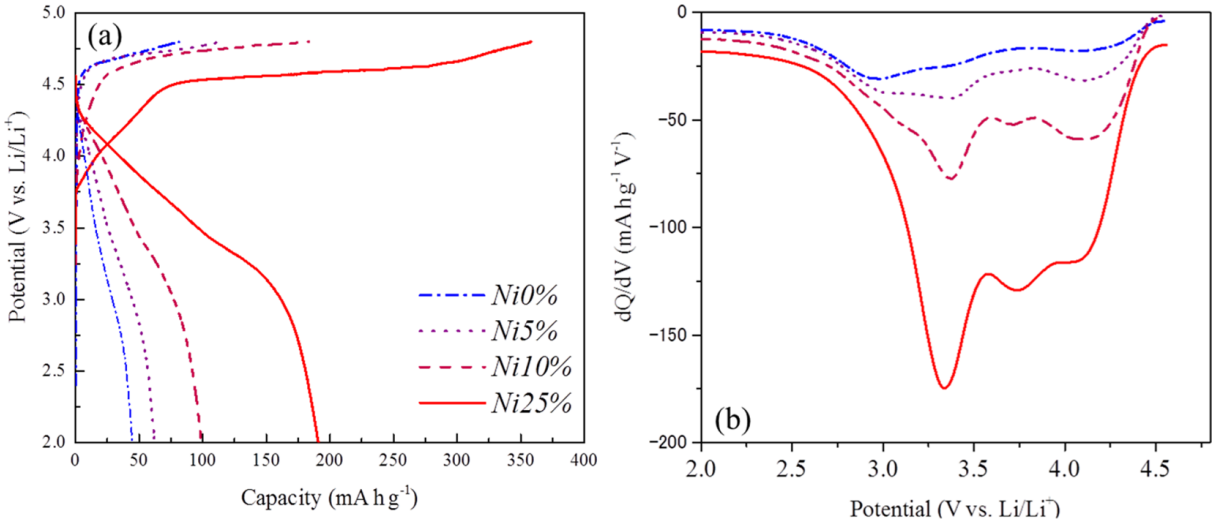

Figure 3. Electrochemical properties (a) first charging and discharging profiles, (b) dQ/dV curves of Li_2MnO_3 substituted with Ni.

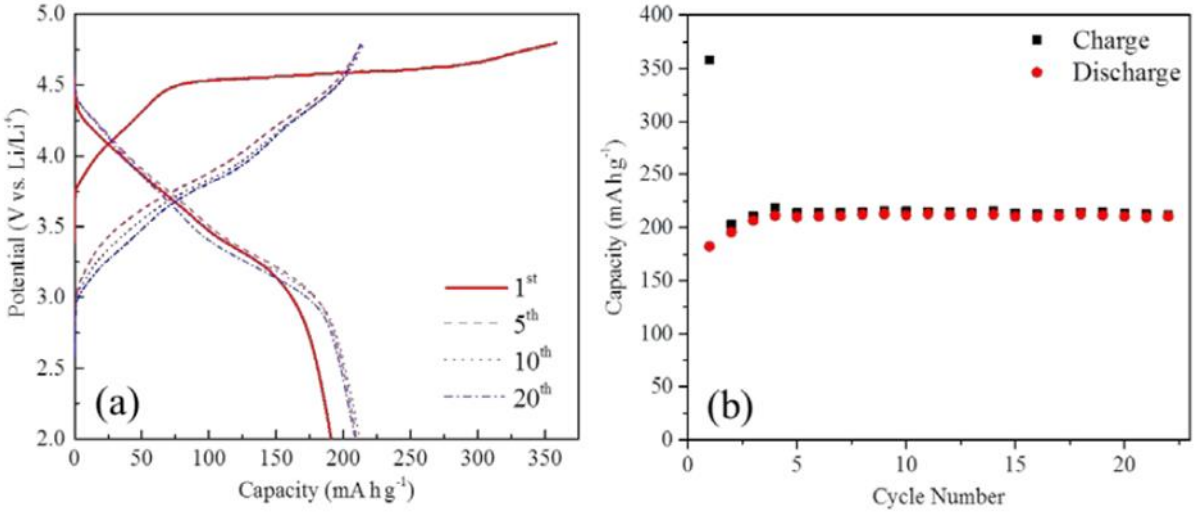

Figure 4. Charge and discharge curve (a) in different cycles and (b) cycle performance of Ni25%. Charging and discharging were operated at 1/50 C (1 C = 412 mA g^{-1}) between 4.8 and 2.0 V.

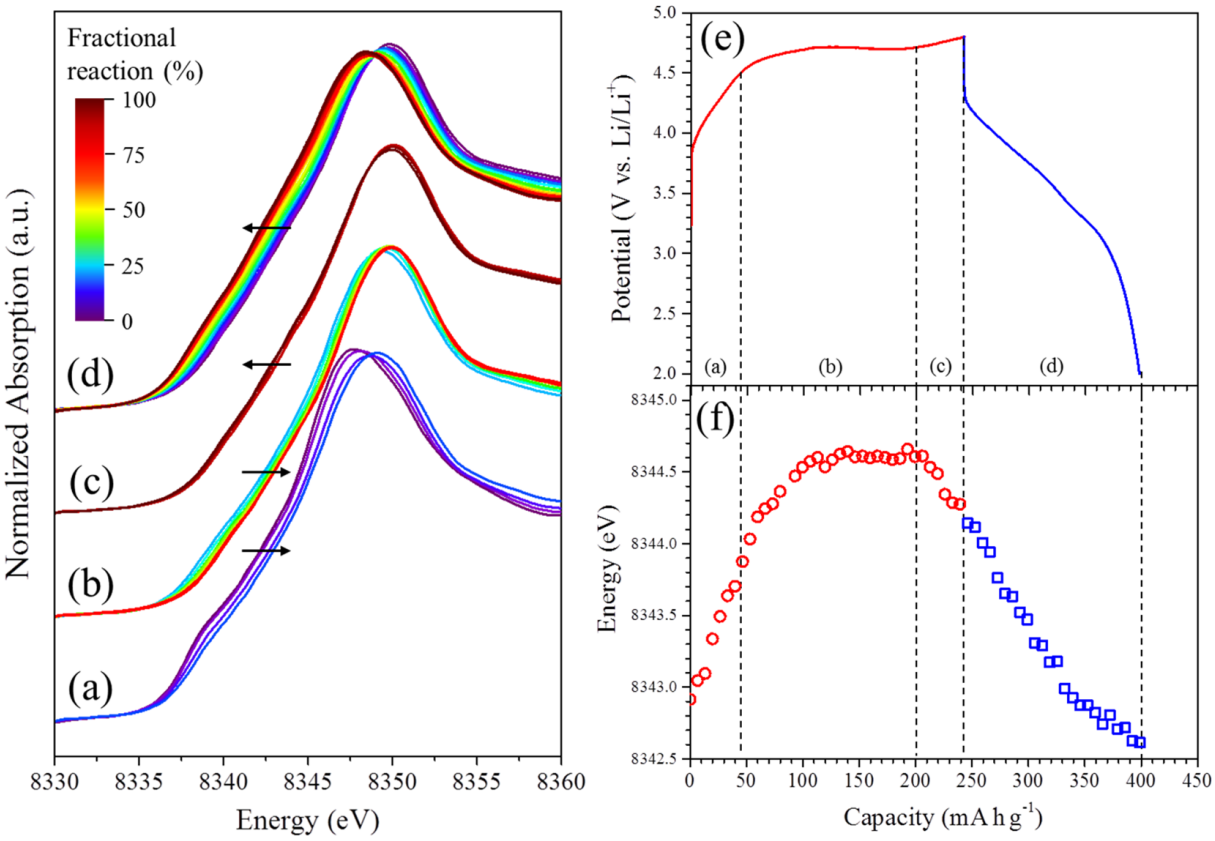

Figure 5. Operando Ni K-edge XAS spectra at (a) first charging to 4.5 V, (b) irreversible plateau region, (c) end of charging region 4.7-4.8 V, (d) discharging to 2.0 V, (e) charging and discharging profiles, and (f) plots of μt = 1 at Ni K-edge XAS spectra. The fractional reaction is defined by the achieved capacity at each process.

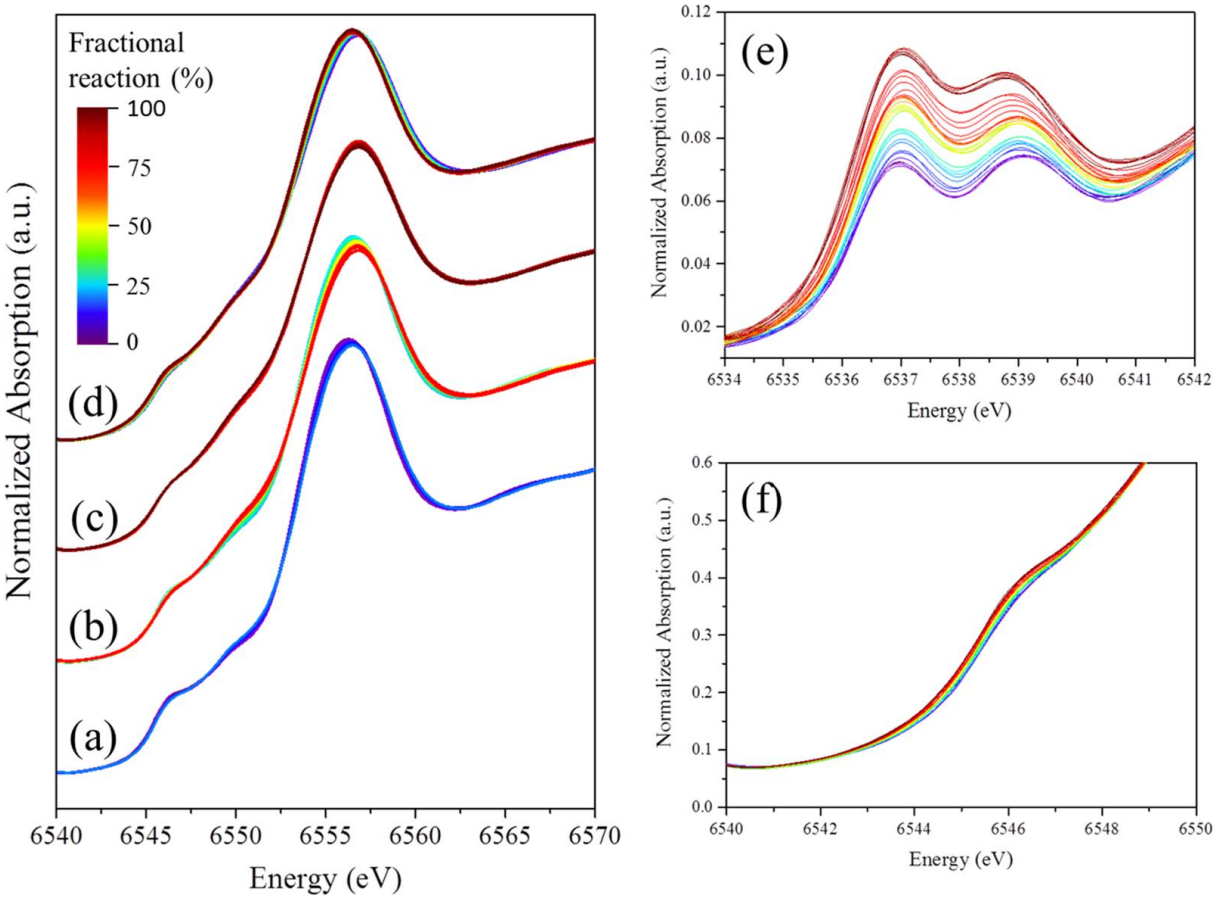

Figure 6. Operando Mn K-edge XAS spectra at (a) first charging to 4.5 V, (b) irreversible plateau region, (c) end of charging region 4.7-4.8 V, (d) discharging to 2.0 V, (e) pre-edge at first charging, (f) and jump-edge at first discharging to 2.0 V.

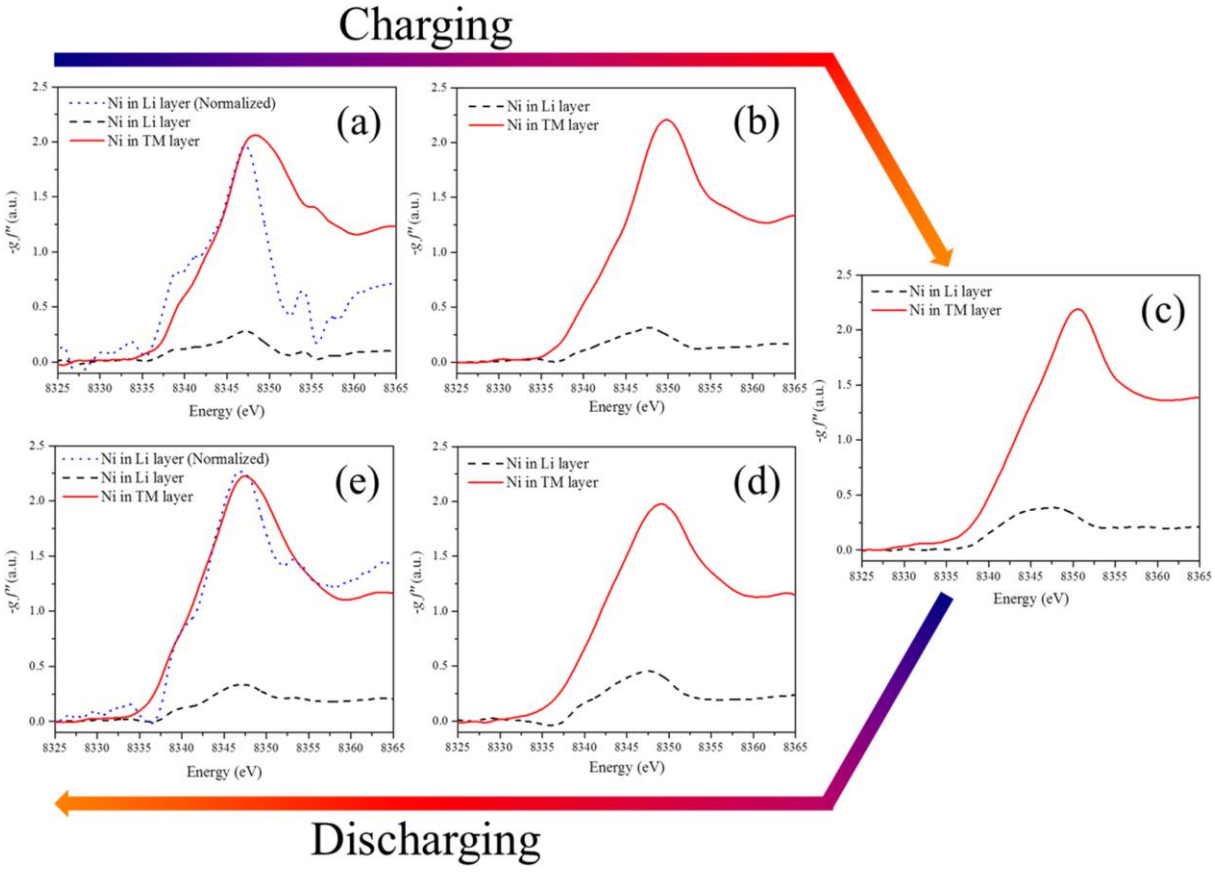

Figure 7. Ni-DANES spectra at first charging and discharging, (a) initial powder, (b) charging to 4.32 V, (c) charging to 4.8 V, (d) discharging to 3.5 V, and (e) discharging to 2.0 V.

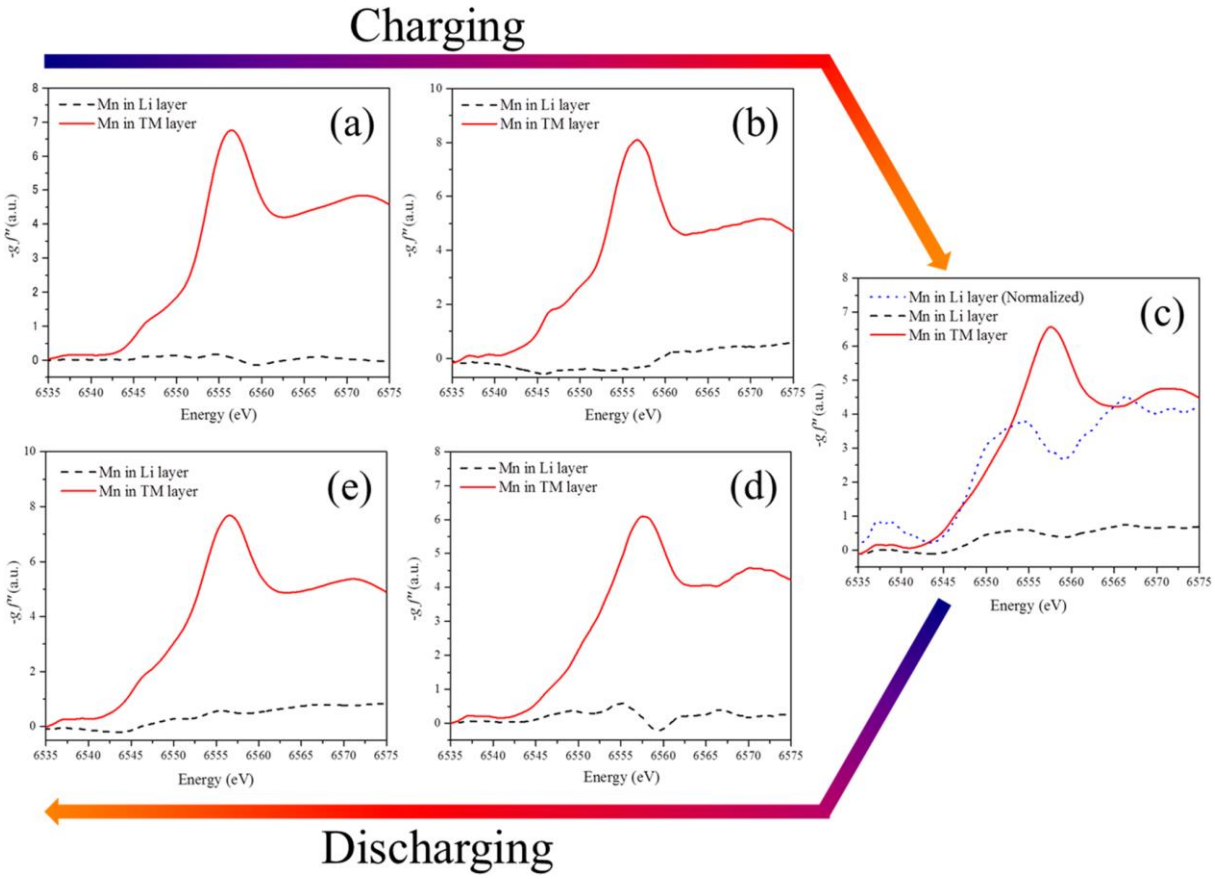

Figure 8. Mn-DANES spectra at first charging and discharging, (a) initial powder, (b) charging to 4.32 V, (c) charging to 4.8 V, (d) discharging to 3.5 V and (e) discharging to 2.0 V.

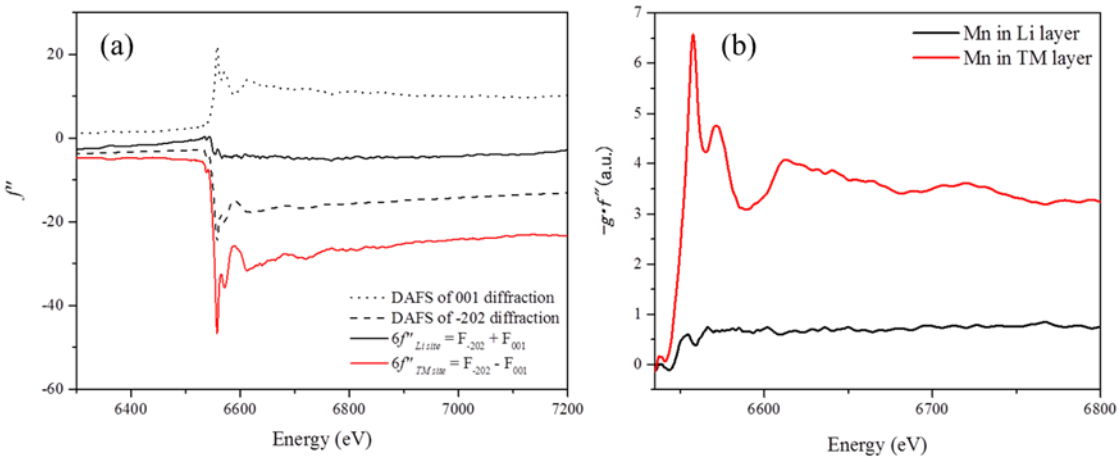

Figure 9. Analytical method of semi-quantitatively XDS (a) DAFS spectrum obtained from Mn 001 and $\bar{2}02$ diffraction, and (b) EDAFS of Mn in Li layer site (black line) and Mn in TM layer site (red line). Mn in Li layer site was obtained from the sum of $F_{\bar{2}02}$ and F001 DAFS spectra. Mn in TM layer site was obtained from the difference in $F_{\bar{2}02}$ and F001 DAFS spectra.

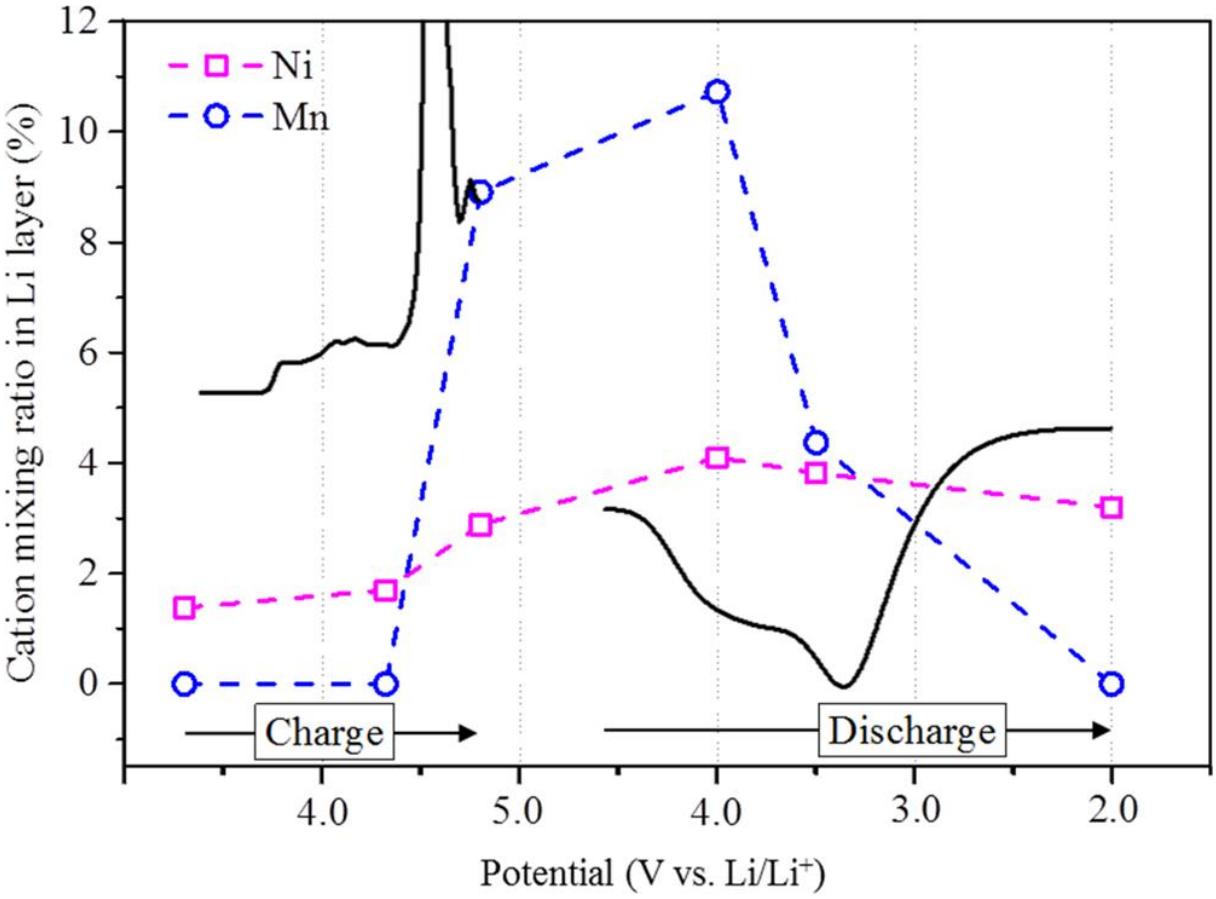

Figure 10. Plots of the amount of cation mixing ratio in the Li layer site and dQ/dV curves at first charging and discharging. The cation mixing ratio means the amount of each atom in the Li layer for each total quantity.

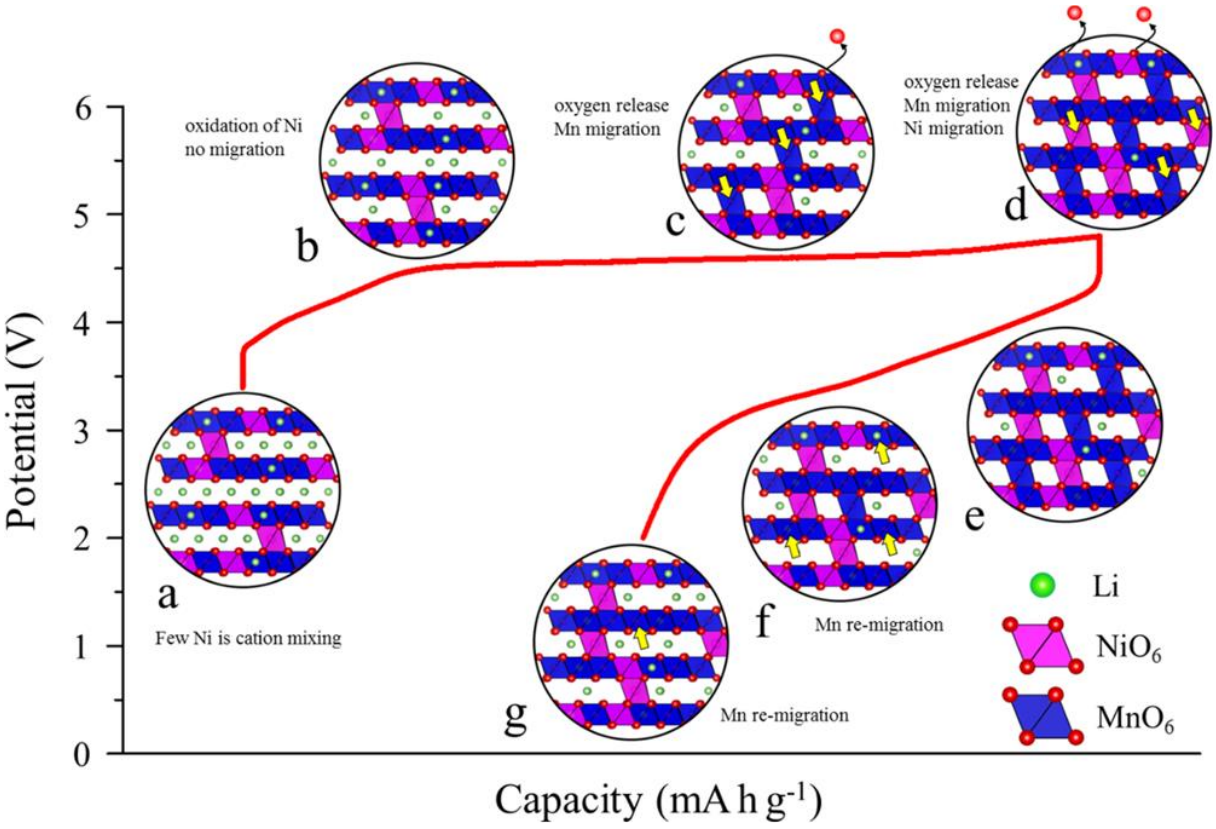

Figure 11. Reaction scheme of Li-rich manganese oxide materials introduced in Ni, (a) initial powder, (b) before plateau, (c) plateau region, (d) charging to 4.8 V, (e) discharging to 4.0 V, (f) discharging to 3.5 V, and (g) discharging to 2.0 V, respectively.

Reference

[1] H. Yu, H. Zhou, *J. Phys. Chem. Lett.* **2013**, *4*, 1268.

[2] P. Rozier, J. M. Tarascon, *J. Electrochem. Soc.* **2015**, *162*, A2490

[3] Z. Lu, J. R. Dahn, *J. Electrochem. Soc.* **2002**, *149*, A815.

[4] M. Sathiya, K. Ramesha, G. Rousse, D. Foix, D. Gonbeau, A. S. Prakash, M. L. Dupont, K. Hemalatha, J. M. Tarascon, *Chem. Mater.* **2013**, *25*, 1121.

[5] M. Oishi, T. Fujimoto, Y. Takanashi, Y. Orikasa, A. Kawamura, T. Ina, H. Yamashige, D. Takamatsu, K. Sato, H. Murayama, H. Tanida, H. Arai, H. Ishii, C. Yogi, I. Watanabe, T. Ohta, A. Mineshige, Y. Uchimoto, Z. Ogumi, *J. Power Sources* **2013**, *222*, 45.

[6] M. Saubanére, E. McCalla, J. M. Tarascon, M. L. Doublet, *Energy Environ. Sci.* **2016**, *9*, 984.

[7] D. Seo, J. Lee, A. Urban, R. Malik, S. Y. Kang, G. Ceder, *Nat. Chem.* **2016**, *8*, 692.

[8] M. Oishi, K. Yamanaka, I. Watanabe, K. Shimoda, T. Matsunaga, H. Arai, Y. Ukyo, Y. Uchimoto, Z. Ogumi, T. Ohta, *J. Mater. Chem. A* **2016**, *4*, 9293.

[9] R. Wang, X. He, L. He, F. Wang, R. Xiao, L. Gu, H. Li, L. Chen, *Adv. Energy Mater.* **2013**, *3*, 1358.

[10] A. Ito, D. Li, Y. Ohsawa, Y. Sato, *J. Power Sources* **2008**, *183*, 344.

[11] A. Ito, D. Li, Y. Sato, M. Arao, M. Watanabe, M. Hatano, H. Horie, Y. Ohsawa, *J. Power Sources* **2010**, *195*, 567.

[12] G. Kobayashi, Y. Irii, F. Matsumoto, A. Ito, Y. Ohsawa, S. Yamamoto, Y. Cui, J. Y. Son, Y. Sato, *J. Power Sources* **2016**, *303*, 250.

[13] B. Song, S. J. Day, T. Sui, L. Lu, C. C. Tang, A. M. Korsunsky, *Phys. Chem. Chem. Phys.* **2016**, *18*, 4745.

[14] C. J. Chen, W. K. Pang, T. Mori, V. K. Peterson, N. Sharma, P. H. Lee, S. H. Wu, C. C. Wang, Y. F. Song, R. S. Liu, *J. Am. Chem. Soc.* **2016**, *138*, 8824.

[15] M. M. Thackeray, S. H. Kang, C. S. Johnson, J. T. Vaughey, R. Benedek, S. A. Hackney, *J. Mater. Chem.* **2007**, *17*, 3112.

[16] J. Bréger, M. Jiang, N. Dupré, Y. S. Meng, Y. Shao-Horn, G. Ceder, C. P. Gray, *J. Solid State Chem.* **2005**, *178*, 2575.

[17] A. Boulineau, L. Simonin, J. F. Colin, C. Bourbon, S. Patoux, *Nano Lett.* **2013**, *13*, 3857.

[18] A. Ito, Y. Sato, T. Sanada, M. Hatano, H. Horie, Y. Ohsawa, *J. Power Sources* **2011**, *196*, 6828.

[19] H. Stragier, J. O. Cross, J. J. Rehr, L. B. Sorensen, C. E. Bouldin, J. C. Woicik, *Phys. Rev. Lett.* **1992**, *69*, 3064.

[20] V. Petříček, M. Dušek, L. Palatinus, *Kristallogr.* **2014**, *229*, 345.

[21] T. Matsunaga, H. Komatsu, K. Shimoda, T. Minato, M. Yonemura, T. Kamiyama, S. Kobayashi, T. Kato, T. Hirayama, Y. Ikuhara, H. Arai, Y. Ukyo, Y. Uchimoto, Z. Ogumi, *J. Phys. Chem. Lett.* **2016**, *7*, 2063.

[22] T. Kawaguchi, K. Fukuda, K. Tokuda, K. Shimada, T. Ichitsubo, M. Oishi, J. Mizuki, E. Matsubara, *J. Synchrotron Radiat.* **2014**, *21*, 1247.

[23] P. Strobel, B. Lanbert-Andron, *J. Solid State Chem.* **1988**, *75*, 90.

[24] K. Shimoda, T. Minato, K. Nakanishi, H. Komatsu, T. Matsunaga, H. Tanida, H. Arai, Y. Ukyo, Y. Uchimoto, Z. Ogumi, *J. Mater. Chem. A* **2016**, *4*, 5909.

[25] A. D. Robertson, P. G. Bruce, *Chem. Mater.* **2003**, *15*, 1984.

[26] J. R. Croy, K. G. Gallagher, M. Balasubramanian, Z. Chen, Y. Ren, D. Kim, S. H. Kang, D. W. Dees, M. M. Thackeray, *J. Phys. Chem. C* **2013**, *117*, 6525.

[27] S. F. Amalraj, B. Markovsky, D. Sharon, M. Talianker, E. Zinigrad, R. Persky, O. Haik, J. Grinblat, J. Lampert, M. Schulz-Dobrick, A. Garsuch, L. Burlaka, D. Aurbach, *Electrochim. Acta* **2012**, *78*, 32.

[28] A. N. Mansour, J. McBreen, C. A. Melendres, *J. Electrochem. Soc.* **1999**, *146*, 2799.

[29] T. Kawaguchi, K. Fukuda, K. Tokuda, M. Sakaida, T. Ichitsubo, M. Oishi, J. Mizuki, E. Matsubara, *Phys. Chem. Chem. Phys.* **2015**, *17*, 14064.

[30] N. Yabuuchi, K. Yoshii, S. T. Myung, I. Nakai, S. Komaba, *J. Am. Chem. Soc.* **2011**, *133*, 4404.

[31] X. Zhang, X. Meng, J. W. Elam, I. Belharouak, *Solid State Ionics* **2014**, *268*, 231.

[32] A. R. Armstrong, M. Holzapfel, P. Novak, C. S. Johnson, S. H. Kang, M. M. Thackeray, P. G. Bruce, *J. Am. Chem. Soc.* **2006**, *128*, 8694.

[33] A. Deb, U. Bergmann, S. P. Cramer, E. J. Caims, *J. Appl. Phys.* **2005**, *97*, No. 113523.

Chapter 7. General Conclusions

Lithium-ion batteries have been used for all kinds of electronics from the appearance in 1991 to the present and have supported people's comfortable life. In order to realize a more comfortable and sustainable energy consumption society, it is necessary to further improve the performance of lithium-ion batteries. Therefore, it is important to understand complicated phenomena at future promising next generation battery materials. In this research, we focused on elucidating the reaction mechanisms of the next generation high energy cathode materials by using advanced analysis technology. Dynamic analysis of the cathode materials was investigated using an in operando high rate measurement technique which has developed remarkably with synchrotron radiation facility in recent years to understand the origin of high rate delithiation/lithiation mechanism. Moreover, several ex situ measurements optimized in battery materials were carried out to comprehend the fine structural analysis at equilibrium state.

In chapter 1, outline of lithium-ion battery and its operation principle were described. The measures to increase the energy of batteries were briefly discussed and summarized the research objective with introduced of the advanced analysis technologies.

In chapter 2, delithiation and lithiation behaviors of ordered spinel $LiNi_{0.5}Mn_{1.5}O_4$ and disordered spinel $LiNi_{0.4}Mn_{1.6}O_4$ were investigated by using in operando ^{7}Li NMR and ex situ ^{6}Li MAS NMR spectroscopy. The in situ ^{7}Li monitoring of the ordered spinel revealed a clear appearance and subsequent disappearance of a new signal from the well-defined phase $Li_{0.5}Ni_{0.5}Mn_{1.5}O_4$, suggesting the two-phase reaction processes among $Li_{1.0}Ni_{0.5}Mn_{1.5}O_4$, $Li_{0.5}Ni_{0.5}Mn_{1.5}O_4$, and $Li_{0.0}Ni_{0.5}Mn_{1.5}O_4$. Also, for the

disordered spinel, $Li_{0.5}Ni_{0.4}Mn_{1.6}O_4$ was identified with a broad distribution in Li environment. The tetragonal phases $Li_{2.0}Ni_{0.5}Mn_{1.5}O_4$ and $Li_{2.0}Ni_{0.4}Mn_{1.6}O_4$, which occurred when the cell was discharged down to 2.0 V, were very different in the Li environment from each other.

In chapter 3, the phase transition dynamics of $Li_xNi_{0.5}Mn_{1.5}O_4$ is elucidated on high rate charging-discharging using operando time-resolved X-ray diffraction (TR-XRD). The TR-XRD results indicate the existence of intermediate states, in addition to the thermodynamically stable phases, and it is shown that the origin of such intermediate states is ascribed to the solid-solution domains at the phase transition front, as supported by the analysis using transmission electron microscopy coupled with electron energy-loss spectroscopy. The phase transition pathways dependent on the reaction rate are shown, together with possible explanation for this unique transition behavior.

In chapter 4, we examined the crystal structures of $Li_2(Ni_xMn_{1-x})O_{3(-\delta)}$ (x = 0, 1/10, 1/6, and 1/4) to elucidate the relationship between the initial structure and electrochemical performance of the compounds using neutron and synchrotron X-ray powder diffraction analyses in combination. Our examination revealed that these crystals exhibit significant cation mixing in the transition-metal layers with gap of stoichiometric ratio; the cation mixing becomes significant with an increase in the Ni concentration. Charge-discharge measurements showed that the replacement of Mn with Ni lowers the potential of the charge plateau and leads to higher charge-discharge capacities.

In chapter 5, the oxidation/reduction behaviors of lattice oxygen and transition metals in a Li-rich manganese-based layered oxide $Li_2(Ni_xMn_{1-x})O_{3(-\delta)}$ (x = 1/4) are investigated by using hard X-ray photoelectron spectroscopy (HAX-PES). We clearly

confirm the formation of O^- ions as bulk oxygen species in the active material in the first cycling. The cation-anion dual charge compensation involving Ni and O ions is suggested during the voltage slope region of the charging process. The Ni ions in the material are considered to increase the capacity delivered by a reversible anion redox reaction with the suppression of O_2 as release. On the other hand, we found structural deterioration after the fifth cycled material. The O^- species are still observed but are electrochemically inactive during the fifth charge-discharge cycle. The structural rearrangement occurring after the activation process during the first charging, leading to the formation of spinel- or rocksalt-like domains in the sub-surface region of the particles.

In chapter 6, we examined $Li_2(Ni_xMn_{1-x})O_{3(-\delta)}$ (x = 1/4) as a model of Ni-substituted Li_2MeO_3 solid-solution cathodes to understand the effect of the substituted Ni on the electrode performances by using a combination of resonant X-ray diffraction spectroscopy (RXDS) and operando X-ray absorption spectroscopy. The change in the oxidation state and transbilayer migration of the transition metals as a function of the operating potential during the first charge-discharge processes were revealed by the site-selective analysis of RXDS. A part of the Ni ions irreversibly migrates to the Li layer during the charging and discharging processes. The Ni ions in the Li layer do not contribute to the charge compensation of the electrode. In contrast, all the Mn ions reversibly migrated to the Li layer re-migrate to the TM layer during the discharging processes. Remigration of the Mn ions to form the Li vacancy also contributes to the increase of the discharge capacity.

In chapter 7, the results of this thesis were summarized. By applying several advanced analysis techniques such as in operando NMR, in operando TR-XRD, neutron and synchrotron joint analysis, HAX-PES, in operando XAS and RXDS are proved that

the nonequilibrium and local structure of active materials play important roles for the performance of lithium ion battery. This thesis mainly focuses on the understanding the high-rate reaction and high-capacity mechanism of lithium ion battery.

For practical application of high energy lithium-ion battery materials, understanding of dynamic behavior and roles of all elements with spatial identification are required with these of multilateral and multiple analysis.

List of Publications

Chapter 2

Keiji Shimoda, Miwa Murakami, **Hideyuki Komatsu**, Hajime Arai, Yoshiharu Uchimoto, Zempachi Ogumi

"Delithiation/Lithiation Behavior of $LiNi_{0.5}Mn_{1.5}O_4$ Studied by In Situ and Ex Situ $^{6,7}Li$ NMR Spectroscopy"

J. Phys. Chem. C **2015**, *119*, 13472.

Chapter 3

Hideyuki Komatsu, Hajime Arai, Yukinori Koyama, Kenji Sato, Takeharu Kato, Ryuji Yoshida, Haruno Murayama, Ikuma Takahashi, Yuki Orikasa, Katsutoshi Fukuda, Tsukasa Hirayama, Yuichi Ikuhara, Yoshio Ukyo, Yoshiharu Uchimoto, Zempachi Ogumi

"Solid Solution Domains at Phase Transition Front of $Li_xNi_{0.5}Mn_{1.5}O_4$"

Adv. Energy Mater. **2015**, *5*, 1500638.

Chapter 4

Toshiyuki Matsunaga, **Hideyuki Komatsu**, Keiji Shimoda, Taketoshi Minato, Masao Yonemura, Takashi Kamiyama, Shunsuke Kobayashi, Takeharu Kato, Tsukasa Hirayama, Yuichi Ikuhara, Hajime Arai, Yoshio Ukyo, Yoshiharu Uchimoto, Zempachi Ogumi

"Structural Understanding of Superior Battery Properties of Partially Ni-Doped Li_2MnO_3 as Cathode Material"

J. Phys. Chem. Lett. **2016**, *7*, 2063.

Chapter 5

Keiji Shimoda, Taketoshi Minato, Koji Nakanishi, **Hideyuki Komatsu**, Toshiyuki Matsunaga, Hajime Tanida, Hajime Arai, Yoshio Ukyo, Yoshiharu Uchimoto, Zempachi Ogumi

"Oxidation behavior of lattice oxygen in Li-rich manganese-based layered oxide studied by hard X-ray photoelectron spectroscopy"

J. Mater. Chem. A **2016**, *4*, 5909.

Chapter 6

Hideyuki Komatsu, Taketoshi Minato, Toshiyuki Matsunaga, Keiji Shimoda, Tomoya Kawaguchi, Katsutoshi Fukuda, Koji Nakanishi, Hajime Tanida, Shunsuke Kobayashi, Tsukasa Hirayama, Yuichi Ikuhara, Hajime Arai, Yoshio Ukyo, Yoshiharu Uchimoto, Eiichiro Matsubara, Zempachi Ogumi

"Site-Selective Analysis of Nickel-Substituted Li-Rich Layered Material: Migration and Role of Transition Metal at Charging and Dischargign"

J. Phys. Chem. C **2018**, *122*, 20099.

Acknowledgements

The study on this thesis has been carried out at Office of Society-Academia Collaboration for Innovation and Graduate School of Human and Environmental Studies, Kyoto University.

First, I would like to wish to express my special gratitude to Prof. Yoshiharu Uchimoto at Graduate School of Human and Environmental Studies, Kyoto University, for his suggestion go on to the doctoral course, precise indications and valuable advices. I am also grateful to Prof. Hajime Arai at School of Materials and Chemical Technology Department of Chemical Science and Engineering, Tokyo Institute of Technology, for his useful discussions and advices to writing papers empathetically.

I would like to appreciate Dr. Yukinori Koyama at National Institute for Materials Science, for his effective suggestions of analysis method. I would also like to appreciate Dr. Taketoshi Minato, Dr. Keiji Shimoda, Dr. Koji Nakanishi and Prof. Toshiyuki Matsunaga at Office of Society-Academia Collaboration for Innovation, Kyoto University, for their effective discussions and advices to writing papers. I would also like to appreciate Dr. Tomoya Kawaguchi at Institute for Materials Research, Tohoku University, for his support on measuring and analysis RXDS. I would also like to thank to Dr. Ikuma Takahashi, Dr. Ito Atsushi, Dr. Masaharu Hatano at Nissan Research Center for support my study and financial support.

Special thanks are expressed to Prof. Yuichi Ikuhara, Dr. Tsukasa Hirayama, Dr. Takeharu Kato, Dr. Shunsuke Kobayashi at Japan Fine Ceramics Center for their helps on measuring TEM images and discussion these results.

I would like to thank to all the members of RISING project for their helps, discussions and precious experience. I also would like to appreciate Prof. Jun-ichi Yamaki at Office of Society-Academia Collaboration for Innovation, Kyoto University, for his encouragement to study lithium-ion battery. I am indebted to him for research on batteries form the postgraduate degree at Kyushu University. Also, I would like to appreciate Prof. Yuichi Sato at Faculty of Engendering, Kanagawa University, for his encouragement to study lithium-ion battery. He was a professor of my undergraduate and he has always been careful in doctoral studies. I am very happy to have valuable time with such many teachers.

Finally, I would like to appreciate my parents and my brother for their understanding, support and encouragement. I dedicate this thesis to my deceased father Tsutomu Komatsu.

Hideyuki Komatsu

20 November 2018

著作権等

"Oxidation behaviour of lattice oxygen in Li-rich manganese-based layered oxide studied by hard X-ray photoelectron spectroscopy" Keiji Shimoda, Taketoshi Minato, Koji Nakanishi, Hideyuki Komatsu, Toshiyuki Matsunaga, Hajime Tanida, Hajime Arai, Yoshio Ukyo, Yoshiharu Uchimoto, Zempachi Ogumi ("Journal of Materials Chemistry A" May 2016, Volume 4, Issue 16, pp 5909-5916). doi: 10.1039/c6ta01152g

"Site-Selective Analysis of Nickel-Substituted Li-Rich Layered Material: Migration and Role of Transition Metal at Charging and Discharging" Hideyuki Komatsu, Taketoshi Minato, Toshiyuki Matsunaga, Keiji Shimoda, Tomoya Kawaguchi, Katsutoshi Fukuda, Koji Nakanishi, Hajime Tanida, Shunsuke Kobayashi, Tsukasa Hirayama, Yuichi Ikuhara, Hajime Arai, Yoshio Ukyo, Yoshiharu Uchimoto, Eiichiro Matsubara, Zempachi Ogumi ("The Journal of Physical Chemistry C" August 2018, Volume 122, Issue 35, pp 20099-20107). doi: 10.1021/acs/jpcc.8b05539